Dissertation

submitted to the

Combined Faculty of Natural Sciences and Mathematics

of Heidelberg University, Germany

for the degree of

Doctor of Natural Sciences

Put forward by

Sarah May Rose Jeffreson

Born in:	Malvern East, Australia
Oral examination:	28.10.2020

Giant molecular clouds under the influence of the galactic environment

Referees: Dr. Diederik Kruijssen

Dr. Sabine Reffert

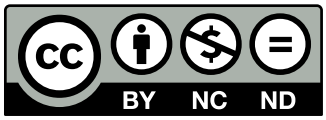

Zusammenfassung

Sternentstehung in Galaxien beginnt zu überwiegender Mehrheit in kalten, dichten und fraktal strukturierten Reservoirs von molekularem Wasserstoff, die als Riesenmolekülwolken bekannt sind. Aus den unmittelbaren Eigenschaften dieser Wolken und den Zeitskalen, auf denen sie sich entwickeln, können Modelle über die empirischen Eigenschaften der Sternentstehung auf galaktischer Skala entwickelt werden, welche zum Verständnis dieses Prozesses beitragen. In dieser Arbeit stellen wir zunächst einen einfachen analytischen Rahmen vor, um die erwartete Variation der physikalischen Eigenschaften und der Lebensdauer von Riesenmolekülwolken als Reaktion auf Veränderungen in ihrer galaktisch-dynamischen Umgebung zu quantifizieren. Dabei zeigt sich, dass sie innerhalb eines wesentlichen Parameterraums variieren, welcher die Bahnwinkelgeschwindigkeit der umgebenden Galaxie, das Ausmaßder galaktischen Scherung, die Gravitationsstabilität und den hydrostatischen Druck in der galaktischen Mittelebene umfasst. Anschließend erforschen wir diesen Parameterraum mit einer Reihe von hochauflösenden numerischen Simulationen von milchstraßenähnlichen Galaxien. Aufgrund ihrer hohen Dichten und Drücke relativ zur galaktischen Mittelebene stellen wir fest, dass Riesenmolekülwolken in milchstraßenähnlichen Galaxien selbstgravitierend und von der galaktischen Dynamik entkoppelt sind, im Gegensatz zu ihren Vorläuferwolken aus atomarem Gas geringerer Dichte, die systematische, galaktisch-dynamische Variationen aufweisen. Abschließend analysieren wir die gesamte Entwicklungsgeschichte jeder simulierten Wolkenpopulation in Abhängigkeit von der räumlichen Ausdehnung der Wolken. In allen milchstraßenahnlichen Umgebungen stellen wir fest, dass die Lebensdauer von selbstgravitierenden Wolken abnimmt je kleiner die Wolke im Vergleich zu der Aquivalenzhohe der dunnen galaktischen Gasscheibe, jedoch konvergiert sie zu der Scheibendurchquerungszeit sobald die Wolkenhohe die Aquivalenzhohe erreicht.

Abstract

The vast majority of star formation in galaxies begins in cold, dense, fractally-structured reservoirs of molecular hydrogen known as giant molecular clouds. The instantaneous properties of these clouds and the time-scales on which they evolve can therefore be built up into models of the empirical properties of galactic-scale star formation, and so can be used to understand this process. In this thesis, we first propose a simple analytic framework to quantify the expected variation in the physical properties and lifetimes of giant molecular clouds in response to changes in their galactic-dynamical environments, finding that they vary within a fundamental parameter space spanned by the orbital angular velocity of the host galaxy, the degree of galactic shearing, the gravitational stability, and the mid-plane hydrostatic pressure. We then explore this parameter space using a set of high-resolution numerical simulations of Milky Way-like galaxies. Due to their high densities and pressures relative to the galactic mid-plane, we find that giant molecular clouds in Milky Way-like galaxies are self-gravitating and decoupled from galactic dynamics, by contrast to their lower-density progenitor clouds of atomic gas, which display systematic, galactic-dynamical variations. Finally, we analyse the full evolutionary history of each simulated cloud population as a function of the cloud spatial scale. Across all Milky Way-like environments, we find that the lifetimes of self-gravitating clouds decrease with their spatial scale below the scale-height of the thin gas disc of the galaxy, and converge to the disc crossing time at its scale-height.

Contents

Chapter 1

Introduction and background

In the broadest terms, the field of star formation aims to determine the physical processes that control the conversion of gas to stars in galaxies. This entails the study of the gas, dust and cosmic radiation of interstellar medium, which permeates the space between the stars and extends its hierarchical structure over five orders of magnitude in spatial scale, from entire galaxies down to individual proto-stellar cores. Energy is fed from the largest to the smallest scales by a cascade of turbulent eddies, and from the smallest back to the largest scales by the vast shockwaves associated with the supernova explosions of massive, dying stars. These and countless other phenomena couple together the hierarchical strata, so that each depends intimately on the physical state of the others. Although the past few decades have seen great advancements in our understanding of the separate phases and physical mechanisms at work in the interstellar medium, its complexity has so far obstructed the path to a comprehensive model connecting our empirical picture of galactic star formation to the processes that drive it on smaller scales.

One promising approach to tackling this problem is to study and to model the observable galactic sites of star formation, their interaction with the wider interstellar medium on larger scales, and their physical, star-forming properties on smaller scales. With this goal in mind, the work presented in the following chapters addresses the influence of the large-scale galactic environment on the properties and evolution of *giant molecular clouds*: the large, cold reservoirs of molecular gas that provide the raw material for star formation.

This course of action presents its own unique set of challenges, associated primarily with bridging the gap between a *molecular cloud* as observable object and as a theoretical concept. In this thesis, we therefore remain agnostic to theoretical definitions of giant molecular clouds. The analytic portion of this work focusses on a set of hypothesised galactic-dynamical drivers for molecular cloud evolution, without reference to the properties of the clouds themselves. In order to identify and to pick molecular clouds out of our numerical simulations, we prefer to use observational selection criteria across a range of spatial resolutions. Finally, we perform a systematic examination of the role of the large-scale galactic environment in shaping the properties and evolution of giant molecular clouds in Milky Way-like galaxies, by comparing our numerical results to the analytic predictions.

The remainder of this chapter is devoted to an overview of the observational and theoretical connections between star formation and the molecular gas of the interstellar medium. We focus in particular on the observed properties of giant molecular clouds, the models of their evolution that have so far been put forward, and the implications of

these models for galactic-scale star formation.

1.1 Star formation and molecular gas

Much of our understanding of star formation in galaxies has its origin in empirical *star formation relations*. Each star formation relation shows the dependence of the star formation rate column density $\Sigma_{\rm SFR}$ on the column density of a particular kind of gas in the interstellar medium. Simply put, it tells us the degree to which star formation is correlated with the concentration of this gas type, when both quantities are measured at a particular scale.

The seminal form of the star formation relation (Kennicutt, 1998; Schmidt, 1959) examines the correlation between $\Sigma_{\rm SFR}$ and the total (atomic plus molecular) gas column density $\Sigma_{\rm gas}$ on the scales of entire galaxies. That is, one measurement for each quantity is made for each galaxy in the observed sample. These measurements are found to obey a power-law scaling of the form

$$\Sigma_{\rm SFR} \propto \Sigma_{\rm gas}^{1.4}, \tag{1.1}$$

so that the rate of star formation increases non-linearly with the total density of the gas in which the stars are formed. At first glance, the qualitative meaning of Equation (1.1) is unsurprising: denser gas is more likely to collapse under gravity and to form more stars. The mystery is contained in the non-linear form of the relation, and in the measured time-scale $\tau_{\rm dep}$ over which the gas is depleted via conversion to stars, known as the *depletion time-scale*. This is observed to have values spanning the range from 10^9 to 10^{10} Myr, which is over one hundred times longer than the gravitational free-fall time-scale in the gas! (Williams and McKee, 1997; Zuckerman and Palmer, 1974) This tells us that the physics of star formation is more complicated than simple gravitational collapse.

We note that in the two decades since the publication of the original star formation relation, further unresolved samples of different types of galaxies have been added to the $\Sigma_{\rm gas}$-$\Sigma_{\rm SFR}$ plane. High-redshift galaxies (Daddi et al., 2010; Genzel et al., 2010), dwarf galaxies and galaxies of low surface-brightness (Wyder et al., 2009) now complement the original selection of spiral galaxies and star-bursting galaxies. The additional data provide some evidence for a number of distinct 'star-formation sequences' at different locii in the plane, however the array of different measurement techniques employed by the authors mean that these results are tentative (Krumholz, 2015).

For the purpose of this thesis, we are more interested in the work that has been done to distinguish the sites of star formation themselves. This entails higher-resolution observations of the molecular gas column density $\Sigma_{\rm H_2}$ on sub-galactic scales. On spatial scales between 0.5 pc and 1 kpc, a much tighter correlation with the star formation rate surface density is observed for $\Sigma_{\rm H_2}$ than for $\Sigma_{\rm gas}$ (Bigiel et al., 2008; Leroy et al., 2013b; Rownd and Young, 1999; Schruba et al., 2011; Wong and Blitz, 2002), along with a constant depletion time on the order of 2×10^9 yr (Leroy et al., 2009; Saintonge et al., 2011a,b), such that

$$\frac{\Sigma_{\rm SFR}}{\rm M_\odot\ kpc^{-2}\ yr^{-1}} \sim 2 \times 10^9 \frac{\Sigma_{\rm H_2}}{\rm M_\odot\ kpc^{-2}}. \tag{1.2}$$

These studies provide the primary evidence that the majority of star formation is localised to giant molecular clouds (Kennicutt and Evans, 2012), along with the close observed association between molecular gas and the ionised bubbles around massive stellar clusters,

known as *HII regions* (Morris and Rickard, 1982). Despite having 'zoomed in' on the regions of star formation, however, the measured depletion time remains hundreds of times longer than the free-fall time-scale.[1] The physical processes that limit the conversion of gas to stars in clouds correspond to the physical processes that limit the conversion of gas to stars in galaxies.

A particularly interesting set of case studies for the low efficiency of star formation is provided by the central few kiloparsecs of galaxies, known as *galactic centres*. Our own Galactic centre (also known as the *Central Molecular Zone*) is the most conveniently-located for observations, and is found to contain a larger concentration of high-density molecular gas than at any other location in the Milky Way (Ferrière et al., 2007; Morris and Serabyn, 1996). Its average volume density exceeds that of the galactic disc by over one hundred times, and its temperature is over ten times higher (Ao et al., 2013; Bally et al., 1987; Longmore et al., 2013a). In spite of these differences in the physical state of the molecular gas, it falls on the same $\Sigma_{\rm H_2}$-$\Sigma_{\rm SFR}$ relation as the outer Galactic disc, with depletion times of around 10^8 yr (Barnes et al., 2017; Kauffmann et al., 2017; Kruijssen et al., 2014; Longmore et al., 2013a). In Chapter 3 we examine the galactic-dynamical time-scales on which the molecular gas evolves in the Galactic centre, and quantify the probability that it is largely supported against gravitational collapse by a high degree of differential rotation, with episodes of star formation triggered by close pericentre passages (Henshaw et al., 2016; Longmore et al., 2013b; Rathborne et al., 2014).

The large value of the molecular gas depletion time indicates that one of three following scenarios (or a combination of multiple of these) applies:

1. The temporal duration of star-forming episodes $\tau_{\rm SF}$ within molecular gas is much longer than the free-fall time-scale, $\tau_{\rm ff}$. Each star-forming episode converts gas to stars at a high overall efficiency $\epsilon_{\rm SF}$, but the self-gravity of the region is opposed by some physical process that provides support against global gravitational collapse, slowing it down (e.g. Goldreich and Kwan, 1974; Liszt et al., 1974).

2. The individual episodes of star formation are short and produce stars at a high-efficiency, but punctuated by long periods of quiescence, $\tau_{\rm q}$. The molecular gas survives and remains coherent for long periods of time before it is 'activated' to form stars, for example by a collision with another cloud (e.g. Tan, 2000; Tasker and Tan, 2009; Whitworth et al., 2018) or by interaction with a galactic bar or spiral arm (e.g Ho et al., 1997; Meidt et al., 2013; Roberts, 1969; Wyse, 1986; Wyse and Silk, 1989).

3. The individual episodes of star formation occur quickly, but are highly-inefficient at converting gas into stars, peaking at a conversion effiency of $\epsilon_{\rm SF} \sim 1$ per cent per unit of the molecular gas mass. This could be due to the fractal structure of the interstellar medium (e.g. Elmegreen, 1990, 1993, 2002; Elmegreen and Falgarone, 1996; Heitsch et al., 2009; Mac Low and Ossenkopf, 2000; Rosolowsky et al., 1999; Vázquez-Semadeni, 2004), to incomplete collapse of independent molecular clouds (e.g. Federrath and Klessen, 2012; Hennebelle and Chabrier, 2011; Krumholz

[1]It is interesting to note that in the densest observable regions of molecular clouds, at around one hundred to one thousand times the average molecular gas volume density, the depletion times are slightly shorter than the average values for entire clouds. However, they are still around one hundred times the value of the local free-fall time-scale.

et al., 2018; Krumholz and McKee, 2005; Padoan et al., 2014; Padoan and Nordlund, 2011), or due to the disruption of gravitational collapse by stellar feedback (e.g. Ostriker and Shetty, 2011).

Despite vast differences in the physics considered by the theories cited above, all reproduce the power-law form of the star formation relation. That is, the time-scales $\tau_{\rm SF}$ and $\tau_{\rm q}$ and the efficiency $\epsilon_{\rm SF}$ contain important information about the physics of star formation, but are observationally-degenerate in the $\Sigma_{\rm gas}$-$\Sigma_{\rm SFR}$ plane, as

$$\Sigma_{\rm SFR} = \frac{\epsilon_{\rm SF}}{\tau_{\rm life}}\Sigma_{\rm H_2} \equiv \frac{\epsilon_{\rm SF}}{\tau_{\rm SF}+\tau_{\rm q}}, \tag{1.3}$$

where we have defined $\tau_{\rm life}$ as the *giant molecular cloud lifetime*: the overall survival time for coherent, observable regions of molecular gas on the spatial scale at which $\epsilon_{\rm SF}$ is measured[2]. The properties of molecular clouds and the time-scales associated with their evolution are therefore crucial pieces of information that are required to distinguish between theories of star formation. With this motivation in mind, this thesis examines the lifecycles of giant molecular clouds and the physical processes that drive them.

1.2 Giant molecular clouds

As discussed in the previous section, molecular hydrogen (H_2) is the reservoir that directly feeds star formation. The reason that stars form preferentially at high molecular fractions is suggested by the sharp increase in the prevalence of H_2 in the interstellar medium as the total volume density of hydrogen increases from one atom per cm^{-3} up to 100 cm^{-3}. The precise location of this transition is observed to depend primarily on the background field strength of ultraviolet (UV) photons emitted by stars, and on the metallicity of the interstellar medium (Dobbs et al., 2008, 2014; Glover and Mac Low, 2007; Gnedin et al., 2009; Krumholz, 2014; Krumholz et al., 2008, 2009; Pelupessy et al., 2006; van Dishoeck and Black, 1986). The dependence on metallicity can be explained in terms of the formation pathway of H_2 from atomic hydrogen, which relies on dust grain surfaces as a catalyst (Gould and Salpeter, 1963; Hollenbach and Salpeter, 1971; McCrea and McNally, 1960; van de Hulst, 1948). On the other hand, the dependence of the molecular transition on the UV radiation field is mainly due to the dissociation of H_2: unless the hydrogen molecules are well-shielded from the onslaught of UV photons, the energy imparted upon absorption of these photons splits the molecules apart faster than they can be re-formed. The fraction of hydrogen in the molecular phase is therefore strongly-dependent on how well H_2 is shielded from UV radiation, either by dust grains or by dense envelopes of other H_2 molecules.

Coincidentally, the background UV radiation field is also the primary process that heats the dense gas of the interstellar medium. The UV photons are not only absorbed by molecular hydrogen, but also interact with dust grains, imparting enough energy to eject high-energy electrons, which in turn interact with and heat the surrounding gas. This means that where dense gas is shielded from the destruction of its molecular hydrogen reservoir, it is also shielded from heating, and so is likely to reach much lower temperatures than the surrounding ambient medium. At lower temperatures, the Jeans mass (Jeans,

[2]We will later see that it is crucial to define the spatial scale on which the molecular cloud lifetime is measured, on account of the fractal structure of molecular gas in the interstellar medium.

1928), above which a spherical region of volume density ρ overcomes its internal thermal support and collapses under its own self-gravity, decreases as $M_{\rm J} \propto T^{3/2}$, so that colder gas is more likely to collapse and to form stars. As such, at the high densities for which hydrogen is shielded from UV radiation, and so arises predominantly in its molecular form, temperatures can also drop to the values of ~ 10 K at which star formation can occur.

1.2.1 Observations of giant molecular clouds

Unfortunately, the molecular hydrogen in giant molecular clouds is very difficult to observe directly. This is because the production of observable radiative emission from any molecule requires the loss of energy as it falls from a high-energy *excited state* to the lower-energy *ground state*. The lowest-energy excited state of H_2 with an allowed transition to the ground state is at a temperature of 510 K, or 500 K above the mean cloud temperature of 10 K. For each gram of material in a giant molecular cloud, only a single H_2 molecule can emit radiation directly, rendering it all but invisible to telescopes. Instead, observers of molecular clouds rely on emission of radiation from, or absorption of background radiation by, the other materials with which molecular hydrogen is commonly mixed up. Among others, these include absorption and emission of radiation by dust grains, line emission from the rotational transitions of the CO molecule, and at the highest gas densities within molecular clouds, from other molecules such as CS, HCO^+, HNC, HCN, and NH_3. Of these, the ^{12}CO $J1 \rightarrow 0$ rotational line is by far the most useful for tracing molecular gas for two reasons: (1) it is the second most common molecule in the interstellar medium after molecular hydrogen, and (2) it traces the location of molecular hydrogen because the two primary pathways to CO formation require chemical reactions that involve H_2.

The history of observational advances in detecting CO emission has driven much of the theoretical advancement in models of the interstellar medium and of the molecular clouds it harbours. Even before interstellar molecular hydrogen was detected, however, the concept of an interstellar medium filled with distinct 'clouds' was put forward (Blaauw, 1952; Routly and Spitzer, 1952) as an interpretation for interstellar optical absorption lines (Adams, 1949). At this time, the medium surrounding the clouds was thought to be of a sufficiently-high temperature to confine the clouds via thermal pressure, and so they were treated as interacting spheres (Clark, 1965; Field et al., 1969; Oort, 1954; Oort and Spitzer, 1955; Spitzer, 1956).

The first detection of molecular hydrogen in the interstellar medium (Carruthers, 1970) and of the ^{12}CO $J1 \rightarrow 0$ transition (Wilson et al., 1970) were made in 1970. This was followed in the late 1970s by the first maps of CO emission across the Galactic plane (Blitz and Thaddeus, 1980; Kutner et al., 1977; Lada, 1976), and in the late 1980s by the first survey of molecular gas in the Milky Way (Dame et al., 1987). With these observational developments came the discovery that a large fraction (by mass) of the interstellar medium is in the molecular phase (Burton and Gordon, 1978; Gordon and Burton, 1976; Sanders et al., 1984; Scoville and Solomon, 1975), and the first catalogues of giant molecular cloud properties were compiled (Scoville et al., 1987; Solomon et al., 1987).

Crucially, advancements in the detection of molecular tracers made it possible to observe that the gas within molecular clouds is supersonic and compressible (Larson, 1981; Myers and Benson, 1983). Turbulent motions dominate over thermal motions, such that

clouds cannot be thermally-confined, and are rather dynamically-evolving, interacting entities. This finding was complemented by the emergence of a new picture of the interstellar medium, as hierarchically-fragmented in its spatial structure, consistent with the self-similar distribution of densities expected due to turbulence (Falgarone et al., 1991; Pfenniger and Combes, 1994; Scalo, 1990, 1985). This turbulent picture of the interstellar medium explained the fact that many properties of molecular clouds obey scaling relations, including densities, velocity dispersions, sizes, masses and internal pressures.

Despite this hierarchical picture of the interstellar medium, the concept of clouds as distinct entities has remained popular for the simple reason mentioned in Section 1.1: these CO-luminous regions can be considered as units of star formation on a particular spatial scale. It is therefore useful to study the distributions of physical properties for large samples of these objects, as has been assembled by several large surveys to date (Bolatto et al., 2008; Colombo et al., 2014, 2019; Heyer et al., 2001; Miville-Deschênes et al., 2017; Oka et al., 2001; Rice et al., 2016; Roman-Duval et al., 2010; Schinnerer et al., 2013). Such surveys measure the properties of molecular gas across two spatial dimensions and one velocity dimension, where the latter is derived from the Doppler-shifts of the observed emission lines, enabling observers to determine not just the masses, sizes and column densities of the clouds, but also their dynamical properties (velocity dispersions, virial parameters and internal turbulent pressures).

Over the last few years, another approach has emerged, shying away from the identification of distinct molecular clouds and instead characterising the properties of the molecular gas across a range of spatial scales (Leroy et al., 2013a; Sun et al., 2020, 2018). This approach has the advantage of avoiding the ambiguity of cloud-identification algorithms, and of making explicit the scale- or resolution-dependence of each observable. However, it also suffers from a lack of versatility when making comparisons to analytic theory and numerical simulations, in the sense that the centres of the molecular gas over-densities are not defined on any spatial scale, and so it is not possible to make predictions about their rotational properties or interaction time-scales. In this thesis, we identify molecular clouds predominantly via a threshold on the CO luminosity, to select cloud-like objects in two dimensions across a range of spatial scales (Chapters 4 and 5). In Chapter 4, we also report some molecular gas properties without reference to any cloud identification procedure, as discussed above.

1.2.2 Observable properties of giant molecular clouds

Following the discussion of Section 1.2.1, it is possible to define molecular clouds observationally as large, cold over-densities at a particular spatial scale within the hierarchical structure of the interstellar medium, whose molecular hydrogen content is high-enough to allow the formation of, and line emission from, a significant population of CO molecules. Certainly, the molecular clouds studied in the simulations performed for this thesis, presented first in Chapter 4, are identified as such, by projecting the modelled CO luminosity of the simulated gas along the observer's line of sight. Structures identified in this way epitomise the typical mean properties of giant molecular clouds: masses ranging between 10^4 and 10^7 solar masses, temperatures of around 10 K, and a mean hydrogen volume density of ~ 100 cm^{-3}, one hundred times that of the ambient interstellar medium.

Larson's scaling relations

Despite their low temperatures, corresponding to a thermal sound speed of $c_s \approx 0.2\,\mathrm{kms}^{-1}$, the observed velocity dispersions of giant molecular clouds, measured via the molecular line-width of the rotational CO $J1 \rightarrow 0$ transition, generally range between much higher values from 3 to 10 kms^{-1}. This additional velocity spread famously follows a power-law relation with the spatial scale ℓ, or equivalently with the molecular cloud size (Larson, 1981). The original form of this *size-linewidth relation* is given by

$$\sigma/\mathrm{km\ s}^{-1} = 1.10(\ell/\mathrm{pc})^{0.38}, \tag{1.4}$$

where σ is the internal three-dimensional velocity dispersion of the cloud, although more recent measurements of the relation for clouds in Milky Way-like environments produce a wider range of power-law slopes from 0.3 to 0.7 (Beaumont et al., 2012; Caselli and Myers, 1995; Falgarone et al., 1992; Kauffmann et al., 2010a,b; Leisawitz, 1990; Shetty et al., 2012; Solomon et al., 1987). The relation is therefore approximately equivalent to the prediction for velocities driven by supersonic turbulence of a compressible fluid, for which the expected scaling is $\sigma \propto \ell^{0.5}$ (e.g. Federrath and Klessen, 2013; Kritsuk et al., 2007; McKee and Ostriker, 2007; Padoan, 1995).

Equation (1.4) was produced using a catalogue of molecular clouds identified across several orders of magnitude in spatial and density scales; that is, across several orders of magnitude in the hierarchical structure of the interstellar medium. From the same catalogue, Larson (1981) also presents a relation between the cloud mass M and velocity dispersion, demonstrating that most clouds are in a state of approximate virial balance between self-gravitation and internal turbulent support, as

$$\sigma/\mathrm{km\ s}^{-1} = 0.42(M/\mathrm{M}_\odot)^{0.42}. \tag{1.5}$$

The final relation presented in the original paper is between the average molecular hydrogen number density n_{H_2} and cloud size, implying that molecular clouds have a column density that is invariant with spatial scale, such that

$$n_{\mathrm{H}_2}/\mathrm{cm}^{-3} = 3400(\ell/\mathrm{pc})^{-1.10}. \tag{1.6}$$

The degeneracy of relations (1.4)-(1.6) presents a problem in determining the chain of causality and therefore the physical origin of each. Fortunately, as further data have been collected at better sensitivity and over a wider range of galactic environments (Bolatto et al., 2008; Heyer et al., 2009; Lombardi et al., 2010), the form of Larson's relations has been modified slightly: it has become clear that there is in fact a variation in the column densities Σ of molecular clouds as a function of their scales and velocity dispersions, such that

$$\frac{\sigma}{\ell^{0.5}} \propto \Sigma^{0.5}, \tag{1.7}$$

as reported by Heyer et al. (2009), which replaces Equation (1.6) and challenges the simple interpretation of Equation (1.4) in terms of a universal *turbulent cascade* of energies from eddies at the largest galactic scales down to the scales of viscous dissipation. Instead, it makes room for the interpretation that magnetohydrodynamic turbulence is the pervading source of supersonic motions in the interstellar medium (Cho et al., 2009; Lazarian, 1995; Mouschovias, 1987; Ostriker et al., 2001; Vestuto et al., 2003).

Surface density-linewidth relation at fixed spatial scale

Equation (1.7) implies one further modification to the original relations of Larson (1981): that the virial parameter $\alpha_{\rm vir} \propto \sigma^2/\Sigma$ varies with the spatial scale ℓ. At a fixed spatial scale, the Σ-σ plane is then a useful probe of a cloud's state of gravitational boundedness relative to its pressure confinement, as quantified by its internal turbulent pressure, $P_{\rm turb} \propto \Sigma\sigma^2$. Recent studies examining cloud populations across a range of extragalactic environments in this plane (Colombo et al., 2014; Sun et al., 2020, 2018) have found that giant molecular clouds sit along lines of constant virial parameter, spanning the range between $\alpha_{\rm vir} = 0.1$ (tightly gravitationally-bound) and $\alpha_{\rm vir} = 10$ (gravitationally-unbound).

Mass and size spectra

For the range of giant molecular cloud masses above $\sim 10^4$ $M_\odot$ that can reliably be resolved in observations, there exists a well-constrained mass spectrum with an upper truncation mass that varies between 3 and 8×10^6 $M_\odot$. This mass spectrum can robustly be described by a power-law of the form

$$\frac{N}{M} \sim M^{-\beta} \tag{1.8}$$

$$\implies N(>M) \sim M^{-\beta+1}, \tag{1.9}$$

where the second expression is the cumulative distribution of the first, and β is consistently measured to fall within the range $1.6 \leq \beta \leq 1.8$ (Colombo et al., 2019; Freeman et al., 2017; Heyer et al., 2001; Kramer et al., 1998; Miville-Deschênes et al., 2017; Roman-Duval et al., 2010; Rosolowsky et al., 2003; Solomon et al., 1987; Williams and McKee, 1997). The relatively low value of β implies that a large fraction of the molecular gas in galaxies is contained within the most massive clouds or cloud complexes, across all spatial scales of cloud identification.

The approximate sizes of giant molecular clouds can also be measured (Bolatto et al., 2008, 2013; Heiderman et al., 2010; Heyer et al., 2009; Roman-Duval et al., 2010; Solomon and Vanden Bout, 2005), though with the caveat that their footprints on the plane of the sky are assumed to be described by an ellipsoidal *effective radius* (Bertoldi and McKee, 1992; Colombo et al., 2019; Rosolowsky and Leroy, 2006; Solomon et al., 1987). When plotted as a spectrum, the spectral shape is observed to obey a power-law of the form

$$\frac{N}{\ell} \sim \ell^{-\beta_\ell} \tag{1.10}$$

$$\implies N(>\ell) \sim \ell^{-\beta\ell+1}, \tag{1.11}$$

with $\beta_\ell \sim 2.8$ (Colombo et al., 2019). The position of the turnover in the spectrum and of the upper truncation size depends on the scale at which the molecular cloud sample is identified, but we find in Chapter 5 that the slope of the power-law in our simulations is relatively constant as a function of the spatial resolution.

1.2.3 Modelling cloud formation and evolution

Following the measurement of the empirical star formation relation (Kennicutt, 1998; Schmidt, 1959) and the discovery that the molecular hydrogen of the interstellar medium is supersonically-turbulent and compressible (Larson, 1981; Myers and Benson, 1983),

there emerged two broad schools of thought relating the formation and evolution of molecular gas to its observable properties. The first begins from the observation that the molecular gas of the interstellar medium is hierarchically and fractally structured, forming part of the larger hierarchy of gas densities observed across different galactic environments (Bally et al., 1991, 1987; Elmegreen and Falgarone, 1996; Falgarone et al., 2009, 1991; Lee et al., 1990; Scalo, 1990, 1985). It obeys an approximately log-normal probability distribution of volume densities (Klessen, 2000; Nordlund and Padoan, 1999; Ostriker et al., 1999; Vazquez-Semadeni, 1994; Wada and Norman, 2001), and the power-law forms of the cloud-mass and cloud-size spectra can be derived directly from this density hierarchy (Burkhart, 2018; Elmegreen and Falgarone, 1996; Hopkins, 2012). Across three orders of magnitude of spatial scale, star formation is observed to occur in one or two crossing times (Efremov and Elmegreen, 1998; Elmegreen, 2000; Elmegreen and Efremov, 1996), implying that the turbulence-driven structure of the molecular gas produces high-density star-forming clumps at the intersections of turbulently-driven converging flows (Ballesteros-Paredes et al., 1999a,b; Elmegreen, 1991, 1993, 2007; Hartmann et al., 2001; Heitsch et al., 2005, 2006; Hennebelle and Pérault, 2000; Koyama and Inutsuka, 2002; Vázquez-Semadeni et al., 2007, 2006; Zamora-Avilés and Vázquez-Semadeni, 2014), while the majority of the remaining H_2 remains at densities too low for star formation. Cloud formation is therefore distinct from star formation (Elmegreen, 2000, 2002, 2003).

The connection of the hierarchical picture to the empirical form of the star formation relation can be seen via a simple argument, presented here following Elmegreen (2002, 2003). A volume density threshold $\rho_{\rm c}$ is hypothesised, above which star formation occurs in over-dense clumps. The efficiency of star formation within these clumps is assumed to be independent of the environment, taking a value of around 50 per cent (Matzner and McKee, 2000). If star formation occurs on a dynamical time-scale of $\tau_{\rm SF} \sim 1/\sqrt{G\rho}$ (approximately equal to the turbulent crossing time on galactic scales, and to the free-fall time on clump scales), then one can re-formulate the galactic-scale star formation relation in terms of the local rate $\tau_{\rm c} \sim 1/\sqrt{G\rho_{\rm c}}$ and efficiency $\epsilon_{\rm c}$ of star formation within the clumps, and the fraction $f_{\rm c}$ of the total galactic gas mass that they contain, such that

$$\Sigma_{\rm SFR} \sim \frac{\epsilon_{\rm SF}}{\tau_{\rm SF}}\Sigma_{\rm gas} \iff \rho_{\rm SFR} \sim \frac{\epsilon_{\rm c}}{\tau_{\rm c}} f_{\rm c}\rho_{\rm gas}. \tag{1.12}$$

Equation (1.12) is only valid if a constant disc scale-height is assumed for all galaxies falling on the empirical relation; a point to which we will shortly return. The relationship between $f_{\rm c}$ and $\rho_{\rm c}$ can then be determined in two separate ways: (1) by the log-normal distribution of volume densities due to supersonic turbulence, and (2) by the galactic-scale star formation relation. The intersection of (1) and (2) is found to be at $\rho_{\rm c}/\rho \sim \rho_{\rm c}/{\rm cm}^{-3} \sim 10^5$ and $f_{\rm c} \sim 10^{-4}$. Therefore, if it is assumed that stars form only above $\rho_{\rm c} \sim 10^5$ cm^{-3}, then the observed density distribution of gas in the galaxy gives a reasonable star formation efficiency of $\epsilon_{\rm SF} \sim 3$ per cent, and is consistent with the empirical location of galaxies in the $\Sigma_{\rm SFR}$-$\Sigma_{\rm gas}$ plane, as required.

One of the central problems with the above argument is that it reproduces the star formation relation $\Sigma_{\rm SFR} \propto \Sigma_{\rm gas}^{1.4}$ only when the dynamical time scales as $\tau \sim \Sigma^{-0.5}$, which assumes a constant scale-height for all galaxies that obey the empirical power-law. Another problem is that it assumes a fixed density $\rho_{\rm c}$ for the star-forming clumps, although there is little evidence for the existence of such a threshold. These problems have led to a second school of thought, which treats giant molecular clouds as distinct, virialised, turbulent entities moving within a lower-density inter-cloud medium (Federrath

and Klessen, 2012; Hennebelle and Chabrier, 2011; Krumholz and McKee, 2005; Padoan et al., 2014; Padoan and Nordlund, 2011). Collapse occurs within these clouds only for the fraction of gas that is sufficiently over-dense for self-gravity to overcome the support from supersonic turbulence, determined by the observed size-linewidth relation and by the log-normal distribution of gas densities. A key advantage of such a model is that it self-consistently reproduces the low star formation efficiency $\epsilon_{\rm SF} \sim 1$ per cent inside molecular clouds, by virtue of the small fraction of gas that actually collapses. However, the exact value of $\epsilon_{\rm SF}$ is also very sensitive to the adopted value of the cloud virial parameter $\alpha_{\rm vir}$ in particular, rising to 10 per cent if $\alpha_{\rm vir}$ is increased in value from one to two. Given that the universal gravitational boundedness of giant molecular clouds has recently been brought into question by both observations (Colombo et al., 2014) and simulations (Dobbs et al., 2011), the assumption that clouds are virialised entities is unfortunate. This is also a significant problem for theories of star formation that assume long periods of quiescence and coherence for independent clouds, preceding a 'triggering event' that activates star formation via compression, such as a cloud-cloud collision (Tan, 2000; Tasker, 2011; Tasker and Tan, 2009) or the passage of a spiral arm density wave (Ho et al., 1997; Wyse, 1986; Wyse and Silk, 1989). Theories of molecular cloud evolution that invoke turbulent support also give rise to a further question: how is the internal turbulence of molecular clouds maintained? This question is of course no threat to the theory itself, given that the size-linewidth relation is an empirical property of interstellar molecular gas. Nevertheless, it is interesting to note that some of the leading theories for cloud turbulence driving rely on hierarchical gravitational collapse itself, external driving by supernovae Kim and Ostriker (2015a,b), radiation pressure from massive stars, and converging flows associated with the process of cloud formation (Klessen and Hennebelle, 2010).

To date, no model has been able to self-consistently predict all of the measured observables relating to star formation (Kennicutt and Evans, 2012; Krumholz, 2014; McKee and Ostriker, 2007). In this thesis we make the connection between observable, CO-luminous molecular clouds and the wider galactic environment in which they live, by means of examining their coupling to large-scale galactic-dynamical processes. In so doing, we aim to provide a possible pathway between the empirical star formation relation and the regions of star formation that it describes.

Galaxy-scale simulations of giant molecular clouds

Aside from the analytic and sub galactic-scale numerical models presented above, much work has been done to simulate the formation, evolution and destruction of giant molecular clouds in larger-scale simulations of isolated disc galaxies, and even in fragments of cosmological volumes. Numerical studies of this kind can guide the development of future analytic models by isolating the minimal set of physical processes required to produce realistic populations of giant molecular clouds: they are closely comparable to the numerical simulations presented in Chapters 3 and 4 of this thesis. With just one (Dobbs et al., 2006) or two non-interacting (Dobbs, 2008; Dobbs and Bonnell, 2007) isothermal phases, the formation of a realistic mass distribution of giant molecular clouds is possible, via the combination of self-gravity and compression by the spiral density wave. With the addition of supernova explosions and magnetic fields, a realistic span of cloud virial parameters from $\alpha_{\rm vir} = 0.1$ up to $\alpha_{\rm vir} = 10$ can be obtained (Dobbs et al., 2011). Then, with supernovae plus the self-consistent modelling of H_2 and CO formation with the heating

and cooling of the interstellar medium (Dobbs et al., 2018, 2019), realistic populations of clouds can be produced that obey all the key observables: scaling relations, mass spectrum and size spectrum. Finally, with the addition of a few further physical ingredients, including the pressure from ionised gas around massive stellar clusters and the resolved conversion of the thermal to kinetic energy conversion from supernovae, the larger-scale star-forming properties of simulated galaxies can be matched to observations, in addition to the cloud-scale properties (Fujimoto et al., 2019, 2018). These include the resolved empirical star formation relation, the radial profiles of the galactic-scale gas and stellar velocity dispersions, column densities and scale-heights, and the partitioning of the interstellar medium among distinct phases of density and temperature. Beyond isolated disc galaxies, the influence of galaxy mergers on the cloud population (Tress et al., 2020), and the influence of the wider cosmological environment (Benincasa et al., 2019), can now also be evaluated.

1.2.4 Interaction with the large-scale galactic environment

One of the focal points of this thesis is to quantify systematically the role of large-scale galactic dynamics in shaping the lifecycles and properties of giant molecular clouds, beginning with clouds in Milky Way-like galaxies. In the future, we intend that a comparison between cloud-scale observations and the work presented in Chapters 2-5 will allow us to gauge the relative influence of galactic-scale and sub cloud-scale physics in setting the time-scales for star formation.

The motivation for this approach stems directly from a growing body of observational evidence that molecular cloud properties vary according to the galactic environments into which they are born. Recent improvements in the sensitivity of sub-millimeter and radio interferometers such as the Atacama Large Millimeter/Sub-millimeter Array (ALMA) have enabled observers of the interstellar medium to resolve cloud-scale properties of molecular gas outside the Milky Way (Elmegreen et al., 2017; Faesi et al., 2018; Schinnerer et al., 2013). These new measurements span a large dynamic range of environments over three orders of magnitude in the hydrostatic midplane pressure, incorporating clouds both inside and outside galactic spiral arms and bars, in high- and low-mass galaxies, and in a number of major mergers. They have revealed the following systematic trends:

1. An exponential decrease in the integrated star formation efficiency with galactocentric radius, implying a variation in the depletion time with the large-scale environment (Leroy et al., 2008).

2. A variation in the star formation efficiency per gravitational free-fall time $\epsilon_{\rm ff}$ with galaxy mass (Krumholz et al., 2019; Leroy et al., 2017; Utomo et al., 2018), whereby $\epsilon_{\rm ff}$ increases for lower-mass galaxies.

3. A positive dependence of cloud-scale velocity dispersions, surface densities and turbulent pressures on galaxy mass, along with elevated values in the central regions of strongly-barred galaxies (Sun et al., 2018).

4. A correlation of the cloud-scale turbulent pressure and of the integrated star formation rate with the mid-plane hydrostatic pressure of the galaxy (Sun et al., 2020).

In addition to these results, large samples of clouds across different environments within the Milky Way are also seen to depend on the galactic environment with the following systematic trends:

1. A variation of the slope of the size-linewidth and surface density-linewidth scaling relations across different Galactic environments (Colombo et al., 2019; Miville-Deschênes et al., 2017; Rice et al., 2016), including the outer disc (Heyer et al., 2001) and the Galactic centre (Oka et al., 2001), when measured on kpc-scales.

2. A variation in the galactic column density of molecular gas with the galacto-centric radius, as well between spiral-arm and inter-arm environments (Roman-Duval et al., 2010).

3. A variation in the mass spectra of giant molecular clouds with the Galactic environment, including the upper truncation mass and the slope of the power-law (Rice et al., 2016).

Each one of the above observational findings suggests that the local galactic potential and ambient environment plays a non-negligible role in setting the properties and evolutionary trajectories of giant molecular clouds. Given that each large-scale environment hosts its own distinct set of galactic-dynamical time-scales, in Chapter 2 of this thesis we introduce a theory to quantify the roles of different galactic-dynamical processes in setting molecular cloud lifetimes. In Chapters 4 and 5 we use the galactic-dynamical parameter space spanned by this theory to determine the roles of these same processes in setting cloud properties, by means of a direct comparison to numerical simulations.

1.2.5 The molecular cloud lifetime

As discussed in the previous section, the giant molecular cloud lifetime is a time-dependent quantity, which observationally must be inferred from a snapshot of information at a single time. This means that empirical values of the cloud lifetime have traditionally been determined by one of two methods: (1) recognising an evolutionary sequence for a chain of molecular clouds along a spatial trajectory at an instant in time and measuring their velocities and separations, and (2) assuming that the numbers of clouds distributed across a set of evolutionary phases at an instant in time are proportional to the respective temporal intervals for which they remain in each phase. Some examples of methods that adopt approach (1) are as follows:

1. Scoville and Hersh (1979); Solomon et al. (1979) use an evolutionary sequence in which clouds form predominantly in the shocks behind spiral arms and move into the inter-arm regions due to the difference in orbital angular velocities between the spiral arms and the galactic disc. Their presence in the inter-arm regions therefore indicates that giant molecular clouds live for hundreds of Myr.

2. Engargiola et al. (2003) note that molecular clouds are typically formed in filaments of atomic hydrogen, then move away from the filaments with a differential velocity that can be measured. By observing this differential velocity and counting the number of clouds outside atomic filaments, an upper limit on the cloud lifetime is obtained (10-20 Myr).

3. Meidt et al. (2015) identify sequences of evolving clouds in the inter-arm regions of M51, and compute the cloud lifetime as a fraction of the inter-arm travel time, giving values of 20-30 Myr.

The above models have the advantage of temporal precision if the differential velocities and spatial separations of the observed molecular clouds can be measured. However, they may over-estimate the cloud lifetime if the sampling interval is much longer than the actual time-scale for cloud disruption and re-formation. For example, the long lifetimes measured by Scoville and Hersh (1979) and Solomon et al. (1979), have been shown to characterise the survival times of hydrogen molecules that are cycled through many shorter phases of molecular cloud evolution (e.g. Kruijssen et al., 2019). In this sense, method (2) is more robust, and some examples of its application are as follows:

1. Blitz et al. (2007); Corbelli et al. (2017); Kawamura et al. (2009) identify three stages of the molecular cloud evolutionary sequence: (1) quiescence, (2) the appearance of HII regions around massive young stars, and (3) the appearance of stellar clusters, in combination with the HII regions. The time spent in each phase is taken to be proportional to the number of clouds observed in each phase at a given time. The time-scales associated with (1), (2) and (3) are normalised to an absolute reference time-scale given by the ages of the stellar clusters. This delivers a cloud lifetime of 20-30 Myr.

2. Murray (2011) note that the fraction of each cloud that forms stars can be related to its mass, when this mass is large ($> 10^6$ $M_\odot$). The cloud lifetime is then given by the average age spread of the stellar clusters formed, weighted by a mass ratio that quantifies the likelihood that a cloud is forming stars. This gives a cloud lifetime of 2-3 free-fall times for massive giant molecular clouds.

Although the use of models of type (2) does not require that clouds pass through a set of evolutionary stages in a particular order, it does imply that the clouds considered are independent regions, in the sense that they do not interact. If cloud mergers are common then a spuriously-small number of clouds could be observed in a particular evolutionary state, due to their identification as a single, larger cloud. Dobbs et al. (2015) find that such mergers occur frequently in their isolated galaxy simulations, at a rate of one every 0.1 Myr in spiral galaxies. In Chapter 5 we discuss a similar result for our numerical simulations in detail, and relate its implications.

To circumvent this problem, Kruijssen and Longmore (2014); Kruijssen et al. (2019, 2018) have proposed a method for constraining the lifetimes of molecular clouds on the scale-height of the galactic gas disc. By fitting the spatial variation of the observed bias in the flux ratio of molecular gas to stellar tracers both below and above the disc scale-height, constraints can be placed on the time-scale over which these large regions typically form and disperse, assuming that they are independent of each other. In Chapter 5 we show that this assumption of region-independence is approximately valid on large scales, and make a comparison between our numerically-derived cloud lifetimes and the results of this statistical method (Chevance et al., 2020).

1.3 This thesis

The body of work in this thesis represents a synthesis of analytic theory and numerical simulations to investigate (1) the role of the large-scale galactic environment in driving the evolution of giant molecular clouds, and (2) the variation of cloud properties and evolution as a function of spatial scale.

In Part I we propose an analytic framework through which to explore the influence of large-scale galactic-dynamics on molecular cloud properties and evolution. Within this model, we aim to make as few theoretical assumptions as possible about the nature of giant molecular clouds. This includes their sizes, shapes, degree of gravitational-boundedness and mode of gravitational collapse. Both observationally and in numerical simulations, wide ranges in all of these properties have been observed for objects identified as 'clouds': if we wish to systematically compare our theoretical work with observations, such assumptions should be avoided where possible. Instead, to gauge the influence of different galactic-dynamical processes on molecular clouds, we refer to the relative lengths of the time-scales on which they act.

In Part II we perform high-resolution numerical simulations to probe the theory presented in Part I, and to use its predictions as a guide for interpreting statistical correlations between cloud properties and their environments, as related in Chapter 4. In particular, the data from our simulations can be used to offer insight into the time-dependent evolution of giant molecular clouds, which is not directly-accessible in observations. With this information in hand, in Chapter 5 we also explore the inter-dependence of the spatial and temporal scales on which molecular gas evolves coherently.

Finally, we conclude by linking the results of our work back to the wider field of star formation, and examining how the properties, time-scales and correlations we have derived can be used to understand the empirical characteristics of star formation on larger scales.

Part I

An analytic model

Chapter 2

A general theory for the lifetimes of giant molecular clouds under the influence of galactic dynamics

Authors:
Sarah M. R. Jeffreson and J. M. Diederik Kruijssen

Published in *MNRAS 476 (2018) 3688*.

Sarah Jeffreson is the principal author of this article. The original idea was suggested by Diederik Kruijssen. Sarah Jeffreson developed this idea, derived the analytical model, performed the calculations, and produced the figures. Sarah Jeffreson wrote the manuscript with input from Diederik Kruijssen in the form of corrections and suggestions. Sarah Jeffreson responded to and implemented the improvements and changes suggested by the reviewer.

Monthly Notices of the ROYAL ASTRONOMICAL SOCIETY

MNRAS **476,** 3688–3715 (2018) doi:10.1093/mnras/sty594
Advance Access publication 2018 March 6

A general theory for the lifetimes of giant molecular clouds under the influence of galactic dynamics

Sarah M. R. Jeffreson★ and J. M. Diederik Kruijssen
Astronomisches Rechen-Institut, Zentrum für Astronomie der Universität Heidelberg, Mönchhofstraße 12-14, D-69120 Heidelberg, Germany

Accepted 2018 March 1. Received 2018 March 1; in original form 2017 November 28

ABSTRACT

We propose a simple analytic theory for environmentally dependent molecular cloud lifetimes, based on the large-scale (galactic) dynamics of the interstellar medium. Within this theory, the cloud lifetime is set by the time-scales for gravitational collapse, galactic shear, spiral arm interactions, epicyclic perturbations, and cloud–cloud collisions. It is dependent on five observable quantities, accessible through measurements of the galactic rotation curve, the gas and stellar surface densities, and the gas and stellar velocity dispersions of the host galaxy. We determine how the relative importance of each dynamical mechanism varies throughout the space of observable galactic properties, and conclude that gravitational collapse and galactic shear play the greatest role in setting the cloud lifetime for the considered range of galaxy properties, while cloud–cloud collisions exert a much lesser influence. All five environmental mechanisms are nevertheless required to obtain a complete picture of cloud evolution. We apply our theory to the galaxies M31, M51, M83, and the Milky Way, and find a strong dependence of the cloud lifetime upon galactocentric radius in each case, with a typical cloud lifetime between 10 and 50 Myr. Our theory is ideally suited for systematic observational tests with the Atacama Large Millimetre/submillimetre array.

Key words: stars: formation – ISM: clouds – ISM: evolution – ISM: kinematics and dynamics – galaxies: evolution – galaxies: ISM.

1 INTRODUCTION

As the sites of the majority of galactic star formation, giant molecular clouds (GMCs) and their life cycles are of critical importance in understanding and predicting the galactic star formation efficiency (SFE). In particular, the molecular cloud lifetime sets a time-scale for star formation that is degenerate with the SFE in the observational relation between the galactic star formation rate (SFR) and the gas mass (Kennicutt 1998). The SFE for a given unit of gas quantifies its ability to form stars, and so offers crucial insight into the conditions most conducive to star formation in the interstellar medium (ISM). To constrain this quantity from observations of the SFR, a reliable theory of the molecular cloud lifetime is required.

In contrast to past observational data supporting the notion of 'long' cloud lifetimes of order $\gtrsim$100 Myr (Scoville & Hersh 1979; Scoville & Wilson 2004; Koda et al. 2009), recent observations of the molecular ISM at high spatial resolution by Engargiola et al. (2003), Blitz et al. (2007), Kawamura et al. (2009), Murray (2011), Miura et al. (2012), and Meidt et al. (2015) have favoured much shorter lifetimes between 10 and 55 Myr. These shorter lifetimes are consistent with the characteristic time-scale of collapse for overdense clumps within the cloud substructure (Elmegreen 2000; Hartmann, Ballesteros-Paredes & Bergin 2001). While theories of long-lived GMCs support the view of clouds as distinct, gravitationally bound, virialized entities, as distinguished by a tight correlation between virial mass and CO luminosity (e.g. Solomon et al. 1987), short-lived GMCs appear to be dynamic and continually evolving, with highly complex life cycles (Dobbs & Pringle 2013). Observations such as those by Colombo et al. (2014) support this view, demonstrating a large scatter in the relationship between virial mass and CO luminosity, and thus a significant fraction of GMCs that may be gravitationally unbound. In fact, Dobbs, Burkert & Pringle (2011a) point out that over 50 per cent of the clouds observed by Heyer et al. (2009) are strictly unbound, with virial parameters $\alpha_{\rm vir} > 2$. These observations are in line with numerical simulations of molecular cloud evolution (Dobbs et al. 2011a; Dobbs & Pringle 2013), which produce largely unbound GMCs with star formation occurring in localized bound regions.

The diversity in the observed dynamical states of GMCs presents a challenge to theories of cloud formation and evolution that rely on theoretical assumptions about what constitutes a molecular cloud. Cloud evolution shaped by frequent intercloud collisions is proposed by Tan (2000) to be in agreement with the scaling relations between the gas surface density and the SFR surface density observed by Kennicutt (1998), however the theory accounts only for those clouds that are gravitationally bound (Gammie, Ostriker & Jog 1991) and supported against collapse by hydrostatic and magnetized

★ E-mail: s.jeffreson@uni-heidelberg.de

turbulent pressure, such that they live long enough for collisions to actually occur. Additionally, the anticorrelation between SFE and the shear parameter β expected in this model is not observed in spiral and dwarf galaxies (Leroy et al. 2008). Although cloud–cloud collisions may contribute to the evolution of certain clouds at certain values of β, it does not account for molecular clouds in all observable regions of the ISM.

Molecular clouds that persist in a state of gravitational free-fall throughout their lives without reaching virial equilibrium, via global collapse (Elmegreen 1993; Ballesteros-Paredes, Vázquez-Semadeni & Scalo 1999a; Ballesteros-Paredes, Hartmann & Vázquez-Semadeni 1999b; Hartmann et al. 2001; Vázquez-Semadeni, Ballesteros-Paredes & Klessen 2003; Vázquez-Semadeni et al. 2006; Heitsch et al. 2005, 2006) or via hierarchical collapse (Elmegreen 2007; Zamora-Avilés, Vázquez-Semadeni & Colín 2012; Zamora-Avilés & Vázquez-Semadeni 2014; Ibáñez-Mejía et al. 2016), are gravitationally bound by definition. Therefore, theories of cloud evolution that are dominated by gravitational collapse, as first proposed by Goldreich & Kwan (1974) and Liszt et al. (1974), do not account for clouds that are super-virial or unbound. If all clouds were bound and collapsing, we would expect a clear correlation between the Toomre Q stability parameter and the number of GMCs. Given that the majority of star formation occurs in molecular clouds, this would lead to a correlation between Q and the SFE per unit gas and per unit time, which is not observed (Leroy et al. 2008). Clouds that are not bound or collapsing may also play an important role in star formation. Like theories of cloud–cloud collisions, theories of cloud evolution dominated by gravitational collapse do not account for the wide variety of observable GMC properties.

The great variety and complexity of physics that may influence molecular clouds is further emphasized by the large number of physical processes that can successfully account for their large non-thermal line widths (Fukui et al. 2001; Engargiola et al. 2003; Rosolowsky & Blitz 2005). These include, but are not limited to, bulk radial motions due to a persistent state of gravitational free-fall (Ballesteros-Paredes et al. 1999c; Hartmann et al. 2001; Heitsch & Hartmann 2008), energy input due to cloud–cloud collisions (Tan 2000; Tasker & Tan 2009; Tasker 2011), external driving by supernovae (e.g. Kim & Ostriker 2015a,b), accretion of material via converging flows associated with cloud formation (Klessen & Hennebelle 2010), and large-amplitude, long-wavelength Alfvén standing-waves (e.g. Tassis & Mouschovias 2004; Mouschovias et al. 2006). Given that the virial state of GMCs scales with their velocity dispersions squared, it is to be expected that the variety of processes affecting GMC velocity dispersions also affect their boundedness, and hence their life cycles. It is therefore undesirable to limit the scope of cloud evolution theories to clouds with size scales, mass scales, and structures imposed by the assumptions of gravitational boundedness and virialization. The spread of $\approx$50 Myr among 'short' observed cloud lifetimes points towards a diverse range of astrophysical objects that can be observationally identified as GMCs. If a theory is to successfully account for the entire population, it must be correspondingly flexible.

A solution to this problem is suggested by the work of Leroy et al. (2017b), which shows that the SFE per unit time (i.e. the inverse of the gas depletion time) scales nearly linearly with the ratio of the squared velocity dispersion to the surface density, an indicator of cloud boundedness. As the majority of star formation occurs in GMCs, this environmental dependence of the SFR indicates that the evolution of GMCs is also strongly environmentally dependent, and a theory for molecular cloud lifetimes should be able to capture this environmental influence on cloud evolution. Using only the observable properties of the ISM, the time-scales of large-scale dynamical processes can be derived and combined to predict the environmentally dependent cloud lifetime, independent of the precise properties of GMCs, and of the theoretical distinction between processes of cloud formation and evolution.

In this work, we take a systematic approach to predicting the cloud lifetime, combining the time-scales for those dynamical processes with the greatest potential to influence molecular cloud evolution. These include gravitational collapse and cloud–cloud collisions, as well as epicyclic perturbations in the plane of the host galaxy, galactic shear, and spiral arm crossings, where applicable. We propose a theory of molecular cloud lifetimes that quantifies the complexities of GMC evolution as naively as possible, providing a platform upon which increasing levels of detail can be built in future work. Taking a simple but expansive approach allows us to dispense with arbitrary theoretical definitions of what exactly constitutes a molecular cloud, such that we do not need to make assumptions about its state of gravitational-boundedness, state of virialization, scale or structure. Rather than focusing on one particular evolutionary mechanism, we account for the coexistence of different mechanisms and how they may augment each other or compete against each other. Using this theory, we can provide systematic predictions of cloud lifetimes throughout the parameter space of observed galactic properties.

Our theory of GMC formation and evolution, being dependent upon large-scale galactic dynamics, will be observationally testable by applying the new statistical technique of the 'uncertainty principle for star formation' (Kruijssen & Longmore 2014) to the recently available wealth of high-resolution observations of the ISM, both at low and high redshifts (e.g. Hodge et al. 2012; Leroy et al. 2016). With this method, we gain access to cloud lifetimes, feedback time-scales and cloud separation lengths for a statistically representative sample of galaxies (Kruijssen et al. 2018; Haydon et al., in preparation; Hygate et al., in preparation), enabling the evolutionary life cycle of GMCs to be probed beyond the limited environment of the most nearby galaxies (Kruijssen et al., in preparation, Hygate et al., in preparation, Chevance et al., in preparation, Schruba et al., in preparation). This will provide a much more complete and systematic perspective than previously available, making a global theory of cloud evolution pertinent, viable, and testable.

The structure of this paper is as follows. In Section 2, we derive the time-scales of galactic-scale dynamics which may determine the rate of GMC formation and evolution. In Section 3, we describe how our model combines these time-scales to provide a comprehensive picture of cloud evolution over all of parameter space. In Section 4, we examine the competition between time-scales and their different regions of dominance in parameter space, the interpretation of which we discuss in Section 5. In Section 6, we apply our theory to predict cloud lifetimes in real galaxies, and finally we summarize our results and conclusions in Section 7.

2 TIME-SCALES OF CLOUD EVOLUTION

Here, we derive the time-scales for six different large-scale dynamical processes that affect the ISM and its constituent molecular clouds. Each time-scale is dependent only on the physical, observable properties of the ISM, presented in Table 1. In this work, we systematically develop a theory of cloud evolution and the cloud lifetime based exclusively on the observable large-scale dynamics of the ISM. As such, we refer to these time-scales throughout the remainder of this paper as the 'time-scales of cloud evolution'. The first five of these time-scales have a compressive effect on

Table 1. Dynamic ranges for the parameters in Section 2, listed in the first column. The second column gives the parameter ranges explored in this work (corresponding to the black vertical bars in Fig. 3). The choice of variable range for each of the other parameters is justified in Section 3.1. The third column gives the fiducial values of each parameter corresponding to the open circles in Fig. 3, and the literature references for these values are given in the fourth column. References: (1) Krumholz & McKee (2005), (2) Tan (2000), and (3) Gerhard (2011).

Variable	Dynamic range	Fiducial value	References
β	[0, 1)	0.5	–
Ω_P/Ω	[0.01, 8]	2	(3)
m	1,2,4	1,2,4	–
Q	[0.5, 15]	1.3	(1)
ϕ_P	[1, 9]	3	(1)
f_G	0.5	0.5	(2)

molecular clouds, while the sixth has a dispersive effect. We implicitly assume that the compressive processes lead to star formation and subsequently to cloud dispersal on a time-scale appropriate to stellar feedback, assumed to be shorter than the time-scales considered here.

2.1 Gravitational collapse of the ISM ($\tau_{\rm ff,\,g}$)

On scales shorter than the Toomre length λ_T within the galactic disc, approximately spherical regions of the ISM are susceptible to collapse on the local free-fall time-scale. We follow the derivation of Krumholz & McKee (2005), beginning with the generalization of gas pressure within the galactic plane to include the contribution of the stellar population, such that

$$P_g \approx \frac{\pi}{2}\phi_P G \Sigma_g^2. \tag{1}$$

The quantity ϕ_P is given according to Elmegreen (1989) as

$$\phi_P = 1 + \frac{\Sigma_s}{\Sigma_g}\frac{\sigma_g}{\sigma_s}, \tag{2}$$

where Σ_s and Σ_g are the stellar and gas surface densities respectively, while σ_s and σ_g are the stellar and gas velocity dispersions. The case of pure gas then corresponds to $\phi_P = 1$. Given that the mid-plane ISM volume density ρ_g scales with the mid-plane ISM pressure P_g, we can scale the Jeans equations by the constant factor ϕ_P from equation (1), to obtain the scale height h_g as

$$h_g = \frac{\sigma_g}{\sqrt{2\pi G \phi_P \rho_g}}, \tag{3}$$

which leads to the definition of ρ_g (Equation 36 in Krumholz & McKee 2005),

$$\rho_g = \frac{\phi_P \kappa^2}{2\pi Q^2 G}, \tag{4}$$

where $Q = \kappa\sigma_g/\pi G\Sigma_g$ is the Toomre stability parameter (Toomre 1964). Using this mid-plane ISM density, we can straightforwardly calculate the free-fall time-scale as

$$\tau_{\rm ff,\,g} = \sqrt{\frac{3\pi^2}{32\phi_P(1+\beta)}}\frac{Q}{\Omega}, \tag{5}$$

in terms of the Toomre Q, the orbital speed Ω, and the shear parameter β, which is defined by the rotation curve of the galaxy $v_c(R)$ as

$$\beta = \frac{{\rm d}\ln v_c(R)}{{\rm d}\ln R}. \tag{6}$$

Lower values of β indicate a higher degree of differential rotation, and for a given value of the angular speed Ω, this corresponds to a higher degree of galactic shearing. Note that $\tau_{\rm ff,\,g}$ is dependent only upon the properties β, Q, Ω, and ϕ_P of the ISM, via equation (5). It increases linearly as Q and decreases inversely as Ω^{-1}, with weaker dependencies on β and ϕ_P as $(1+\beta)^{-1/2}$ and $\phi_P^{-1/2}$, respectively. The time-scale $\tau_{\rm ff,\,g}$ is therefore dependent only on the rotation curve, the surface density profiles Σ_g and Σ_s, and the velocity dispersion profiles σ_g and σ_s of the host galaxy, via the definition of the Toomre Q parameter and the definition of ϕ_P (equation 2). Importantly, $\tau_{\rm ff,\,g}$ does not assume any properties of the cloud itself, and can therefore be used to quantify the rate of collapse across the varied spectrum of objects that are observationally classified as GMCs. In the next section, we will see that the introduction of a characteristic cloud mass scale restricts the applicability of the free-fall time-scale to gravitationally bound clouds of a particular size and structure. These assumptions are not appropriate to all GMCs, so we will argue that $\tau_{\rm ff,\,g}$ is the gravitational free-fall time-scale we require to encode gravitational free-fall in our theory.

2.2 Gravitational collapse of a Toomre-mass cloud ($\tau_{\rm ff,\,cl}$)

Given that the free-fall time of a roughly spherical region of gas scales as $\tau \propto \rho^{-1/2}$, we can relate the collapse time-scale $\tau_{\rm ff,\,cl}$ for a cloud of mean density $\rho_{\rm cl}$ to the collapse time-scale $\tau_{\rm ff,\,g}$ in the mid-plane, as

$$\frac{\tau_{\rm ff,cl}}{\tau_{\rm ff,g}} = \left(\frac{\rho_{\rm cl}}{\rho_g}\right)^{-1/2} \equiv \phi_\rho^{-1/2}, \tag{7}$$

where ρ_g is the mean mid-plane density of the ISM gas and the second equality defines the ratio of cloud to mid-plane densities $\phi_\rho = \rho_{\rm cl}/\rho_g$. Given that the cloud is formed via gravitational collapse of the ISM, it must have a higher overall density than the surrounding gas, such that $\phi_\rho > 1$. To calculate this ratio, we again follow Krumholz & McKee (2005) to obtain the cloud density $\rho_{\rm cl}$ in terms of its pressure $P_{\rm cl}$ and mass $M_{\rm cl}$ as

$$\rho_{\rm cl} = \left(\frac{375}{4\pi}\right)^{1/4}\left(\frac{P_{\rm cl}^3}{\alpha_{\rm vir}^3 G^3 M_{\rm cl}^2}\right)^{1/4}, \tag{8}$$

where $\alpha_{\rm vir}$ is the standard virial parameter (e.g. MacLaren, Richardson & Wolfendale 1988; Bertoldi & McKee 1992), given by

$$\alpha_{\rm vir} = \frac{5\sigma_{\rm cl}^2}{G\sqrt{\pi M_{\rm cl}\Sigma_{\rm cl}}}, \tag{9}$$

and $P_{\rm cl}$ is given by their equation (47) as,

$$P_{\rm cl} = \frac{3\pi}{20}\alpha_{\rm vir} G \Sigma_{\rm cl}^2. \tag{10}$$

Rather than taking the typical cloud mass scale $M_{\rm cl}$ to be the Jeans mass M_J, we instead opt to use the Toomre mass M_T (Toomre 1964), as in Reina-Campos & Kruijssen (2017). This ensures that we are looking at the largest collapsing scales, given by the Toomre length. In practice, this change is consistent with Krumholz & McKee (2005) due to their assumption of $Q \approx 1$, which gives an approximate equality between M_T and M_J, as mentioned in their section 3.

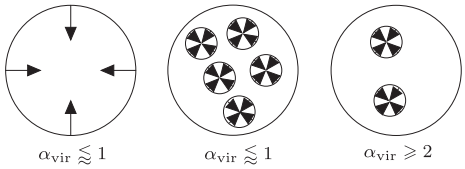

Figure 1. Illustration of possible modes of gravitational collapse. Global gravitational collapse towards the centre of mass necessarily means that the molecular cloud is gravitationally bound, with $\alpha_{\rm vir} \lesssim 1$ (left). A molecular cloud can also be gravitationally bound if it is collapsing hierarchically (centre), such that smaller regions within a larger diffuse envelope are collapsing. A cloud which is collapsing hierarchically can also be gravitationally unbound (right) if its overall internal kinetic energy is larger than its potential energy.

The critical Toomre mass corresponding to the maximum unstable length-scale is given by

$$M_{\rm T} = \frac{4\pi^5 G^2 \Sigma_{\rm g}^3}{\kappa^4}. \tag{11}$$

Following through with the derivation of ϕ_ρ, we obtain

$$\phi_\rho = \left(\frac{375}{32\pi^4}\right)^{1/4} \left(\frac{\phi_{\bar{\rm P}}^3}{\phi_{\rm P}\alpha_{\rm vir}^3}\right)^{1/4} Q^2, \tag{12}$$

where $\phi_{\bar{\rm P}}$ is defined as in equation (46) of Krumholz & McKee (2005), i.e.

$$P_{\rm cl} = \phi_{\bar{\rm P}} P_{\rm mp} = \frac{\pi}{2}\phi_{\bar{\rm P}}\phi_{\rm P} G \Sigma_{\rm g}^2, \tag{13}$$

cf. Elmegreen (1989) and Blitz & Rosolowsky (2004), with $P_{\rm mp}$ the mid-plane gas pressure in the galaxy. Since $\phi_\rho \geq 1$ by definition and $\phi_{\rm P} \geq 1$ according to equation (2), the range of $\alpha_{\rm vir}$ and $\phi_{\bar{\rm P}}$ values possible for a cloud of mass $M_{\rm T}$ is limited by equation (12) to

$$\frac{\phi_{\bar{\rm P}}}{\alpha_{\rm vir}} \gtrapprox \frac{2}{Q^{8/3}}. \tag{14}$$

The value of the time-scale, given by substituting equation (12) into equation (7), is

$$\tau_{\rm ff,cl} = \frac{\pi^{3/2}}{2}\left(\frac{3\alpha_{\rm vir}}{10\phi_{\rm P}\phi_{\bar{\rm P}}}\right)^{3/8} \frac{1}{\Omega}\frac{1}{\sqrt{1+\beta}}. \tag{15}$$

We note that in contrast to the time-scale $\tau_{\rm ff,\,g}$ in Section 2.1, $\tau_{\rm ff,\,cl}$ depends upon a set of pre-defined properties for each molecular cloud. Namely, it depends on the virial parameter $\alpha_{\rm vir}$ that quantifies the gravitational boundedness of the cloud, and the ratio of cloud pressure to that of the ambient gas, $\phi_{\bar{\rm P}}$. The values of these properties must be determined for each cloud, in order to compute its free-fall time-scale. Additionally, the introduction of a characteristic collapsing mass scale $M_{\rm T}$ assumes that the cloud is in a state of *global collapse* (i.e. collapsing radially towards its centre of mass) as depicted in the left-hand panel of Fig. 1. Global gravitational collapse necessarily implies gravitational boundedness ($\alpha_{\rm vir} < 1$). Combined with the assumption of a roughly spherical cloud, the mass scale $M_{\rm T}$ also sets a characteristic length-scale $\lambda_{\rm T}$ for the cloud, corresponding to the Toomre scale. The use of the time-scale $\tau_{\rm ff,\,cl}$ to quantify the influence of gravitational collapse on GMCs therefore implies a restriction to gravitationally bound, globally collapsing clouds of diameter $\lambda_{\rm T}$.

In the middle and right-hand panels of Fig. 1, we depict two situations in which a time-scale for gravitational collapse is required to describe the evolution of molecular clouds that do not fit the restrictions described above. In the middle panel, we demonstrate the possibility of a gravitationally bound cloud which is not collapsing globally but hierarchically, as theorized by Elmegreen (2007) and observed in simulations by Ibáñez-Mejía et al. (2016). In the right-hand panel, we demonstrate the possibility of hierarchical collapse within a molecular cloud that is not gravitationally bound at all, but that may be in fact be gravitationally unbound ($\alpha_{\rm vir} \geq 2$).

In this work, we aim to examine the processes affecting the evolution of all molecular clouds, rather than restricting ourselves to processes affecting the subset of gravitationally bound, globally collapsing clouds of radius $\lambda_{\rm T}$. As such, we opt hereafter to work with the free-fall time-scale of the ISM $\tau_{\rm ff,\,g}$, which also provides an upper bound on $\tau_{\rm ff,\,cl}$ via the definition of $\phi_\rho > 1$. While this allows our theory to be as general as possible, it is conceivable that it leads to an overestimation of the molecular cloud lifetime in atomic gas-dominated environments, in which only the gas density peaks are molecular. We return to this caveat in Section 6. For the remainder of this paper, we will refer to $\tau_{\rm ff,\,g}$ alone as the 'gravitational free-fall time-scale'. We do not need to assume values of the cloud properties $\alpha_{\rm vir}$ and $\phi_{\bar{\rm P}}$, leaving only the properties β, Q, Ω, and $\phi_{\rm P}$ of the ISM. These quantities can be determined observationally, and do not require us to impose theoretical constraints on the nature of molecular clouds.

2.3 Cloud–cloud collisions ($\tau_{\rm cc}$)

Tan (2000) derives a time-scale for collisions between gravitationally bound molecular clouds, as

$$\tau_{\rm cc} \approx \frac{2\pi Q}{9.4 f_{\rm G}\Omega(1+0.3\beta)(1-\beta)}. \tag{16}$$

The parameter $f_{\rm G}$ represents the 'probability of collision' associated with any single encounter between GMCs. Tan (2000) hypothesizes that such collisions trigger star formation by inducing compressions in parts of the interacting clouds. We will use $\tau_{\rm cc}$ to quantify the effect of cloud–cloud collisions on cloud evolution and the cloud lifetime, via compressions (Tan 2000), shocks, or simply mixing between regions of gas with different surface densities.

In principle, the time-scale $\tau_{\rm cc}$ increases monotonically with β. However, the range of β is limited to $0 < \beta < 0.12$, due to the underlying assumptions. equation (16) is based on the work of Gammie et al. (1991), who derive gas velocity dispersions for $0 < \beta < 0.12$, by considering the gravitational scattering between clouds due to galactic differential rotation, using an expansion about the equilibrium perturbative solution at $\beta = 0$ to first order in β. The perturbative solution is then numerically extended over a range corresponding to $-0.06 < \beta < 0.12$. By including higher orders, we could obtain a real (physical) value of the velocity dispersion up to $\beta = 0.36$, but this would involve an extrapolation of the numerical fit outside the range for which it has been verified in Gammie et al. (1991). Throughout this paper, we therefore use the value of $\tau_{\rm cc}$ at $\beta = 0.12$ for higher values of β, which is justified because it acts as a lower limit on the collision time-scale at $\beta > 0.12$. Given that the collisions are caused by differential rotation, the assumption that the collision time-scale will monotonically increase with β is also justified intuitively. Thus, the time-scale $\tau_{\rm cc}$ in our model increases with β over the range $0 \leq \beta < 0.12$ and remains constant with β over the range $0.12 \leq \beta$. Like the time-scale $\tau_{\rm ff,\,g}$ for gravitational collapse, $\tau_{\rm cc}$ decreases inversely as Ω^{-1}, since a higher angular speed gives a shorter time between collisions for clouds at different galactocentric radii, when differential rotation is present ($\beta \neq 1$).

The Q dependence of τ_{cc} is linear, because the mean-free time between cloud collisions scales inversely with the surface number density of gravitationally bound clouds (Tan 2000), which in turn is inversely proportional to Q. However, we must note that, in using τ_{cc} for values of gravitational stability $Q \gg 1$, we assume that these relations hold for very low number densities of bound clouds. In reality, for very small numbers of bound clouds in an ISM of finite scale height h_g, the time between collisions will approach infinity much faster than Q does. This assumption is therefore likely to overestimate the number of cloud collisions per unit time, and thus (again) to provide a lower limit to the cloud lifetime due to cloud–cloud collisions. Despite this, we will see later that cloud–cloud collisions are rarely significant in comparison to the other dynamical mechanisms of cloud evolution, from $Q \sim 0.5$ up to 15. We will therefore use τ_{cc} as the time-scale for cloud–cloud collisions for all Q, and will comment on the interpretation of the resulting cloud lifetimes, where appropriate.

2.4 Pattern speed perturbations (τ_{Ω_P})

The passage of spiral arms through the ISM at pattern speed Ω_P has a wide variety of possible effects on GMCs (for more detailed discussions, see Meidt et al. 2013; Dobbs & Baba 2014). The sudden change in mass surface density, pressure, and gravitational potential associated with a spiral arm encounter induces a shock in the ISM (Roberts 1969), although whether this shock triggers gravitational collapse remains uncertain (e.g. Elmegreen & Elmegreen 1986; Eden et al. 2012, 2015). Aside from the shock itself, the cloud is subjected to varying tidal and Coriolis forces by a non-axisymmetric gravitational potential (Elmegreen 1979), with a generally compressive effect. The conservation of angular momentum then implies that the degree of azimuthal shearing is also lower in the spiral arm than in the galactic disc (Elmegreen 1994). Both of these effects promote gravitational collapse, possibly explaining the high density of high-mass GMCs in spiral arms, an interpretation that is supported by the formation of massive, bound fragments in the magnetohydrodynamic simulations of Kim & Ostriker (2002) and Kim & Ostriker (2006). Meidt et al. (2013) show that in the case of M51, the gravitational potential associated with the grand-design spiral structure creates torques that drive large radial excursions of gas along the spiral arms at a much greater amplitude than within the galactic disc.

In addition to these dynamical effects, it is observed in simulations by Dobbs (2008) that the rate of cloud–cloud collisions is increased within spiral arms, due to increased levels of radial motion and an overall increase in cloud density. This may lead to an increased rate of gravitational collapse and star formation as in Tan (2000), or an increased rate of cloud agglomeration to produce more massive clouds. The non-axisymmetric structure of the galaxy itself may also influence the rate at which clouds are subjected to external sources of stellar feedback, as the majority of star formation in M51 is observed to preferentially occur along its spiral arms (Meidt et al. 2013).

The higher density of massive GMCs observed in simulations by Dobbs, Burkert & Pringle (2011b) also raises the question of whether clouds are swept up in spiral arms, or whether they preferentially form in spiral arms (e.g. Casoli & Combes 1982; Dobbs et al. 2008). Once a cloud enters a spiral arm, the time for which it remains there is not generally known.

We take the simplest possible approach to quantifying the effect of spiral arm interactions on GMCs. We do not consider the precise mechanisms by which clouds are affected by spiral arms, but instead consider only the time-scale on which encounters occur. This time-scale is given by

$$\tau_{\Omega_P} = \frac{2\pi}{m\Omega|1 - \Omega_P/\Omega|}, \tag{17}$$

where m is the number of spiral arms in the galaxy. In common with the time-scales derived previously, τ_{Ω_P} depends inversely on Ω. However, it has no dependence on β or Q, and is instead a function of two new parameters, m and Ω_P/Ω, associated with the presence of spiral arms. The time-scale decreases inversely with increasing numbers of spiral arms m, and increases asymptotically towards the radius of corotation as Ω_P/Ω approaches unity.

Our use of τ_{Ω_P} to quantify the effect of spiral arms on GMCs implicitly assumes that the effect of each encounter is life changing for the cloud, i.e. that in the absence of all other effects, the average cloud lifetime is determined by the average time before which it encounters a spiral arm. Given the large differences in cloud properties observed between arm and interarm regions (Elmegreen & Elmegreen 1983; Meidt et al. 2013; Dobbs et al. 2008, 2011b), along with the large differences in the density of clouds between these regions, this assumption appears to be justified.

Inclusion of this spiral arm crossing time-scale must be considered on a case-by-case basis when considering molecular clouds in real galaxies. For example, it would not be appropriate for clouds which spend their whole lives inside a spiral arm, in which case it would be better to consider just the environmental conditions within the spiral arm. The case of very weak spiral arms might equally be treated by setting $m = 0$ (see Section 6.1).

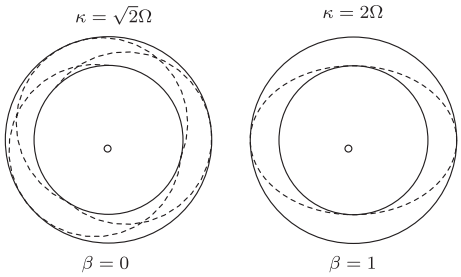

Figure 2. Epicyclic orbits in the plane of the galactic disc for the case of a flat rotation curve (left, $\kappa = \sqrt{2}\Omega$) and a solid-body rotation curve (right, $\kappa = 2\Omega$). Note that in the case of a higher shear parameter β (right), the number of epicycles performed per orbit of the galactic centre is greater, and thus for fixed Ω, the number of epicycles performed per unit time is also greater. This effect outweighs the slight decrease in epicyclic amplitude as β increases at fixed Ω.

2.5 Epicyclic perturbations (τ_κ)

Within the epicyclic approximation, the ambient ISM and its constituent molecular clouds are subjected to harmonic radial perturbations relative to the guiding centres of circular orbits about the galactic centre. The epicyclic frequency κ of these oscillations is set by the angular speed and the shear parameter β as

$$\kappa = \Omega\sqrt{2(1+\beta)}, \tag{18}$$

which has extreme values of $\kappa = \sqrt{2}\Omega$ for a flat rotation curve (left-hand panel of Fig. 2) and $\kappa = 2\Omega$ in the solid-body regime (right-hand panel of Fig. 2). On the galactic scale, the primary effect of epicycles is to introduce eccentricity to an otherwise circular orbit around the galactic centre. On cloud scales, epicycles cause a

molecular cloud to perform small elliptical circuits about a guiding centre that moves with the angular velocity Ω of the bulk ISM at some galactocentric radius R_g. These circuits subject the cloud to radial variations in galactic environment, such as variations in tidal force and pressure, and also to tangential variations relative to the guiding centre (i.e. relative to a cloud that is moving on a non-epicyclic, circular orbit at angular frequency Ω). Such tangential variations may include an increased number of interactions with other objects (that may be undergoing similar excursions), as well as stretching and compression due to acceleration relative to the guiding centre.

As with the other cloud evolutionary mechanisms, we aim to quantify all the possible effects of epicycles using a single time-scale τ_κ. We consider the time-scale

$$\tau_\kappa = \frac{\pi}{\kappa} \frac{\pi R_g / N}{\pi \sqrt{\frac{X^2+Y^2}{2}}}, \tag{19}$$

where N is the number of epicycles around the guiding centre per revolution around the galactic centre, given by

$$N = \frac{\kappa}{\Omega}, \tag{20}$$

and (X, Y) are the amplitudes of epicyclic oscillations from the guiding centre in the radial and tangential directions, respectively. The first term in equation (19), π/κ, gives the time required for the cloud to move from its orbital apocentre to its orbital pericentre, or vice versa. [1] This is scaled by a second term, which quantifies the effect of epicycles relative to an object at the same galactocentric radius on a circular orbit, moving with the bulk ISM at an angular velocity Ω. Relative to such an object, the cloud with epicyclic motion moves a distance $\pi\sqrt{(X^2+Y^2)/2}$ during the time π/κ, while the object itself moves a distance $\pi R_g/N$ relative to the galactic centre. Any large-scale galactic variations experienced by the cloud as it orbits the galactic centre, such as encounters with spiral arms or with other clouds, will be experienced by any object at the radius R_g, regardless of whether epicycles are performed. Thus, we normalize the relative epicyclic motion, $\pi\sqrt{(X^2+Y^2)/2}$, by the guiding centre motion, $\pi R_g/N$. Due to the expression X^2+Y^2, the influence of epicycles becomes greater if the amplitude of epicyclic motion is greater, while the terms κ and N indicate that the influence of epicycles becomes greater when they occur at a higher frequency relative to the bulk motion of the ISM.

Our theory aims to be as general as possible, so does not assume a precise cause for epicyclic perturbations. We do not set initial conditions for epicyclic motion and so do not explicitly calculate the quantity X/R_g. Instead, we quantify the magnitude of this ratio by taking the average value of a uniform distribution between $X/R_g = 0$ and the upper bound $X/R_g = 1/2$, set by the conservation of angular momentum within the epicyclic approximation (see Appendix A). This gives a value of

$$\frac{X}{R_g} \approx \frac{1}{4}. \tag{21}$$

Bringing together equations (19)–(21), and substituting $\gamma = \sqrt{2/(1+\beta)}$ (see equation A6), the expression for τ_κ can be reduced to

$$\begin{aligned}\tau_\kappa &= \frac{\pi}{\kappa}\frac{R_g}{X}\sqrt{\frac{2}{1+\gamma^2}}\frac{\Omega}{\kappa} \\ &= \frac{4\pi}{\kappa}\sqrt{\frac{2(1+\beta)}{3+\beta}}\frac{1}{\sqrt{2(1+\beta)}} \\ &= \frac{4\pi}{\Omega\sqrt{2(1+\beta)}}\frac{1}{\sqrt{3+\beta}}.\end{aligned} \tag{22}$$

That is, the time-scale on which epicyclic oscillations make a significant contribution to cloud evolution increases weakly as the rotation curve flattens (towards low β). This is due to the reduction in epicyclic frequency κ with decreasing β at fixed Ω, which increases the number of epicyclic oscillations performed per unit time, and per unit distance travelled around the galactic centre by a cloud on a circular, non-epicyclic orbit. This effect balances the increasing circumference of each epicycle with decreasing β. Like the time-scales previously derived, τ_κ is inversely dependent on Ω, due to the linear correspondence between κ and Ω for fixed β. It is also independent of Q, having nothing to do with gravitational stability.

2.6 Shear within the galaxy (τ_β)

The shear time-scale τ_β is the time-scale on which a cloud is pulled apart by differential rotation, thus limiting the available growth time of gravitational instabilities (Goldreich & Lynden-Bell 1965; Elmegreen 1987). It is given by the inverse Oort constant, such that

$$\tau_\beta = \frac{2}{\Omega(1-\beta)}. \tag{23}$$

If the shear time-scale is comparable to or shorter than the gravitational free-fall time-scale $\tau_{\rm ff,\,g}$, the separation of radially correlated gas reduces the rate at which overdensities form, as well as slowing their subsequent collapse, thus increasing the cloud lifetime. If the shear time-scale is shorter than the gravitational free-fall time-scale $\tau_{\rm ff,\,g}$, shear may disperse clouds completely, or break them up into smaller entities (Dobbs et al. 2011a; Dobbs & Pringle 2013). This scenario also increases the cloud lifetime according to the statistical method for measuring cloud lifetimes from Kruijssen & Longmore (2014) and Kruijssen et al. (2018), which adds up the total time a Lagrangian mass element spends as a cloud, prior to star formation. That is, if a cloud is dispersed by shear and later reforms, the durations of both phases are added to calculate the observed lifetime. Galactic shear therefore works against the formation of collapsing overdensities in the ISM to generally elongate the lifetimes of GMCs. Shearing is strongest at high degrees of differential rotation (low β) and at high values of the angular speed Ω, such that τ_β displays the same Ω^{-1} dependence as all other time-scales derived in this section.

3 COMPARISON OF TIME-SCALES

3.1 Variable ranges

We now turn to a comparison of the time-scales derived in Section 2. A crucial insight in this regard is that all time-scales carry an inverse dependence on the orbital speed Ω, such that this quantity is irrelevant for the relative importance of the different time-scales, and acts as an overall normalization of the cloud lifetime. Throughout large parts of this paper, we will therefore express the time-scales in the

[1] Relative to the guiding centre, epicyclic motion is symmetric between the first and second halves of the circuit, and thus its time-scale is calculated for half an epicycle.

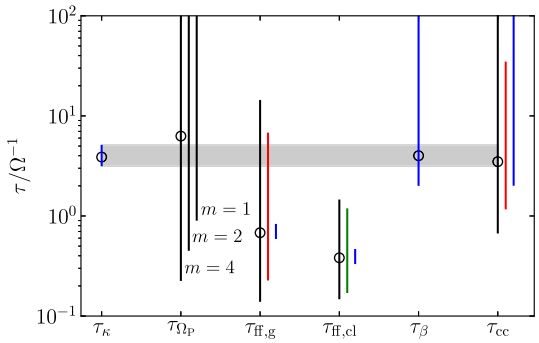

Figure 3. Dynamic ranges of each time-scale for the ranges of physical quantities given in Table 1, normalized by the orbital period Ω^{-1}. Black bars represent the total dynamic ranges of each time-scale, red bars represent the dynamic ranges due to varying Toomre Q alone, and blue bars represent the dynamic ranges due to varying the shear parameter β alone. The green bar represents the dynamic range of $\tau_{\rm ff,\,cl}$ due to simultaneously varying all three of the parameters $\alpha_{\rm vir}$, $\phi_{\rm P}$, and $\phi_{\bar{\rm P}}$. The black open circles indicate the fiducial values from the literature, listed in the third column of Table 1. The grey shaded region demonstrates that there exists a region of overlap for the dynamic ranges of all time-scales other than $\tau_{\rm ff,\,cl}$, which we omit in favour of $\tau_{\rm ff,\,g}$ (see Sections 2.1 and 2.2). The non-zero width of this grey shaded region is a necessary but not sufficient condition that, for at least one choice of quantities in Table 1, any one of these five relevant time-scales might be shorter than all others.

dimensionless form τ/Ω^{-1}. As discussed in Sections 2.1 and 2.2, we also omit the parameters $\alpha_{\rm vir}$ and $\phi_{\bar{\rm P}}$ that are associated with the free-fall time-scale $\tau_{\rm ff,\,cl}$ for globally collapsing, gravitationally bound clouds of size equal to the Toomre scale. We opt instead to work with the more general time-scale $\tau_{\rm ff,\,g}$ for the gravitational collapse of the ISM, to quantify the influence of gravity on GMCs that do not necessarily adhere to these assumptions. The parameter space over which τ/Ω^{-1} varies is then spanned by the six variables β, Q, $\Omega_{\rm P}/\Omega$, m, $\phi_{\rm P}$, and $f_{\rm G}$. Out of these, we fix $f_{\rm G}$ to its fiducial value of $f_{\rm G} = 0.5$, and both m and $\Omega_{\rm P}/\Omega$ are relevant only in the presence of spiral arms. The fundamental parameter space is therefore spanned by β and Q, with a secondary dependence on $\phi_{\rm P}$. This parameter space is extended with m and $\Omega_{\rm P}/\Omega$ when considering spiral galaxies.

The importance of the Fundamental Plane (β, Q, Ω) in determining cloud evolution and the cloud lifetime is demonstrated visually in Fig. 3. The black vertical bars represent the total dynamic ranges of the five cloud evolutionary time-scales used in this work, plus $\tau_{\rm ff,\,cl}$, due to simultaneously varying all the quantities in Table 1 (other than $f_{\rm G}$, which is fixed). The blue bars represent the dynamic ranges for each time-scale due to variation in β alone, while the red bars represent the dynamic ranges for each time-scale due to variation in Q alone. We see that the time-scales τ_κ, τ_β, and $\tau_{\rm cc}$ are completely determined by the Fundamental Plane variables (β, Q, Ω). The time-scale $\tau_{\rm ff,\,g}$ is additionally controlled by $\phi_{\rm P}$, but to a much weaker extent than Q, as demonstrated by comparing the sizes of its black and red bars in Fig. 3. Thus, the time-scales in galaxies without spiral arms vary primarily within the Fundamental Plane (β, Q, Ω), with secondary variations in $\phi_{\rm P}$. The only time-scale that is not accounted for by (β, Q, Ω) is the spiral arm crossing time-scale $\tau_{\Omega_{\rm P}}$, which depends instead on the quantities m and $\Omega_{\rm P}/\Omega$ in the extended parameter space (β, Q, Ω, m, $\Omega_{\rm P}/\Omega$).

One of the goals of our theory is to cover the entire parameter space of galactic properties which may feasibly be observed. In order to perform our first comparison of cloud evolutionary time-scales, we therefore choose upper and lower limits for the dynamic ranges in Table 1 that correspond to the highest and lowest observed values of these parameters. Natural upper and lower limits on the shear parameter β are defined by solid-body rotation and a flat rotation curve, respectively. The dynamic range for $\Omega_{\rm P}/\Omega$ is calculated using the pattern speed for the Milky Way, $\Omega_{\rm P} = 0.026 \pm 0.002{\rm Myr}^{-1}$ (Gerhard 2011), and a reasonable range of angular speeds Ω between $\log(\Omega/{\rm Myr}^{-1}) = -2.5$ and $\log(\Omega/{\rm Myr}^{-1}) = 0.5$. We choose an upper limit for the Toomre Q parameter of the ISM according to the work of Leroy et al. (2008), which shows that values of $Q > 10$ may be readily obtained in both spiral and dwarf galaxies, and may be as large as $Q \approx 15$, a range which is matched in observations of the central $\sim$500 pc of the Milky Way by Kruijssen et al. (2014). Our lower limit for the Toomre Q parameter is extended to $Q < 1$ according to the work of Genzel et al. (2014), who find Toomre Q values as low as $Q \approx 0.2$ for a sample of 19 main-sequence star-forming galaxies. We will see later in the paper that the strong influence of gravitational free-fall at low Q makes it uninteresting to look at values of $Q < 0.5$, so we adopt a range of $0.5 < Q < 15$. Krumholz & McKee (2005) estimate a value of the stellar contribution to the mid-plane gas pressure, $\phi_{\rm P} \sim 3$, by considering a variety of cases from normal disc galaxies to starbursts. Since the lowest possible value of $\phi_{\rm P}$ is unity (no stellar contribution to mid-plane gas pressure), we adopt a conservative range of $1 < \phi_{\rm P} < 9$.

We emphasize that our theory is able to deal with values of Q, β, $\phi_{\rm P}$, m, and $\Omega_{\rm P}/\Omega$ which fall outside the extended parameter space defined here. The analytic time-scales derived in Section 2 do not impose any restrictions on the values of these quantities, and so we are free to substitute any physically reasonable, observed values that we choose. The boundaries defined here represent a physically and observationally motivated window through which we can view our parameter space, to draw conclusions about the trends in cloud evolutionary mechanisms and the cloud lifetime for the vast majority of real-Universe galactic environments. Our theory is also sufficiently flexible that we can extend the window at any time, to account for future observations.

3.2 Preliminary comparison of time-scales

In Fig. 3, we make a preliminary comparison between the dynamic ranges of all six time-scales, represented by vertical black bars, over all values of the quantities in Table 1. In the initial comparative discussion carried out here, we assume that the value of a given time-scale can be adjusted without altering the values of the other time-scales, or equivalently that no two time-scales are dependent upon the same physical quantities. This assumption, although incorrect, gives a preliminary indication of whether the coexistence of cloud evolutionary mechanisms is an important consideration in theories of the cloud lifetime. Where the dynamic ranges of two time-scales in Fig. 3 overlap, it is *possible* that there exist values of the quantities in Table 1 for which these time-scales are equal. Conversely, if the ranges of two time-scales do not overlap in Fig. 3, then there exist *no values* of the quantities in Table 1 for which equality between these time-scales is obtained. This would indicate that a subset of the mechanisms does not govern the cloud life cycle anywhere in parameter space.

For the fiducial values of the physical quantities in Table 1, represented by open circles in Fig. 3, the two time-scales for gravitational collapse $\tau_{\rm ff,\,g}$ and $\tau_{\rm ff,\,cl}$ are up to an order of magnitude lower than all other time-scales. For these values it is clear that

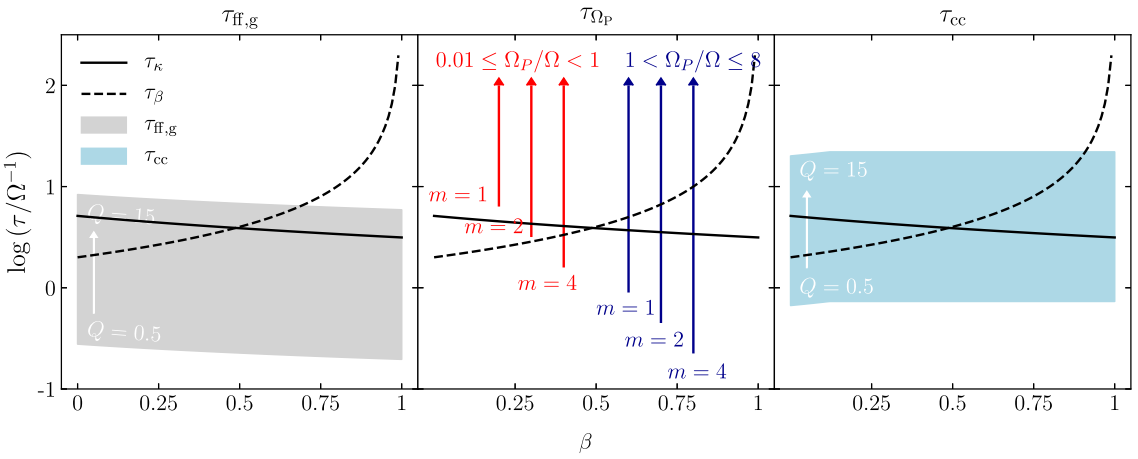

Figure 4. Variation of each time-scale, normalized by the orbital period Ω^{-1}, with the shear parameter β. The two time-scales τ_κ (radial perturbations) and τ_β (shear) are dependent only on β and are therefore represented by lines in each panel. Left: the grey region highlights the range of values for the free-fall time-scale $\tau_{\rm ff,\,g}$ over the range of Q values given in Table 1, with $\phi_{\rm P} = 3$. For high values of Q, we see that τ_β and τ_κ become the dominant time-scales relative to $\tau_{\rm ff,\,g}$. Centre: the red arrows indicate the range of values for the arm-crossing time-scale $\tau_{\Omega_{\rm P}}$ within the radius of corotation of the Milky Way (≈8 kpc, Gerhard 2011), while the blue arrows indicate the range of $\tau_{\Omega_{\rm P}}$ outside the radius of corotation. The variable m indicates the number of spiral arms in the galaxy. At the radius of corotation, this time-scale becomes infinite, because the spiral arms do not move relative to the ISM. Note that $\tau_{\Omega_{\rm P}}$ is independent of β, so the horizontal placement of the arrows is arbitrary. Right: the blue region highlights the range of values for the cloud–cloud collision time-scale $\tau_{\rm cc}$ over the extended range of Q values. This region appears independent of β for $\beta > 0.12$ because equation (16) is only valid within the range $0 < \beta < 0.12$ and thus we take a lower bound on $\tau_{\rm cc}$ for $\beta > 0.12$ (see Section 2.3). Although we see an overlap between the blue and grey regions on the left and right, $\tau_{\rm cc}$ is in fact always larger than $\tau_{\rm ff,\,g}$, as they both depend linearly on Q.

gravitational collapse dominates the formation and evolution of molecular clouds. The dynamic range of $\tau_{\rm ff,\,cl}$ in particular does not overlap with the dynamic range of the shear time-scale τ_β or the time-scale of epicyclic perturbations τ_κ, indicating that no choice of values from Table 1 allows significant competition between $\tau_{\rm ff,\,cl}$ and either of these time-scales. However, in Sections 2.1 and 2.2, we have justified the use of $\tau_{\rm ff,\,g}$ rather than $\tau_{\rm ff,\,cl}$ to quantify the effect of gravitational collapse on GMCs. In this case, Fig. 3 shows a region of overlap between the dynamic range for gravitational free-fall $\tau_{\rm ff,\,g}$ and the dynamic ranges of *all* other time-scales. This is indicated by the grey shaded region in Fig. 3. It is therefore possible that all time-scales of cloud evolution have comparable values in some region of our extended parameter space. Coexistence between these mechanisms is potentially an important factor in determining the cloud lifetime, which requires further investigation. In the rest of this paper, we will examine the coexistence of different cloud evolutionary mechanisms in much greater depth, taking into account that the quantities in Table 1 may affect several different time-scales simultaneously. We will also examine the nature of coexistence, and in particular the potential for time-scales of comparable magnitude to augment, or compete against, each other.

3.3 Variation of time-scales with β

As a first step towards a full analysis of all five cloud evolutionary time-scales throughout our entire parameter space, we present here a comparison of these time-scales as a function of β, the most prevalent physical quantity in our models. Each panel in Fig. 4 displays the time-scale τ_κ for epicyclic perturbations (solid black lines) and the time-scale τ_β for shear (dashed black lines), both of which depend *only* on β. We see that these time-scales intersect at around $\beta = 0.5$, indicating that for $\beta < 0.5$, galactic shear exerts more control over cloud evolution than do epicyclic perturbations, but that for $\beta > 0.5$, the opposite is true.

The left-hand panel of Fig. 4 compares the dynamic ranges of τ_β and τ_κ to the dynamic range of the time-scale $\tau_{\rm ff,\,g}$ for gravitational free-fall, which is additionally controlled by the Toomre Q parameter. The variation in $\tau_{\rm ff,\,g}$ with Q is indicated by the grey filled region, where higher values of Q correspond to higher values of $\tau_{\rm ff,\,g}$. The variation of $\tau_{\rm ff,\,g}$ with $\phi_{\rm P}$ has been neglected in this figure, due to its small effect relative to that of the Toomre Q parameter. For $Q \lesssim 4$, gravitational free-fall is more influential than either τ_β or τ_κ over all values of β, but its value becomes comparable with these time-scales for $Q \gtrsim 4$. For $Q \sim 15$, gravitational free-fall is the least influential mechanism of the three except at $\beta \to 1$, where τ_β diverges asymptotically. We can conclude that across the window of (β, Q, Ω) parameter space defined in Section 3, there exist points for which each of the three time-scales τ_β, τ_κ, and $\tau_{\rm ff,\,g}$ is more influential than the other two. It is therefore necessary to consider all three of these time-scales and their contributions to the cloud lifetime.

In the right-hand panel of Fig. 4, we see that the time-scale $\tau_{\rm cc}$ for cloud–cloud collisions (blue shaded region) is shorter than τ_β and τ_κ at all β for $Q \lesssim 2$, but longer than these time-scales for most β at $Q \gtrsim 2$. Looking at Fig. 4 alone, we conclude that when calculating the cloud lifetime, the contributions of all three time-scales must be considered. However, a comparison between the left- and right-hand panels of Fig. 4 hints that the influence of cloud–cloud collisions might always be less significant than the influence of gravitational free-fall. Both of the time-scales $\tau_{\rm ff,\,g}$ and $\tau_{\rm cc}$ have the same functional dependence on the Toomre Q parameter (see equations 5 and 16), such that the grey and blue regions in Fig. 4 have equal areas in the space of (β, $\log \tau/\Omega^{-1}$).

As Q is decreased, both time-scales decrease monotonically, and since $\tau_{\rm cc} > \tau_{\rm ff,\,g}$ for both $Q = 0.5$ (lower limits of blue and grey shaded regions) and $Q = 15$ (upper limits of blue and grey shaded regions), this implies that cloud–cloud collisions can *never* be more influential than gravitational collapse. In the following section, we will perform a more detailed comparison between time-scales, taking the $\phi_{\rm P}$-dependence of $\tau_{\rm ff,\,g}$ into account, and will show that the influence of cloud–cloud collisions on the cloud lifetime is indeed limited by its inability to compete with gravitational free-fall.

The centre panel of Fig. 4 presents the dynamic range of the time-scale $\tau_{\Omega_{\rm P}}$ for spiral arm crossings, for the extended parameter space (β, Q, Ω, m, $\Omega_{\rm P}/\Omega$). We have used the pattern speed $\Omega_{\rm P}$ for the Milky Way in this figure. Since $\tau_{\Omega_{\rm P}} \rightarrow \infty$ at the radius of corotation ($\Omega_{\rm P}/\Omega = 1$), the dynamic range for each value of m has no upper limit, so is represented by arrows. Red arrows indicate a dynamic range below the radius of corotation ($\Omega_{\rm P}/\Omega < 1$), while blue arrows indicate a dynamic range above the radius of corotation ($\Omega_{\rm P}/\Omega > 1$). In general, the frequency with which a cloud encounters spiral arms is multiplicative in m, such that the lower limit on the time-scale $\tau_{\Omega_{\rm P}}$ is brought to lower and lower values as m is increased. There are clearly values of (β, Ω, m, $\Omega_{\rm P}/\Omega$) for which each of the time-scales τ_β, τ_κ, and $\tau_{\Omega_{\rm P}}$ has a greater influence on cloud evolution than the other two time-scales. In addition, $\tau_{\Omega_{\rm P}}$ is independent of Q, so we can infer from the overlap of the red and blue arrows with the grey and blue shaded regions that there exist values of (β, Q, Ω, m, $\Omega_{\rm P}/\Omega$) for which $\tau_{\Omega_{\rm P}} = \tau_{\rm ff,\,g}$ or $\tau_{\Omega_{\rm P}} = \tau_{\rm cc}$. It is therefore clear that, in addition to considering the contributions of τ_κ, τ_β, $\tau_{\rm ff,\,g}$, and $\tau_{\rm cc}$ to the cloud lifetime, we should take into account the effect of spiral arm crossings on time-scale $\tau_{\Omega_{\rm P}}$.

In summary, Fig. 4 demonstrates that, over the ranges of physical parameters displayed in Table 1, equality between all pairs of time-scales can be obtained, with the possible exception of equality between $\tau_{\rm ff,\,g}$ and $\tau_{\rm cc}$. In the next section, we will confirm that there are non-negligible regions of parameter space for which all five cloud evolutionary mechanisms have comparable time-scales, and all contribute to setting the cloud lifetime.

4 CLOUD LIFETIMES THROUGHOUT PARAMETER SPACE: THE DOMINANCE AND COEXISTENCE OF CLOUD EVOLUTIONARY MECHANISMS

Here, we establish the procedure by which cloud lifetimes will be characterized in our theory, throughout the parameter space of observable quantities defined in Table 1. We begin by introducing an equation to quantify the cloud lifetime, using the time-scales for cloud evolution derived in Section 2. We apply this equation first to the simplest case of clouds in galaxies with no spiral arms ($m = 0$), in the (β, Q, Ω) Fundamental Plane. We present figures of the minimum time-scale of cloud evolution throughout this plane, and use these figures to determine the regions of parameter space for which each time-scale is *dominant* over all others in setting the cloud lifetime. We then present figures of the cloud lifetime throughout the (β, Q, Ω) Fundamental Plane, in which we determine the regions of *relevance* for each mechanism. This tells us where different cloud evolutionary mechanisms coexist. Having developed the machinery of our theory for the simplest case, we finally extend our formalism to encompass the extended parameter space (β, Q, Ω, m, $\Omega_{\rm P}/\Omega$) appropriate to galaxies with spiral arms.

4.1 Calculation of cloud lifetime

Our theory is expansive, making as few assumptions as possible about the size, structure, and gravitational boundedness of molecular clouds. It does not aim to capture the precise way in which GMCs are affected by the five dynamical cloud evolutionary mechanisms presented in Section 2. Instead, we calculate the cloud lifetime by characterizing each mechanism according to its rate τ^{-1}.

In combining the five rates of cloud evolution, we make the assumption that galactic shear is primarily a dynamically dispersive process, while the other four mechanisms are dynamically compressive. This categorization of evolutionary mechanisms is based on the effect of each on gravitational collapse and star formation. An increase in the level of galactic shear is found to lower the efficiency of star formation (Leroy et al. 2008), the majority of which occurs within dense, collapsing regions of molecular gas (Hartmann et al. 2001; Elmegreen 2007; Dobbs et al. 2011a; Dobbs & Pringle 2013). This suggests that galactic shear suppresses star formation by supporting against gravitational free-fall. Dynamically, this is an intuitive result, because gravitational collapse causes molecular gas to increase its density, while galactic shear disrupts the structure. By contrast, the other four cloud evolutionary mechanisms, characterized by the time-scales $\tau_{\rm ff,\,g}$, $\tau_{\Omega_{\rm P}}$, τ_κ, and $\tau_{\rm cc}$, each have the potential to compress molecular gas and thus to promote gravitational collapse and star formation. We therefore add together the four rates $\tau_{\rm ff,g}^{-1}$, $\tau_{\Omega_{\rm P}}^{-1}$, τ_κ^{-1}, and $\tau_{\rm cc}^{-1}$, but *subtract* the rate of galactic shear, τ_β. In doing this, we implicitly assume that the destruction of molecular clouds by stellar feedback occurs on a time-scale that is much shorter than the five dynamical time-scales presented here, such that the processes of compression, star formation, and cloud destruction are all quantified within each of the time-scales $\tau_{\rm ff,\,g}$, $\tau_{\Omega_{\rm P}}$, τ_κ, and $\tau_{\rm cc}$. The addition of dynamical rates gives a cloud lifetime of

$$\tau = |\tau_\kappa^{-1} + \tau_{\Omega_{\rm P}}^{-1} + \tau_{\rm ff,g}^{-1} + \tau_{\rm cc}^{-1} - \tau_\beta^{-1}|^{-1}, \tag{24}$$

where we take the absolute value of the sum of the rates, so that the cloud lifetime is still positive if shear outpaces all other mechanisms of cloud evolution. We will show below that this only occurs in a very small part of parameter space.

This method of calculating the cloud lifetime makes two major assumptions. First, it ignores non-linearities arising from interactions between the different cloud evolutionary mechanisms. It assumes that the rates of the different mechanisms can simply be added together. Secondly, equation (24) is statistical in the sense that it combines rates. At each point in parameter space, it represents the ensemble-averaged value of the cloud lifetime for a theoretically infinite population of clouds. It therefore ignores the *discrete* and *random* (i.e. Poissonian) nature of cloud–cloud collisions and spiral arm crossings. In practice, these events may occur at any time between the 'birth' of a molecular cloud and the value of the time-scale $\tau_{\rm cc}$ or $\tau_{\Omega_{\rm P}}$.

The major advantage of taking this simplified approach is that it allows us to introduce an analytic expression for the cloud lifetime in terms of observable, physical quantities, and to systematically examine its behaviour throughout the parameter space (β, Q, Ω, $\phi_{\rm P}$, m, $\Omega_{\rm P}/\Omega$). The use of cloud evolutionary rates means that we do not need to define a time of cloud 'birth' and therefore do not require an arbitrary theoretical threshold between states of cloud existence and non-existence. By comparing the predictions of our simple dynamical theory to observations of molecular cloud lifetimes, we will be able to assess the importance of complex effects such as non-linearity, cloud chemistry, and stellar feedback.

Under the assumption that deviations from equation (24) are driven by these effects, we will be able to separate the influence of these effects from the dynamics of the ISM itself.

It could be argued that equation (24) underestimates the cloud lifetime if a large number of clouds undergo global collapse, because the rate of collapse of a cloud cannot be augmented or accelerated by other mechanisms once it becomes decoupled from the large-scale turbulent flow. However, we will see below that as Q decreases and global collapse becomes more prevalent among molecular clouds, the gravitational free-fall time-scale $\tau_{\rm ff,\,g}$ becomes strongly dominant over the other time-scales, which therefore become irrelevant. Therefore, our model of the cloud lifetime naturally produces a situation in which the time-scales τ_κ, τ_β, $\tau_{\Omega_{\rm P}}$, and $\tau_{\rm cc}$ make a negligible contribution to the cloud lifetime when many clouds are undergoing global gravitational collapse.

As pointed out by Elmegreen (2007), molecular clouds can be destroyed in a number of different ways. A cloud can undergo *consumption*, by which it is eventually eroded away by star formation and stellar feedback, *dispersal* such that it is torn apart, possibly into smaller entities, or *phase change* such that it is converted back into atomic form. Within our formalism, a *phase change* may be caused by stellar feedback, in which case it is analogous to cloud *consumption*.

By comparing the rate of galactic shear τ_β^{-1} to the combined rates of the dynamically compressive mechanisms $\tau_\kappa^{-1} + \tau_{\rm ff,g}^{-1} + \tau_{\Omega_{\rm P}}^{-1} + \tau_{\rm cc}^{-1}$, our theory can discern the regimes in which clouds will typically undergo *dispersal* rather than *consumption*. We define the regimes (s) as those regions for which

$$\tau_\beta^{-1} > \tau_\kappa^{-1} + \tau_{\Omega_{\rm P}}^{-1} + \tau_{\rm ff,g}^{-1} + \tau_{\rm cc}^{-1}, \tag{25}$$

and we expect the primary mechanism of cloud destruction in these regions to be related to cloud *dispersal*, with minimal opportunity for star formation. We define the regimes (c) as those regions of parameter space for which

$$\tau_\beta^{-1} < \tau_\kappa^{-1} + \tau_{\Omega_{\rm P}}^{-1} + \tau_{\rm ff,g}^{-1} + \tau_{\rm cc}^{-1}, \tag{26}$$

and in these regions, we expect clouds to be destroyed mainly by *consumption*, due to gravitational collapse and the ensuing stellar feedback.

4.2 Regions of dominance and relevance

The evolution of clouds in different parts of parameter space, and thus in different galactic environments, is governed by different dynamical processes. We quantify this division of parameter space by defining *regions of dominance*. The *region of dominance* for a mechanism of cloud evolution is the region of parameter space for which its time-scale is shorter than all other time-scales.

While the mechanism with the shortest time-scale has the greatest influence on cloud evolution, other processes with comparable rates may also contribute. For this reason, we introduce the concept of *relevance* in addition to *dominance*. The threshold for *relevance* should be lenient enough to allow several mechanisms to be relevant at some points in parameter space, but strict enough that only one mechanism is relevant in others. In order to quantify *relevance*, we begin by dividing the parameter space into two regimes, (i) and (ii).

(i) Lifetime $\tau <$ minimum time-scale $\tau_{\rm min}$: the minimum time-scale is augmented by other compressive time-scales, resulting in a cloud lifetime that is shorter than the minimum time-scale.

(ii) Lifetime $\tau >$ minimum time-scale $\tau_{\rm min}$: competition between shear support and the compressive time-scales extends the lifetime beyond the minimum time-scale.

In regime (i), the relevance of a given time-scale should be determined by comparison to $\tau_{\rm min}$, as $\tau_{\rm min}$ sets the upper bound on the cloud lifetime. Any mechanism that is not competitive with $\tau_{\rm min}$ will not have time to appreciably influence the cloud's evolution before the end of its life. Conversely, in regime (ii) the relevance of a given time-scale should be determined by comparison to the lifetime itself, τ. The extension of cloud lifetime via shear support means that even if a given mechanism occurs at a substantially slower rate than $\tau_{\rm min}$, it can have an influence on the evolution of the cloud, although this influence will be small relative to $\tau_{\rm min}$.

Within these two regimes, the *regions of relevance* are defined by computing the ratio of each time-scale with either the minimum time-scale in regime (i) or the cloud lifetime in regime (ii). Where this ratio is smaller than 2, the time-scale is deemed to be relevant. That is, the regions of relevance for a cloud evolutionary mechanism in regime (i) are those regions for which its rate is no less than half the rate of the dominant cloud evolutionary mechanism. In regime (ii), the regions of relevance are those regions for which a given cloud evolutionary mechanism occurs at a rate no less than half the sum of all cloud evolutionary rates, as on the right-hand side of equation (24).

Since several different cloud evolutionary mechanisms may be *relevant* in each point in parameter space, the *regions of relevance* reveal the environmental conditions for which cloud evolution is either controlled by a single dynamical process, or is controlled by a combination of dynamical processes that coexist.

4.3 Galaxies without spiral arms, $m = 0$

We begin with the case of clouds in galaxies without spiral arms, such that we may neglect the arm-crossing time-scale $\tau_{\Omega_{\rm P}}$ and its parameters m and $\Omega_{\rm P}/\Omega$. The parameter space is then composed of the Fundamental Plane (β, Q, Ω) with a (weak) secondary dependence on $\phi_{\rm P}$.

4.3.1 Regions of dominance, m = *0*

We first divide the parameter space into *regions of dominance*, by distinguishing the mechanism with the greatest influence on cloud evolution for each region of parameter space. We determine which process occurs at the fastest rate by computing the normalized minimum cloud evolutionary time-scale $\tau_{\rm min}/\Omega^{-1}$ across all values of β, Q, and $\phi_{\rm P}$. In Fig. 5, the value of the minimum time-scale is indicated by the colours, while the solid black lines represent divisions between the regions of dominance, along which two time-scales are equal in value.

The most gravitationally unstable regions of parameter space at the bottom of each panel ($Q \lesssim 4$, i.e. gas-rich, star-forming galaxies) are dominated comprehensively by gravitational free-fall 'f'. Conversely, regions of higher gravitational stability are dominated either by galactic shear 'β' for flatter rotation curves ($Q \gtrsim 4$ and $\beta \lesssim 0.5$, i.e. in early-type galaxies or ETGs and outer galactic bulges) or by epicyclic perturbations 'κ' for approximately solid-body rotation ($Q \gtrsim 4$ and $\beta \gtrsim 0.5$, i.e. near galactic centres). For gas that is highly gravitationally stable with a flat rotation curve (very top left corner of each panel with $Q \sim 15$ and $\beta \sim 0$), the dynamically dispersive mechanism of galactic shear may dominate over the combined influence of all dynamically compressive

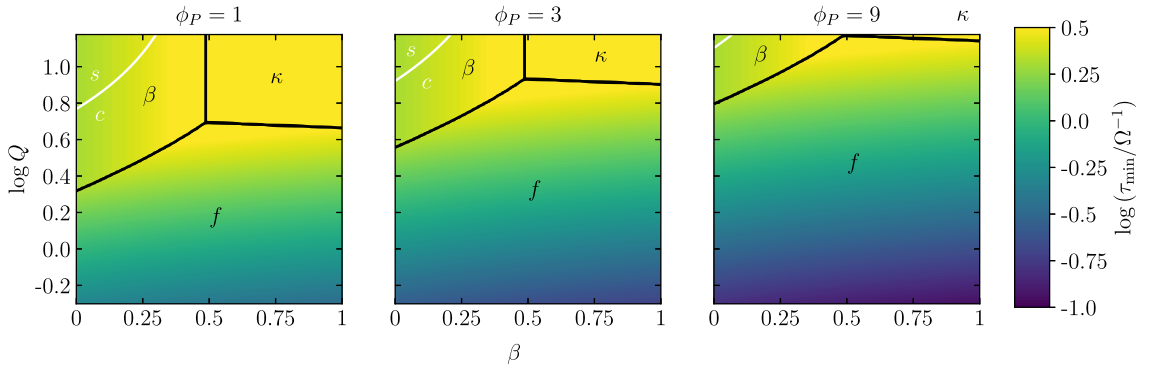

Figure 5. The minimum time-scale and its value for three cross-sections of the parameter space (β, $\log Q$, Ω, $\phi_{\rm P}$), where $\phi_{\rm P}$ is given by equation (7) and no spiral arms are present ($m = 0$). The dependence on Ω is included as a normalization of the time-scale, as all evolutionary time-scales depend on Ω in the same way. The dominant time-scales here are τ_κ, τ_β, and $\tau_{\rm ff,\,g}$, denoted by κ, β, and f respectively. The solid black lines delineate boundaries along which two time-scales are equal; the *regions of dominance* are separated by these lines. The solid white lines divide the regions for which the rate of galactic shear is higher than the combined rates of all other mechanisms (s) from the regions in which it is lower (c).

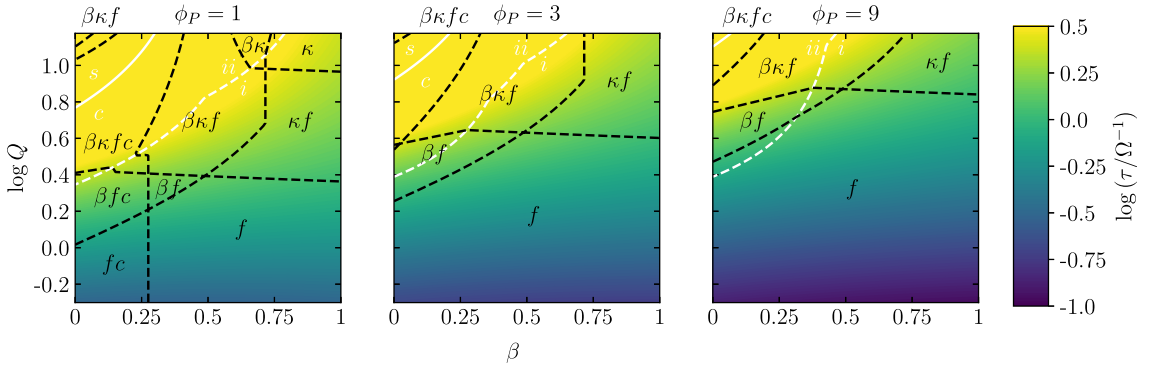

Figure 6. The predicted cloud lifetime for three cross-sections of the parameter space (β, $\log Q$, Ω, $\phi_{\rm P}$), without spiral arms ($m = 0$). The dependence on Ω is included as a normalization of the time-scale, as all evolutionary time-scales depend on Ω in the same way. The relevant time-scales are τ_κ, τ_β, $\tau_{\rm ff,\,g}$, and $\tau_{\rm cc}$, denoted by κ, β, f, and c, respectively. The dashed black lines enclose the *regions of relevance* for each time-scale (see Section 4.2). The dashed white lines divide the regions for which the cloud lifetime is longer than the minimum evolution time-scale (ii) from the regions in which it is shorter (i). The solid white lines divide the regions for which the rate of galactic shear is higher than the combined rates of all other mechanisms (s) from the regions in which it is lower (c).

mechanisms, such that $\tau_\beta^{-1} > \tau_{\rm ff,\,g}^{-1} + \tau_\kappa^{-1} + \tau_{\rm cc}^{-1}$. These regions are labelled (s) in Fig. 5, enclosed by a solid white line. In region (s), many clouds will be pulled apart by galactic shear before they have the chance to collapse and form stars. In region (c), dynamically compressive evolutionary mechanisms dominate, so clouds are more likely to be destroyed by gravitational collapse and the subsequent stellar feedback.

As the stellar contribution to the mid-plane surface density of the ISM is increased from $\phi_{\rm P} = 1$ (i.e. pure gas discs, left-hand panel of Fig. 5) to $\phi_{\rm P} = 9$ (i.e. galaxies with large stellar contributions, right-hand panel of Fig. 5), the time-scale for gravitational collapse decreases in value. This causes the gravity-dominated region of parameter space 'f' to move upwards into regions of higher gravitational stability. For a single value of the Toomre Q stability parameter, an increase in the proportion of stars destabilizes the gas in the galactic mid-plane and thus reduces the gravitational free-fall time-scale. However, it should be noted that this effect is mitigated by, and may even be reversed by, the direct correlation between $\phi_{\rm P}$ and Q. As the stellar contribution is increased, the velocity dispersion of the mid-plane gas and the epicyclic frequency of the galaxy disc are also increased, stabilizing the gas and thus increasing the value of Q. As the gas fraction is decreased, Q therefore increases in proportion to $\phi_{\rm P}$. As shown in equation (5), the free-fall time-scale is inversely proportional to $\sqrt{\phi_{\rm P}}$, but directly proportional to Q. Therefore, it may actually be the case that $\tau_{\rm ff,\,g}$ *increases* with an increase in $\phi_{\rm P}$ (a decrease in the gas fraction), in contrast to the implication of Fig. 5. For the remainder of the paper, we set $\phi_{\rm P} = 3$, the value most appropriate to the Milky Way (e.g. Krumholz & McKee 2005).

4.3.2 *Regions of relevance,* m = 0

We now examine the coexistence of cloud evolutionary mechanisms by dividing the parameter space into *regions of relevance*. We use equation (24) to compute the value of the normalized cloud lifetime τ/Ω^{-1}, represented by the coloured contours in Fig. 6, across all values of β, Q, and $\phi_{\rm P}$. The regions of relevance throughout parameter space are enclosed by black dashed lines.

In Fig. 6, the bottom right side of the white dashed line in each panel corresponds to regime (i), the region of parameter space for which the cloud lifetime is shorter than the minimum time-scale of cloud evolution, $\tau < \tau_{\rm min}$. Regime (i) spans all but the top left corner of each panel, where galactic shear 'β' is most relevant. This is because galactic shear is the only dynamically dispersive cloud evolutionary process, so it is required for $\tau > \tau_{\rm min}$. Without galactic shear, the cloud lifetime results from a combination of several dynamically compressive mechanisms, hence it has a shorter value than any one of the individual time-scales. As mentioned in Section 4.2, we determine the relevance of each time-scale in regime (i) by comparison to $2 \times \tau_{\rm min}$.

In the top left corner of each panel of Fig. 6, the ISM is highly gravitationally stable with a flat rotation curve and can therefore be effectively supported by galactic shear 'β'. Such an environment would be found, for example, in outer galaxy bulges. The competition between cloud compression and shear support 'βf' elongates the cloud lifetime such that it becomes longer than the minimum time-scale of cloud evolution, $\tau > \tau_{\rm min}$. This condition defines regime (ii), which is separated from regime (i) by the white dashed line. In regime (ii), the relevance of each time-scale is determined by comparison to $2 \times \tau$, as the extended cloud lifetime allows slower acting processes to play a small role in cloud evolution before the cloud is destroyed. In region '$\beta\kappa fc$' at the very top left corner of each panel, the cloud survives so long that all mechanisms of cloud evolution have time to influence its evolution.

For gravitationally stable regions of the ISM with $Q \gtrsim 4$ (top half of each panel in Fig. 6), the coexistence of different cloud evolutionary mechanisms is of crucial importance in setting the cloud lifetime. For this region of parameter space, there is a large difference in value between the normalized cloud lifetime τ/Ω^{-1} (colours in Fig. 6) and the normalized minimum time-scale of evolution (colours in Fig. 5). In the top right corner of each panel (i.e. near galactic centres), epicyclic perturbations are augmented by gravitational collapse in the region 'κf' of Fig. 6, reducing the cloud lifetime relative to the dominant time-scale of epicyclic perturbations (region κ of Fig. 5). Conversely, in the top left corner of each panel (i.e. in ETGs and outer galaxy bulges), the cloud lifetime is elongated by the competition between galactic shear and all the compressive mechanisms of cloud evolution, including gravity, epicyclic perturbations, and cloud–cloud collisions (e.g. in region '$\beta\kappa fc$').

For regions of the ISM that are gravitationally unstable ($Q \lesssim 4$, i.e. gas-rich, star-forming galaxies), the overwhelming domination of gravitational free-fall means that the cloud lifetime is almost equal to the minimum time-scale of cloud evolution. This can be seen by comparison of the coloured contours in Figs 5 and 6.

The rarity of regions 'c' in Fig. 6 reveals that cloud–cloud collisions are the least competitive mechanism of cloud evolution. They are only relevant in the case of very gas-rich, highly shearing environments ($\phi_{\rm P} = 1$ and $\beta \lesssim 0.25$, i.e. the left-hand side of the left-hand panel). Such environments may be found in high-redshift galaxies for low values of Toomre Q (e.g. Genzel et al. 2014) or in the outskirts of low-redshift galaxies for high values of Q (e.g. Leroy et al. 2008). For higher stellar contributions, $\phi_{\rm P} = 3$ and 9, cloud–cloud collisions are relevant only in the very top left corner of each panel, and only in conjunction with *all* other mechanisms of cloud evolution. As noted in Section 2.3, the influence of cloud–cloud collisions is likely to be overestimated in this region of parameter space, so their effect is likely to be even smaller than indicated by Fig. 6. In general, cloud–cloud collisions are only relevant in very few circumstances due to their inability to compete with the time-scale $\tau_{\rm ff,\,g}$ for gravitational collapse.

4.4 Galaxies with spiral arms, $m \neq 0$

The introduction of spiral arms requires the introduction of parameters m and $\Omega_{\rm P}/\Omega$. These refer to the number of spiral arms and the ratio of the pattern speed to the orbital speed, respectively. We show the same values of $\tau_{\rm min}/\Omega^{-1}$ and τ/Ω^{-1} as in Section 4.3, but in the new extended parameter space (β, Q, Ω, m, $\Omega_{\rm P}/\Omega$). We examine the (β, Q, Ω) plane in Figs 7 and 9, and we examine the ($\Omega_{\rm P}/\Omega$, Q, Ω) plane in Figs 8 and 10. For each cross-section, we examine the cases of $m = 1$, 2, and 4 spiral arms. As previously discussed, $\phi_{\rm P}$ is set to its fiducial Milky Way value of $\phi_{\rm P} = 3$.

4.4.1 Regions of dominance, m $\neq 0$

In Figs 7 and 8, we display the contours of the minimum normalized time-scale $\tau_{\rm min}/\Omega^{-1}$ and solid black lines delineating the *regions of dominance* for each time-scale. The setup is identical to that in Fig. 5, but extended over the new variables m and $\Omega_{\rm P}/\Omega$.

The panels in the central column of Fig. 7 describe cloud evolution at the radius of corotation ($\Omega_{\rm P}/\Omega = 0.99$) in spiral galaxies with $m = 1$, 2, or 4 spiral arms. Each panel is an exact copy of the central panel in Fig. 5, describing cloud evolution in flocculent or elliptical galaxies, where $m = 0$. This is because the mid-plane gas at the radius of corotation moves in sychronization with the spiral arms, such that they never interact with molecular clouds, and play no role in cloud evolution.

The left-hand column of Fig. 7, with pattern speed $\Omega_{\rm P}/\Omega = 0.01$ far within the radius of corotation, is very similar to the central, corotating column, but with a region of dominance for spiral arm interactions '$\Omega_{\rm P}$' encroaching from the top of each panel as the number of spiral arms is increased. The first noticeable change for spiral galaxies, relative to elliptical and flocculent galaxies, occurs for grand-design spirals ($m = 2$), where highly stable, low-shear gas ($Q \gtrsim 6$ and $\beta \gtrsim 0.4$, e.g. gas in the presence of a nuclear spiral) in the top right corner of the panel switches from epicycle-dominated 'κ' to spiral arm-dominated '$\Omega_{\rm P}$' evolution. This spiral arm-dominated region extends to even lower values of gravitational stability in the case of four spiral arms ($m = 4$, bottom panel in the left-hand column), where it also takes over from the dominance of shear ('β' in the top and middle panels of the column) for highly stable, highly sheared gas ($Q \gtrsim 4$, for all β). That is, given a sufficiently large number of spiral arms, spiral arm perturbations become the dominant mechanism for cloud evolution in the outer regions of galactic bulges as well as near galactic centres.

The influence of spiral arm crossings is further increased for pattern speeds far outside the radius of corotation (right-hand column of Fig. 7), because the ratio $\Omega_{\rm P}/\Omega$ can become very large if the mid-plane angular velocity Ω is very small. In fact, our model imposes no limit on the increase of $\Omega_{\rm P}/\Omega$ as $\Omega \rightarrow 0$. There is no mathematical reason why the pattern speed cannot be made so high that spiral arms dominate throughout the entire space of (β, Q, Ω). Physically, however, this behaviour is limited by the weakening of the spiral shock at large galactocentric radii, such that the perturbation dies off as $\Omega_{\rm P}/\Omega \rightarrow \infty$. Our model does not explicitly account for this effect, but for this reason we only examine values of the pattern speed ratio between $\Omega_{\rm P}/\Omega = 0.01$ and 4.

The right-hand column of Fig. 7 displays a more extreme version of the pattern shown for clouds inside the radius of corotation (left-hand column). Again, the region of spiral arm dominance '$\Omega_{\rm P}$'

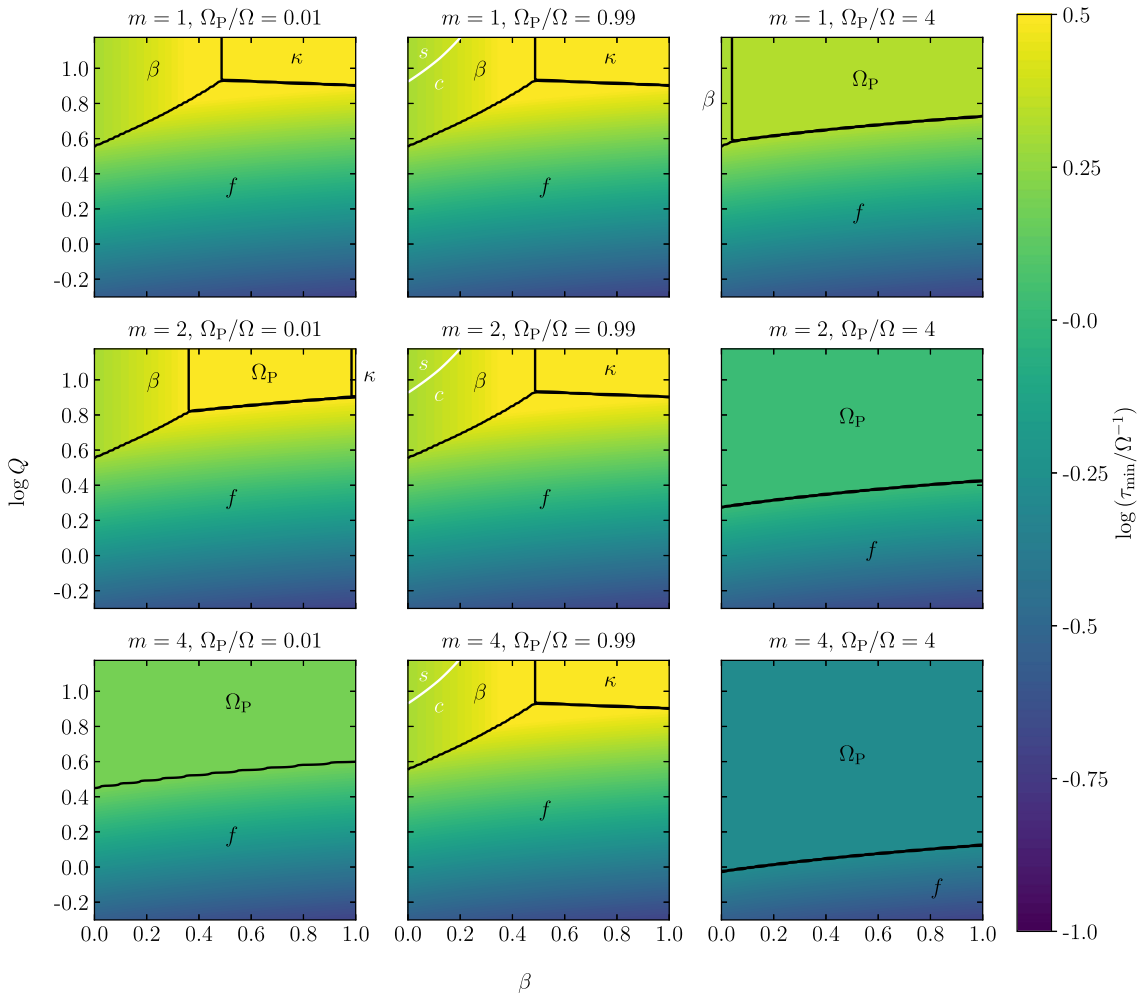

Figure 7. The minimum time-scale and its value for three cross-sections of the parameter space (β, $\log Q$, Ω, Ω_P/Ω) in the (β, Q, Ω) Fundamental Plane, for three numbers of spiral arms $m = 1, 2, 4$, and for $\phi_P = 3$. The dependence on Ω is included as a normalization of the time-scale, as all evolutionary time-scales depend on Ω in the same way. The relevant time-scales here are τ_κ, τ_β, τ_{Ω_P}, and $\tau_{ff,\,g}$, denoted by κ, β, f, and Ω_P, respectively. The solid black lines delineate boundaries along which two time-scales are equal; the *regions of dominance* are separated by these lines. The solid white lines delineate the values of Q and β above which the rate of galactic shear is higher than the combined rates of all other mechanisms, as discussed in Section 5.2.

encroaches from the top right corner of each panel as the number of spiral arms is increased from $m = 1$ through $m = 4$, but unlike the panels in the left-hand column, this effect is already significant in galaxies with $m = 1$ (i.e. a single spiral arm). When two spiral arms are introduced (i.e. for grand-design spirals), spiral arm crossings dominate cloud evolution down to gravitational stability values of $Q \sim 2$, and with four spiral arms, they are dominant down to $Q \sim 1$. This is well into the realm of clumpy, star-forming galaxies, either in the local Universe (e.g. Fisher et al. 2017) or at high redshift (e.g. Genzel et al. 2014).

Fig. 8 displays the same information as Fig. 7, but takes a different cross-section through (β, Q, Ω, m, Ω_P/Ω) parameter space – through the (β, Ω_P/Ω, Ω) plane. In the left-hand column, the panels display the overwhelming dominance of gravitational free-fall 'f' for highly gravitationally unstable gas with $Q \sim 0.5$, in galaxies with one, two, and four spiral arms (i.e. gas-rich, clumpy, star-forming spirals). Moderately stable gas ($Q = 2.7$, central column) in spiral galaxies is also dominated by gravitational free-fall for most galactocentric radii (traced by Ω_P/Ω), with spiral arm perturbations becoming dominant only far outside the radius of corotation (large Ω_P/Ω). At these radii, high absolute differences between the angular speed of the spiral arms and the angular speed of the mid-plane gas can be obtained, particularly as the rotation curve flattens. As in Fig. 7, the dominance of spiral arm crossings becomes more prominent as the number of spiral arms is increased.

The right-hand column of Fig. 8 shows that, for very high-stability gas with $Q \sim 15$, galactic shear 'β', and epicyclic perturbations 'κ' govern cloud evolution under specific environmental conditions. Although spiral arm perturbations 'Ω_P' dominate at galactocentric radii far from the radius of corotation (i.e. the outer and inner regions of spiral galaxies), galactic shear dominates near the radius of corotation for $\beta \lesssim 0.5$, (i.e. when the rotation curve is

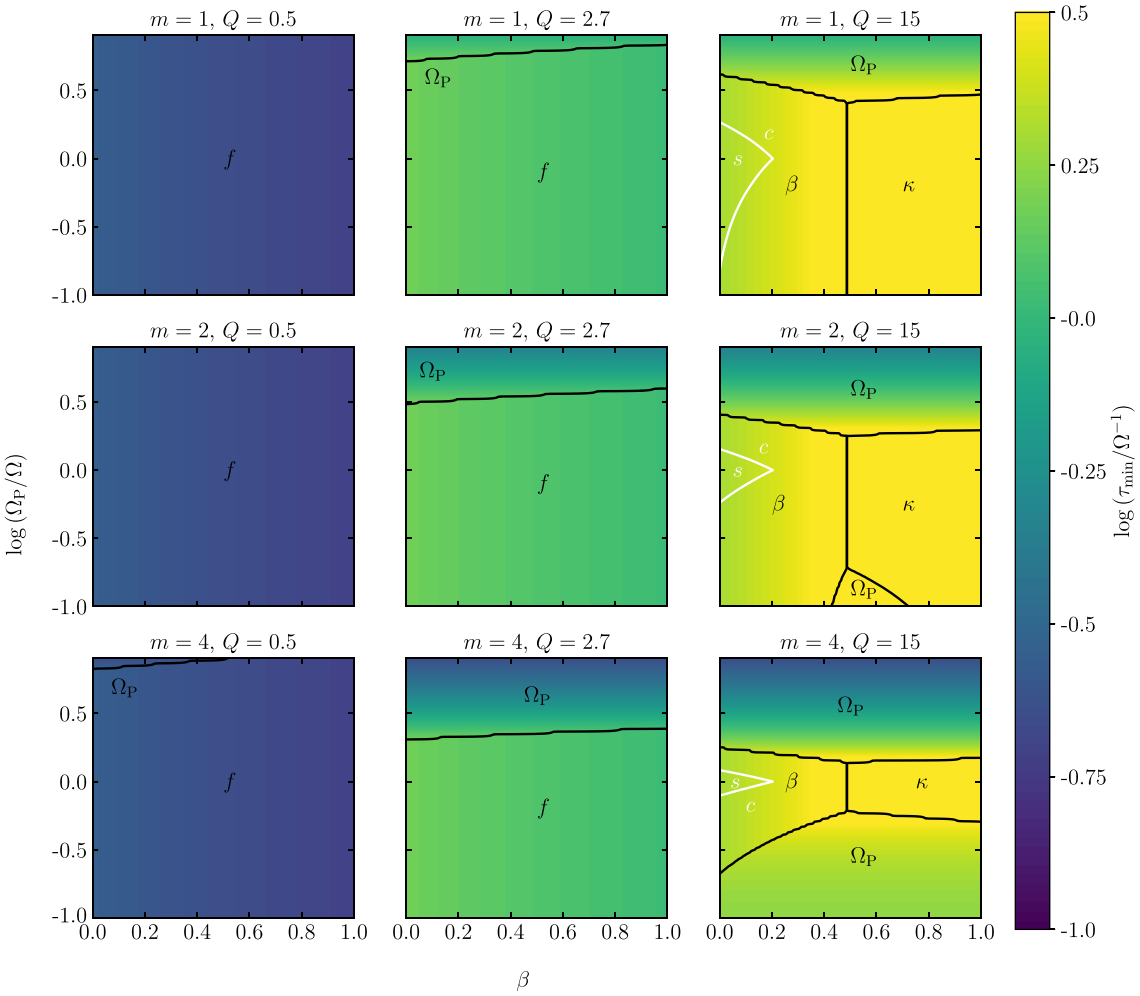

Figure 8. The minimum time-scale and its value for three cross-sections of the parameter space (β, log Q, Ω, Ω_P/Ω) in the (β, Ω, Ω_P/Ω) Fundamental Plane, for three numbers of spiral arms $m = 1$, 2, 4, and for $\phi_P = 3$. The dependence on Ω is included as a normalization of the time-scale, as all evolutionary time-scales depend on Ω in the same way. The relevant time-scales here are τ_κ, τ_β, τ_{Ω_P}, and $\tau_{ff,\,g}$, denoted by κ, β, f, and Ω_P, respectively. The solid black lines delineate boundaries along which two time-scales are equal; the *regions of dominance* are separated by these lines. The solid white lines delineate the values of Q and β above which the rate of galactic shear is higher than the combined rates of all other mechanisms, as discussed in Section 5.2.

approximately flat at the radius of corotation) and epicyclic perturbations dominate at corotation for $\beta \gtrsim 0.5$ (i.e. when the rotation curve is approximately solid body at this radius). While the regions of dominance for spiral arm crossings become very large as m increases, epicyclic perturbations and galactic shear retain their dominance for a significant span of galactocentric radii. Even in case of four spiral arms, using the pattern speed $\sim 0.026 \pm 0.002\,\mathrm{Myr}^{-1}$ of the Milky Way (Gerhard 2011), and assuming that the radius of corotation is at ~ 8 kpc with an average rotational velocity of $\sim 200\,\mathrm{km\,s}^{-1}$ for nearby galactocentric radii, a span of radii from ~ 5 to ~ 13 kpc are not dominated by spiral arm crossings, according to the bottom right panel of Fig. 7.

Note that the solid white lines in the right-hand column of Fig. 8 are analogous to those in the central column of Fig. 7. For highly stable gas at the radius of corotation (regime *s*), galactic shear outpaces the combination of all compressive evolutionary mechanisms. Clouds in this region of parameter space are therefore likely to be torn apart by galactic shear, while clouds in region (*c*) are more likely to be destroyed by gravitational collapse and stellar feedback.

4.4.2 *Regions of relevance,* m ≠ 0

In Figs 9 and 10, we display the contours of the normalized cloud lifetime, τ/Ω^{-1}, with dashed black lines delineating the *regions of relevance*. The setup is identical to that in Fig. 6, but extended over the (β, Q, Ω, m, Ω_P/Ω) parameter space. As in Fig. 6, the parameter space is divided into two regimes labelled (i) and (ii), separated by a white dashed line. In regime (i), the *regions of relevance* are determined by comparison to the minimum cloud evolutionary time-scale, while in regime (ii), the *regions of relevance* are determined by comparison to the cloud lifetime. The threshold for relevance

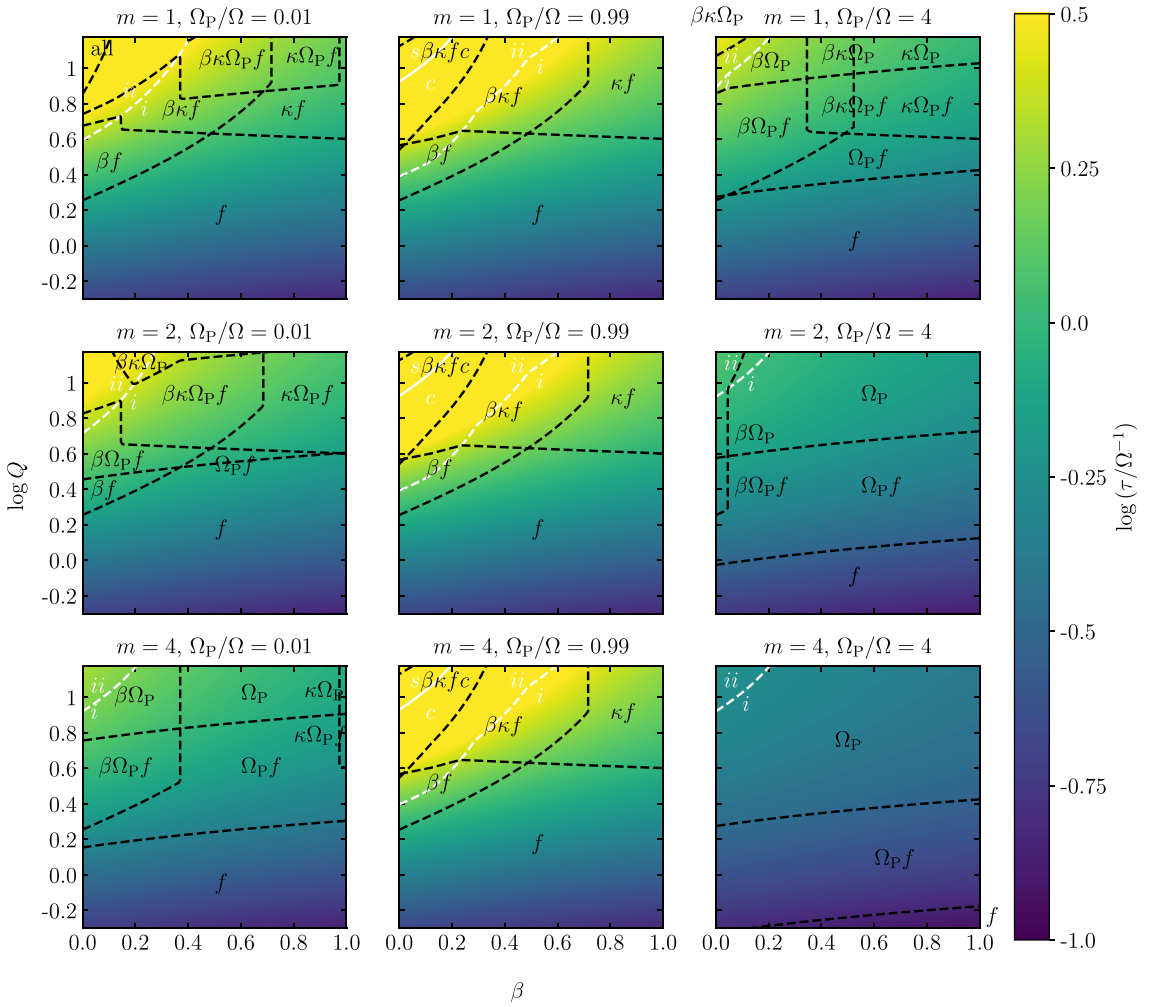

Figure 9. The predicted cloud lifetime for three cross-sections of the parameter space (β, $\log Q$, Ω, Ω_P/Ω) in the (β, Q, Ω) Fundamental Plane, for three numbers of spiral arms $m = 1$, 2, 4, and $\phi_P = 3$. The dependence on Ω is included as a normalization of the time-scale, as all evolutionary time-scales depend on Ω in the same way. The relevant time-scales are τ_κ, τ_β, τ_{Ω_P}, $\tau_{ff,\,g}$, and τ_{cc}, denoted by κ, β, Ω_P, f, and c, respectively. The dashed black lines divide the regions within which each time-scale is relevant from the regions in which it is irrelevant, as described in Section 4.2. The dashed white lines divide the regions for which cloud lifetime is longer than the minimum evolution time-scale (above the line) from the regions in which it is shorter (below the line). These are labelled (ii) and (i), respectively. The solid white lines delineate the values of Q and β above which the rate of galactic shear is higher than the combined rates of all other mechanisms.

is less than twice the magnitude of τ_{min} in regime (i), or twice the magnitude of τ in regime (ii).

As for the regions of dominance displayed in Fig. 7, the panels in the central column of Fig. 9 display the case of spiral arm corotation ($\Omega_P/\Omega = 0.99$) and so have the same division of parameter space as for flocculent gas reservoirs ($m = 0$, central panel of Fig. 6). The left-hand column of Fig. 9, with pattern speed $\Omega_P/\Omega = 0.01$ within the radius of corotation, is similar to the central column, but with a region of relevance for spiral arm interactions emerging from the top of each panel as the number of spiral arms is increased. Although spiral arm crossings do not dominate cloud evolution at any point in (β, Q, Ω) parameter space for a single spiral arm inside the radius of corotation ($m = 1$ and $\Omega_P/\Omega = 0.01$ in the top left panel of Fig. 7), they do still play a non-trivial role in cloud evolution ('Ω_P' regions of relevance for $Q \gtrsim 6$ in the top left panel of Fig. 9). This has the effect of reducing the cloud lifetime relative to the case of spiral arm corotation, which can be seen by comparing the colours of the regions '$\beta\kappa\Omega_P f$', '$\kappa\Omega_P f$', and 'all' in the top left panel of Fig. 9 to those of the regions '$\beta\kappa f$', 'κf', and '$\beta\kappa fc$' in one of the panels of the central column. Due to the compressive effect of spiral arm crossings on molecular clouds, 'Ω_P' augments the epicyclic perturbations 'κ', the gravitational free-fall 'f' and the cloud–cloud collisions 'c', and competes against the galactic shear 'β', so that the elongation of the cloud lifetime by shear support is reduced. This effect becomes more and more pronounced as the number of spiral arms is increased through $m = 2$ and 4 (middle and

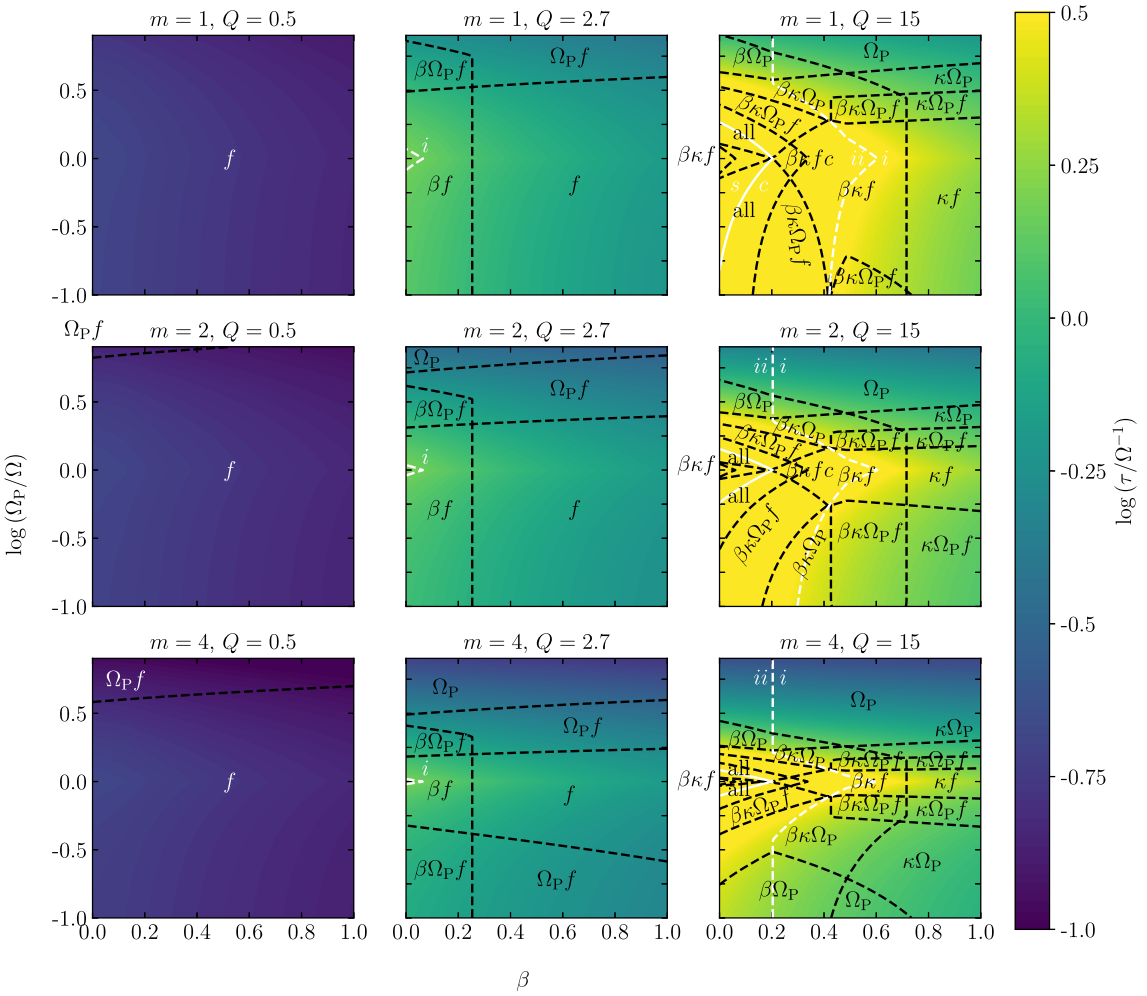

Figure 10. The predicted cloud lifetime for three cross-sections of the parameter space (β, log Q, Ω, Ω_P/Ω) in the (β, Ω, Ω_P/Ω) Fundamental Plane, for three numbers of spiral arms $m = 1$, 2, 4, and $\phi_P = 3$. The dependence on Ω is included as a normalization of the time-scale, as all evolutionary time-scales depend on Ω in the same way. The relevant time-scales are τ_κ, τ_β, τ_{Ω_P}, $\tau_{ff,g}$, and τ_{cc}, denoted by κ, β, Ω_P, f, and c, respectively. The dashed black lines divide the regions within which each time-scale is relevant from the regions in which it is irrelevant, as described in Section 4.2. The dashed white lines divide the regions for which cloud lifetime is longer than the minimum evolution time-scale (above the line) from the regions in which it is shorter (below the line). These are labelled (ii) and (i), respectively. The solid white lines delineate the values of Q and β above which the rate of galactic shear is higher than the combined rates of all other mechanisms.

bottom panels of the left-hand column). The regime (ii) of cloud lifetimes that are longer than the dominant evolutionary time-scale (enclosed by a white dashed line) is therefore progressively eroded by the introduction of more spiral arms. In fact, the regime (*s*), or which galactic shear has a stronger influence than the combined rates of all compressive evolutionary mechanisms (enclosed by a solid white line in the panels of the central column), is completely removed by the introduction of even a single-arm spiral pattern ($m = 1$) at the pattern speeds considered. By causing additional compression of gravitationally stable gas, particularly in the high-shear regime ($Q \gtrsim 4$ and $\beta < 0.5$, i.e. for outer galaxy bulges), spiral arms encourage the collapse of molecular clouds and so shorten their lifetimes. Conversely, the evolution of clouds formed in gas that is highly gravitationally unstable (i.e. in gas-rich, star-forming galaxies) is overwhelmingly governed by gravity, to the extent that no other process is significant in determining the cloud lifetime.

Above the radius of corotation, the effect of spiral arm crossings is further enhanced by the larger absolute difference between the spiral arm pattern speed and the angular velocity of the mid-plane gas for $\Omega_P/\Omega = 4$ (right-hand column of Fig. 9). The three panels of the left-hand column and the bottom two panels of the right-hand column therefore form a sequence of increasing influence for spiral arm crossings. In the most extreme case of four spiral arms above the radius of corotation (bottom right panel), the region of relevance 'Ω_P' for spiral arm crossings extends into the highly gravitational-unstable region of parameter space for $Q \lesssim 1$. In this case, spiral arm perturbations heavily influence the cloud lifetime in gas-rich, star-forming spiral galaxies.

Fig. 10 displays the same information as Fig. 9, but shows this information as a cross-section through the (β, Ω_P/Ω, Ω) plane, rather than as a cross-section through the (β, Q, Ω) plane. Note that the dashed white lines are analogous to those in Fig. 9, separating the regime (i), in which $\tau < \tau_{min}$, from the regime (ii), in which $\tau > \tau_{min}$. Clouds that form from regions of highly unstable molecular gas at $Q \sim 0.5$ (left-hand column) in star-forming, gas-rich galaxies are governed almost exclusively by gravitational collapse 'f', except at galactocentric radii far outside the radius of corotation, when four spiral arms are involved (bottom panel of the left-hand column). Clouds that form outside the radius of corotation in moderately stable gas ($Q = 2.7$, central column) may be influenced by spiral arm perturbations before they collapse under gravity, as depicted by the regions of relevance 'Ω_P' and '$\Omega_P f$' for spiral arms, encroaching from the top of each panel. In case of four strong spiral arms, such perturbations may also affect moderately stable clouds inside the radius of corotation (bottom side of the central bottom panel). Galactic shear also plays a significant role in cloud evolution for regions of moderately stable gas with flat rotation curves ($\beta \lesssim 0.2$, i.e. the main discs of spiral galaxies), where its coexistence '$\beta\Omega_P f$' with spiral arm perturbations and gravitational free-fall slightly extends the cloud lifetime relative to the case of near solid-body rotation ($\beta \gtrsim 0.5$). Finally, the right-hand column of Fig. 10 demonstrates that, for clouds formed in highly gravitationally stable gas that hosts a spiral pattern, the relevant mechanisms of cloud evolution depends very delicately on galactocentric radius (parametrized by Ω_P/Ω) and the slope of the rotation curve (parametrized by β).

5 CLOUD PROPERTIES THROUGHOUT PARAMETER SPACE

In this section, we use the *regions of dominance* and *regions of relevance* identified in Section 4 to systematically predict the observational properties of molecular clouds in different parts of parameter space, and thus in different galactic environments. We begin by characterizing the predicted properties of clouds in those regions of parameter space that are controlled by gravitational collapse on a time-scale $\tau_{ff,g}$, and by galactic shear on a time-scale τ_β. These two mechanisms of cloud evolution form the basis of our analysis, as the majority of star formation is found to occur in dense, gravitationally bound regions within molecular clouds (Hartmann et al. 2001; Elmegreen 2007; Dobbs et al. 2011a; Dobbs & Pringle 2013). The rate of collapse and the subsequent levels of stellar feedback therefore exert a large influence over the galactic SFR, and play an important role in setting the cloud lifetime. Galactic shear is the only mechanism of cloud evolution that manifestly competes against gravitational collapse, by stretching radially correlated gas in the azimuthal direction. Shear is able to destroy clouds in the opposite sense to free-fall, by dispersing the molecular gas.

Both gravitational collapse and galactic shear dominate large parts of our parameter space and form large regions of coexistence with each of the other cloud evolutionary mechanisms. Ultimately, the star-forming properties of molecular clouds will depend on their tendency towards collapse rather than dispersion, and so it is the relationship of each mechanism to gravitational collapse, or its prevention by shear support, that is most interesting observationally. We therefore characterize the predicted properties of molecular clouds for coexisting pairs of cloud evolutionary mechanisms, including either gravitational free-fall or galactic shear. Although a large number of regions are characterized by the overlap of more than two time-scales, the cloud properties in such regions can be inferred to a great extent from these pairings. The only exception arises at very high levels of gravitational stability in the absence of shear, where epicyclic perturbations are most likely to be relevant (top right corners of Figs 6, 9, and 10).

5.1 Dominance of gravitational collapse (f)

In flocculent galaxies with high gas fractions ($m = 0$ and $Q \lesssim 4$), our theory predicts gravity 'f' to dominate the evolution of molecular clouds, without exception (see Fig. 5). For strong spiral arm patterns with $m = 2$ or 4 (i.e. in grand-design spiral galaxies), dominance at $Q \lesssim 4$ may be shared between gravitational free-fall and spiral arm perturbations 'Ω_P', but only above the radius of corotation (see Figs 7 and 8). Within these gravity-dominated regions of parameter space, it is often the case that gravitational collapse is the *only* relevant mechanism of cloud evolution, up to values of gravitational stability as high as $Q \approx 3$ (see e.g. Fig. 6, for example). The relatively short cloud lifetimes in such environments are consistent with clouds having a short quiescent phase, followed by hierarchical or global gravitational collapse. Given that star formation is mainly limited to dense, gravitationally bound regions within molecular clouds (Hartmann et al. 2001; Elmegreen 2007; Dobbs et al. 2011a; Dobbs & Pringle 2013), a large fraction of these clouds should host star-forming regions, such that the average SFE per unit mass for clouds in these regions of parameter space should be significantly higher than the average SFE per unit mass of all observable clouds.

5.2 Dominance of galactic shear (β)

In elliptical galaxies, outer galactic bulges and galaxy outskirts, large regions of gas exist that are both gravitationally stable and have approximately flat rotation curves ($Q \gtrsim 4$ and $\beta \lesssim 0.5$, e.g. figs 9 and 10 of Leroy et al. 2008). In such environments, cloud evolution is dominated by galactic shear (see the top left corners of each panel in Fig. 5). The only exception arises in the presence of spiral arms, where spiral arm perturbations dominate cloud evolution in galaxy outskirts (corresponding to $\Omega_P/\Omega \gtrsim 2$ in the central and right-hand columns of Fig. 8). In particular, the solid white lines in these figures enclose the regions of parameter space (s) for which galactic shear dominates over the combination of all other cloud evolution mechanisms, such that

$$\tau_\beta^{-1} > \tau_\kappa^{-1} + \tau_{\Omega_P}^{-1} + \tau_{ff,g}^{-1} + \tau_{cc}^{-1}. \quad (27)$$

In these regions of parameter space, we predict that clouds of molecular gas are dispersed by shear before they can be encouraged to collapse via any other mechanism. We therefore expect the GMCs in such regions to contain few gravitationally bound, star-forming regions, and to contribute correspondingly little to the galactic SFR. In Figs 9 and 10, we see that the time-scales on which gas is dispersed are up to several orbital times Ω^{-1}. In the outer regions of galactic discs, where orbital times are long and the rotation curve is flat, diffuse envelopes of quiescent gas with low SFRs may survive for up to hundreds of Myr. In the outer regions of the Central Molecular Zone (CMZ) of the Milky Way, which presents regions of highly gravitationally stable, highly shearing gas (Krumholz & Kruijssen 2015), shear support could greatly extend cloud lifetimes (Jeffreson et al. 2018) and explain the very low SFE observed by Longmore et al. (2013a).

5.3 Galactic shear/free-fall coexistence (βf)

In case of flocculent galaxies without a strong spiral arm pattern ($m = 0$, i.e. the central panel of Fig. 6), coexistence between

galactic shear and gravitational collapse is the most influential pairing of cloud evolutionary mechanisms, occupying a large fraction of parameter space 'βf' for $0 < \beta < 0.7$ and $Q > 1.5$. These are the areas of parameter space where *both* $\tau_{\rm ff,\,g}$ and τ_β are shorter than twice the minimum time-scale $t_{\rm min}$, or shorter than twice the cloud lifetime τ, if $\tau > \tau_{\rm min}$. The shear parameter is typically low (indicative of an approximately flat rotation curve) and the Toomre Q stability parameter is typically high (indicative of low gas fractions). In these regions of parameter space, the dispersive effect of galactic shear will elongate the cloud lifetime and slow down the formation of gravitationally bound regions within GMCs, where the efficiency of star formation per unit mass is highest, or will prevent their formation altogether (see also Meidt et al. 2018; Meidt et al., in preparation).

In the case that galactic shear is relevant, but GMC evolution is still governed by dynamically compressive mechanisms, i.e. in regime (*c*) of the region 'βf' (top left corner of the central panel in Fig. 6), shear will slow the formation of bound regions within GMCs, but will not necessarily prevent their formation over a long period of time. That is, it will lower the SFE per unit time, but not the SFE per unit mass. We therefore expect a significant fraction of the mass in such clouds to be converted to stars, but much more slowly and over a much longer lifetime than the star formation in clouds with lower levels of shear.

In the case that galactic shear is both relevant *and* dominant over all dynamically compressive cloud evolutionary mechanisms, i.e. in regime (*s*) of the region 'βf' (top left corner of the central panel in Fig. 6), shear may gradually tear molecular clouds apart, and therefore prevent the formation of bound, star-forming regions, even over a long period of time. In this case, both the SFE per unit time and the SFE per unit mass will be significantly reduced. For clouds in regime (*s*), we therefore expect very long lifetimes combined with very low integrated levels of star formation, such that only a small fraction of the cloud mass is converted to stars.

Overall, for high levels of gravitational stability ($Q \gtrsim 4$), we expect a longer cloud lifetime and a lower SFE per unit time for a flat rotation curve ($\beta \sim 0$) than for approximately solid-body rotation ($\beta \sim 1$). Indeed, Leroy et al. (2008) observe that in spiral galaxies with low levels of galactic shear ($\beta \approx 1$), the average SFE per unit time is almost three times higher than the average SFE per unit time at high levels of galactic shear ($\beta \approx 0$), with a much smaller spread. The larger spread of SFEs down to lower values at $\beta \approx 0$ corresponds with our parameter space diagrams (e.g. Fig. 6), which show a much larger range of cloud lifetimes for $\beta = 0$ than they do for $\beta = 1$. The influence of galactic shear is also expected to manifest itself through elevation of the virial parameter, and observational studies are indeed beginning to find an inverse correlation between the virial parameter and the SFE per unit time (Leroy et al. 2017b).

The elongation of the cloud lifetime, due to the competition between galactic shear and gravitational collapse, should become particularly noticeable about the division between regime (*s*), where the rate of shear outpaces the sum of all the dynamically compressive evolutionary rates, and regime (*c*), where the dynamically compressive mechanisms outpace the shear. These divisions are indicated by solid white lines in the figures of Section 4, on which the cloud lifetime is theoretically infinite, according to equation (24). In practice, the balance between shear support and the other cloud evolutionary mechanisms can never be sufficiently finely tuned to give an infinite cloud lifetime, due first to the influence of small-scale, non-dynamical influences on cloud evolution, and secondly because cloud–cloud collisions, spiral arm crossings and gravitational collapse are discrete stochastic events that may occur at any time in a cloud's life cycle. However, the key point remains that, in the vicinity of these lines, we predict cloud lifetimes to be longer than in any other region of parameter space.

Previous work has suggested that shear support is ineffective by looking at ~30 pc (regions of) clouds, much smaller than the Toomre scale, in the specific environment of the solar neighbourhood (Dib et al. 2012). Indeed, we do not expect shear support to be effective under these conditions. First, we will show in Section 6.1 that the solar neighbourhood occupies a part of parameter space where shear may be relevant, but never dominates over gravitational collapse. Secondly, zooming-in on scales much smaller than the Toomre scale implies looking at locally collapsing regions that are decoupled from the galactic-scale flow, such that shear is already marginalized. This is immediately obvious in Fig. 3, where the dynamic ranges of τ_β and $\tau_{\rm ff,\,cl}$ do not overlap. Once a gravitationally bound and locally collapsing region has formed, we expect it to collapse on a time-scale $\tau_{\rm ff,\,cl}$, independent of its environment. Our theory considers a wider range of objects than those that are gravitationally bound and collapsing, and we find that for gravitationally stable regions of the ISM with $Q \gtrsim 4$, galactic shear has a significant or even dominant influence on cloud evolution.

5.4 Dominance of spiral arm interactions ($\Omega_{\rm P}$)

In spiral galaxies, we find large areas of parameter space that are dominated by spiral arm crossings. These regions of spiral arm dominance are preferentially located outside the radius of corotation ($\Omega_{\rm P}/\Omega > 1$) and at higher levels of gravitational stability, as can be seen by comparing the sizes of the '$\Omega_{\rm P}$' regions in the centre ($Q \sim 2.7$) and right-hand ($Q \sim 15$) columns of Fig. 8 (see also Fig. 7). Spiral arm crossings may also be dominant below the radius of corotation in grand-design spirals ($m = 2$ and 4 panels in the left-hand column of Fig. 7), provided that the inner disc region is sufficiently gravitationally stable ($Q \gtrsim 3$).

In the following two sections, we will describe our predictions regarding molecular cloud evolution in these spiral arm-dominated regions of parameter space. Spiral arms are found to have a strong influence on the organization of star-forming molecular gas, both in observations (e.g. Elmegreen & Elmegreen 1983; Meidt et al. 2013) and in hydrodynamical simulations (e.g. Dobbs et al. 2008, 2011b), sometimes even leading to a 'beads-on-a-string' morphology in which the majority of massive GMCs live in spiral arms. However, the effect of spiral density waves on GMC evolution (and consequently on the galactic SFR), relative to that in non-spiral galaxies, is highly contested. Many observational comparisons between the galactic SFR in grand design and flocculent galaxies (e.g. Elmegreen & Elmegreen 1986; Schinnerer et al. 2017) have found that spiral arms make no significant difference to the rate of star formation on kiloparsec scales. On the other hand, Hart et al. (2017) find that two-armed spiral galaxies form stars more efficiently than flocculent galaxies, even though the absolute SFR is unaffected. Similarly, hydrodynamical simulations by Dobbs et al. (2011b) find that it is possible for spiral arms to enhance the SFE per unit mass by promoting the formation of more massive, longer lived, and gravitationally collapsing GMCs.

5.4.1 Spiral arm crossing/free-fall coexistence ($\Omega_{\rm P}$f)

At low and moderate levels of gravitational stability ($Q \lesssim 6$, i.e. in star-forming regions of galaxies), there exist large regions of parameter space '$\Omega_{\rm P} f$' in which gravitational free-fall and spiral arm

crossings coexist (see e.g. left- and right-hand columns of Fig. 9). Due to gravitational instability, we expect that clouds in such environments will contain dense, gravitationally bound, star-forming regions (e.g. Hartmann et al. 2001; Elmegreen 2007; Dobbs et al. 2011a; Dobbs & Pringle 2013) that are decoupled from the large-scale galactic dynamics and that eventually destroy the cloud via stellar feedback. We expect that spiral arm perturbations will sweep up and collect these star-forming clouds, creating a larger number of massive GMCs than would be expected due to gravity alone. As the degree of gravitational instability is increased, the effect of spiral arm crossings on cloud evolution and the cloud lifetime is reduced, because GMCs are more likely to be destroyed by stellar feedback before encountering a spiral arm. Accordingly, the most gravitationally unstable gas (bottom of each panel, $Q \lesssim 3$) displays a much smaller difference in colour than does the moderately stable gas (middle of each panel, $3 \lesssim Q \lesssim 6$).

5.4.2 *Spiral arm crossing/shear coexistence ($\beta\Omega_{\rm P}$)*

In the outskirts of spiral galaxies, where levels of gravitational stability may be high and the rotation curve is relatively flat (e.g. the top left corner of each panel in the left-hand column of Fig. 9), galactic shear and spiral arm perturbations coexist in regions '$\beta\Omega_{\rm P}$' of parameter space. Due to the high levels of gravitational stability and shear support, we expect that these regions of parameter space correspond to the most diffuse molecular gas, with the lowest levels of gravitational collapse and star formation. We therefore expect that GMCs in such environments are unlikely to be destroyed by stellar feedback before encountering a spiral arm. They are more likely to be affected by spiral arm crossings than GMCs in more gravitationally unstable regions of parameter space. We expect that the spiral arm density wave will shock and compress diffuse molecular gas into a state of higher density, and therefore induce gravitational collapse in some clouds that were previously supervirial and shear supported. This effect becomes stronger as the number of spiral arms is increased, causing the cloud lifetime to be reduced from >3 orbital times in the case of a single spiral arm (top left corner of the $m = 1$ panel) to $\sim$1 orbital time in the case of four spiral arms (top left corner of the $m = 4$ panel).

5.5 Dominance of epicyclic perturbations

Epicyclic perturbations are dominant only in regions of high gravitational stability and approximately solid-body rotation (e.g. the top right corner of each panel in the central column of Fig. 7). Furthermore, in spiral galaxies, they are only dominant in the vicinity of the radius of corotation (e.g. Fig. 8). Due to the high minimum value of τ_κ (see e.g. Fig. 3), epicyclic perturbations are often relevant only in conjunction with two or three other mechanisms of cloud evolution; most often with free-fall or shear.

5.5.1 *Epicyclic perturbations/free-fall coexistence (κf)*

In correspondence with the regions of dominance for epicyclic perturbations, coexistence between epicyclic perturbations and gravitational free-fall occurs only for high levels of gravitational stability ($Q \gtrsim 4$). This indicates that the relevance of gravitational free-fall has little to do with gravitational instability and more to do with the weak competition provided by epicyclic perturbations, which sets the longest value of the minimum time-scales $\tau_{\rm min}/\Omega^{-1}$ throughout all of parameter space (see e.g. Fig. 5). Molecular clouds in these regions of parameter space will host few gravitationally bound, star-forming regions, and will contribute little to the galactic SFR, in comparison to molecular clouds that are dominated by gravitational free-fall. In regions of very high-shear parameter $\beta \rightarrow 1$, these clouds will experience little dispersion by galactic shear, so that the small compressions introduced by orbital eccentricity on a time-scale τ_κ may induce isolated instances of gravitational collapse and star formation. However, given the high values of Toomre Q and the length of the time-scale τ_κ, we do not necessarily expect these instances to be common.

5.5.2 *Shear/epicyclic perturbation coexistence ($\beta\kappa$)*

Regions of coexistence '$\beta\kappa$' for epicyclic perturbations and shear generally occur at high values of gravitational stability and non-negligible levels of galactic shear ($Q \gtrsim 4$ and $\beta \lesssim 0.8$, e.g. top side of each panel in Fig. 6). Furthermore, the influence of spiral arms tends to overpower the effect of epicyclic perturbations, such that they are only relevant for galaxies with one or no spiral arms ($m = 1$ or 0), or close to the radius of corotation in galaxies with strong spiral patterns (e.g. the $\Omega_{\rm P}/\Omega = 0.99$ panels in Fig. 9). Although the regions '$\beta\kappa$' are small, the interplay between galactic shear and epicyclic perturbations may be of critical importance in key galactic environments. For instance, the CMZ of the Milky Way hosts a dense gas stream at a galactocentric radius of $R \sim 100$ pc (e.g. Molinari et al. 2011), with a very high gas fraction, such that $\phi_{\rm P} \sim 1$ (Henshaw, Longmore & Kruijssen 2016). Depending on the distance a cloud has travelled along the stream, the degree of gravitational stability may be as low as $Q \sim 1.7$ (Kruijssen et al. 2014) or as high as $Q \sim 5$ (cf. Henshaw et al. 2016). Additionally, the degree of shear is weak but non-trivial, such that $\beta \sim 0.7$ (Krumholz & Kruijssen 2015). Due to this combination of physical parameters, a molecular cloud in the 100 pc stream may belong to any one of the three regions 'f', 'κf', or '$\beta\kappa f$' in the left-hand panel of Fig. 6, depending on its gravitational stability and thus its position on the stream. That is, clouds in one section of the stream may be supported by galactic shear (region '$\beta\kappa f$'), while clouds in another section may simply collapse (regions 'κf' and 'f'). The relative importance of epicyclic perturbations in these regions of parameter space is consistent with the theory that they trigger the collapse of shear-supported molecular clouds, as these clouds pass through the pericentre of an eccentric orbit along the 100 pc stream (Longmore et al. 2013b; Kruijssen, Dale & Longmore 2015; Henshaw, Longmore & Kruijssen 2016; Kruijssen et al., in preparation). We investigate the mechanisms governing the CMZ cloud life cycle in more detail in Jeffreson et al. (2018).

5.6 Dominance of cloud–cloud collisions

In Figs 5, 7, and 8, we see that the cloud–cloud collision time-scale is never dominant over the time-scale for gravitational collapse, as predicted in Section 3.3. Furthermore, Figs 6, 9, and 10 demonstrate that with the exception of extremely high mid-plane gas fractions ($\phi_{\rm P} \approx 1$), $\tau_{\rm cc}$ is only relevant for high values of gravitational stability and flat rotation curves ($Q \sim 15$ and $\beta \sim 0$), where competition between gravitational free-fall and galactic shear extends the cloud lifetime. Since all mechanisms of cloud evolution are relevant in this region of parameter space, and the importance of cloud–cloud collisions at high Q is likely to be overestimated in our theory (see Section 2.3), we conclude that cloud–cloud collisions only make a meaningful contribution to the cloud lifetime in shearing, gas-right environments ($\beta \sim 0$ and $\phi_{\rm P} \sim 1$), such as extended high-redshift galaxies (at low Q) and low-redshift galaxy outskirts (at high Q). In these discs, we expect that cloud–cloud collisions may shorten the cloud lifetime and slightly enhance the cloud-scale SFR by inducing

gravitational collapse in high-density regions of molecular clouds which are not already bound and collapsing. This effect will be negligible for the galactic-scale SFR, because at low to middle values of the Toomre Q parameter, most star formation will occur in bound, collapsing regions that have already decoupled from the galactic-scale dynamics.

6 CLOUD LIFETIMES IN A SAMPLE OF GALAXIES

Here, we examine the cloud lifetimes predicted by our theory for a sample of four galaxies (the Milky Way, M31, M51, and M83). We use surface density profiles, rotation curves, and velocity dispersion profiles from the literature to derive the quantities β, Q, and $\phi_{\rm P}$ that define our parameter space. We also use information from the literature to justify our choice of the number of spiral arms m for each galaxy, as well as our choice of pattern speed $\Omega_{\rm P}$. We set the stellar contribution to the surface density of the ISM to the value of $\phi_{\rm P} = 3$ appropriate to Milky Way-like disc galaxies (Krumholz & McKee 2005).

We calculate the cloud lifetime using equation (24), with each of the constituent time-scales as derived in Section 2, and consider our predictions as a function of galactocentric radius. For comparison, we also display the divisions between the *regions of relevance* discussed in Sections 4 and 5. In the case of M51, we compare our predictions for the cloud lifetime to the predictions of Meidt et al. (2015).

Before proceeding, it is important to note that our theory predicts the cloud lifetime according to the entire reservoir of gas in the galactic mid-plane, quantified by the mid-plane gas density $\rho_{\rm g}$. That is, we do not consider the emissivity of molecular gas tracers such as CO and their variation with the local gas density, as described in Leroy et al. (2017a). This approach is required to consider and compare the influences of large-scale dynamical processes, which affect molecular gas at all density scales, not only those density scales that are CO bright. Our approach allows us to determine the processes that are *dominant* in setting the cloud lifetime, in the sense that they influence molecular clouds on the shortest time-scales. On the other hand, care must be taken when our predictions of the cloud lifetime are compared to those derived from CO observations. In regions of gas that are purely molecular and have average densities above $\sim 10 M_{\odot} {\rm pc}^{-3}$, the vast majority of gas has a high CO emissivity, such that our predictions should correspond well with CO observations. However, as the average mid-plane H_2 density decreases, an increasing fraction of the cloud lifetime predicted by our theory becomes 'invisible' in the sense that it is not strongly CO emitting. Our theory therefore overpredicts the CO-traced cloud lifetime by an increasing amount as the average H_2 density of the galactic mid-plane decreases. We expect this effect to be particularly significant in the lower density outskirts of galactic discs.

6.1 Milky Way

We predict the cloud lifetimes for the Milky Way using the surface densities from Kennicutt & Evans (2012), the rotation curve from Bland-Hawthorn & Gerhard (2016), and the velocity dispersions from Heiles & Troland (2003), each of which vary with galactocentric radius. These observational data determine the parameters β and Q. We use a pattern speed of $\Omega_{\rm P} \approx 0.026 \pm 0.002\,{\rm Myr}^{-1}$ from Gerhard (2011) along with the rotation curve to set the value of $\Omega_{\rm P}/\Omega$. We represent the galactic bar inside $\sim$5 kpc (Wegg, Gerhard & Portail 2015) using $m = 2$.

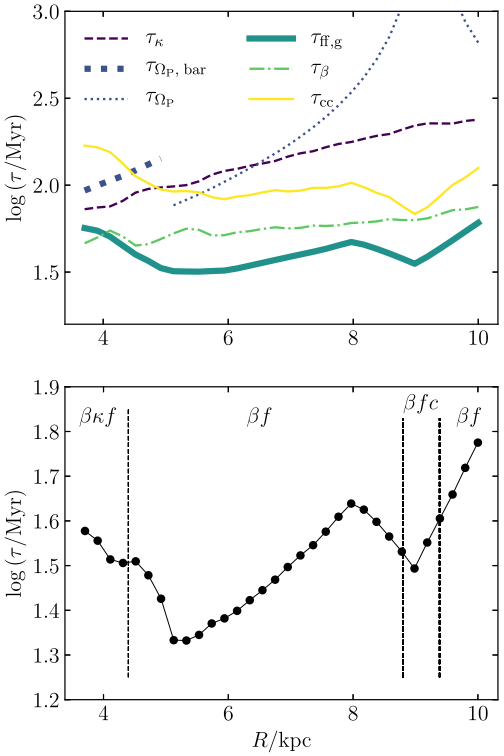

Figure 11. Variation in the predicted cloud lifetimes for the Milky Way with galactocentric radius. The upper panel gives each of the time-scales of dynamical evolution, including the overall minimum time-scale $\tau_{\rm min}$. The time-scale for spiral arm crossings ($m = 4$) is represented by the thin dotted line, while the time-scale for interactions with the Galactic bar ($m = 2$) is represented by the thick dotted line. The lower panel gives the lifetime calculated using equation (24). The regions of relevance are labelled as in Figs 6, 9, and 10, where f corresponds to $\tau_{\rm ff,\,g}$, β corresponds to τ_{β}, κ corresponds to τ_{κ} and c corresponds to $\tau_{\rm cc}$.

The number of spiral arms m that should be used for >5 kpc is not clear, as a large degree of uncertainty remains as to the strength of the spiral pattern for the Milky Way (Antoja et al. 2016). It is not obvious whether $m = 4$ for strong spiral arms, or whether $m = 0$ due to flocculence. However, we find that this uncertainty does not have a large effect on our predictions, because the low observed pattern speed ensures that the time-scale for spiral arm crossings is long outside 5 kpc. In the top panel of Fig. 11, we display the variation in each time-scale with galactocentric radius, and the time-scale for spiral arm collisions $\tau_{\Omega_{\rm P}}$ is displayed as a thick dotted line within the region of the Galactic bar (<5 kpc), and as a thin dotted line outside this region (>5 kpc). The discontinuity between these two sections corresponds to the tip of the Galactic bar. We have used $m = 4$ for strong spiral arms, and even in this extreme case, the time-scale for spiral arm crossings is always longer than twice the minimum time-scale (the thick green line representing $\tau_{\rm ff,\,g}$ in the top panel) and between five and six times longer than the cloud lifetime (the black filled markers in the bottom panel). The regions of relevance displayed in the bottom panel of Fig. 11, which compare each time-scale to twice the minimum time-scale $\tau_{\rm min}$ if $\tau_{\rm min}$ is longer than the cloud lifetime, and compare each time-scale to twice the minimum

cloud lifetime τ if $\tau > \tau_{\rm min}$, confirm the small contribution made by spiral arm crossings – $\tau_{\Omega_{\rm p}}$ is never a *relevant* time-scale.

Comparing the top and bottom panels of Fig. 11 indicates that the cloud lifetime is primarily controlled by gravitational collapse and shear support, over the radial interval considered. The dip in $\tau_{\rm ff,\,g}$ in the vicinity of the solar neighbourhood is due to the dip in the time-scale for gravitational collapse (and to a lesser extent in the time-scale for cloud–cloud collisions), which in turn is caused by a dip in the value of the Toomre Q parameter at this radius. This behaviour is not mirrored by the shear time-scale, reducing the degree of support provided to the cloud. The slight global increase in cloud lifetime with galactocentric radius is due simply to the Ω^{-1} dependence of all the time-scales.

In the vicinity of the solar neighbourhood ($R \sim 8$ kpc), the cloud lifetimes we predict for the Milky Way are between 30 and 40 Myr. This contrasts with the lifetimes of gravitationally bound, star-forming regions described by Elmegreen (2000) and Hartmann et al. (2001), which have lifetimes of <5 Myr within the solar neighbourhood. As described in Section 2.2, these regions are gravitationally decoupled from the galactic-scale dynamics and therefore have lifetimes independent of dynamical time-scales. Our model is more general and accounts not only for globally collapsing regions but for clouds of many different sizes and structures, which may be globally or hierarchically collapsing, bound or unbound. We predict that such a sample of clouds has a median lifetime of 33 Myr, or 0.8 free-fall times $\tau_{\rm ff,\,g}$ in the mid-plane of the Galaxy.

6.2 M31

To predict the cloud lifetimes for M31, we use the surface densities provided by Schruba et al. (in preparation), the rotation curve from Corbelli et al. (2010), and the velocity dispersions from Braun et al. (2009), to calculate the values of the parameters β and Q. Given that there is no evidence for the presence of spiral arms in M31, we set $m = 0$ in our model, to produce the cloud lifetimes shown in the bottom panel of Fig. 12, against galactocentric radius. The top panel shows the variation in individual time-scales, while the bottom panel displays the resulting cloud lifetime calculated using equation (24). The dashed lines delineate the regions of relevance for each cloud evolutionary mechanism.

In the case of M31, the general trend of increasing cloud lifetime due to the Ω^{-1} dependence of all time-scales is obscured by long cloud lifetimes between galactocentric radii of around 8–10 kpc and a large dip at around 12 kpc. This radius corresponds to a ring of gas that characterizes the morphology of M31 (e.g. Braun et al. 2009). The dip at ∼12 kpc is due to a dip in the Toomre Q parameter at this radius, causing the time-scales for gravitational free-fall and cloud–cloud collisions to decrease in magnitude. The long cloud lifetimes from 8 to 10 kpc are manifestly due to the proximity of the shear and gravitational free-fall time-scales at this radius. The shear time-scale τ_β in the top panel of Fig. 12 comes very close to the gravitational free-fall time-scale $\tau_{\rm ff,\,g}$, such that the rates are nearly balanced. Galactic shear competes against gravitational collapse to disperse the cloud rather than to collapse it, the balance between these two time-scales leads to longer cloud lifetimes via equation (24).

In general, M31 displays longer values of all cloud evolutionary time-scales than the Milky Way, by a consistent factor of ∼3. This leads to a higher median lifetime of ∼64 Myr, corresponding to ∼0.9 free-fall times $\tau_{\rm ff,\,g}$ in the plane of the galaxy. The orbital time Ω^{-1} is the only dynamical parameter that affects all time-scales in the same way, indicating that the slower angular speed of mid-plane gas rotation at these larger radii is responsible for the elongation of cloud lifetimes in M31, relative to the Milky Way.

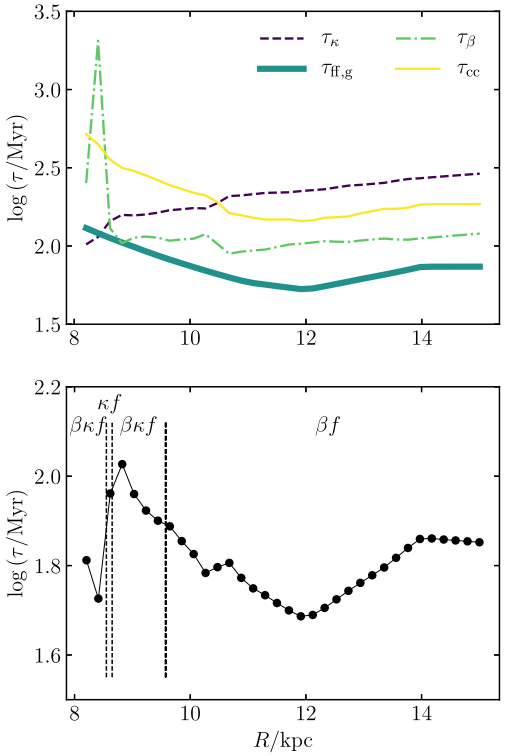

Figure 12. Variation in cloud lifetimes predicted for the galaxy M31 by our model, with radius from its centre in kpc. The upper panel gives each of the time-scales of dynamical evolution, including the overall minimum time-scale $\tau_{\rm min}$. The lower panel gives the lifetime calculated using equation (24) (black filled circles). The regions of relevance are labelled as in Figs 6, 9, and 10, where f corresponds to $\tau_{\rm ff,\,g}$, β corresponds to τ_β, and κ corresponds to τ_κ.

6.3 M51

Our predictions for the cloud lifetimes in M51 are calculated using the surface densities, velocity dispersions, and rotation curve from Schuster et al. (2007), from which we calculate the values of the parameters β and Q. The striking grand-design structure of M51 consists of two main spiral arms (Henry, Quillen & Gutermuth 2003), such that we take $m = 2$ in our models at all galactocentric radii. The pattern speed of these spiral arms has been extensively studied at varying radii, and while Zimmer, Rand & McGraw (2004) use the Tremaine–Weinberg method to derive a global pattern speed of $\Omega_{\rm P} \approx 0.039\,{\rm Myr}^{-1}$ for these spiral arms, Meidt et al. (2008, 2013) find evidence for at least two different pattern speeds inside a radius of 4 kpc, both of which are significantly higher than this value, around $0.09\,{\rm Myr}^{-1}$. In the top panel of Fig. 13, it can be seen that the time-scale $\tau_{\Omega_{\rm P}}$ for spiral arm crossings is significantly altered by the choice of pattern speed. The thin dotted line corresponds to the value from Zimmer et al. (2004), while the thick dotted line corresponds to the value from Meidt et al. (2013). In the bottom panel, we see that the predicted cloud lifetimes are also altered by choosing one of these pattern speeds over the other. The Zimmer

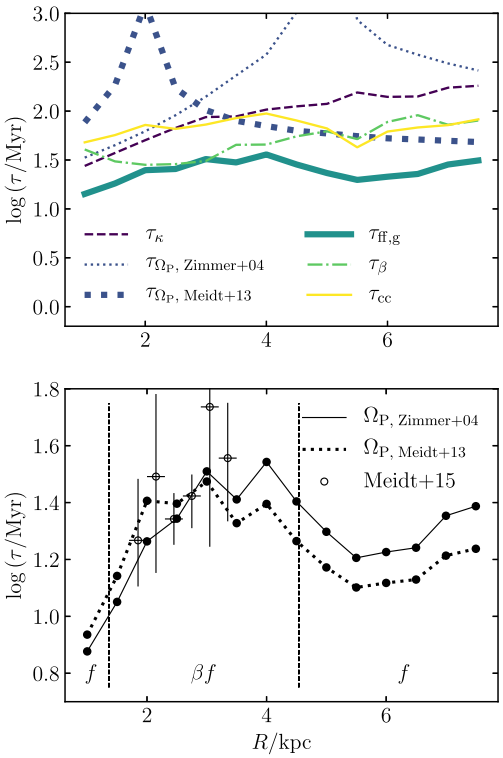

Figure 13. Variation in cloud lifetimes predicted for the galaxy M51 by our model, with radius from its centre in kpc. The upper panel gives each of the time-scales of dynamical evolution, including the overall minimum time-scale $\tau_{\rm min}$. The lower panel gives the lifetime calculated using equation (24), with two different values of the pattern speed (see Section 6.3). Black filled circles represent lifetimes calculated using the value from Zimmer et al. (2004) (Zimmer+04), while red filled circles represent lifetimes calculated using the higher value from Meidt et al. (2013) (Meidt+13). The black open circles represent the cloud lifetimes calculated in Meidt et al. (2015) (Meidt+15). We see that there is satisfactory agreement between their results and our predictions for both pattern speeds. The regions of relevance are labelled only for the Zimmer et al. (2004) pattern speed, as in Figs 6, 9, and 10, where f corresponds to $\tau_{\rm ff,\,g}$ and β corresponds to τ_β.

et al. (2004) value is represented by a solid line, while the Meidt et al. (2013) value is represented by a dotted line. Both sets of cloud lifetimes agree well with the lifetimes estimated from observations by Meidt et al. (2015), who use the higher pattern speed from Meidt et al. (2013, black open circles).

For simplicity, we show the regions of relevance in Fig. 13 (dashed lines) only for the Zimmer et al. (2004) value of $\Omega_{\rm P}$, as discussion about the exact radial dependence of the multiple pattern speeds in Meidt et al. (2013) is ongoing. The authors suggest that the higher pattern speed may even apply to a bar which terminates at its radius of corotation ($\approx$2.3 kpc) and give way to a much lower value of 0.056 Myr^{-1}. We note that while spiral arm crossings are never relevant for the Zimmer et al. (2004) pattern speed (thin dotted line in the top panel of Fig. 13), they are relevant at $R \gtrsim 6$ kpc for the Meidt et al. (2013) value (thick dotted line).

Our broad brush strokes theory captures the overall dominance of gravitational free-fall and galactic shear, as well as the transition between shear- and gravity-dominated behaviour proposed in Meidt et al. (2015). Shear is much more important at smaller galactocentric radii, while at larger radii ($R > 4.5$ kpc), only gravity is significant. Accordingly, these are the galactocentric radii at which Meidt et al. (2015) find strong signatures of high-mass star formation. In the context of our models, we would also expect the mechanism of cloud destruction to depend on the degree of shear support provided against the four dynamically compressive time-scales. We would expect more clouds to be destroyed by dispersion for galactocentric radii $R < 4.5$ kpc, and for more clouds to be destroyed by collapse and feedback for $R > 4.5$ kpc. This prediction also agrees with the discussion in Meidt et al. (2015).

Overall, the smaller galactocentric radii at which the observations for M51 are taken, relative to the observations for the Milky Way and M31, mean that the orbital time Ω^{-1} is shorter for M51. This is reflected in the values of all the cloud evolutionary time-scales, which are $\sim$2 shorter for M51 than for the Milky Way, giving a cloud lifetime which is also a factor of $\sim$2 shorter. The median cloud lifetime is $\sim$21 Myr, equivalent to $\sim$0.8 free-fall times $\tau_{\rm ff,\,g}$ in the mid-plane of the galaxy. The longest lifetimes occur where the competition between galactic shear and gravitational collapse is closest.

6.4 M83

We predict the cloud lifetimes in M83 using the observational data given in fig. 6 of Freeman et al. (2017). These consist of the total (atomic and molecular) gas surface density curve, the rotation curve from Walter et al. (2008) and the total velocity dispersion inferred from the Atacama Large Millimeter/submillimeter Array (ALMA) CO and THINGS 21-cm data, weighted by the relative surface densities of the atomic and molecular components. From these data, we obtain the values β, Q, and Ω in our Fundamental Plane. Like M51, M83 has two main spiral arms, so we use a value of $m = 2$ and a pattern speed of $\Omega_{\rm P} = 0.045$ Myr^{-1} from Zimmer et al. (2004). The predicted cloud lifetimes are displayed in the bottom panel of Fig. 14 as a function of galactocentric radius, while the individual time-scales are shown in the panel above.

To remove noise on short scales from these data, we have used a Savitzky–Golay filter with fourth-order polynomials and a window size of 35 data points (Savitzky & Golay 1964). With this setup, each smoothed data point is calculated using $(35 - 1)/2 = 17$ data points to either side of its own position, weighted by a set of 35 analytic coefficients. These analytic coefficients are constrained by the fourth-order polynomial coefficients, of which there are five. In simple terms, each window of 35 data points is therefore described using five coefficients, giving an effective 'smoothing length' of $\sim$0.4 kpc. This procedure removes noise on scales $\sim$0.1 kpc without removing the physical oscillations on kpc scales, which are most visible in the profiles of τ_β and τ_κ, and that also persist in the cloud lifetime (bottom panel of Fig. 14).

The large peak in the cloud lifetime at $R \sim 3.5$ in the bottom panel of Fig. 14 illustrates an important caveat in our use of equation (24) to combine the time-scales of cloud evolution. The peak occurs when the rate of galactic shear approaches the combined rates of the dynamically compressive mechanisms of cloud evolution, such that $\tau_\beta^{-1} \rightarrow \tau_\kappa^{-1} + \tau_{\Omega_{\rm P}}^{-1} + \tau_{\rm ff,\,g}^{-1} + \tau_{\rm cc}^{-1}$. At such closely balanced values of dispersive and compressive evolutionary rates, the cloud lifetime predicted by equation (24) becomes very sensitive to β, which in turn is very sensitive to the rotation curve. Any noise in the rotation curve may then produce sharp peaks in the cloud lifetime, with $\tau \rightarrow \infty$. That is, the simple statistical approach we have taken

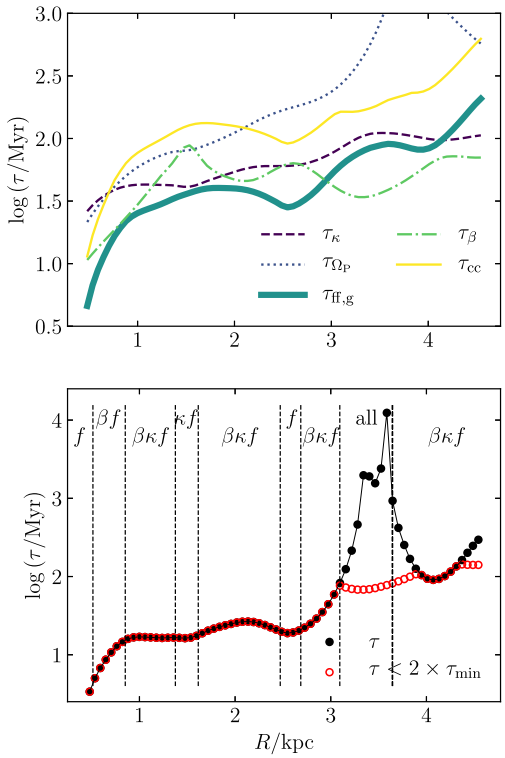

Figure 14. Variation in cloud lifetimes predicted for the galaxy M83 by our model, with radius from its centre in kpc. The upper panel gives each of the time-scales of dynamical evolution, including the overall minimum time-scale $\tau_{\rm min}$. The black filled circles in the lower panel give the lifetime calculated using equation (24), while the red open circles give the lifetime below a threshold of twice the minimum cloud evolutionary time-scale. This prevents the cloud lifetime from becoming unreasonably long due to an unphysical degree of precision in the balance between galactic shear and the other cloud evolutionary mechanisms (see Section 6.4). The regions of relevance are labelled as in Figs 6, 9, and 10, where f corresponds to $\tau_{\rm ff,\,g}$, β corresponds to τ_β, κ corresponds to τ_κ, and 'all' indicates that all time-scales are relevant.

to account for the coexistence of cloud evolutionary mechanisms and the phenomenon of shear support (adding their rates) means that cloud lifetimes can increase asymptotically if the shear and the collective other time-scales are balanced. This asymptotic increase in the cloud lifetime is unphysical, and results from the following characteristics of our theory:

(i) Our theory is statistical in the sense that it combines rates. However, when stochastically drawing from these rates and their associated probabilities, one cloud evolutionary mechanism will always occur first in practice, with the exception of galactic shear and epicyclic perturbations, which have a continuous effect over time. This stochasticity 'smoothes out' the sensitivity of cloud lifetime to the rotation curve, in the sense that it does not allow extremely close balance between cloud evolutionary mechanisms. Even if large-scale dynamics alone are responsible for the evolution of molecular clouds, the cloud lifetime cannot become infinite when shear balances all other time-scales, due to their random nature.

(ii) Our theory considers the influence of large-scale dynamics on the cloud lifetime, but not the influences of many other possible non-dynamical evolutionary mechanisms on smaller scales. When the large-scale dynamical mechanisms of cloud evolution approximately negate each other, all other cloud evolutionary mechanisms become comparatively more important. We would therefore expect that in regions of parameter space where the dynamical mechanisms of cloud evolution predict very long cloud lifetimes, GMCs will actually be destroyed on much shorter time-scales by non-dynamical or smaller scale mechanisms of cloud evolution than those which we have considered, such as ionization by ultraviolet radiation, or stellar feedback from gravitationally bound regions on subcloud scales (e.g. Elmegreen 2007).

To illustrate the effect of these stated assumptions, we include an additional set of 'cloud lifetimes' in the bottom panel of Fig. 14, represented by the open circles. These values are identical to the lifetimes from equation (24) (indicated by the filled circles), but with an imposed upper limit of twice the minimum evolutionary time-scale. At $R \sim 3.5$ kpc, the minimum time-scale is the shear time-scale τ_β, so the cloud lifetime is limited by the assumption that the influence of galactic shear can only be reduced partially, by a factor of 1/2, due to competition with dynamically compressive mechanisms of cloud evolution. This causes the maximum predicted lifetime to drop to $\tau \sim 100$ Myr at $R \sim 3.5$ kpc. Given that galactic shear has a continuous effect on an object that is extended along the galactocentric radial direction, while spiral arm crossings and cloud–cloud collisions are discrete, stochastic events, such partial balance is more likely to occur than the infinite lifetime produced by exact balance between compressive and dispersive dynamical time-scales. By this reasoning, the $\sim 10^4$ Myr height of the sharp peak in the cloud lifetime between 3 and 4 kpc should not be viewed as a physically accurate prediction. However, we do predict that the close balance between dynamically compressive and dynamically dispersive mechanisms of cloud evolution results in elongated cloud lifetimes between 3 and 4 kpc in M83.

Overall, we find that cloud lifetimes in M83 are controlled primarily by the interplay between gravitational collapse and galactic shear, with gravity dominating below $R \approx 3$ kpc ($\tau_{\rm ff,\,g}$ is manifestly the shortest time-scale for $R \lesssim 3$ in the top panel of Fig. 14) and shear dominating above $R \approx 3$ kpc (τ_β is manifestly the shortest time-scale for $R \gtrsim 3$ in the top panel of Fig. 14). Correspondingly, we expect a decrease of the SFE at $R > 3$ kpc, which in turn may explain the drop of the cluster formation efficiency at these radii (Adamo et al. 2015). Epicyclic perturbations are also relevant at most galactocentric radii, as indicated by the regions of relevance labelled with κ in the bottom panel of Fig. 14, however τ_κ is never dominant over $\tau_{\rm ff,\,g}$ or τ_β. The predicted importance of gravity and shear is consistent with the work of Freeman et al. (2017), who have found that significant gravitational contraction and regulation by galactic shear is implied by the cloud mass distribution. These authors also show that both the maximum cloud mass and the average mass of the five most massive GMCs drop systematically from the central regions of the galaxy out to 4.5 kpc. Our predictions demonstrate a corresponding systematic *increase* in the cloud lifetime between these galactocentric radii (ignoring the sharp peak between 3 and 4 kpc), due primarily to the Ω^{-1} dependence of all cloud evolutionary time-scales. Combining our theoretical predictions with the observational analysis of Freeman et al. (2017) therefore suggests that the cloud mass may be anticorrelated with the cloud lifetime. Such a result would also be consistent with the view that the majority of star formation occurs in the most massive

clouds (Murray 2011; Reina-Campos & Kruijssen 2017), which collapse faster, have higher SFRs, and are shorter lived.

7 CONCLUSIONS

We have developed an analytic theory for the molecular cloud lifetime that depends on the large-scale dynamics of the ISM, independent of theoretical assumptions about the size, structure, mode of gravitational collapse, and gravitational boundedness of GMCs. This theory includes the mechanisms of gravitational free-fall, galactic shear, epicyclic perturbations, spiral arm interactions, and cloud–cloud collisions. We have made as few assumptions as possible about the exact way in which clouds interact with each of the proposed environmental mechanisms, instead characterizing the influence of each by its time-scale and by describing its dynamical relationship to the other evolutionary mechanisms in the context of a hydrostatic equilibrium galaxy disc. Our approach represents an advancement both in its systematic approach and in its expansiveness, by accounting simultaneously for multiple influences on cloud evolution. Here, we briefly summarize the main results and conclusions of our work.

7.1 Theoretical approach

To our knowledge, no theory prior to this work has produced a formalism for considering the interplay between environmental mechanisms of cloud evolution across parameter space. Our systematic approach enables an overview of the influences on GMC evolution to be obtained without having to make assumptions that may only be relevant to a subset of GMCs. By comparing our simple analytic expression for the cloud lifetime to observations that will soon be available through currently ongoing efforts (see Section 7.4), the accuracy of our predictions will be testable. The comparison between observation and theory will shed light on the influence of ISM dynamics relative to the effects not considered in our theory, such as the degree of non-linear interplay between the evolutionary mechanisms and the details of stellar feedback. Our theory also provides a broad brush strokes platform upon which physical complexity and detail can be systematically built. We briefly discuss our ongoing work in this direction in Section 7.4.

7.2 Significance of each cloud evolutionary mechanism

We find that the large-scale dynamical mechanisms affecting cloud evolution can be described within a fundamental parameter space (β, Q, Ω), with a secondary dependence on $\phi_{\rm P}$, a parameter that reflects the (inverse of the) local gas fraction. These are all observable properties of the ISM that can be derived using the galactic rotation curve, along with the gas and stellar surface densities and velocity dispersions. In galaxies with spiral arms, the fundamental parameter space is extended to include the number of spiral arms m and the pattern speed as a fraction of the ISM angular velocity, $\Omega_{\rm P}/\Omega$. We have predicted the environmentally and dynamically dependent cloud lifetimes throughout the region of parameter space that is currently observable, considering the possibility of augmentation and competition between cloud evolutionary mechanisms. For each cloud evolutionary mechanism, we have systematically determined the *regions of dominance* (i.e. the regions of parameter space for which each mechanism occurs on a shorter time-scale than all other mechanisms) and the *regions of relevance* (i.e. the regions of parameter space for which each mechanism occurs on a time-scale no longer than twice the minimum time-scale, or no longer than twice the cloud lifetime, if the cloud lifetime is elongated by competition between different mechanisms). Via examination of the resulting parameter space maps, we have reached the following main conclusions.

(i) Throughout the currently observable region of parameter space, chosen according to the ranges of physical parameters presented in Leroy et al. (2008), gravitational collapse on a time-scale $\tau_{\rm ff,\,g}$ is by far the most prevalent and influential mechanism in setting the cloud lifetime. Gravitational free-fall is *relevant* throughout most of our parameter space, excluding the most gravitationally stable (high Toomre Q) regions of spiral galaxies. It is *dominant* for levels of gravitational stability up to $Q \sim 4$ in most spiral galaxies and up to $Q \sim 8$ in elliptical and flocculent galaxies.

(ii) In galactic environments for which the rotation curve is approximately flat and gravitational stability is high ($\beta \lesssim 0.5$ and $Q \gtrsim 4$), galactic shear provides a *relevant* degree of support against the dynamically compressive mechanisms of gravitational free-fall, epicyclic perturbations and cloud–cloud collisions. This causes the cloud lifetime to be elongated. At the highest levels of shear ($\beta \sim 0$), shear support *dominates* cloud evolution down to Toomre Q values as low as $Q \sim 4$. With the introduction of spiral arms, the regions of *relevance* and *dominance* for galactic shear are reduced, but still occupy a significant region of parameter space in the cases of low pattern speeds $\Omega_{\rm P}/\Omega$ and few spiral arms m.

(iii) Spiral arm crossings on a time-scale $\tau_{\Omega_{\rm p}}$ are most *relevant* at high values of gravitational stability (high Toomre Q), where interactions between clouds and spiral arms may occur before clouds are destroyed by gravitational collapse and the resulting stellar feedback. At high pattern speeds $\Omega_{\rm P}/\Omega$ and high numbers of spiral arms m, spiral arm crossings may be *relevant* at all values of Q, with regions of *dominance* extending as low as $Q \sim 1$. At lower numbers of spiral arms and lower pattern speeds, the dominance of spiral arm crossings is limited to values of $Q \gtrsim 6$.

(iv) In non-spiral galaxies, the regions of *relevance* and *dominance* for epicyclic perturbations on a time-scale τ_κ are restricted to high values of Toomre Q, where the resulting orbital eccentricity of clouds and the ISM can influence the evolution of GMCs before gravitational collapse sets in. They are also restricted to high values of the shear parameter β, where clouds are not significantly dispersed before an epicycle is completed. Such conditions exist near the centres of disc galaxies like the Milky Way. In galaxies with spiral arms, epicyclic perturbations are only relevant close to the radius of corotation, where spiral arms play no role in cloud evolution, or in the case of a weak spiral pattern below the radius of corotation. When present, the influence of spiral arms easily dominates over the effect of epicycles.

(v) Cloud–cloud collisions on a time-scale $\tau_{\rm cc}$ are never *dominant*. They are *relevant* only in the case of a pure gas disc $\phi_{\rm P} = 1$ or at very high levels of stability and shear ($\beta \sim 0$ and $Q \sim 15$) in galaxies without spiral arms, where all cloud evolutionary mechanisms become relevant. This negligible influence of cloud–cloud collisions throughout most of parameter space is primarily due to the similar environmental scaling of the free-fall time and the cloud collision time, such that the rate of gravitational collapse always outpaces the rate of collisions, especially at low values of Toomre Q. The gravitationally bound clouds needed to sustain regular cloud–cloud collisions are typically destroyed by collapse and stellar feedback before a collision can occur.

Combining the above considerations for individual cloud evolutionary mechanisms, we can describe which mechanisms set the

cloud lifetime in the specific parts of the parameter space that describes galaxies. Our conclusions in this area are as follows.

(i) In highly star-forming, gas-rich galaxies such as high-redshift galaxies, with large reservoirs of gravitationally unstable gas ($Q \lesssim 4$), the cloud lifetime is controlled almost exclusively by gravitational free-fall.

(ii) Far from the radius of corotation in grand-design spiral galaxies ($|\Omega_{\rm P}/\Omega - 1| \gg 1$ with $m = 2$ or 4), spiral arm perturbations have a *dominant* influence on the cloud lifetime for all $Q \gtrsim 1$. Gravitational collapse is still *dominant* up to the case of marginal stability ($Q \lesssim 1$).

(iii) Close to galactic centres, where molecular gas may be highly gravitationally stable with low levels of shear ($\beta \gtrsim 0.5$ and $Q \sim 15$), the cloud lifetime is controlled by epicyclic perturbations (i.e. orbital eccentricity). If strong spiral arms are also present (e.g. in the presence of a nuclear spiral), then the cloud lifetime is set by a combination of epicycles and spiral arm perturbations.

(iv) For outer galaxy bulges, containing regions of highly stable, highly shearing gas ($Q \gtrsim 6$ and $\beta \lesssim 0.5$), cloud lifetimes are governed by the competition between gravitational collapse and galactic shear, along with a lesser contribution from epicyclic perturbations. Clouds in this region of parameter space tend to have longer lifetimes due to the high degree of shear support, allowing dynamical mechanisms with longer time-scales to significantly influence cloud evolution. This region of parameter space is therefore characterized by the coexistence of many different cloud evolutionary mechanisms. For very high levels of stability and shear ($Q \sim 15$ and $\beta \sim 0$), the influence of galactic shear dominates over the combined influence of all the dynamically compressive mechanisms of cloud evolution, such that clouds are more likely to be destroyed by dispersal than by collapse.

The combination of all evolutionary mechanisms across parameter space gives rise to a number of implications for star formation and cloud evolution as a function of the galactic environment. Our conclusions in this area are as follows.

(i) Our results imply that typically, the cloud lifetime increases with the degree of gravitational stability Q.

(ii) Many gravitationally stable environments with $Q \gtrsim 4$ are dominated by spiral arm crossings on a time-scale $\tau_{\Omega_{\rm P}}$. Due to the high degree of gravitational stability in these clouds, we expect that they contain few gravitationally bound, star-forming regions that are decoupled from the galactic-scale dynamics. By inducing compression of previously unbound regions of the ISM, spiral arm interactions may therefore increase the galactic-scale SFE per unit mass, and decrease the cloud lifetime.

(iii) We expect a transition from star-forming clouds to quiescent clouds as the rotation curve flattens and the degree of gravitational stability increases. As β decreases and Q increases, the relevance of shear support increases, leading to a suppression of gravitational collapse, and consequently star formation. This may contribute to the low SFR observed across much of the Galactic Centre environment, which displays high values of gravitational stability, $Q \sim 15$, and a non-trivial degree of galactic shearing, $\beta = 0$–0.7 (e.g. Krumholz & Kruijssen 2015).

(iv) Across our parameter space, comparison of cloud evolutionary time-scales suggests that cloud–cloud collisions are rarely an important factor in setting the course of cloud evolution or the cloud lifetime. Gravitational collapse of the ISM occurs on a much shorter time-scale, suggesting that collisions between clouds do not play an important role in setting either the cloud-scale SFR or the galactic-scale SFR.

7.3 Cloud lifetimes

We have applied our theory to four galaxies and find that the predicted cloud lifetimes typically range between 10 and 100 Myr, with the exception of a few extreme regimes in M83 and one extreme regime in M31, where shear balances almost exactly with gravitational collapse. In practice, this delicate balance of rates cannot ever be maintained, due to the stochastic, quantized nature of several of the considered mechanisms.

(i) Milky Way ($R = 4$–10 kpc): cloud lifetimes fall between 21 and 60 Myr with a median of 33 Myr. The dominant mechanisms of cloud evolution are galactic shear and gravitational collapse of the ISM, with minor contributions from the spiral arms and cloud–cloud collisions.

(ii) M31 ($R = 8$–15 kpc): cloud lifetimes fall between 49 and 106 Myr with a median of 64 Myr, mainly due to relatively high values of the orbital time-scale Ω^{-1} at these galactocentric radii. The lifetimes are dominated by galactic shear and gravitational collapse of the ISM.

(iii) M51 ($R = 1$–8 kpc): cloud lifetimes are the shortest of the four galaxies, falling between 8 and 35 Myr with a median of 21 Myr. This is due mainly to the short values of the orbital time Ω^{-1} at the radii considered. These predictions are in good agreement with the lifetimes estimated by Meidt et al. (2015). Again, the dominant mechanisms of evolution are galactic shear and gravitational collapse.

(iv) M83 ($R = 0.5$–5 kpc): M83 hosts a transition between short and long cloud lifetimes. Cloud lifetimes are short (10–30 Myr) for $R < 3$ kpc and long ($\sim$100 Myr) for $R > 3$ kpc, with a median of $\sim$25 Myr.

7.4 Future work

Our theory for molecular cloud lifetimes represents a first step towards a more detailed understanding of cloud evolution. While this theory provides a reasonably accurate description of the highly limited number of observed cloud lifetimes presently available and is straightforward to interpret by virtue of its analytic approach, we have also identified areas where its idealized nature may obstruct further insights. Our predicted cloud lifetimes do not consider the constraints on observable molecular gas densities imposed by the use of tracers such as CO, and will therefore overestimate the cloud lifetime in regions of galaxies with low average H_2 densities. Additionally, in galactic environments where the time-scales of different mechanisms are expected to be very similar, our predicted cloud lifetimes are highly sensitive to the assumption that individual evolutionary mechanisms are not correlated and occur ergodically in time, in the sense that the behaviour of a typical cloud corresponds approximately to the average behaviour of an infinite succession of clouds observed over an infinitely long time period. We are currently extending this work by exploring the presented parameter space with hydrodynamical simulations of disc galaxies, allowing us to consider the (plausibly non-linear) interaction between the mechanisms introduced here. Such numerical simulations enable a closer study of the detailed physics that have been absorbed into the dynamical time-scales in the present work, such as stellar feedback. They will allow us to examine the relationship between cloud lifetimes observable via CO emission, as well as the cloud lifetimes

predicted by our analytic theory. Finally, they will provide insight into how galaxy evolution drives changes of the cloud lifetime, and possibly the SFE, as the host galaxy evolves through the parameter space identified here.

In addition to these theoretical and numerical efforts, systematic observational measurements of the cloud life cycle have now become accessible with the ALMA. By applying the statistical method of Kruijssen & Longmore (2014) and Kruijssen et al. (2018) to high-resolution ALMA maps of galaxies in the local Universe and potentially out to high redshift (e.g. Kruijssen et al., submitted; Hygate et al., in preparation; Schruba et al., in preparation; Chevance et al., in preparation; Ward et al., in preparation), it will be possible to systematically test our theory and (inevitably) revise, extend, or rule out its key physical ingredients. This will provide important insight into the cloud life cycle and will contribute to the ongoing progress towards a bottom-up, cloud-scale synthesis of galactic star formation."

ACKNOWLEDGEMENTS

SMRJ and JMDK gratefully acknowledge funding from the German Research Foundation (DFG) in the form of an Emmy Noether Research Group (grant number KR4801/1-1, PI: Kruijssen). JMDK acknowledges support from the European Research Council (ERC) under the European Union's Horizon 2020 research and innovation programme via the ERC Starting Grant MUSTANG (grant agreement number 714907, PI: Kruijssen) and from Sonderforschungsbereich SFB 881 'The Milky Way System' (subproject P1) of the DFG. We are grateful to Mélanie Chevance, Bruce Elmegreen, Eve Ostriker, Marta Reina-Campos, and Andreas Schruba for helpful discussions. We thank an anonymous referee for their careful reading of the manuscript.

REFERENCES

Adamo A., Kruijssen J. M. D., Bastian N., Silva-Villa E., Ryon J., 2015, MNRAS, 452, 246
Antoja T., Roca-Fàbrega S., de Bruijne J., Prusti T., 2016, A&A, 589, A13
Ballesteros-Paredes J., Vázquez-Semadeni E., Scalo J., 1999a, ApJ, 515, 286
Ballesteros-Paredes J., Hartmann L., Vázquez-Semadeni E., 1999b, ApJ, 527, 285
Ballesteros-Paredes J., Hartmann L., Vázquez-Semadeni E., 1999c, ApJ, 527, 285
Bertoldi F., McKee C. F., 1992, ApJ, 395, 140
Binney J., Tremaine S., 1987, Galactic Dynamics. Princeton Univ. Press, Princeton, NJ
Bland-Hawthorn J., Gerhard O., 2016, ARA&A, 54, 529
Blitz L., Rosolowsky E., 2004, ApJ, 612, L29
Blitz L., Fukui Y., Kawamura A., Leroy A., Mizuno N., Rosolowsky E., 2007, Protostars and Planets V. Univ. Arizona Press, Tucson, AZ, p. 81
Braun R., Thilker D. A., Walterbos R. A. M., Corbelli E., 2009, ApJ, 695, 937
Casoli F., Combes F., 1982, A&A, 110, 287
Colombo D. et al., 2014, ApJ, 784, 3
Corbelli E., Lorenzoni S., Walterbos R., Braun R., Thilker D., 2010, A&A, 511, A89
Dib S., Helou G., Moore T. J. T., Urquhart J. S., Dariush A., 2012, ApJ, 758, 125
Dobbs C. L., 2008, MNRAS, 391, 844
Dobbs C., Baba J., 2014, PASA, 31, e035
Dobbs C. L., Pringle J. E., 2013, MNRAS, 432, 653
Dobbs C. L., Glover S. C. O., Clark P. C., Klessen R. S., 2008, MNRAS, 389, 1097
Dobbs C. L., Burkert A., Pringle J. E., 2011a, MNRAS, 413, 2935
Dobbs C. L., Burkert A., Pringle J. E., 2011b, MNRAS, 417, 1318
Eden D. J., Moore T. J. T., Plume R., Morgan L. K., 2012, MNRAS, 422, 3178
Eden D. J., Moore T. J. T., Urquhart J. S., Elia D., Plume R., Rigby A. J., Thompson M. A., 2015, MNRAS, 452, 289
Elmegreen B. G., 1979, ApJ, 231, 372
Elmegreen B. G., 1987, ApJ, 312, 626
Elmegreen B. G., 1989, ApJ, 338, 178
Elmegreen B. G., 1993, ApJ, 419, L29
Elmegreen B. G., 1994, ApJ, 433, 39
Elmegreen B. G., 2000, ApJ, 530, 277
Elmegreen B. G., 2007, ApJ, 668, 1064
Elmegreen B. G., Elmegreen D. M., 1983, MNRAS, 203, 31
Elmegreen B. G., Elmegreen D. M., 1986, ApJ, 311, 554
Engargiola G., Plambeck R. L., Rosolowsky E., Blitz L., 2003, ApJS, 149, 343
Fisher D. B. et al., 2017, MNRAS, 464, 491
Freeman P., Rosolowsky E., Kruijssen J. M. D., Bastian N., Adamo A., 2017, MNRAS, 468, 1769
Fukui Y., Mizuno N., Yamaguchi R., Mizuno A., Onishi T., 2001, PASJ, 53, L41
Gammie C. F., Ostriker J. P., Jog C. J., 1991, ApJ, 378, 565
Genzel R. et al., 2014, ApJ, 785, 75
Gerhard O., 2011, Mem. Soc. Astron. Ital. Suppl., 18, 185
Goldreich P., Kwan J., 1974, ApJ, 189, 441
Goldreich P., Lynden-Bell D., 1965, MNRAS, 130, 97
Hart R. E., Bamford S. P., Casteels K. R. V., Kruk S. J., Lintott C. J., Masters K. L., 2017, MNRAS, 468, 1850
Hartmann L., Ballesteros-Paredes J., Bergin E. A., 2001, ApJ, 562, 852
Heiles C., Troland T. H., 2003, ApJ, 586, 1067
Heitsch F., Hartmann L., 2008, ApJ, 689, 290
Heitsch F., Burkert A., Hartmann L. W., Slyz A. D., Devriendt J. E. G., 2005, ApJ, 633, L113
Heitsch F., Slyz A. D., Devriendt J. E. G., Hartmann L. W., Burkert A., 2006, ApJ, 648, 1052
Henry A. L., Quillen A. C., Gutermuth R., 2003, AJ, 126, 2831
Henshaw J. D., Longmore S. N., Kruijssen J. M. D., 2016, MNRAS, 463, L122
Heyer M., Krawczyk C., Duval J., Jackson J. M., 2009, ApJ, 699, 1092
Hodge J. A., Carilli C. L., Walter F., de Blok W. J. G., Riechers D., Daddi E., Lentati L., 2012, ApJ, 760, 11
Ibáñez-Mejía J. C., Mac Low M.-M., Klessen R. S., Baczynski C., 2016, ApJ, 824, 41
Jeffreson S. M. R., Kruijssen J. M. D., Krumholz M. R., Longmore S. N., 2018, MNRAS, submitted
Kawamura A. et al., 2009, ApJS, 184, 1
Kennicutt R. C., Jr, 1998, ARA&A, 36, 189
Kennicutt R. C., Evans N. J., 2012, ARA&A, 50, 531
Kim W.-T., Ostriker E. C., 2002, ApJ, 570, 132
Kim W.-T., Ostriker E. C., 2006, ApJ, 646, 213
Kim C.-G., Ostriker E. C., 2015a, ApJ, 802, 99
Kim C.-G., Ostriker E. C., 2015b, ApJ, 815, 67
Klessen R. S., Hennebelle P., 2010, A&A, 520, A17
Koda J. et al., 2009, ApJ, 700, L132
Kruijssen J. M. D., Longmore S. N., 2014, MNRAS, 439, 3239
Kruijssen J. M. D., Longmore S. N., Elmegreen B. G., Murray N., Bally J., Testi L., Kennicutt R. C., 2014, MNRAS, 440, 3370
Kruijssen J. M. D., Dale J. E., Longmore S. N., 2015, MNRAS, 447, 1059
Kruijssen J. M. D., Schruba A., Hygate A. P. S., Hu C.-Y., Haydon D. T., Longmore S. N., 2018, MNRAS, submitted
Krumholz M. R., Kruijssen J. M. D., 2015, MNRAS, 453, 739
Krumholz M. R., McKee C. F., 2005, ApJ, 630, 250

Leroy A. K., Walter F., Brinks E., Bigiel F., de Blok W. J. G., Madore B., Thornley M. D., 2008, AJ, 136, 2782
Leroy A. K. et al., 2016, ApJ, 831, 16
Leroy A. K. et al., 2017a, ApJ, 835, 217
Leroy A. K. et al., 2017b, ApJ, 846, 71
Liszt H. S., Wilson R. W., Penzias A. A., Jefferts K. B., Wannier P. G., Solomon P. M., 1974, ApJ, 190, 557
Longmore S. N. et al., 2013a, MNRAS, 429, 987
Longmore S. N. et al., 2013b, MNRAS, 433, L15
MacLaren I., Richardson K. M., Wolfendale A. W., 1988, ApJ, 333, 821
Meidt S. E., Rand R. J., Merrifield M. R., Shetty R., Vogel S. N., 2008, ApJ, 688, 224
Meidt S. E. et al., 2013, ApJ, 779, 45
Meidt S. E. et al., 2015, ApJ, 806, 72
Meidt S. E. et al., 2018, ApJ, 854, 100
Miura R. E. et al., 2012, ApJ, 761, 37
Molinari S. et al., 2011, ApJ, 735, L33
Mouschovias T. C., Tassis K., Kunz M. W., 2006, ApJ, 646, 1043
Murray N., 2011, ApJ, 729, 133
Reina-Campos M., Kruijssen J. M. D., 2017, MNRAS, 469, 1282
Roberts W. W., 1969, ApJ, 158, 123
Rosolowsky E., Blitz L., 2005, ApJ, 623, 826
Savitzky A., Golay M. J. E., 1964, Anal. Chem., 36, 1627
Schinnerer E. et al., 2017, ApJ, 836, 62
Schuster K. F., Kramer C., Hitschfeld M., Garcia-Burillo S., Mookerjea B., 2007, A&A, 461, 143
Scoville N. Z., Hersh K., 1979, ApJ, 229, 578
Scoville N. Z., Wilson C. D., 2004, in Lamers H. J. G. L. M., Smith L. J., Nota A., eds, ASP Conf. Ser. Vol. 322, The Formation and Evolution of Massive Young Star Clusters. Astron. Soc. Pac., San Francisco, p. 245
Solomon P. M., Rivolo A. R., Barrett J., Yahil A., 1987, ApJ, 319, 730
Tan J. C., 2000, ApJ, 536, 173
Tassis K., Mouschovias T. C., 2004, ApJ, 616, 283
Tasker E. J., 2011, ApJ, 730, 11
Tasker E. J., Tan J. C., 2009, ApJ, 700, 358
Toomre A., 1964, ApJ, 139, 1217
Vázquez-Semadeni E., Ballesteros-Paredes J., Klessen R. S., 2003, ApJ, 585, L131
Vázquez-Semadeni E., Ryu D., Passot T., González R. F., Gazol A., 2006, ApJ, 643, 245
Walter F., Brinks E., de Blok W. J. G., Bigiel F., Kennicutt R. C., Jr, Thornley M. D., Leroy A., 2008, AJ, 136, 2563
Wegg C., Gerhard O., Portail M., 2015, MNRAS, 450, 4050
Zamora-Avilés M., Vázquez-Semadeni E., 2014, ApJ, 793, 84
Zamora-Avilés M., Vázquez-Semadeni E., Colín P., 2012, ApJ, 751, 77
Zimmer P., Rand R. J., McGraw J. T., 2004, ApJ, 607, 285

APPENDIX A: AN UPPER BOUND ON THE EPICYCLIC AMPLITUDE

We use the conservation of angular momentum to put an upper bound on the relative magnitude of epicyclic oscillations $X/R_{\rm g}$, following the derivation of Binney & Tremaine (1987). Within a locally harmonic minimum of the gravitational potential $\Phi(R)$, the radial motion of a cloud is governed by the equation of motion

$$\ddot{x} = -\kappa^2 x, \tag{A1}$$

for epicyclic frequency κ. This is solved by the sinusoidal form

$$x(t) = X\cos(\kappa t + \alpha), \tag{A2}$$

where X is the epicyclic amplitude and α is its phase, both of which are set by the initial conditions that perturb the cloud from a circular orbit. Using the conservation of angular momentum, we then obtain

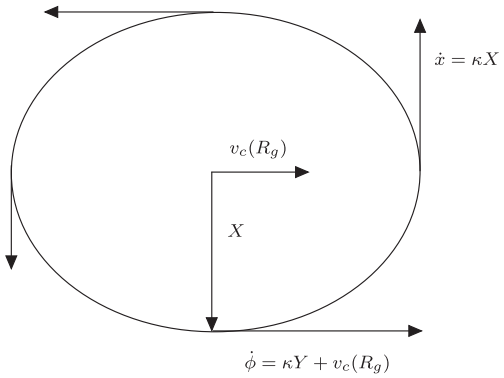

Figure A1. Schematic representation of a particle undergoing epicyclic motion, in the reference frame of the host galaxy. Equations (A2) and (A5) dictate that the maximum tangential velocity occurs at the pericentre of the orbit, where the trajectory of the particle is parallel to the velocity of the guiding centre.

the instantaneous angular velocity $\dot{\phi}$ of the cloud in the reference frame of the host galaxy, given by

$$\dot{\phi}(R) = \frac{L_z}{R^2} = \frac{L_z}{(R_{\rm g}+x)^2} = \Omega_{\rm g}\left(1 - \frac{2x}{R_{\rm g}}\right), \tag{A3}$$

where L_z is the azimuthal angular velocity, $\Omega_{\rm g}$ is the angular velocity of the guiding centre $\Omega_{\rm g} = L_z/R_{\rm g}^2$, and x is defined by equation (A2). Using the restriction $X \ll R$ within the epicyclic approximation, We have expanded to first order in $X/R_{\rm g}$. Equation (A3) can be integrated to obtain

$$\phi = \Omega_{\rm g} t + \phi_0 - \gamma\frac{X}{R_{\rm g}}\sin(\kappa t + \alpha), \tag{A4}$$

where $\gamma = 2\Omega/\kappa$. Therefore, the tangential motion in the reference frame of the guiding centre is given by

$$y(t) = -Y\sin(\kappa t + \alpha), \tag{A5}$$

with

$$\gamma = \frac{2\Omega}{\kappa} \equiv \frac{Y}{X}. \tag{A6}$$

Together, equations (A2) and (A5) define a set of axes with origin at the guiding centre, x-axis pointing in the radial direction and y-axis pointing in the direction of motion of the guiding centre. By the conservation of angular momentum in the reference frame of the host galaxy, it is obvious that the cloud's trajectory at the orbital pericentre must be parallel to the velocity of the guiding centre, as depicted in Fig. A1. At the apocentre, the cloud's trajectory is antiparallel to the guiding centre velocity, and equation (A3) gives

$$\dot{\phi} = \Omega_{\rm g}\left(1 - \frac{2X}{R_{\rm g}}\right). \tag{A7}$$

In the reference frame of the host galaxy, the cloud must be moving in the same direction as the guiding centre at its point of closest approach, thus the conservation of angular momentum requires that it always be travelling in this direction relative to the galactic centre, such that

$$\dot{\phi} > 0. \tag{A8}$$

This gives an upper bound on the amplitude of epicyclic oscillations,

$$\frac{X}{R_g} < \frac{1}{2}. \tag{A9}$$

A given perturbation from a circular orbit might therefore cause a cloud to undergo epicyclic motion with amplitude X in the range $0 < X/R_g < 1/2$, and since we make no assumption about these initial conditions in our theory, we will assume for now a uniform distribution between the two extremes, such that the typical epicyclic amplitude is given by

$$\frac{X}{R_g} \approx \frac{1}{4}. \tag{A10}$$

This paper has been typeset from a TEX/LATEX file prepared by the author.

Chapter 3

On the physical mechanisms governing the cloud lifecycle in the Central Molecular Zone of the Milky Way

Authors:
S. M. R. Jeffreson, J. M. D. Kruijssen,
M. R. Krumholz and S. N. Longmore

Published in *MNRAS 478 (2018) 3380*.

Sarah Jeffreson is the principal author of this article. The application of the theory to the Central Molecular Zone was suggested by Diederik Kruijssen. Sarah Jeffreson developed this idea, performed the calculations and produced the figures. Sarah Jeffreson wrote the manuscript, with active input from all co-authors in the form of corrections and suggestions. Sarah Jeffreson responded to and implemented the improvements and changes suggested by the reviewer.

MNRAS 000, 1–6 (2017) Preprint 9 May 2018 Compiled using MNRAS LATEX style file v3.0

On the physical mechanisms governing the cloud lifecycle in the Central Molecular Zone of the Milky Way

S. M. R. Jeffreson[1⋆], J. M. D. Kruijssen[1], M. R. Krumholz[2] and S. N. Longmore[3]
[1]*Astronomisches Rechen-Institut, Zentrum für Astronomie der Universität Heidelberg, Mönchhofstraße 12-14, 69120 Heidelberg, Germany*
[2]*Research School of Astronomy & Astrophysics, Australian National University, Canberra, ACT 2611, Australia*
[3]*Astrophysics Research Institute, Liverpool John Moores University, 146 Brownlow Hill, Liverpool L3 5RF, UK*

Accepted 2018 May 1. Received 2018 April 9; in original form 2018 January 23.

ABSTRACT

We apply an analytic theory for environmentally-dependent molecular cloud lifetimes to the Central Molecular Zone of the Milky Way. Within this theory, the cloud lifetime in the Galactic centre is obtained by combining the time-scales for gravitational instability, galactic shear, epicyclic perturbations and cloud-cloud collisions. We find that at galactocentric radii $\sim$ 45-120 pc, corresponding to the location of the '100-pc stream', cloud evolution is primarily dominated by gravitational collapse, with median cloud lifetimes between 1.4 and 3.9 Myr. At all other galactocentric radii, galactic shear dominates the cloud lifecycle, and we predict that molecular clouds are dispersed on time-scales between 3 and 9 Myr, without a significant degree of star formation. Along the outer edge of the 100-pc stream, between radii of 100 and 120 pc, the time-scales for epicyclic perturbations and gravitational free-fall are similar. This similarity of time-scales lends support to the hypothesis that, depending on the orbital geometry and timing of the orbital phase, cloud collapse and star formation in the 100-pc stream may be triggered by a tidal compression at pericentre. Based on the derived time-scales, this should happen in approximately 20 per cent of all accretion events onto the 100-pc stream.

Key words: Galaxy: centre — stars: formation — ISM: clouds — ISM: evolution — ISM: kinematics and dynamics — galaxies: ISM

1 INTRODUCTION

The Central Molecular Zone (CMZ) of the Milky Way contains the largest concentration of high-density molecular gas in the Galaxy (Ferrière et al. 2007). Despite this large gas reservoir, coupled with high gas pressures and velocity dispersions (e.g. Oka et al. 2001), the observed star formation rate (SFR) in the CMZ is 10-100 times lower than that predicted by standard star formation relations (Yusef-Zadeh et al. 2009; Immer et al. 2012; Longmore et al. 2013a; Kauffmann et al. 2013; Barnes et al. 2017). Galactic dynamical processes appear to play a dominant role in driving the evolution of the high-density clouds. This is supported by a growing body of observational evidence that star formation in the '100-pc stream' of gas at galactocentric radii of $\sim$ 100 pc may be triggered by a tidal compression event, either at the pericentre of an eccentric orbit (Longmore et al. 2013b; Rathborne et al. 2014; Kruijssen et al. 2015; Henshaw et al. 2016b) or due to the change of the gravitational potential during accretion onto the inner CMZ (Kruijssen et al. 2018). The global gas properties of the CMZ can be successfully reproduced by large-scale gas flows driven towards the central supermassive black hole (SMBH) by a combination of gravitational and acoustic instabilities, driving an episodic cycle of large-scale star formation and quiescence (Kruijssen et al. 2014; Krumholz & Kruijssen 2015; Krumholz et al. 2017). The CMZ therefore presents a nearby example of the interplay between galactic dynamics, large-scale gas flows, the feeding of a central SMBH, star formation, and feedback. Its gas reservoir has similar properties to those observed in high-redshift galaxies (Kruijssen & Longmore 2013), such that an understanding of the baryon cycle in our Galactic centre may also shed light on extragalactic star formation.

Throughout the Galaxy, giant molecular clouds (GMCs) host the majority of star formation (Kennicutt & Evans 2012). In order to understand the baryon cycle in the CMZ, it is therefore necessary to understand its cloud-scale physics. In Jeffreson & Kruijssen (2018), we developed a theory for the cloud lifetime, dependent upon the large-scale dynamics of the galactic environment. Applied to the CMZ, our theory can be used to quantitatively predict the cloud lifetime and to understand the role played by galactic dynamics in cloud evolution and subsequent star formation. In this paper, we combine the analytic theory of Jeffreson & Kruijssen (2018) with the model of Krumholz et al. (2017). We determine which large-scale dynamical processes are most important in setting the course of cloud evolution, and consequently star formation, in the gas inflow from radii of $\sim$ 500 pc down to the 100-pc stream. This not only gives a quantitative prediction for the variation in cloud lifetime with radius, but also divides the CMZ into dynamical regimes, in which cloud evolution is dominated by different dynamical processes. The dynamically-driven gas flows described in Krumholz et al. (2017) must pass through each of these dynamical regimes on their way towards the central SMBH.

⋆ s.jeffreson@uni-heidelberg.de

Table 1. The dynamical time-scales used in the cloud lifetime theory of Jeffreson & Kruijssen (2018) and their physical interpretations.

Time-scale	Symbol	Physical meaning	Analytic form	Physical variables
τ_κ	κ	Time-scale for the effect of epicyclic perturbations on GMCs.	$\frac{4\pi}{\Omega\sqrt{2(1+\beta)}}\frac{1}{\sqrt{3+\beta}}$	Ω, β
$\tau_{\rm ff,g}$	f	Time-scale for the gravitational collapse of the ISM on approximately sub-Toomre length scales, as in Krumholz et al. (2012).	$\sqrt{\frac{3\pi^2}{32\phi_P(1+\beta)}}\frac{Q}{\Omega}$	Q, Ω, β, ϕ_P
$\tau_{\rm cc}$	c	Time-scale for collisions between GMCs (Tan 2000).	$\frac{2\pi Q}{9.4 f_G \Omega(1+0.3\beta)(1-\beta)}$	Q, Ω, β
τ_β	β	Time-scale on which galactic shear pulls a cloud apart in the azimuthal direction. This is the only time-scale that has a fundamentally dispersive effect on molecular clouds. As such, the rate of galactic shear τ_β^{-1} is *subtracted* from the other rates in Equation 1.	$\frac{2}{\Omega(1-\beta)}$	Ω, β

2 THEORY

In Jeffreson & Kruijssen (2018), we introduced a theory for the molecular cloud lifetime, dependent upon the large-scale dynamics of the interstellar medium (ISM). Here we develop the salient points of this theory in relation to the central 500 pc of the Milky Way. For a more detailed overview of the theory, we refer the reader to Jeffreson & Kruijssen (2018).

Our theory of the molecular cloud lifetime is independent of the size, structure and gravitational boundedness of molecular clouds, in accordance with the diverse range of objects that can observationally be classified as GMCs. It calculates the cloud lifetime as an environmentally-dependent quantity, consistent with the observed environmental dependence of the star formation efficiency per unit time in spiral and dwarf galaxies (Leroy et al. 2008). Using only the observable properties of the ISM, the cloud lifetime τ in the CMZ can be quantified by adding the rates of the relevant large-scale dynamical processes in parallel, such that

$$\tau = |(\tau_\kappa^{-1} + \tau_{\rm ff,g}^{-1} + \tau_{\rm cc}^{-1} - \tau_\beta^{-1})|^{-1}. \quad (1)$$

The different time-scales in this equation and their physical variables are summarised in Table 1, where Ω is the angular velocity of the midplane ISM, β is the galactic shear parameter

$$\beta = \frac{{\rm d}\ln v_c}{{\rm d}\ln R}, \quad (2)$$

for circular velocity $v_c(R)$ at galactocentric radius R, and Q is the Toomre (1964) Q parameter for the ISM midplane gas

$$Q = \frac{\kappa\sigma_g}{\pi G\Sigma_g}, \quad (3)$$

for an epicyclic frequency κ, midplane gas velocity dispersion σ_g, and midplane gas surface density Σ_g. The variable ϕ_P quantifies the contribution of the stellar potential to the ISM pressure, as defined in Elmegreen (1989),

$$\phi_P = 1 + \frac{\Sigma_s}{\Sigma_g}\frac{\sigma_g}{\sigma_s}, \quad (4)$$

where σ_s and Σ_s refer to the stellar velocity dispersion and surface density, respectively. The variable $f_G = 0.5$ in $\tau_{\rm cc}$ is a 'collision probability' parameter defined and fitted to observations in Tan (2000). All time-scales depend inversely on the angular velocity Ω, such that the normalised cloud lifetime τ/Ω^{-1} is described within a parameter space spanned by the four physical variables β, Q, ϕ_P and f_G. Of these, we fix f_G to its above fiducial value, and note that only the time-scale $\tau_{\rm ff,g}$ for gravitational free-fall depends weakly on ϕ_P. The cloud lifetime therefore varies within a fundamental parameter space spanned by β, Q and Ω, with a secondary dependence on ϕ_P. Values of these variables for the CMZ are accessible through measurements of its rotation curve, velocity dispersion profile, and surface density profile. Since neither the Galactic bar nor the Galactic spiral arms extend down to the maximum galactocentric radius of ~ 500 pc considered here, we have excluded the dynamical time-scale $\tau_{\Omega_{\rm P}}$ for spiral-arm crossings, although it is discussed in Jeffreson & Kruijssen (2018).

3 APPLICATION TO THE CMZ

In order to use Equation 1 to calculate the cloud lifetime in the CMZ, we require its rotation curve, velocity dispersion profile and surface density profile. The accurate measurement of velocity dispersions in the CMZ is currently an active topic of research (Shetty et al. 2012; Henshaw et al. 2016a,b), while the edge-on CMZ viewing angle prohibits the acquisition of an accurate face-on surface density profile. As such, we use observational data for the rotation curve of the CMZ from Launhardt et al. (2002), but use the gas velocity dispersions and gas surface densities produced by simulation run m10r050f10 from the dynamical model of Krumholz et al. (2017), which are consistent with the gas properties inferred observationally for the CMZ (see e.g. their Figures 10 and 14 and compare to Kruijssen et al. 2014; Henshaw et al. 2016a,b). This numerical simulation successfully reproduces several of the observed properties of the CMZ, in particular the large-scale gas distribution.

In Figure 1, we display the time-scales of each cloud evolutionary mechanism (top panel) and the resulting cloud lifetimes (bottom panel) as a function of galactocentric radius, at a simulation time of 485 Myr in the model m10r050f10, corresponding to the gas properties that best match those observed at the current epoch. We also display the standard deviation in each quantity at each radius over the whole range of model parameters during the most recent 100 Myr in Krumholz et al. (2017), to provide an indication of how much they vary.[1] The value of ϕ_P has been calculated at each galactocentric radius using the stellar velocity dispersion of $\sigma_{\rm s} \approx 100$ kms^{-1} from de Zeeuw (1993), the rotation curve from Launhardt et al. (2002), and the gas surface density and velocity dispersion profiles from Krumholz et al. (2017). As in Jeffreson & Kruijssen (2018), we indicate *regions of relevance*, enclosed by black dashed lines. The *relevance* of a single cloud evolutionary mechanism depends on the ratio of its time-scale to the minimum evolutionary time-scale $\tau_{\rm min}$ (where $\tau < \tau_{\rm min}$), or to the cloud lifetime τ (where $\tau > \tau_{\rm min}$ due to shear support). If this ratio exceeds a value of 2, i.e. the mechanism occurs at under half the rate of the dominant evolutionary mechanism for $\tau < \tau_{\rm min}$, or at under half the rate of cloud destruction for $\tau > \tau_{\rm min}$, then its effect on cloud evolution is deemed *irrelevant*.

We find that the CMZ can be divided into two distinct regimes,

[1] The standard deviation is computed by sampling the last 100 Myr of evolution at 5 Myr intervals for the models m01r050f10, m03r025f10, m03r050f05, m03r050f10, m03r050f20 and m10r050f10.

corresponding to the grey- and white-shaded areas in the bottom panel of Figure 1. The grey-shaded areas ($R \gtrsim 120$ pc and $R \lesssim 45$ pc) indicate the galactocentric radii that are dominated by galactic shear, to the extent that the rate of shearing outpaces the combined rates of all dynamically-compressive cloud evolutionary mechanisms ($\tau_\beta^{-1} > \tau_\kappa^{-1} + \tau_{\rm ff,g}^{-1} + \tau_{\rm cc}^{-1}$). The white-shaded area ($45 \lesssim R/{\rm pc} \lesssim 120$) indicates the radii that are dominated by dynamically-compressive mechanisms of cloud evolution. Due to the extremely low gas column density at galactocentric radii $R \lesssim 45$ pc, we will ignore the innermost grey-shaded area from hereon. We will identify the shear-dominated regime with the outer CMZ (labelled 'A') and will identify the dynamically-compressive regime with the radii close to the 100-pc stream (labelled 'B').

In the vicinity of the 100-pc stream ('B', $45 \lesssim R \lesssim 120$ pc in Figure 1), the majority of GMCs are expected to collapse and form stars, due to the dominance of dynamically-compressive cloud evolutionary mechanisms. At radii from 50 to 110 pc, gravitational free-fall 'f' is the only relevant mechanism of cloud evolution, leading to short cloud lifetimes between 0.3 and 5 Myr at the current epoch. The only exception to the dominance of gravity arises at the entrance to the 100-pc stream at ~ 120 pc, where the volume density of gas entering the star-forming ring is still low enough that epicyclic perturbations and galactic shear compete with gravitational free-fall (note the equality of all time-scales at ~ 120 pc in the top panel of Figure 1). The importance of epicyclic perturbations at ~ 120 pc is consistent with the hypothesis that star formation in the ~ 100 pc stream may be triggered by tidal compressions due to pericentre passages of molecular clouds on epicyclic orbits (Longmore et al. 2013b; Kruijssen et al. 2015; Henshaw et al. 2016b). In the outer CMZ 'A', cloud lifetimes are consistently longer, around 10 Myr, due to the increased degree of shear support, which balances closely with the dynamically-compressive mechanisms of cloud evolution. At these radii, self-gravity is irrelevant and thus cloud evolution is controlled by shear and epicyclic perturbations, '$\beta\kappa$'. We expect the majority of GMCs in the outer CMZ to have low star formation efficiencies per unit mass, and eventually to be dispersed by galactic shear.

As indicated by the standard deviations in $\tau_{\rm ff,g}$, $\tau_{\rm cc}$ and the cloud lifetime τ, the results do not vary much over the past 100 Myr (despite considerable variations in the SFR), nor do they depend strongly on the parameter choices of the Krumholz et al. (2017) model. That is, gravitational free-fall always dominates in the vicinity of the 100-pc stream, and a combination of galactic shear and epicyclic perturbations dominate elsewhere. The cloud lifetimes themselves vary by 3 per cent at ~ 200 pc (region A) and by up to 30 per cent at ~ 100 pc (region B), which corresponds to a shift from 0.3 to 0.2 Myr in the minimum cloud lifetime for region B. The major downward uncertainty between 120–150 pc arises because region B extends to ~ 150 pc in a small subset of the complete range of models considered.

In the bottom panel of Figure 1, we also include the feedback-adjusted cloud lifetime. In the model of Jeffreson & Kruijssen (2018), we assume that the lifetime of a cloud is determined by its evolution towards star formation, and that destruction by feedback occurs on a much shorter time-scale. This assumption is appropriate for galactic discs, where the dynamical time-scales generally greatly exceed the time-scale for gas removal by feedback, but breaks down in the 100-pc stream, where the dynamical time-scales are short. We thus add a feedback time-scale of $\tau_{\rm fb} = 1.1$ Myr to the calculated cloud lifetime, which corresponds to the time taken to traverse the section of the 100-pc stream between Sgr B2, where stellar feedback first sets in, and Sgr B1, where the most of the

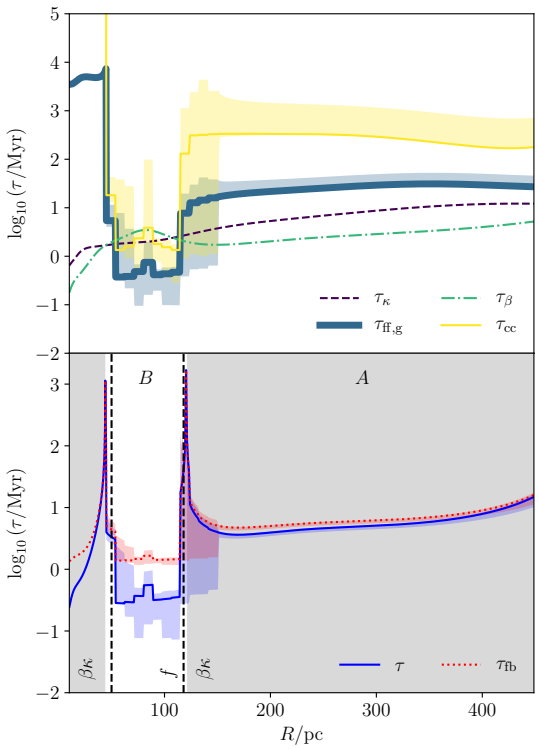

Figure 1. Values of the cloud lifetime predicted by our model for the current gas distribution in the best-matching simulation of Krumholz et al. (2017), including the standard deviation in the model-dependent time-scales across the last 100 Myr of all models (see the text). The upper panel gives each of the time-scales of dynamical evolution. The blue solid line in the lower panel gives the lifetime calculated using Equation 1, and the red dotted line adds a feedback time-scale $\tau_{\rm fb} \sim 1.1$ Myr to this lifetime (see the text). The grey shaded areas indicate the galactocentric radii at which the rate of galactic shear τ_β^{-1} is higher than the combined rates of all other mechanisms, while the black dashed vertical lines delineate the *regions of relevance*, discussed in Section 3 and labelled according to Table 1. The labels 'A' and 'B' refer to the outer CMZ and the vicinity of the 100-pc stream, respectively.

molecular gas has been blown out (Kruijssen et al. 2015; Barnes et al. 2017). With the addition of this feedback time-scale, the range of cloud lifetimes predicted for the 100-pc stream is raised to 1.4–3.9 Myr. We emphasise that the feedback time-scale is the only result in this paper that depends on an evolutionary progression of cloud evolution along the 100-pc stream, from Sgr B2 to Sgr B1.

In Figure 2, we show the CMZ model by Krumholz et al. (2017) in the fundamental parameter space (β, Q), over which the normalised cloud lifetime, τ/Ω^{-1}, varies. Triangular points denote the data at the current epoch, corresponding to the cloud lifetimes in Figure 1. Circular points denote the data at all other epochs. The values of β are taken from the observed rotation curve, which is assumed to be constant in time, and the *regions of relevance* are delineated by black dashed lines. The shear-dominated regime 's', corresponding to the grey-shaded regions in Figure 1, is separated by a white solid line from the dynamically-compressive regime 'c'. We set $\phi_P \sim 1$, the value appropriate to the 100-pc stream (c.f. de Zeeuw 1993; Launhardt et al. 2002; Krumholz et al. 2017), be-

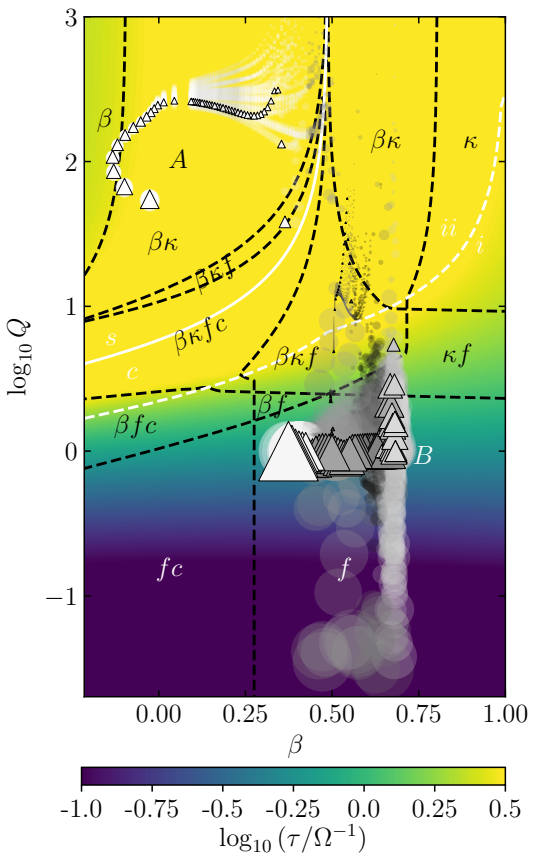

Figure 2. Values of the predicted cloud lifetime in units of angular velocity Ω (coloured contours) for a cross-section of $(\beta, \log Q)$ parameter space with $\phi_P \sim 1$, overlaid with values of β and $\log Q$ (translucent circles) for the CMZ, at 10 Myr intervals from 100 to 500 Myr in the best-matching simulation of Krumholz et al. (2017). The data at 485 Myr (the current epoch) are given by triangles. The data points are colour-coded on a grey scale between black and white by galactocentric radius, where a lighter colour corresponds to a larger radius. Their area is weighted on a linear scale by the total gas mass in each radial interval, where the largest data points represent the largest quantities of molecular gas. The dashed black lines enclose the *regions of relevance* for each time-scale, labelled as in Figure 1. The dashed white lines divide the regimes 'ii' in which the cloud lifetime is longer than the minimum evolutionary time-scale from the regimes 'i' in which it is shorter. The solid white lines divide the shear-dominated regime 's' from the dynamically-compressive regime 'c' (grey- and white-shaded regions, respectively, in Figure 1). The labels 'A' and 'B' denote the regions of the CMZ shown in Figure 1 and discussed in Section 3.

cause it only affects $\tau_{\rm ff,g}$ and the effect of gravitational free-fall is strongest in the 100-pc stream. We note that higher values of $12 \lesssim \phi_P \lesssim 100$, appropriate to radii of 120–500 pc, do not significantly alter the predicted cloud lifetime outside the 100-pc stream.

We find that the two distinct regimes 'A' and 'B', corresponding to different galactocentric radii in Figure 1, are also distinct in (β, Q, Ω) parameter space. The outer ('A', $\gtrsim$ 120 pc) region of the CMZ, through which gas flows inwards with large scale heights and low volume densities, is characterised by an approximately-flat rotation curve and very high levels of gravitational stability ($\beta < 0.5$ and $Q \gtrsim 60$). According to the model of Krumholz et al. (2017), 'A' can be interpreted as a body of gas spiralling in towards the star-forming, ring-shaped stream 'B' at $\sim$ 100 pc, propelled by shear-driven acoustic instabilities. Due to high levels of shearing and gravitational stability, GMCs in the outer CMZ fall exclusively in the dynamically-dispersive regime 's' of parameter space, and are governed by a combination of galactic shear and epicyclic perturbations '$\beta\kappa$'. The competition between dynamically-compressive and dynamically-dispersive mechanisms of cloud evolution in this regime elongates the cloud lifetime to between 2.3 and 3.3 orbital times $1/\Omega$. Note that we have excluded $> 3\sigma$ outliers for this and all subsequent ranges, in order to reflect the typical cloud lifetime at each interval of galactocentric radii.

In the vicinity of the 100-pc stream 'B', between galactocentric radii of 45 and 120 pc, the gas inflow stalls due to a local shear minimum in the rotation curve (Krumholz & Kruijssen 2015), where $0.5 \lesssim \beta \lesssim 0.75$. It condenses to small scale heights ($\sim$ 3 pc) and high volume densities ($\sim$ 500 $M_\odot {\rm pc}^{-3}$), such that the level of gravitational stability falls as low as $Q \sim 0.1$. At these radii, we expect that the majority of GMCs are governed by gravity alone (in regime 'f' of parameter space), and are therefore destroyed by gravitational collapse and the subsequent stellar feedback. In particular, we expect cloud lifetimes on the outside of the 100-pc stream (between 100 and 120 pc, corresponding to the lighter-coloured data points in region 'B') to be very short ($\sim$ 1 orbital time $1/\Omega$). On the inside of the stream (between 45 and 100 pc, corresponding to the darker-coloured points in region 'B'), the molecular gas surface density is depleted by star formation (Krumholz et al. 2017), leading to gas masses as low as one 1000th of the mass on the outside of the stream (compare the areas of the dark- and light-coloured data points in region 'B' of Figure 2). Due to its low gas fraction, this remaining material has a high degree of gravitational stability, leading to longer cloud lifetimes (between 1 and 3 orbital times).

The molecular gas that survives the star-forming ring exits the local shear minimum and makes its way towards the nuclear cluster and eventually the central SMBH (Krumholz et al. 2017). This inner region of the CMZ is not shown in Figure 2, because the vast majority of molecular gas in the Krumholz et al. (2017) model is either consumed by star formation or blown out by feedback at earlier times in the star-forming ring, producing unreliable values of Q at $\lesssim$ 45 pc. However, we do expect that the cloud lifecycle in the inner CMZ ($R \lesssim 45$ pc) is controlled by similar mechanisms as in the outer CMZ 'A' due to its flat ($\beta < 0.5$) rotation curve, but with higher levels of gravitational stability due to its even lower gas density.

Comparing the triangular (current, quiescent phase) and circular (all snapshots) data points in Figure 2, it is clear that there is little time-variation of the parameters β and Q between the starburst and quiescent phases of the Krumholz et al. (2017) model, resulting in CMZ cloud lifetimes that are also relatively time-invariant. Over a period of $\sim$ 500 Myr in simulation time, the radial extent of the gravity-dominated regime 'c' and the radial extents of each region of relevance are constant to within 10 per cent. This is a direct result of the shape of the gravitational potential and, hence, the rotation curve. As the CMZ evolves, the time-scales on which gravity-dominated clouds are destroyed by collapse and feedback in the 100-pc stream 'B', and on which shear-dominated clouds are dispersed by galactic shear outside the 100-pc stream 'A', is relatively constant. The most notable exception to time-invariance occurs in the vicinity of the 100-pc stream 'B', where a sharp drop in the cloud lifetime occurs during each starburst phase, corresponding to the scatter of points down to $Q \sim 0.1$ in regime 'f' of Fig-

ure 2. This is due to the simultaneous drop in the turbulent velocity dispersion and the rise in the molecular gas surface density that accompanies a starburst, producing a sudden drop in Toomre Q.

Although gravitational free-fall is the only relevant cloud evolutionary mechanism throughout the majority of the 100-pc stream (see regime 'f' of Figure 2) a number of data points are also located in regimes 'κf' and '$\beta\kappa f$', where we expect epicyclic perturbations to have a significant influence on cloud evolution. This is consistent with the hypothesis that tidal compressions may trigger cloud collapse and star formation in the 100-pc stream, due to pericentre passages of molecular clouds on eccentric orbits, or by accretion onto the stream (Longmore et al. 2013b; Kruijssen et al. 2018).

We may estimate the fraction of clouds whose collapse is triggered by epicycles, by first calculating the fraction of clouds $N(R)$ that survive until they reach galactocentric radius R in the gravity-dominated regime 'c' (i.e. in the vicinity of the 100-pc stream). This is given by the differential equation

$$v_R \frac{\mathrm{d}N(R)}{\mathrm{d}R} = -\tau^{-1}(R)N(R), \tag{5}$$

where v_R is the radial inflow velocity, calculated self-consistently at each radius in the model of Krumholz et al. (2017), and $\tau^{-1}(R)$ is the rate of cloud destruction, as calculated in Equation (1). Solving this equation numerically for $N(R)$, we find that at the current epoch, 100 per cent of clouds are destroyed between $R = 120$ pc and $R = 115$ pc, at the very outer edge of the gravity-dominated regime. That is, the inflow velocity of the clouds drops significantly as they spiral inwards towards the local shear minimum, so that all are destroyed before their apocentric radii shrink from 120 to 115 pc. This demonstrates that the groups of darker-coloured points (indicating smaller radii) in regimes 'κf' and '$\beta\kappa f$' of Figure 2 do not give meaningful information about the course of cloud evolution: for radii close to 45 pc, very few molecular clouds remain.

Of the clouds that are destroyed in each interval of galactocentric radius, we may estimate the statistical fraction $F(R)$ of cloud destruction through star formation and feedback that is driven by epicycles, i.e. the fraction of star formation events that is driven by pericentre passages. This is defined to exclude cloud dispersal by shear and (in regime 'c' of parameter space) is given by

$$F(R) = \frac{\tau_\kappa^{-1}}{\tau_\kappa^{-1} + \tau_{\mathrm{ff,g}}^{-1} + \tau_{\mathrm{cc}}^{-1}}, \tag{6}$$

The overall fraction of clouds F that are destroyed by epicycles is then given by the product of $F(R)$ and the fraction of clouds destroyed between R and $R + \Delta R$, summed over all radii, so that

$$F = \sum_R [N(R + \Delta R) - N(R)]F(R) \approx 0.2, \tag{7}$$

at the current epoch. That is, 20 per cent of cloud destruction, upon accretion onto the 100-pc stream, is caused by epicyclic perturbations (i.e. pericentre passages). Across the full duty cycle at times close to the current epoch, the fraction of cloud destruction caused by epicyclic perturbations does not vary significantly and remains (with mostly downward variations) in the range 10–30 per cent.

4 CONCLUSIONS

Using the theoretical output of Krumholz et al. (2017), along with the observed rotation curve in the CMZ of the Milky Way, we have applied the theory of cloud lifetimes presented in Jeffreson & Kruijssen (2018) to the Galactic centre.

From a cloud evolutionary perspective, we find that the CMZ is divisible into two dynamical regimes. At galactocentric radii from $\sim$ 120-500 pc, the cloud lifecycle is primarily dominated by galactic shear, to the extent that the rate of shearing is faster than the combined rates of all other cloud evolutionary mechanisms. At these galactocentric radii we expect clouds to be sheared apart on time-scales between 3 and 9 Myr, before collapse and star formation can occur, leading to low star formation efficiencies. Conversely, at galactocentric radii from $\sim$ 45-120 pc, we expect to find clouds that collapse and form stars on much shorter time-scales, with median lifetimes between $\sim$ 0.3 and 2.8 Myr. If we lift the assumption of instantaneous stellar feedback and include a gas removal time-scale of $\tau_{\mathrm{fb}} = 1.1$ Myr, motivated by observations, this range of cloud lifetimes becomes 1.4–3.9 Myr.

At the outer edge of the 100-pc stream, the time-scale for epicyclic perturbations, which quantifies the influence of orbital eccentricity on the cloud lifecycle, obtains equality with the free-fall time-scale. This result is consistent with the hypothesis of tidally-triggered collapse in the 100-pc stream, as initially proposed by Longmore et al. (2013b) and later expanded by Kruijssen et al. (2015) and Henshaw et al. (2016b). While the similarity of the free-fall and epicyclic time-scales implies that some accreting gas streams may collapse due to a tidal compression at pericentre (in approximately 20 per cent of cases), it also means that some gas streams may undergo free-fall collapse due to their arrival on the 100-pc stream, before pericentre is reached (in around 80 per cent of cases). This simple time-scale argument corroborates the numerical simulations presented by Kruijssen et al. (2018), who show that the compressive tidal field at the radii of the 100-pc stream may have an equal, if not stronger effect on cloud evolution than the pericentre passage. Since the gas is flowing in from larger radii, both collapse mechanisms lead to an evolutionary progression of star formation, either post-pericentre, or after their moment of accretion onto the 100-pc stream. In combination with the known orbits of the CMZ gas streams, this provides an absolute evolutionary timeline that allows the cloud lifetimes predicted here to be directly tested with currently available observations.

ACKNOWLEDGEMENTS

SMRJ and JMDK acknowledge funding from the German Research Foundation (DFG) in the form of an Emmy Noether Research Group (grant number KR4801/1-1). JMDK acknowledges support from the European Research Council (ERC) under the European Union's Horizon 2020 research and innovation programme via the ERC Starting Grant MUSTANG (grant number 714907). MRK acknowledges support from the Australian Research Councils Discovery Projects funding scheme (project DP160100695). We thank an anonymous referee for a constructive report, which improved the paper.

REFERENCES

Barnes A. T., Longmore S. N., Battersby C., Bally J., Kruijssen J. M. D., Henshaw J. D., Walker D. L., 2017, MNRAS, 469, 2263
Elmegreen B. G., 1989, ApJ, 338, 178
Ferrière K., Gillard W., Jean P., 2007, A&A, 467, 611
Henshaw J. D., et al., 2016a, MNRAS, 457, 2675
Henshaw J. D., Longmore S. N., Kruijssen J. M. D., 2016b, MNRAS, 463, L122
Immer K., Schuller F., Omont A., Menten K. M., 2012, A&A, 537, A121
Jeffreson S. M. R., Kruijssen J. M. D., 2018, MNRAS submitted

Kauffmann J., Pillai T., Zhang Q., 2013, ApJ, 765, L35
Kennicutt R. C., Evans N. J., 2012, ARA&A, 50, 531
Kruijssen J. M. D., Longmore S. N., 2013, MNRAS, 435, 2598
Kruijssen J. M. D., Longmore S. N., Elmegreen B. G., Murray N., Bally J., Testi L., Kennicutt R. C., 2014, MNRAS, 440, 3370
Kruijssen J. M. D., Dale J. E., Longmore S. N., 2015, MNRAS, 447, 1059
Kruijssen J. M. D., et al., 2018, MNRAS to be submitted
Krumholz M. R., Kruijssen J. M. D., 2015, MNRAS, 453, 739
Krumholz M. R., Dekel A., McKee C. F., 2012, ApJ, 745, 69
Krumholz M. R., Kruijssen J. M. D., Crocker R. M., 2017, MNRAS, 466, 1213
Launhardt R., Zylka R., Mezger P. G., 2002, A&A, 384, 112
Leroy A. K., Walter F., Brinks E., Bigiel F., de Blok W. J. G., Madore B., Thornley M. D., 2008, AJ, 136, 2782
Longmore S. N., et al., 2013a, MNRAS, 429, 987
Longmore S. N., et al., 2013b, MNRAS, 433, L15
Oka T., Hasegawa T., Sato F., Tsuboi M., Miyazaki A., Sugimoto M., 2001, ApJ, 562, 348
Rathborne J. M., et al., 2014, ApJ, 786, 140
Shetty R., Beaumont C. N., Burton M. G., Kelly B. C., Klessen R. S., 2012, MNRAS, 425, 720
Tan J. C., 2000, ApJ, 536, 173
Toomre A., 1964, ApJ, 139, 1217
Yusef-Zadeh F., et al., 2009, ApJ, 702, 178
de Zeeuw T., 1993, in Dejonghe H., Habing H. J., eds, IAU Symposium Vol. 153, Galactic Bulges. p. 191

This paper has been typeset from a TEX/LATEX file prepared by the author.

Part II

Numerical simulations

Chapter 4

The role of galactic dynamics in shaping the physical properties of giant molecular clouds in Milky Way-like galaxies

Authors:
S. M. R. Jeffreson, J. M. D. Kruijssen, B. W. Keller,
M. Chevance and S. C. O. Glover

In press at *MNRAS tmp. 5875922.*

Sarah Jeffreson is the principal author of this paper. The combination of analytic theory and numerical simulations was suggested by Diederik Kruijssen, and Sarah Jeffreson produced the framework for making this connection. Sarah Jeffreson implemented the numerical prescription within the moving mesh code Arepo and performed the simulations, with active input from Benjamin Keller and Simon Glover. Sarah Jeffreson post-processed the output of the simulations, performed all the calculations, produced all the figures and wrote the manuscript, with active input from all co-authors of the article, in the form of corrections and suggestions. Mélanie Chevance ran the synthetic observations using simulation maps produced by Sarah Jeffreson. Sarah Jeffreson responded to and implemented the improvements and changes suggested by the reviewer.

MNRAS **000**, 1–36 (2020) Preprint 2 July 2020 Compiled using MNRAS LATEX style file v3.0

The role of galactic dynamics in shaping the physical properties of giant molecular clouds in Milky Way-like galaxies

Sarah M. R. Jeffreson*[1], J. M. Diederik Kruijssen[1], Benjamin W. Keller[1], Mélanie Chevance[1] and Simon C. O. Glover[2]

[1] *Astronomisches Rechen-Institut, Zentrum für Astronomie der Universität Heidelberg, Mönchhofstraße 12-14, 69120 Heidelberg, Germany*
[2] *Institut für Theoretische Astrophysik, Zentrum für Astronomie der Universität Heidelberg, Albert-Ueberle-Str. 2, 69120 Heidelberg, Germany*

Accepted Xxxxx XX. Received 2020 July 1; in original form 2020 May 8.

ABSTRACT

We examine the role of the large-scale galactic-dynamical environment in setting the properties of giant molecular clouds in Milky Way-like galaxies. We perform three high-resolution simulations of Milky Way-like discs with the moving-mesh hydrodynamics code AREPO, yielding a statistical sample of $\sim 80,000$ giant molecular clouds and $\sim 55,000$ HI clouds. We account for the self-gravity of the gas, momentum and thermal energy injection from supernovae and HII regions, mass injection from stellar winds, and the non-equilibrium chemistry of hydrogen, carbon and oxygen. By varying the external gravitational potential, we probe galactic-dynamical environments spanning an order of magnitude in the orbital angular velocity, gravitational stability, mid-plane pressure and the gradient of the galactic rotation curve. The simulated molecular clouds are highly overdense ($\sim 100\times$) and over-pressured ($\sim 25\times$) relative to the ambient interstellar medium. Their gravo-turbulent and star-forming properties are decoupled from the dynamics of the galactic mid-plane, so that the kpc-scale star formation rate surface density is related only to the number of molecular clouds per unit area of the galactic mid-plane. Despite this, the clouds display clear, statistically-significant correlations of their rotational properties with the rates of galactic shearing and gravitational free-fall. We find that galactic rotation and gravitational instability can influence their elongation, angular momenta, and tangential velocity dispersions. The lower pressures and densities of the HI clouds allow for a greater range of significant dynamical correlations, mirroring the rotational properties of the molecular clouds, while also displaying a coupling of their gravitational and turbulent properties to the galactic-dynamical environment.

Key words: stars: formation — ISM: clouds — ISM: evolution — ISM: kinematics and dynamics — galaxies: evolution — galaxies: ISM

1 INTRODUCTION

Within the hierarchical structure of the interstellar medium, giant molecular clouds (GMCs) correspond to the spatial scales and densities at which the vast majority of star formation occurs (e.g. Kennicutt & Evans 2012). The physics that drive the formation, evolution and destruction of molecular clouds are therefore the physics that control galaxy-scale observables such as the star formation relation of Kennicutt (1998). In particular, the large scatter in the observed gas depletion times of nearby galaxies on sub-kpc scales (Bigiel et al. 2008; Leroy et al. 2008; Blanc et al. 2009; Liu et al. 2011; Rahman et al. 2011; Schruba et al. 2010, 2011; Rahman et al. 2012; Leroy et al. 2013) indicates that star formation is not controlled exclusively by the quantity of molecular gas available on kpc-scales, but is governed to a great extent by cloud-scale ($\sim$ 5-200 pc) processes (e.g. Feldmann et al. 2011; Calzetti et al. 2012; Kruijssen & Longmore 2014; Kruijssen et al. 2018).

The set of possible physical mechanisms governing the properties of GMCs is wide and varied (e.g. Chevance et al. 2020a). Large-scale dynamical processes such as galactic shear (Luna et al. 2006; Leroy et al. 2008; Suwannajak et al. 2014; Colombo et al. 2018), interactions with spiral arms (Koda et al. 2009; Meidt et al. 2013), and gravitational instability on the Toomre scale (Freeman et al. 2017; Marchuk 2018) are observed to vary the star-forming properties of the ISM on cloud scales. Epicyclic motions driven by the galactic rotation curve (Meidt et al. 2018, 2020; Kruijssen et al. 2019b; Utreras et al. 2020), accretion flows from galactic scales down to GMC scales (Klessen & Hennebelle 2010), and collisions between clouds (Tan 2000; Tasker & Tan 2009; Tasker

* s.jeffreson@uni-heidelberg.de

2011) can drive turbulence in GMCs and so explain their large non-thermal line-widths (Fukui et al. 2001; Engargiola et al. 2003; Rosolowsky & Blitz 2005). Stellar feedback processes such as supernovae (de Avillez & Breitschwerdt 2005; Joung et al. 2009; Walch & Naab 2015; Martizzi et al. 2015; Iffrig & Hennebelle 2015; Kim & Ostriker 2015a,b; Padoan et al. 2016, 2017), photoionisation by massive stars (e.g. Matzner 2002; Krumholz & Matzner 2009; Gritschneder et al. 2009; Walch et al. 2012; Kim et al. 2018), and stellar winds (Haid et al. 2016, 2018; Rahner et al. 2017) are seen to destroy GMCs in simulations, and to inject turbulence into the wider ISM, providing support against gravitational collapse on large scales (Ostriker et al. 2010; Ostriker & Shetty 2011). These theoretical results are borne out in observations, which show a correlation between the mid-plane hydrostatic pressures of galaxies and their star formation rates (Sun et al. 2020), and which host clouds that are typically destroyed within a dynamical time, by the feedback from massive stars (Kruijssen et al. 2019b; Chevance et al. 2020b,a). Cloud collapse can also be slowed (Tassis & Mouschovias 2004; Mouschovias et al. 2006) or its onset delayed (Girichidis et al. 2018; Hennebelle & Inutsuka 2019) by the presence of magnetic fields, which are observed to penetrate into star-forming regions and can provide pressure support (see the review by Crutcher 2012). While simulations by Su et al. (2017) show that magnetic fields have a much smaller effect on the galactic-averaged SFR than does stellar feedback, Nixon & Pringle (2018) argue against the implication that magnetic fields are irrelevant in GMC evolution, instead explaining this result in terms of local magnetic dissipation in the highly star-forming regions within clouds.

With the recent advent of large interferometric instruments such as the Atacama Large Millimeter/Submillimeter Array (ALMA), it has become possible to resolve cloud-scale observables outside the Milky Way. These signatures of cloud-scale physics can now be retrieved across the local galaxy population (Schinnerer et al. 2013; Elmegreen et al. 2017; Faesi et al. 2018), permitting a statistical sample of GMC properties across a wide range of galactic environments. Measurements of the star formation efficiency per free-fall time (Utomo et al. 2018), as well as the GMC turbulent velocity dispersion, turbulent pressure, surface density and spatial extent (Leroy et al. 2017; Sun et al. 2018, 2020) have already revealed a strong correlation with the galaxy-scale properties. A systematic variation in the dense gas fraction across galaxy discs has similarly been observed by Usero et al. (2015); Bigiel et al. (2016), and is correlated with the molecular gas surface density, the stellar surface density, and the dynamical equilibrium pressure (Gallagher et al. 2018). Within the Milky Way, a large scatter in the 'size-linewidth' relation of Larson (1981) is observed between the Central Molecular Zone (Oka et al. 2001; Shetty et al. 2012; Kruijssen & Longmore 2013; Kauffmann et al. 2017), the outer disc (Heyer et al. 2001), and the collective GMC population of the entire Galaxy (Heyer et al. 2009; Roman-Duval et al. 2010; Rice et al. 2016; Miville-Deschênes et al. 2017; Colombo et al. 2019).

Combined with these observations, a systematic theoretical study of observable cloud properties across different galactic environments is necessary to discern the dominant physical mechanisms controlling the GMC lifecycle. Given that each distinct galactic environment hosts a unique set of galactic-dynamical processes (e.g. Jeffreson & Kruijssen 2018), we conduct in this work a systematic examination of the correlations between the average physical properties of GMCs and the galactic-dynamical timescales of their host galaxies. We use a spatially-resolved, statistical sample of $\sim 80,000$ GMCs, drawn from three numerical simulations of Milky Way-pressured disc galaxies that we perform using the moving-mesh hydrodynamics code AREPO (Springel 2010). In this context, 'Milky Way-pressured' refers to the fact that our simulated galaxies have a Milky Way-like division of mass between the galactic disc, bulge and halo, as well as between stars and atomic and molecular gas, leading to Milky Way-like values of the mid-plane pressure. To obtain further insight into the origin of each dynamical correlation, we also examine the sample of $\sim 55,000$ HI clouds across the three galaxies, in addition to the GMCs. The HI clouds represent a level up in the hierarchical structure of the ISM, i.e. they comprise the atomic gas out of which GMCs condense on time-scales of around 30 Myr in Milky Way-like environments (Larson 1994; Goldsmith et al. 2007; Ward et al. 2020).

The remainder of the paper is structured as follows. In Section 2, we describe the three isolated galaxy simulations used in this work to explore the properties of GMCs across different galactic-dynamical environments. We explain the set of numerical methods that we have employed and the basic analysis methods that we have used to identify GMCs and HI clouds. In Section 3 we compare our simulations to key observable properties of Milky Way-like galaxies and their GMCs from the literature, demonstrating an acceptable level of agreement. Section 4 reviews the analytic theory of Jeffreson & Kruijssen (2018) for GMC evolution under the influence of galactic dynamics, and maps the simulation data into the environmental parameter space spanned by the theory to reveal galactic-dynamical trends in the properties of our simulated GMCs. Our results and their implications are explored in Section 5. In Section 6, we discuss our results in the context of existing ISM models and simulations of GMCs, and additionally examine the caveats of our simulations. Finally, we present a summary of our conclusions in Section 7.

2 SIMULATIONS

We consider three simulated galaxy discs, spanning a range of galactic-dynamical environments at Milky Way ISM mid-plane pressures. The simulations are set up as isolated gaseous discs in an external gravitational potential that models the dark matter halo, the stellar disc, and the stellar bulge. Subsequent star formation produces live stellar particles.

2.1 Initial conditions

The initial conditions for each galaxy are generated using MAKENEWDISK (Springel et al. 2005) with 9×10^6 gas cells each. The velocity of each cell centroid is determined by its acceleration due to the external potential described in Section 2.2, with all parameters given in Table 1. The density distribution of the gas disc follows an exponential profile of the form

$$\rho_{\rm gas}(R,z) = \frac{M_{\rm gas}}{4\pi R_{\rm gas} z_{\rm gas}} \exp\left(-\frac{R}{R_{\rm gas}}\right) \exp\left(-\frac{|z|}{z_{\rm gas}}\right), \quad (1)$$

where R is the galactocentric radius, z is the height above the galactic mid-plane, and $M_{\rm gas}$ is the total gas mass of the disc. The disc scale-length $R_{\rm gas}$ is fully-determined by the external potential and the disc scale-height $z_{\rm gas}$ is set by the condition of hydrostatic equilibrium.

To each initial condition, we add a background grid of side-length 500 kpc, composed of 32 cells per side. The large size of this box ensures no interaction between the simulation boundaries and the gas cells in the isolated disc galaxy. We set an upper limit

Table 1. Physical parameters for the disc galaxies modelled in this work, including the values of the analytic constants for the background potentials in Section 2.2. Properties of the gas disc ($M_{\rm gas}$, $R_{\rm gas}$ and $z_{\rm gas}$) are quoted at the fiducial simulation time of $\sim$ 600 Myr, at which point molecular cloud properties are measured. All masses are given in units of $10^{10}{\rm M}_{\odot}$, while all length-scales are given in units of kpc. The columns report: (1) Halo mass, (2) halo scale-radius, (3) core cut-off radius, (4) bulge mass, (5) bulge turnover radius, (6) stellar disc mass, (7) stellar disc scale-radius, (8) stellar disc scale-height, (9) final gas disc mass, (10) gas disc scale-radius, (11) gas disc scale-height.

Sim.	$M_{\rm h}$ (1)	$a_{\rm h}$ (2)	$a_{\rm c}$ (3)	$M_{\rm b}$ (4)	$a_{\rm b}$ (5)	$M_{\rm d}$ (6)	$a_{\rm d}$ (7)	$b_{\rm d}$ (8)	$M_{\rm gas}$ (9)	$R_{\rm gas}$ (10)	$z_{\rm gas}$ (11)
FLAT	116	47	-	1.5	0.4	3.5	2.6	0.4	5.8	7.4	0.38
SLOPED	130	49	-	0.5	2	3.5	5.4	0.3	5.9	7.7	0.28
CORED	150	51.5	5	-	-	3.5	6	1	6	7.4	0.25

of 1.25×10^5 kpc^3 on the gas cell volume for each simulation, limiting the size of the background grid cells under the adaptive mesh refinement scheme described in Section 2.3.

Finally, we 'warm up' the initial condition for 500 Myr by injecting kinetic and thermal energy into all cells above a hydrogen number density threshold of 100 cm^{-3}. We use the supernova feedback prescription outlined in Section 2.6, but circumvent the creation of star particles to inject this feedback instantaneously into the relevant gas cells. This period of evolution allows for the dispersal of resonant rings formed within the galactic mid-plane, as the gas cells refine and re-distribute within the potential well. It produces a flocculent spiral-arm structure, and so significantly reduces the run-time required for the simulation to settle into a state of dynamical equilibrium.

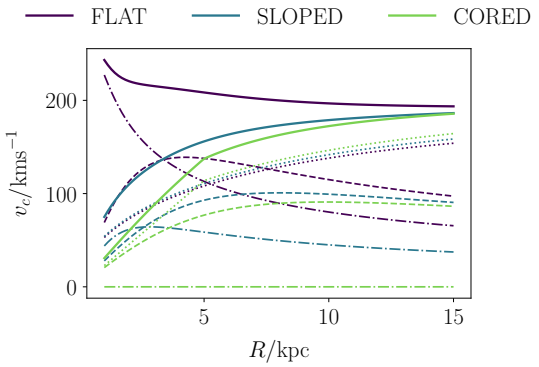

Figure 1. Contribution of the disc (dashed lines, Equation 3), the bulge (dash-dotted lines, Equation 5) and the halo (dotted lines, Equation 7) components of the analytic external gravitational potential to the galactic circular velocity (bold lines) of each simulated galaxy.

2.2 External potential

We consider two different classes of external potential, which span values of the galactic shear parameter β from the high-shear case of $\beta = 0$ for a flat rotation curve up to $\beta = 1$ for solid-body rotation. The FLAT ($\beta \sim 0$) and SLOPED ($\beta \lesssim 0.5$) initial conditions follow a Milky Way-like external potential consisting of a stellar bulge, a (thick) stellar disc and a cusped dark matter halo (e.g. Bland-Hawthorn & Gerhard 2016). In this initial study we do not consider the influence of the Galactic bar, which is likely to create a higher-pressure environment with higher levels of star formation than the Galactic disc (e.g. Sun et al. 2020). The CORED ($0 \lesssim \beta \lesssim 1$) initial condition follows an M33-like potential profile with a stellar disc, a cored dark matter halo, and no stellar bulge (e.g. Corbelli 2003). All analytic parameters are presented in Table 1, and have been chosen to achieve a maximum rotational velocity within the gas disc of $\sim$ 220 kms^{-1}. The contribution of the halo, bulge and disc components to the galactic circular velocity of each simulation is shown as a function of the galactocentric radius in Figure 1.

2.2.1 *Stellar disc*

The stellar disc component is modelled using a Miyamoto & Nagai (1975) potential of the form

$$\Phi_{\rm d} = \frac{GM_{\rm d}}{\sqrt{R^2 + [a_{\rm d} + (z^2 + b_{\rm d}^2)^{1/2}]^2}}, \tag{2}$$

where G is the gravitational constant, R is the galactocentric radius within the galactic mid-plane and z is the perpendicular distance from this plane, such that $r = \sqrt{R^2 + z^2}$ for any distance r away from the disc centre. The parameters $M_{\rm d}$, $a_{\rm d}$ and $b_{\rm d}$ are the mass, scale-length and scale-height, respectively, of the stellar disc. The corresponding rotation curve is given by

$$v_{\rm c,d}(R) = \frac{\sqrt{GM_{\rm d}}R}{([a_{\rm d} + b_{\rm d}]^2 + R^2)^{3/4}}. \tag{3}$$

Since $a_{\rm d}$ and $b_{\rm d}$ both fall within the gas disc, the stellar disc potential contributes a solid-body ($v_{\rm c} \propto R$) component to the rotation curve for very small galactocentric radii $R \ll a_{\rm d} + b_{\rm d}$, which turns over at large radii to follow the Hernquist profile ($v_{\rm c} \propto \sqrt{R}$) for $R \gg a_{\rm d} + b_{\rm d}$. For each disc, this rotation profile is given by the dashed lines in Figure 1.

2.2.2 *Stellar bulge*

We model the stellar bulge component in the FLAT and SLOPED simulations using a Plummer (1911) potential of the form

$$\Phi_{\rm b}(r) = -\frac{GM_{\rm b}}{\sqrt{r^2 + a_{\rm b}^2}}, \tag{4}$$

where $M_{\rm b}$ is the mass of the bulge and $a_{\rm b}$ is the turnover radius of the density core. This potential gives a rotation curve of

$$v_{\rm c,b} = \frac{\sqrt{GM_{\rm b}}R}{(R^2 + a_{\rm b}^2)^{3/4}} \tag{5}$$

in the galactic plane, which is identical in form to the stellar disc rotation curve, but with its peak at the bulge turnover radius $a_{\rm b}$. These profiles correspond to the dash-dotted lines in Figure 1.

2.2.3 *Spherical dark matter halo*

The cuspy dark matter halo for the FLAT and SLOPED simulations follows a Hernquist (1990) potential of the form

$$\Phi_{\rm h}(r) = -\frac{GM_{\rm h}}{r + a_{\rm h}}, \tag{6}$$

where $M_{\rm h}$ is the halo mass and $a_{\rm h}$ is the halo scale radius. The corresponding rotation profile in the galactic plane is given by

$$v_{\rm c,h}(R) = \sqrt{R\frac{{\rm d}\Phi_{\rm h}}{{\rm d}R}} = \frac{\sqrt{GM_{\rm h}R}}{R + a_{\rm h}}, \tag{7}$$

which peaks at $R \sim a_{\rm h}$, far outside the star-forming disc. The dark matter halo therefore contributes a component $v_{\rm c} \propto \sqrt{R}$ to the rotation curve within the star-forming disc, corresponding to a shear parameter of $\beta = 1/2$. These profiles are given by the purple (FLAT) and blue (SLOPED) dotted lines in Figure 1.

The dark matter potential for the CORED simulation combines the above Hernquist profile with a uniform-density core in a piece-wise fashion, such that

$$\Phi_{\rm h,core}(r) = \begin{cases} \frac{GM_{\rm h}R^2}{2a_{\rm c}(a_{\rm c}+a_{\rm h})^2} & 0 \leqslant r \leqslant a_{\rm c} \\ \Phi_{\rm h}(r) & a_{\rm c} \leqslant r \end{cases}, \tag{8}$$

where $a_{\rm c}$ is the cut-off radius of the core. The resulting rotation curve is solid-body for $R < a_{\rm c}$ and follows Equation (7) for $R \geqslant a_{\rm c}$. It is shown as the green dotted line in Figure 1.

2.3 Adaptive mesh refinement

The adaptive refinement and de-refinement of gas cells in AREPO is determined according to the mass and density aggregated at each grid point. In contrast to Eulerian codes, the mesh moves along with the gas flow, reducing the number of gas cells that must be refined and de-refined during each time-step (Springel 2010). As such, we need only to set a 'target' mass resolution for the Voronoi cells, corresponding to the mode of the distribution of cell masses. We use a value of 900 $\rm M_\odot$, so that the spatial resolution of each simulation extends down to cell diameters of $\sim$ 3 pc at our star formation threshold of $n_{\rm thresh} = 2000$ cm^{-3} (see Section 2.4). The distribution of cell masses and sizes is shown in Figure 2. We do not impose the non-thermal pressure floor that is often used to prevent gravitational fragmentation in regions for which the Jeans length $\lambda_{\rm J} = (\pi c_s^2/G\rho)^{1/2}$ is unresolved. According to the criterion of Truelove et al. (1997), such fragmentation is a numerical artefact that can be avoided if λ_J is sampled by four or more gas cells at all times. However, this would require us to inflate the Jeans length inside our simulated molecular clouds to an unphysical value of $\lambda_J \sim 10$ pc, preventing the physical (but unresolved) gravitational fragmentation required to attain densities close to our star formation threshold, as discussed by Teyssier (2015); Hopkins et al. (2018b). Instead, we fulfil the three requirements tested by Nelson (2006) for thin isolated discs using Lagrangian methods: namely that (1) the Toomre mass is resolved, (2) the scale-height of the disc is resolved, and (3) fully-adaptive gravitational softening is used up to density threshold for star formation. The first requirement can be formulated as a maximum resolvable surface density $\Sigma_{\rm max}$, given in Equation (11) of Nelson (2006) as $\Sigma_{\rm max} = (\pi/G) \cdot (c_s^4/m_{\rm H}N_{\rm reso})$, where c_s is the sound speed, $m_{\rm H}$ is the proton mass and $N_{\rm reso}$ is the SPH neighbour number. For use with AREPO, we set $N_{\rm reso} = 9$ for the linear stencil used to reconstruct the hydrodynamical gradients (the central cell plus eight adjacent cells). Using the average sound speed in our simulations[1] ($c_s \sim 7$ kms^{-1}), we obtain $\Sigma_{\rm max} \sim 3000$ $\rm M_\odot$ pc^{-2}: larger than the maximum surface density of ~ 1000 $\rm M_\odot$ pc^{-2} attained in our galaxies. The second requirement is manifestly fulfilled for our gas disc scale-heights of several hundreds of parsec (see Table 1). To fulfil the third requirement, we employ the adaptive gravitational softening scheme in AREPO with a softening length of 1.5 times the cell diameter and a minimum value of 3 pc to match the spatial resolution at $n_{\rm thresh} = 2000$ cm^{-3}.

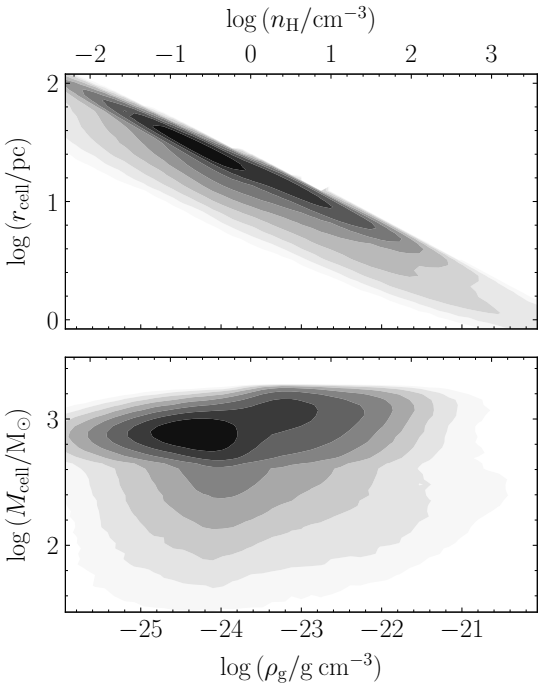

Figure 2. Distribution of gas cell radii $r_{\rm cell}$ (top) and gas cell masses $M_{\rm cell}$ (bottom) as a function of mass density for the FLAT simulation after 600 Myr of evolution. The cells are not perfectly-spherical, so $r_{\rm cell}$ corresponds to the radius of a sphere with the same volume. The colours are logarithmically-related to the total number of gas cells, at a spacing of 0.3 dex.

2.4 Star formation prescription

We follow a simple prescription for the star formation rate volume density that reproduces the observed relationship between the star formation rate surface density and the gas surface density (Kennicutt 1998). For a gas cell i with volume density ρ_i, the volume

[1] Both the sound speed and the turbulent velocity dispersion in the highest-density (molecular) gas are much lower than is the average ISM sound speed. However, the Toomre length in this cold gas is also much longer, ballooning out to kpc-scales for $n_{\rm H} \sim 100$ cm^{-3}. Even in the densest gas, the average ISM sound speed is therefore the appropriate quantity to use in our calculation of $\Sigma_{\rm max}$.

density of the star formation rate is computed as

$$\frac{\mathrm{d}\rho_{*,i}}{\mathrm{d}t} = \begin{cases} \frac{\epsilon\rho_i}{t_{\mathrm{ff},i}}, & n_i \geqslant n_{\mathrm{thresh}} \\ 0, & n_i < n_{\mathrm{thresh}} \end{cases} , \tag{9}$$

where $t_{\mathrm{ff},i} = \sqrt{3\pi/(32G\rho_i)}$ is the local free-fall time, n_i is the local hydrogen number density, and $n_{\mathrm{thresh}} = 2000$ cm^{-3} is the threshold above which star formation is allowed to occur. The star formation threshold is chosen to ensure that the star-forming gas in our simulations is Jeans-unstable, provided that the gas temperature does not exceed 100 K, a constraint that is satisfied by all of the dense gas in our simulation (see Section 3). We assign a star formation efficiency per free-fall time of $\epsilon = 0.01$ in accordance with observations of the gas depletion time in nearby galaxies (Leroy et al. 2017; Krumholz & Tan 2007; Utomo et al. 2018; Krumholz et al. 2018). In practice, Equation (9) is fulfilled on average for a large number of gas cells by stochastically generating star particles from the set of cells with $n > n_{\mathrm{thresh}}$, at a probability of $P_i = 1 - \exp\left(-\mathrm{d}\rho_{*,i}/\mathrm{d}t \cdot \Delta t/\rho_i\right)$. Gas cells with masses larger than twice the simulation mass resolution (900 M$_\odot$ here) 'spawn' a star particle of mass equal to the mass resolution, and the gas cell mass is reduced by the corresponding amount. Smaller gas cells are deleted entirely and replaced by star particles of an equal mass. In both cases, the velocity of the new star particle is equal to the velocity of the parent gas cell. As for the gas particles, we use a gravitational force softening of 3 pc for the star particles in our simulations.

One significant concern with the prescription outlined above, which relies solely on a gas density threshold to determine where stars form, is that it may lead to star formation in gas that is not gravitationally-bound. This may occur in gas flows with a high Mach numbers, in which the gas is Jeans unstable with $|U_{\mathrm{grav}}| > U_{\mathrm{therm}}$ but the ram pressure is high, such that $|U_{\mathrm{grav}}| < U_{\mathrm{kin}} = 1/2\, mv^2$. This is a common occurrence in radiative shocks, where the material is cool and at high density, but still has sufficient kinetic energy to prevent it from undergoing gravitational collapse (see e.g. the discussion in Federrath et al. 2010; Gensior et al. 2020). To check whether this is a problem for the gas in our simulations, we have computed the total energy $U_{\mathrm{grav}} + U_{\mathrm{therm}} + U_{\mathrm{kin}} < 0$ for the gas cells in our simulations that fall above the star formation threshold, $n > n_{\mathrm{thresh}}$. The gravitational potential for each gas cell of mass M_{cell} and size r_{cell} is defined at its edge, such that $U_{\mathrm{grav}} = -GM_{\mathrm{cell}}^2/r_{\mathrm{cell}}$. We find that only $\lesssim 0.04$ per cent of these cells are not self-gravitating at a simulation time of 600 Myr.

2.5 Stochastic stellar population synthesis

We synthesise a stellar population for every star particle in our simulations using the Stochastically Lighting Up Galaxies (SLUG) model (da Silva et al. 2012, 2014; Krumholz et al. 2015). Here we briefly describe the methods used within SLUG to track the evolution of each stellar population, but refer to the reader to the cited works for a complete and detailed explanation. The stellar population for a star particle of birth mass M_{birth} is formed via the Monte-Carlo sampling of N stars from a Chabrier (2003) initial stellar mass function (IMF). The integer N is chosen by drawing from the Poisson distribution with an expectation value of $M_{\mathrm{birth}}/\overline{M}$, where $\overline{M}$ is the expectation value for the mass of a single star. Averaged over a large number of assignments, this procedure ensures that the assigned masses of the stellar populations converge to the birth masses of the star particles. Each stellar population evolves as a function of the simulation time according to Padova solar metallicity tracks (Fagotto et al. 1994a,b; Vázquez & Leitherer 2005) with Starburst99-like spectral synthesis (Leitherer et al. 1999). As such, SLUG provides the number of supernovae N_{SN}, the ejected mass Δm and the ionising luminosity S for each star particle at every time-step, all of which are used in our numerical prescription for stellar feedback. By basing our feedback on the stochastic sampling of the IMF, we avoid arbitrary (but important) choices regarding the time interval over and delay with which stellar feedback acts, which have a qualitative effect on the structure of the ISM (Keller & Kruijssen 2020).

2.6 Stellar feedback

Here we describe in detail the numerical methods used to inject stellar feedback from supernovae, stellar winds and HII regions into the simulated ISM. We provide convergence tests for each of the components of our stellar feedback model in a separate paper, Jeffreson et al. (prep).

2.6.1 Supernovae and stellar winds

For each star particle i in our simulations, we use SLUG to calculate the mass Δm_i lost during each numerical time-step, along with the number of supernovae $N_{i,\mathrm{SN}}$ that have occurred. If $N_{i,\mathrm{SN}} = 0$, then we assume that the mass loss results from stellar winds, and deposit the mass into the star's nearest-neighbour (NN) gas cell. We do not account for the thermal energy and momentum injected by stellar winds, and we discuss the possible consequences of this in Section 6.2. If $N_{i,\mathrm{SN}} > 0$, then we assume that all mass loss results from Type II supernovae, and we inject mass, energy and momentum according to the prescription described in Keller et al. (prep). We give a brief overview of this algorithm below.

(i) For each star particle i, find the NN gas particle j.

(ii) Determine the total mass Δm_j, momentum $\Delta \mathbf{p}_{j,\mathrm{SN}}$ and energy $\Delta E_{j,\mathrm{SN}}$ delivered by all of the star particles for which j is the NN, such that

$$\Delta m_j = \sum_i \Delta m_i \tag{10}$$

$$\Delta \mathbf{p}_{j,\mathrm{SN}} = \sum_i \Delta \mathbf{p}_{i,\mathrm{SN}} \tag{11}$$

$$\Delta E_{j,\mathrm{SN}} = \sum_i \Delta E_{i,\mathrm{SN}} + \sum_i \frac{|\Delta \mathbf{p}_{i,\mathrm{SN}}|^2}{2\Delta m_i} - \frac{|\sum_i \Delta \mathbf{p}_{i,\mathrm{SN}}|^2}{2\sum_i \Delta m_i} \tag{12}$$

where $\Delta \mathbf{p}_{i,\mathrm{SN}} = \Delta m_i \mathbf{v}_i$ and $\Delta E_{i,\mathrm{SN}} = N_{i,\mathrm{SN}} \times 10^{51}$erg. The total energy $\Delta E_{j,\mathrm{SN}}$ received by gas cell j via Equation (12) is a combination of the blast-wave energies of the individual SN ejecta (first term on the LHS) and the energy dissipated in the inelastic collisions between these ejecta (second and third terms on the LHS).

(iii) For each gas cell j that has received feedback mass, momentum and energy, find the set of neighbouring gas cells k with which it shares a Voronoi face. Compute the radial terminal momentum $p_{t,k}$ for the blast-wave as it passes through each cell k, using the (unclustered) parametrization of Gentry et al. (2017), as

$$\frac{p_{\mathrm{t},k}}{\mathrm{M}_\odot \mathrm{kms}^{-1}} = 4.249 \times 10^5 \left(\frac{w_k \Delta E_{j,\mathrm{SN}}}{10^{51}\mathrm{erg}}\right)\left(\frac{n_k}{\mathrm{cm}^{-3}}\right)^{-0.06}, \tag{13}$$

where the weight factor w_k is the fractional Voronoi face area shared between cells j and k, such that

$$w_k = \frac{A_{j\rightarrow k}}{\sum_k A_{j\rightarrow k}}, \tag{14}$$

ensuring isotropic energy injection. In the above, n_k is the gas number density in cell k, and solar metallicity is assumed. Equation (13) approximates the mechanical (PdV) work done by the blast-wave on the surrounding gas during the Sedov-Taylor (energy-conserving, momentum-generating) phase of its expansion. As we do not resolve this phase of the blast-wave expansion, the momentum given by Equation (13) would not be retrieved by simply dumping the energy $w_k \Delta E_{j,\rm SN}$ into cell k as thermal energy (Katz 1992; Slyz et al. 2005; Smith et al. 2018).

(iv) Using the terminal momentum $p_{t,k}$, calculate the final momentum $p_{k,\rm new}$ of cell k following the energy-conserving procedure of Hopkins et al. (2018a), as

$$\begin{aligned} \mathbf{p}_{k,\rm new} &= \mathbf{p}_k + \Delta\mathbf{p}_{k,\rm SN} \\ \Delta\mathbf{p}_{k,\rm SN} &= p_{\rm fb,}k\hat{\mathbf{r}}_{j\rightarrow k} + w_k \Delta\mathbf{p}_{j,\rm SN}, \end{aligned} \tag{15}$$

where $p_{\rm fb,}k$ is the smallest of the terminal and energy-conserving momenta in cell k, such that

$$p_{\rm fb,}k = \min\left\{w_k p_{t,k},\ \sqrt{2(m_k + w_k\Delta m_j)w_k \Delta E_{j,\rm SN}}\right\}. \tag{16}$$

(v) Calculate the final mass $m_{k,\rm new}$ and final energy $E_{k,\rm new}$ of the cell k, as

$$\begin{aligned} m_{k,\rm new} &= m_k + \Delta m_k \\ \Delta m_k &= w_k \Delta m_j, \end{aligned} \tag{17}$$

and

$$\begin{aligned} E_{k,\rm new} &= E_k + \Delta E_k \\ \Delta E_k &= \frac{|\mathbf{p}_k + \Delta\mathbf{p}_{k,\rm SN}|^2}{2(m_k + \Delta m_k)} - \frac{|\mathbf{p}_k|^2}{2m_k}. \end{aligned} \tag{18}$$

(vi) Finally, ensuring linear momentum conservation to machine precision requires that the new momentum $\mathbf{p}_{j,\rm new}$ of the central cell j is given by

$$\mathbf{p}_{j,\rm new} = \mathbf{p}_j - \sum_k \Delta\mathbf{p}_{k,\rm SN}. \tag{19}$$

Similarly, to ensure energy conservation to machine precision requires that the updated total energy $E_{j,\rm new}$ of the central cell j be given by

$$E_{j,\rm new} = E_j + E_{j,\rm SN} - \sum_k \left(\Delta E_{k,\rm SN} - \frac{w_k |\Delta\mathbf{p}_{j,\rm SN}|^2}{2\Delta m_j}\right), \tag{20}$$

where the final term accounts for the frame-change from the SN frame to the frame of gas cell j.

In the above, we do not adjust the chemical state of the cells into which SN mass, momentum and thermal energy is injected. The evolution of chemistry, heating and cooling via SGCHEM (see Section 2.7) occurs immediately after the injection of feedback, and deals with the change in the ionisation state of the gas cells caused by the injection of thermal energy. Aside from this, we do not evolve metal abundances in our simulations.

2.6.2 *HII region momentum*

We inject thermal and kinetic energy from HII region feedback according to the model of Jeffreson et al. (prep). The momentum provided by a hemispherical 'blister-type' HII region to the surrounding ISM is given by the momentum of the thin bounding shell at the ionisation front, swept up in its initial rapid expansion to the Strömgren radius (Matzner 2002; Krumholz & Matzner 2009). The momentum equation for the shell of an HII region with ionising luminosity S and age t can be solved to give a momentum per unit time of

$$\begin{aligned} \frac{{\rm d}p}{{\rm d}t} \sim 1.2\times10^3 M_\odot\ {\rm kms}^{-1}{\rm Myr}^{-1}\times \\ S_{49}\left\{1 + \left[\frac{3}{2}\frac{t^2}{t_{\rm ch}^2} + \left(\frac{25}{28}\frac{t^2}{t_{\rm ch}^2}\right)^{6/5}\right]^{1/6}\right\}, \end{aligned} \tag{21}$$

where $S_{49} = S/10^{49}{\rm s}^{-1}$. The characteristic time $t_{\rm ch}$ at which radiation pressure and gas pressure make equal contributions to the momentum delivered is given approximately by

$$t_{\rm ch} \sim 45\,\overline{n}_{\rm H,2}^{1/6} S_{49}^{7/6}\ {\rm yr}, \tag{22}$$

where $\overline{n}_{\rm H,2} = n_{\rm H}/100{\rm cm}^{-2}$ with $n_{\rm H}$ the birth number density of the star particle. The full derivations of Equations (21) and (22) are given in Jeffreson et al. (prep). Following Krumholz & Matzner (2009), the enhancement of the radiation pressure made by photon trapping (via stellar winds, infrared photons and Lyman-α photons) contributes a factor of $f_{\rm trap} \sim 2$ to the first term on the right-hand side of Equation (21), relative to the case of direct radiation pressure. We calculate the physical momentum delivered by each AREPO star particle i by grouping together all star particles that have overlapping ionisation front radii, given by

$$r_{\rm II,i}(t) \sim 0.5\times^{-2} S_{49,i}\,{\rm pc}\left\{\frac{3}{2}\left(\frac{t_i}{t_{\rm ch,i}}\right)^2 + \left[\frac{25}{28}\left(\frac{t_i}{t_{\rm ch,i}}\right)^2\right]^{6/5}\right\}^{1/3}. \tag{23}$$

This ensures that the amount of momentum injected varies with the size of the physical HII regions in our simulations, and not with the masses of the individual star particles, which in turn depend on the simulation resolution. In practice, we form Friends-of-Friends (FoF) groups of star particles, where two particles are linked together if either falls within the ionisation front of the other. The FoF linking length is then given by $\max\left(r_{\rm II,1}, r_{\rm II,2}\right)$ for star particles with ionisation fronts $r_{\rm II,1}$ and $r_{\rm II,2}$. The entire FoF group injects a momentum per unit time that is given by the sum over the group members, as

$$\begin{aligned} \left(\frac{{\rm d}p}{{\rm d}t}\right)_{\rm FoF} = 1.2\times10^3\ {\rm M}_\odot\ {\rm km\,s}^{-1}{\rm Myr}^{-1}\times \\ \sum_{i=1}^{N} S_{49,i}\left\{1 + \left[\frac{3}{2}\left(\frac{\langle t\rangle_S}{t_{\rm ch,FoF}}\right)^2 + \left(\frac{25}{28}\frac{\langle t\rangle_S}{t_{\rm ch,FoF}}\right)^{6/5}\right]^{1/6}\right\}, \end{aligned} \tag{24}$$

where $\langle ...\rangle_S$ denotes the luminosity-weighted average over the star particles $i = 1...N$ in the group, and the characteristic time is given by

$$t_{\rm ch,FoF} = \sqrt{0.6\,{\rm s}^2\left(\sum_{i=1}^{N} S_{49,i}\right)^{7/3}\langle\overline{n}_{\rm H,2}\rangle_S^{1/3}\,{\rm pc}}. \tag{25}$$

The group injects the momentum $\Delta p_{\rm FoF} = ({\rm d}p/{\rm d}t)_{\rm FoF}\Delta t$ at its luminosity-weighted centre, given by

$$\langle\mathbf{x}\rangle_S = \frac{\sum_{i=1}^{N} S_{49,i}\mathbf{x}_i}{\sum_{i=1}^{N} S_{49,i}}. \tag{26}$$

We ensure that the values of $({\rm d}p/{\rm d}t)_{\rm FoF}$ and $\langle\mathbf{x}\rangle_S$ are consistent across all FoF group members at every time, by updating the FoF

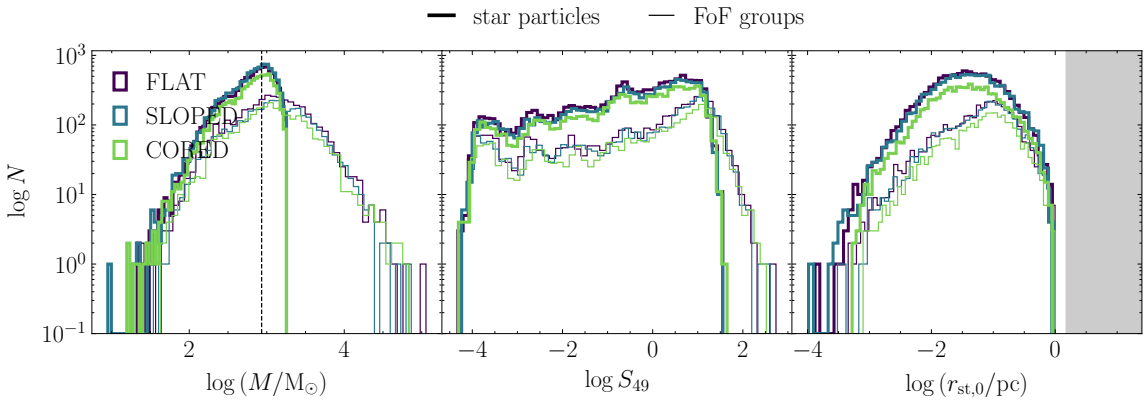

Figure 3. Distribution of cell masses (left), ionising luminosities (centre) and Strömgren radii (right) for individual star particles (bold lines) and for FoF groups with overlapping Strömgren spheres (thin lines). The vertical dashed line in the left-hand panel represents the target gas cell resolution of 900 $M_\odot$. The grey shaded region in the right-hand panel represents the range $r_{\rm st,0} > 1.5$ pc of Strömgren radii that would be resolved in our simulations. It is clear that all Strömgren spheres are unresolved, even at the peak gas cell resolution.

groups on global time-steps only. In Jeffreson et al. (prep), we argue that this procedure incurs a maximum positional error of 1 pc on the star particle members that are included in a group: one third the size of the smallest Voronoi cell in our simulations. The numerical time-step Δt of momentum injection between updates is set to the numerical time-step of an arbitrary group member. All star particles in each FoF group have comparable time-steps, which are determined according to their instantaneous accelerations.

The injection procedure for the HII region momentum is identical to that employed for supernovae, as described in Section 2.6.1. The nearest-neighbour gas cell j to the centre $\langle \mathbf{x} \rangle_S$ of the FoF group accumulates the net radial momenta of all the FoF groups that it hosts, then distributes the momentum to its facing neighbour cells k according to

$$\Delta p_{k,\rm HII} = w_k(\theta_k, A_k) \hat{\mathbf{r}}_{j\rightarrow k} \Delta p_{j,\rm HII}, \tag{27}$$

where $\hat{\mathbf{r}}_{j\rightarrow k}$ is the unit vector connecting the centroid of cell j to that of cell k, and the weight factor $w_k(\theta_k, A_k)$ is the fractional Voronoi face area shared between these cells, rescaled to account for the directionality of momentum injection from a blister-type HII region, such that

$$\begin{aligned} w(\theta_k, A_k) &= \frac{A_{j\rightarrow k} f(\theta_k)}{\sum_k A_{j\rightarrow k} f(\theta_k)} \\ f(\theta_k) &= \left[\log\left(\frac{2}{\Theta}\right)(1 + \Theta^2 - \cos^2\theta_k) \right]^{-1}. \end{aligned} \tag{28}$$

Here, $\Theta = \pi/12$ controls the width of the directed momentum 'beam' and θ_k is the angle between the beam-axis and the unit vector $\hat{\mathbf{r}}_{j\rightarrow k}$ connecting cells j and k, defined by

$$\cos\theta_k = \frac{\hat{\mathbf{r}}_{j\rightarrow k} \cdot \hat{\mathbf{z}}_{\rm FoF}}{|\hat{\mathbf{z}}_{\rm FoF}|}. \tag{29}$$

For each star particle, the vector $\hat{\mathbf{z}}_i$ defining the beam-axis is drawn randomly from a uniform distribution over the spherical polar angles about the star's position at birth, ϕ_i and θ_i. This value is fixed throughout the lifetime of the HII region, and the beam-axis $\hat{\mathbf{z}}_{\rm FoF}$ of each FoF group is calculated as a luminosity-weighted average of $\hat{\mathbf{z}}_i$ across the constituent star particles.

2.6.3 *HII region heating*

We inject enough thermal energy from each HII region to heat the gas inside the Strömgren radius of each FoF group to a temperature of 7000 K, in accordance with Ho et al. (2019). We do this via an approximate photon-counting procedure that assumes all Strömgren radii are either completely unresolved (smaller than the radius of a single Voronoi gas cell) or marginally-resolved (extending into the first layer of neighbouring gas cells). We demonstrate in Figure 3 that this approximation holds for the Strömgren radii in all three simulations. As such, we need only inject photons into the Voronoi gas cells that share a face with the nearest-neighbour cell of the FoF group, and so we use the same injection procedure as for the HII region momentum. We count the photons to be injected via a technique similar to that of Hopkins et al. (2018b), described below, and explained fully in Jeffreson et al. (prep).

(i) For each FoF group, find the NN (host) gas particle j for the luminosity-weighted centre of mass.

(ii) Increment the total number of photons $S_{\rm in}$ per unit time delivered to this gas cell by its enclosed set of N group centres, so that the final value is given by $S_{j,\rm in} = \sum_{\rm FoF=1}^{N} S_{\rm FoF}$, where $S_{\rm FoF}$ is the total ionising luminosity of all stars in the FoF group.

(iii) Calculate the number of photons that can be consumed per unit time by ionising the material inside gas cell j, given by $S_{j,\rm cons} = \alpha_B N_{j,\rm H} n_{j,e}$, with $N_{j,\rm H}$ the number of hydrogen atoms in the cell and $n_{j,e}$ the number density of electrons.

(iv) If $S_{j,\rm in} < S_{j,\rm cons}$, flag cell j as 'ionised' with a probability of $S_{j,\rm in}/S_{j,\rm cons}$. Over a large number of gas cells, the number of injected photons converges to $S_{j,\rm in}$.

(v) If $S_{j,\rm in} > S_{j,\rm cons}$, flag cell j as 'ionised' and calculate the residual ionisation rate $S_{j,\rm res} = S_{j,\rm in} - S_{j,\rm cons}$ that will now be spread over its set of facing Voronoi cells k.

If the Strömgren radius is completely unresolved, i.e. $S_{j,\rm in} < S_{j,\rm cons}$, then the algorithm ends here. If it is marginally-resolved, then we continue as follows.

(vii) For each gas cell j with $S_{j,\rm res} > 0$, find the set of neighbouring cells k with which it shares a Voronoi face, which have

already been identified for the purpose of injecting feedback from supernovae and momentum from HII regions (see Sections 2.6.1 and 2.6.2). Compute the fraction of momentum received by each of these cells k according to

$$S_{k,\rm in} = w_k S_{j,\rm res}, \tag{30}$$

where the weight factor w_k is identical to the weight factor used for the injection of HII region momentum.

(viii) Ionise each facing cell k with a probability of $S_{k,\rm in}/S_{k,\rm cons}$. Summed over the set of facing cells for many HII regions, this ensures that the expectation value for the rate of ionisation converges to $S_{j,\rm res}$.

The injection of thermal energy via the procedure outlined above is immediately followed by the computation of chemistry and cooling for each gas cell using SGChem, as described in Section 2.7. As such, we do not explicitly adjust the chemical state of the gas cells, relying instead on the chemical network to ionise the gas in accordance with the injection of heating. We set a temperature floor of 7000 K during this computation.

2.6.4 *HII region stalling*

The momentum and thermal energy injected by each HII region in Sections 2.6.2 and 2.6.3 is shut off when the rate of HII region expansion drops below the velocity dispersion of the host cloud, such that the ionised and neutral gas are able to mix and the expanding shell loses its coherence (Matzner 2002). Once this transition has occurred, the shell ceases to expand, and its radius and internal energy are no longer well-defined, such that it no longer transfers momentum to the surrounding gas. Equation (23) is no longer valid, and we ensure that such 'stalled' HII regions are removed from the computation of FoF groups, so that they do not link together two active HII regions and distort the position of their centre of luminosity. In practice, the value of the ionising luminosity S also falls steeply at this time, so that it is safe to ignore the thermal energy that is deposited after stalling has occurred. Prior to FoF group computation, we therefore calculate the numerical rate of HII region expansion $\dot{r}_{\rm II,\it i} = \Delta r_{\rm II,\it i}/\Delta t_i$ for each star particle i, where $\Delta r_{\rm II,\it i}$ is the increment in the ionisation front radius during the particle's time-step Δt_i. We compare this value to the cloud velocity dispersion $\sigma_{\rm cl}$, approximated according to Krumholz & Matzner (2009) for a blister-type HII region centred at the origin of a cloud with an average density of $\overline{\rho}(r) = 3/(3-k_\rho)\rho_0 (r/r_0)^{-k_\rho}$. Assuming that the cloud is in approximate virial balance with $\alpha_{\rm vir} = 1$ on the scale of the HII region, this gives

$$\begin{aligned}\sigma_{\rm cl}(r_{\rm II}) &= \sqrt{\frac{\alpha_{\rm vir} G M(<r_{\rm II})}{5 r_{\rm II}}} \\ &= \sqrt{\frac{2\pi}{15}\alpha_{\rm vir} G \overline{\rho}(r_{\rm st,0}) r_{\rm ch}^{2-k_\rho} r_{\rm st,0}^{k_\rho} x_{\rm II}^{2-k_\rho}},\end{aligned} \tag{31}$$

where we again take $k_\rho = 1$. If we find that $\dot{r}_{\rm II,\it i} < \sigma_{\rm cl}$, then we flag the star particle as 'stalled' and shut off its HII region feedback.

2.7 ISM Chemistry, heating and cooling

The chemical evolution of the gas in our simulations is tracked via a simplified set of reactions involving hydrogen, carbon and oxygen, according to the chemical network of Glover & Mac Low (2007a,b) and Nelson & Langer (1997). This chemical network is interfaced with Arepo via the package called SGChem, and will be referred to as such throughout this paper. The network follows the fractional abundances of $\rm H$, $\rm H_2$, $\rm H^+$, $\rm He$, $\rm C^+$, $\rm CO$, $\rm O$ and $\rm e^-$, which are related by the equalities

$$\begin{aligned} x_{\rm H} &= 1 - x_{\rm H^+} - 2x_{\rm H_2} \\ x_{\rm e^-} &= x_{\rm H^+} + x_{\rm C^+} + x_{\rm Si^+} \\ x_{\rm C^+} &= \max(0, x_{\rm C,tot} - x_{\rm CO}) \\ x_{\rm O} &= \max(0, x_{\rm O,tot} - x_{\rm CO}), \end{aligned} \tag{32}$$

with the abundance of helium set to its standard cosmic value of $x_{\rm He} = 0.1$, and the abundances of silicon, carbon and oxygen set in accordance with Sembach et al. (2000), to values consistent with the local warm neutral medium: $x_{\rm Si,tot} = 1.5 \times 10^{-5}$, $x_{\rm C,tot} = 1.4 \times 10^{-4}$ and $x_{\rm O,tot} = 3.2 \times 10^{-4}$. Silicon is assumed to be singly-ionised throughout the simulation, as is any carbon that is not locked up in CO molecules. The evolution of all chemical species is coupled to the heating, cooling, and dynamical evolution of the gas, via the atomic and molecular cooling function presented in Glover et al. (2010). This includes chemical cooling due to fine structure-emission from $\rm C^+$, O and $\rm Si^+$, Lyman α emission from atomic hydrogen, $\rm H_2$ line emission, gas-grain cooling, and electron recombination on grain surfaces and in reaction with polycyclic aromatic hydrocarbons (PAHs). In hot gas, cooling may also occur via the collisional processes of $\rm H_2$ dissociation, Bremsstrahlung, the ionisation of atomic hydrogen, as well as via permitted and semi-forbidden transitions of metal atoms and ions. To treat the contribution from metals, we assume collisional ionization equilibrium and use the cooling rates tabulated by Gnat & Ferland (2012). The dominant heating mechanism is photoelectric emission from dust grains and PAHs, with lesser contributions from cosmic ray ionisation and $\rm H_2$ photodissociation. We assign a value of 1.7 Habing (1968) units for the interstellar radiation field (ISRF) strength according to Mathis et al. (1983), and a value of 2×10^{-16} s^{-1} to the cosmic ray ionisation rate (e.g. Indriolo & McCall 2012). The dust grain number density is computed by assuming the solar value for the dust-to-gas ratio, and the dust temperature is obtained according to the procedure described in Appendix A of Glover & Clark (2012). The full list of heating and cooling processes is given in Table 1 of Glover et al. (2010).

2.8 Thermal and chemical post-processing

To calculate the mass fractions of H and $\rm H_2$ for each Voronoi cell in our simulations, we post-process each snapshot using the astrochemistry and radiative transfer model Despotic (Krumholz 2013).[2] We follow the method used in Fujimoto et al. (2019) and treat each Voronoi gas cell as a separate one-zone, spherical 'cloud' model, characterised by its hydrogen number density $n_{\rm H}$, column density $N_{\rm H}$, and its virial parameter $\alpha_{\rm vir}$. Within Despotic, the line emission from each cloud is computed via the escape probability formalism, which is coupled self-consistently to the chemical

[2] We use the non-equilibrium molecular fraction from the on-the-fly chemistry for cooling, but due to the limitations of our resolution, we cannot accurately compute the self-shielding of molecular hydrogen from the UV radiation field during run-time. In addition, because we do not resolve all of the dense substructures in the clouds that are created by the turbulent velocity field, we tend to underestimate the $\rm H_2$ formation rate within the clouds. This means that the on-the-fly $\rm H_2$ fractions are always too low by a factor of around 2, and so we re-calculate an equilibrium molecular fraction in post-processing.

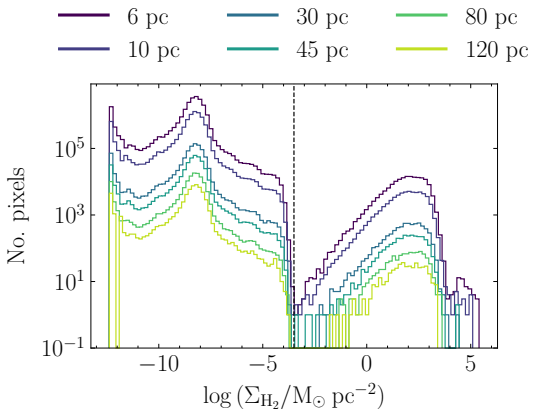

Figure 4. Distributions of the molecular hydrogen column density Σ_{H_2} for six different ray-tracing maps of the FLAT simulation at resolutions of 6 pc, 10 pc, 30 pc, 45 pc, 80 pc and 120 pc. When normalised by the total number of pixels, all six histograms are identical. The snapshot is taken at a simulation time of 600 Myr. The vertical dashed line shows the cutoff used for cloud identification.

and thermal evolution of the gas. The carbon and oxygen chemistry follows the chemical network of Gong et al. (2017), modified by the addition of cosmic rays and the grain photoelectric effect, subject to dust- and self-shielding for each component, line cooling due to C^+, C^+, O and CO, as well as thermal exchange between dust and gas. The ISRF strength and the cosmic ionisation rate are matched to the values used by the live chemistry during our simulations, and the rate of photoelectric heating is held fixed, both spatially and temporally. For each one-zone model, this system of coupled rate equations is converged to a state of chemical and thermal equilibrium.

It would be prohibitively computationally-expensive to perform the above convergence calculation for every gas cell in our simulations, so we instead interpolate over a table of pre-calculated cloud models, spaced at regular logarithmic intervals in n_H, N_H and α_{vir}. The hydrogen volume density can be straight-forwardly calculated for each Voronoi cell as $n_H = \rho/\mu m_H$, where ρ is the mass volume density field for the gas and $\mu \sim 1.4$. Following Fujimoto et al. (2019), the hydrogen column density is computed according to the local approximation of Safranek-Shrader et al. (2017), given as

$$N_H = \lambda_J n_H, \tag{33}$$

where $\lambda_J = (\pi c_s^2/G\rho)^{1/2}$ is the Jeans length, computed using an upper limit of $T = 40$ K on the gas cell temperature. We define the virial parameter as in MacLaren et al. (1988a); Bertoldi & McKee (1992), such that

$$\alpha_{vir} = \frac{5\sigma_g^2}{\pi G \rho L^2}, \tag{34}$$

where σ_g is the turbulent gas velocity dispersion as calculated in Gensior et al. (2020) and L is the smoothing length over which this velocity dispersion is calculated (see Appendix A6). Together with the assumption of equilibrium and the rates of heating and cooling listed above, these three parameters constrain the abundance of atomic hydrogen f_{HI} and the ^{12}CO line luminosity L_{CO} for the the $1 \rightarrow 0$ transition. To mimic observations, we use the latter to compute the molecular hydrogen surface density, as described in Section 2.9.1.

We have also tested an alternative approach to that described above, by applying the TreeCol algorithm (Clark et al. 2012) to attenuate the ISRF in the immediate vicinity of each Voronoi gas cell. This would allow us to account for the dust- and self-shielding of molecular hydrogen during run-time, and to self-consistently couple the resulting abundances to the live, non-equilibrium chemical network described in Section 2.7. However, we have found that at the spatial resolution of our simulations, the resulting molecular hydrogen surface density has a maximum value of 2 M$_\odot$ pc^{-2}: half of the observed value for the Milky Way (Wolfire et al. 2003; Kennicutt & Evans 2012). By contrast, the molecular hydrogen abundances obtained in post-processing fall between values of 1 and 4 M$_\odot$ pc^{-2}, in agreement with observations (see Section 3.3). This behaviour is in keeping with the resolution requirements reported by Seifried et al. (2017) and Joshi et al. (2019), who show that the spatial resolution should reach 0.1 pc in the densest gas, in order to accurately model the H_2 and CO fractions there. We therefore opt to use the Despotic model instead, as we expect that the resolution requirements of this method are less severe than for the computation of abundances via on-the-fly chemistry. That is, at our mass resolution of 900 M$_\odot$, the lack of sub-structure at high gas densities will have a large impact on the time-scale required for the chemical abundances to reach equilibrium during the non-equilibrium SGChem chemistry computation. It will have a lesser impact on the equilibrium abundances themselves, as calculated during post-processing.

2.9 Cloud identification

2.9.1 Molecular clouds

We identify GMCs in our simulations as peaks in the molecular hydrogen column density that are traced by CO, in order to provide the best possible comparison to the properties of observed clouds. We convert the ^{12}CO $1 \rightarrow 0$ line luminosity (L_{CO}[erg s^{-1}] per hydrogen atom) from our Despotic calculation in Section 2.8 to a CO-bright molecular hydrogen surface density using

$$\begin{aligned}\Sigma_{H_2}[\mathrm{M_\odot pc^{-2}}] = &\frac{2.3\times10^{-29}[\mathrm{M_\odot (erg\ s^{-1})^{-1}}]}{m_H[\mathrm{M_\odot}]} \\ &\times \Sigma_g[\mathrm{M_\odot pc^{-2}}] \\ &\times \frac{\int_{-\infty}^{\infty} \mathrm{d}z' \rho_g(z')\, L_{CO}[\mathrm{erg\ s^{-1}}]}{\int_{-\infty}^{\infty} \mathrm{d}z' \rho_g(z')},\end{aligned} \tag{35}$$

where $\rho_g(z)$ is the total gas volume density as a function of distance z away from the galactic mid-plane, Σ_g is the total gas surface density, and m_H is the proton mass. The factor 2.3×10^{-29} (erg s^{-1})$^{-1}$ combines the mass-to-luminosity conversion factor $\alpha_{CO} = 4.3$ M$_\odot$(K kms^{-1} pc^{-2})$^{-1}$ from Bolatto et al. (2013) and the line-luminosity unit conversion factor 5.31×10^{-30} (K kms^{-1} pc^2)/(erg s^{-1}) from Solomon & Vanden Bout (2005), using the observed frequency of 115.3 GHz for the CO $J = 1 \rightarrow 0$ transition at a redshift of $z = 0$. The integral ratio is the 2D density-weighted projection map of the CO line-luminosity per hydrogen atom, computed via the method described in Appendix A. In Section 3.4, we show that the mass of molecular hydrogen identified in this way makes up approximately one third of the combined mass of the warm and neutral media, in ac-

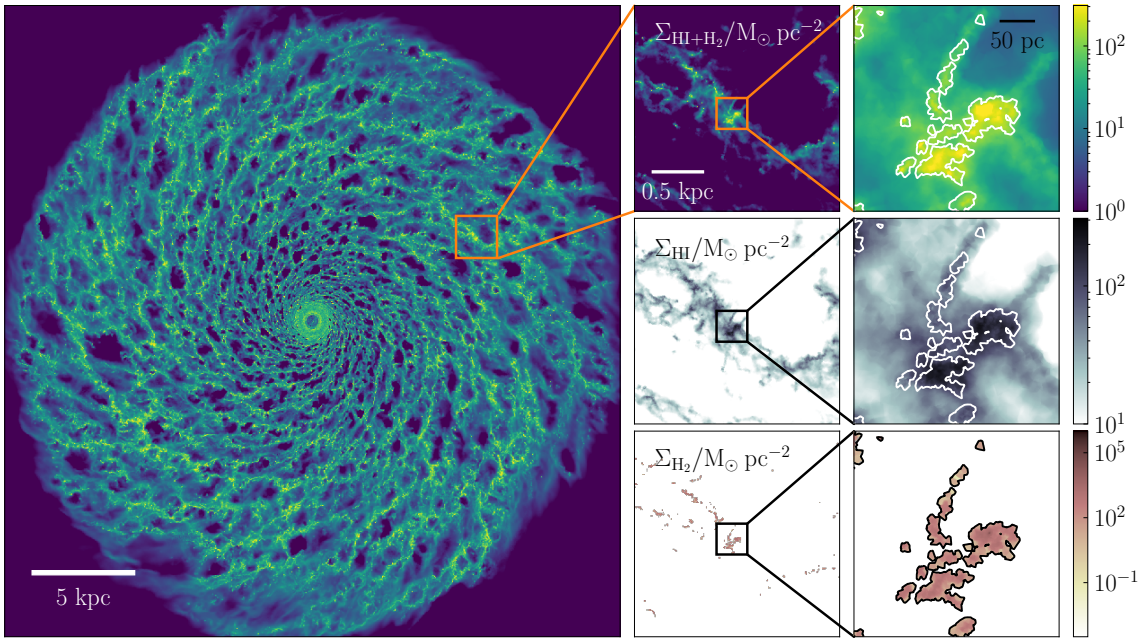

Figure 5. Molecular cloud identification in the FLAT simulation at a time of 600 Myr. *Left:* Column density of the combined HI and H_2 gas distribution. *Centre:* Zoomed 2-kpc section of the disc (white box in the left-hand panel), viewed in total cold gas (top), HI gas only (centre) and H_2 gas only (bottom). *Right:* Zoomed 300-pc section of the disc, viewed in total cold gas (top), HI gas only (centre) and H_2 gas only (bottom). The contours in the right-hand panels indicate the boundaries of GMCs identified via the method described in Section 2.9.

cordance with observed galaxies of a similar mass (e.g. Saintonge et al. 2011).

For each simulation snapshot, we use Equation (35) to compute a 2D projection map of $\Sigma_{\rm H_2}$ with a side-length of 30 kpc and a resolution of 6 pc per pixel, equal to the radius of a typical Voronoi gas cell at our mass resolution of 900 $\rm M_\odot$ and at the minimum molecular cloud hydrogen number density of $\gtrsim$ 30 $\rm cm^{-3}$. We therefore ensure that inside GMCs, each pixel contains at least one Voronoi cell centroid. Using the ASTRODENDRO package for Python, we identify all closed contours at $\log_{10}\left(\Sigma_{\rm H_2}/{\rm M_\odot\ pc^{-2}}\right) = -3.5$, as indicated by the dashed line in Figure 4.[3] We discard contours that enclose fewer than nine pixels in total, allowing us to identify clouds of diameter $\sim 3 \times 6$ pc $= 18$ pc, oversampled by a factor of three. In the right-hand panels of Figure 5, we show a zoom-in of the total gas column density (top), the HI column density (centre) and the H_2 column density (bottom) for a 250-pc patch of the ISM, overlaid with the corresponding set of contours. These correspond to the regions outlined by squares in the central panels, which in turn correspond to the outlined region in the left-most panel, showing the total gas column density of the entire galaxy.

To obtain the gas cell population of each molecular cloud, we apply the two-dimensional pixel mask for each ASTRODENDRO contour to the field of gas cell positions in each snapshot. Any gas cell with a temperature $T < 10^4$ K whose centroid falls inside the contour is considered to be a member of the molecular cloud. We accept only those identified structures with 20 Voronoi gas cells or more, to ensure that the properties of the clouds (e.g. velocity dispersions, angular momenta) are resolved. On top of the 18 pc minimum cloud diameter, this imposes a minimum cloud mass of $18,000$ $\rm M_\odot$. The temperature threshold ensures that we do not include gas cells that fall far from the galactic mid-plane, but we still expect to include many gas cells along the line of sight that have small molecular gas fractions. This is not a concern, as the properties of each molecular cloud are computed as $L_{\rm CO}$-weighted averages.

[3] This very conservative lower limit makes use of the range of molecular hydrogen surface densties calculated within the DESPOTIC model (spanning over 15 orders of magnitude, as shown in Figure 4). We save computation time by ignoring the bulk of the pixels in each map (left-hand side of the dashed line), but avoid taking an arbitrary cut on the value of $\Sigma_{\rm H_2}$. The lowest-density gas on the right-hand side of the dashed line will have little influence on the GMC properties computed in Section 5, as the contribution made by each Voronoi cell is weighted by its H_2 mass. The assumptions associated with our GMC identification procedure are therefore limited to the assumptions made within the DESPOTIC model itself.

2.9.2 *HI clouds*

The HI clouds in our simulations are identified similarly to the GMCs. The only difference is that we consider the HI gas column density derived from the HI abundance $f_{\rm HI}$, such that

$$\Sigma_{\rm HI}[{\rm M_\odot pc^{-2}}] = \Sigma_{\rm g}[{\rm M_\odot pc^{-2}}] \frac{\int_{-\infty}^{\infty} {\rm d}z' \rho_{\rm g}(z') f_{\rm HI}}{\int_{-\infty}^{\infty} {\rm d}z' \rho_{\rm g}(z')}, \qquad (36)$$

where the fraction on the right-hand side is obtained via the ray-tracing procedure described in Appendix A. We do not distin-

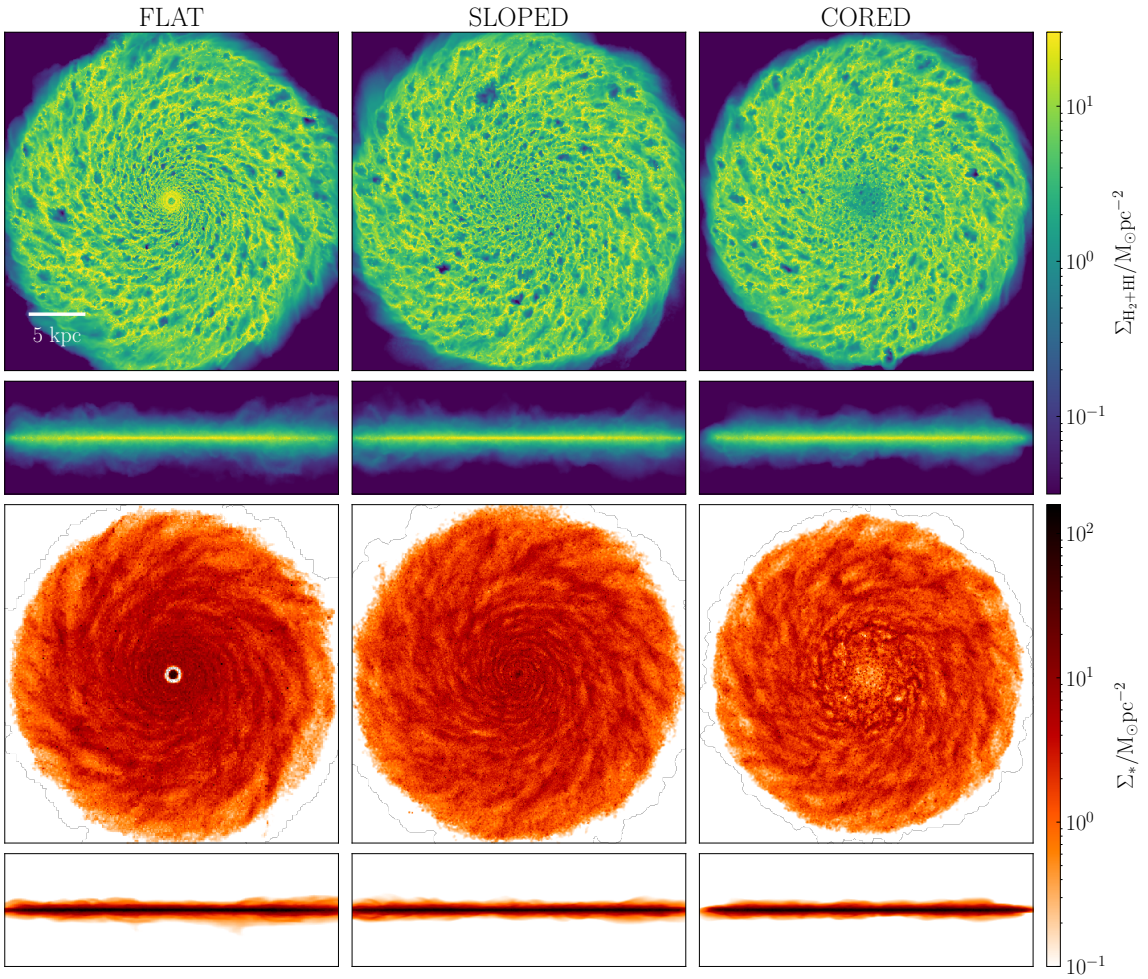

Figure 6. Face-on and edge-on column density maps of the total gas (top two rows) and the live stellar component (bottom two rows) for each galactic disc, at a simulation time of 600 Myr.

guish between atomic and ionised gas during post-processing, in the sense that we take $1 = f_{\rm HI} + 2f_{\rm H_2}$, where $f_{\rm HI}$ and $f_{\rm H_2}$ are the abundances of atomic and molecular hydrogen, respectively. The lowest-density gas in our simulations is assigned an atomic hydrogen abundance of $f_{\rm HI} \sim 1$. We therefore simply choose a lower limit of $\Sigma_{\rm HI} = 10\ {\rm M_\odot\ pc^{-2}}$ on the HI cloud surface density.

3 PROPERTIES OF SIMULATED GALAXIES

The initial conditions for our galaxies are Milky Way-like in their masses, sizes and geometries, so it is a necessary (but not sufficient) test of the input physics that they also reproduce the observable properties of the Milky Way on sub-galactic scales.[4] In this section, we compare the properties of our simulated discs to observations of Milky Way-like galaxies from the literature, and demonstrate an acceptable level of agreement.

3.1 Disc morphology

3.1.1 Disc structure on kpc-scales

The face-on and edge-on total gas and stellar column densities for each simulated galaxy are displayed in Figure 6. As reported in Table 1, stellar feedback inflates the HI gas disc to a scale-height of $\sim$ 250-380 pc, in agreement with the value observed by Savage & Wakker (2009). In Figure 7 we show the stellar velocity dispersion as a function of the height above the galactic mid-plane. The thin stellar disc has a vertical velocity dispersion of 5-6 ${\rm kms^{-1}}$ and a

[4] We do not expect to reproduce the properties of the central few kpc of the Milky Way, as we do not model the Galactic bar in our simulations. That is, differences between the simulations and observations in this region are expected, and do not raise concerns about the general validity of our model.

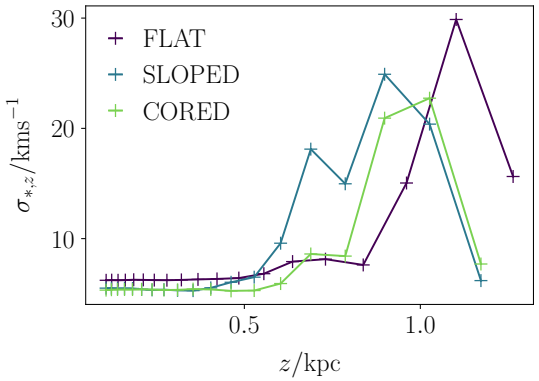

Figure 7. Stellar velocity dispersion as a function of height above/below the galactic mid-plane, over the radial range from 1 to 13 kpc. The thin stellar disc ($\lesssim$ 0.5 kpc) has a velocity dispersion of 5-6 kms^{-1}, while the thick stellar disc ($\gtrsim$ 0.5 kpc) has a velocity dispersion of 20-30 kms^{-1}.

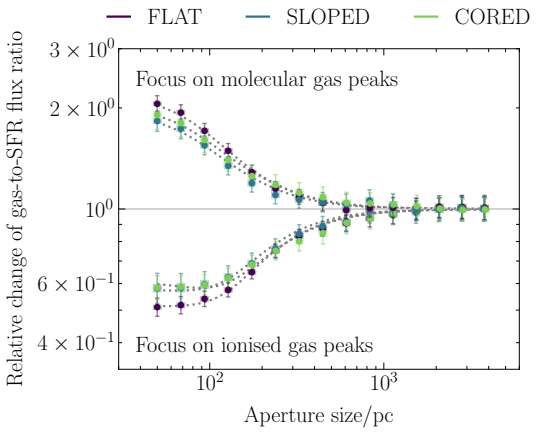

Figure 8. The gas-to-SFR flux ratio relative to the galactic average value as a function of the aperture size, for each of our simulated galaxies at t = 600 Myr. The upper branch represents apertures focused on molecular gas peaks, while the lower branch represents apertures focused on young stellar surface density (stars with ages 0-5 Myr). The errorbars on each data point represent the 1σ uncertainty on the value of the gas-to-SFR flux ratio. the dotted lines show the best-fitting models constraining the separation length, GMC lifetime and stellar feedback time-scale (Kruijssen et al. 2018).

scale-height of 400-500 pc, while the thick stellar disc has a velocity dispersion of 20-30 kms^{-1} and a scale-height of $\sim$ 1000 pc. Each of these measured parameters is in approximate agreement with the values observed in the Milky Way (Rix & Bovy 2013).

High-resolution studies of the nearby Milky Way-like flocculent spiral galaxies NGC 628 and NGC 4254 provide a qualitative point of comparison for the morphology of our HI gas (see Walter et al. 2008), molecular gas (see Sun et al. 2018) and young stars (see Kreckel et al. 2018). In particular, we find that our maps of the molecular gas surface density (top row of Figure 6) are similar in structure to the sub kpc-scale observations of the CO emission in both NGC 628 and NGC 4254. Our maps of the young stellar surface density (central row of Figure 6) may likewise be compared to to the sub kpc-scale structure of the H-α emission in NGC 628, while its observed HI gas profile resembles the structure of the HI gas disc for the FLAT simulation in particular (top left-hand panel of Figure 6).

3.1.2 *Spatial decorrelation between molecular gas and stars*

By contrast with the tight correlation observed between molecular gas and tracers of star formation on galaxy scales (e.g. Kennicutt 1998), a spatial decorrelation between CO clouds and HII regions is observed in nearby galaxies (e.g. Schruba et al. 2010; Kreckel et al. 2018; Kruijssen et al. 2019b; Schinnerer et al. 2019; Chevance et al. 2020b). This spatial decorrelation has been explained by the fact that individual regions in galaxies follow evolutionary lifecycles independent from those of their neighbours, during which clouds assemble, collapse, form stars, and are disrupted by stellar feedback (e.g. Feldmann et al. 2011; Calzetti et al. 2012; Kruijssen & Longmore 2014; Kruijssen et al. 2018). Although in Section 3.1.1 we have found qualitative similarities between our simulations and observations, we note that Fujimoto et al. (2019) also reproduce the observed morphologies of the H_2, HI and stellar components in galaxies like the Milky Way and NGC 628, but fail to correctly capture the spatial decorrelation between young stellar regions and dense molecular gas on small scales. We apply the same analysis as Fujimoto et al. (2019) to the maps of Σ_{H_2} and Σ_{SFR} for our galaxies, degraded in spatial resolution via convolution with a Gaussian kernel of FWHM = 50 pc. The result is illustrated in Figure 8. In summary, we measure the gas-to-stellar flux ratio enclosed in apertures centred on H_2 peaks (top branch) and SFR peaks (bottom branch), for aperture sizes ranging between the native resolution of the convolved maps (50 pc) and large scales (4000 pc). More details about the method can be found in Kruijssen & Longmore (2014) and Kruijssen et al. (2018). Figure 8 shows that our galaxies span approximately a factor 2 in the gas-to-SFR flux ratio. Therefore, by contrast with Fujimoto et al. (2019), we find a similar gas-to-stellar decorrelation as is observed in several nearby disc galaxies by Chevance et al. (2020b), which show gas-to-SFR flux ratios in the range $[0.3, 0.5]$ for cloud-scale apertures ($\sim 30 - 150$ pc) centred on stellar peaks and in the range $[1.3, 5.5]$ for cloud-scale apertures centred on gas peaks. Following the formalism of Kruijssen et al. (2018), this spatial decorrelation can be used to probe the evolutionary timeline of GMCs and star-forming regions. This will be investigated in more detail in Jeffreson et al. (prep).

3.2 Star formation

In Figure 10, we show the total galactic star formation rate as a function of simulation time t for each isolated disc galaxy. Following the initial vertical collapse of the disc and the subsequent star formation 'burst' from $t \sim 30$ Myr to $t \sim 250$ Myr, the SFR settles down to a rate of $\sim$ 2-4 M$_\odot$ yr^{-1}. We make absolutely sure to consider each isolated disc in its equilibrium state by examining the cloud population during a later time interval, between $t = 600$ Myr and $t = 1$ Gyr (grey-shaded region). Over this period, the SFR declines only gradually, by a total of around 0.5 M$_\odot$ yr^{-1}. These values are consistent with the current observed SFR in the Milky Way (Murray & Rahman 2010; Robitaille & Whitney 2010; Chomiuk & Povich 2011; Licquia & Newman 2015). We may also consider the resolved star-forming behaviour on scales of 750 pc,

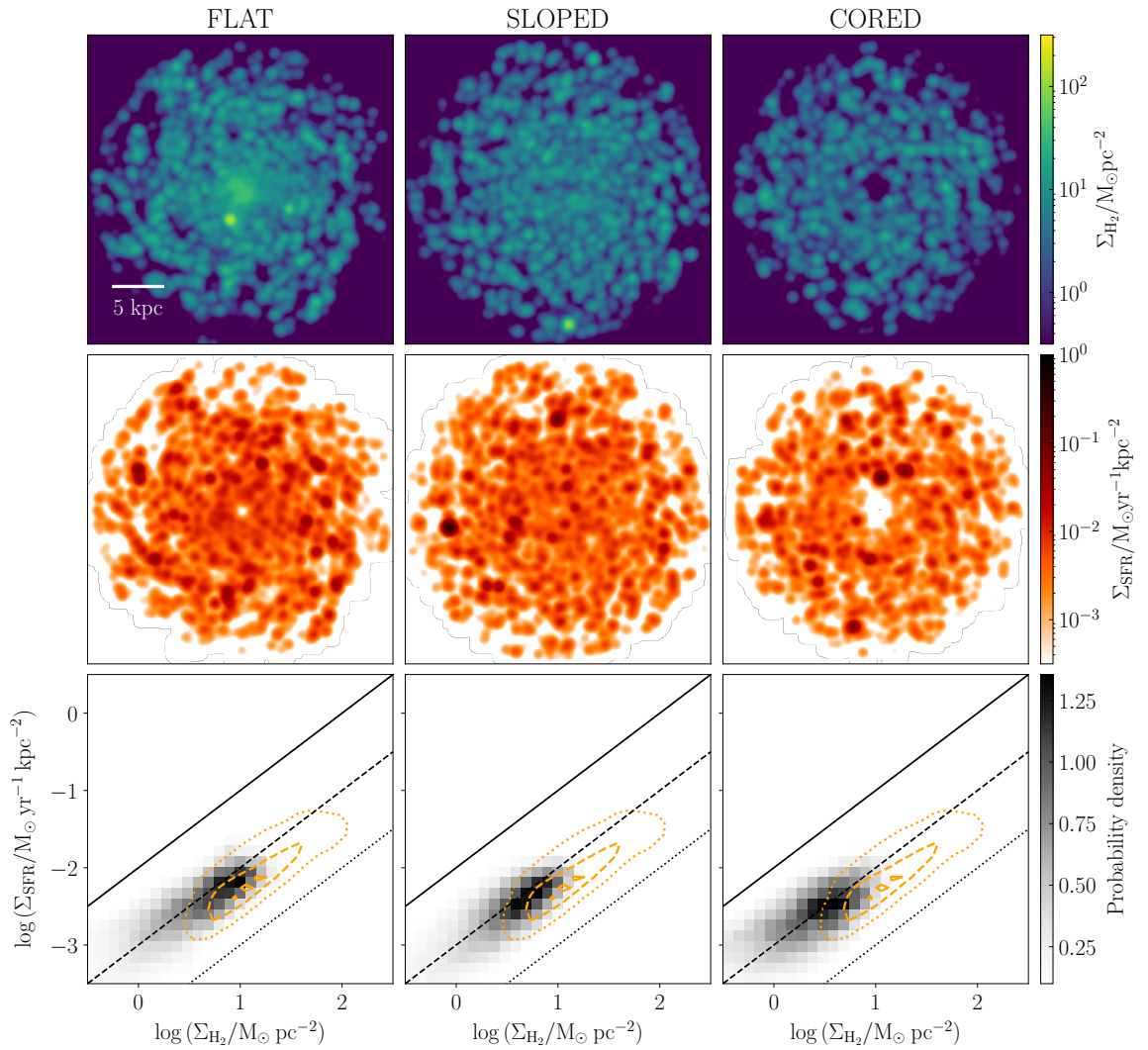

Figure 9. *Top row:* CO-bright molecular gas surface density Σ_{H_2} for each galactic disc, degraded to a spatial resolution of 750 pc. *Middle row:* Star formation rate surface density Σ_{SFR} for each galactic disc, degraded to a spatial resolution of 750 pc. *Bottom row:* Pixel density as a function of Σ_{H_2} and Σ_{SFR} for each disc, corresponding to the resolved molecular star-formation relation of Kennicutt (1998). Gas depletion times of 10^8, 10^9 and 10^{10} Myr are given by the black solid, dashed and dotted lines respectively. The orange contours encircle 90 per cent (dotted), 50 per cent (dashed) and 10 per cent (solid) of the observational data for nearby galaxies from Bigiel et al. (2008). All maps are computed at a simulation time of 600 Myr.

as studied in nearby galaxies by Bigiel et al. (2008). In Figure 9, we display the star formation rate surface density as a function of gas surface density for each of our simulated galaxies, at a simulation time of 600 Myr. The top row shows the 2D projection maps of the CO-bright molecular gas column density Σ_{H_2}. These are computed via the total gas column density in Equation (35) and degraded using a Gaussian filter of FWHM $=$ 750 pc. The corresponding projections of the star formation rate surface densities Σ_{SFR} are displayed in the central row. Details for the production of all maps are given in Appendix A. In the bottom row, the values of Σ_{H_2} and Σ_{SFR} in each pixel of the spatially-degraded projection maps are compiled to produce a single histogram. The loci of our simulation data fall close to the observed star formation relations obtained by Bigiel et al. (2008), denoted by the orange contours, though with a population of points at lower densities and star formation rates than are reached by the observations. These points arise because we consider all CO-emitting gas down to a molecular hydrogen surface density of $\Sigma_{H_2} = 10^{-3.5} M_\odot pc^{-2}$ (see Figure 4). This avoids taking an arbitrary cut on Σ_{H_2}, but also captures much lower levels of CO emission than could be detected by current observatories.

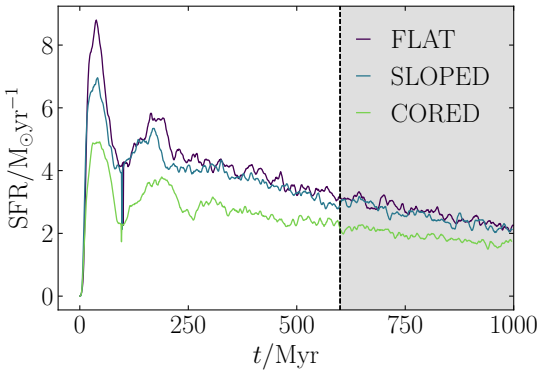

Figure 10. Global galactic star formation rate as a function of simulation time for each galactic disc. The grey shaded region indicates the simulation times 600 Myr-1 Gyr at which we sample the cloud population.

3.3 Resolved disc stability

Our simulated discs have approximately-uniform values of the line-of-sight velocity dispersion $\sigma_{\rm los,g}$ and the surface density $\Sigma_{\rm g}$ for atomic and molecular gas. The radial profiles for $\sigma_{\rm los,g}$ and $\Sigma_{\rm g}$ in each galaxy are displayed in the upper two panels Figure 11, computed in 50 overlapping bins of width 1 kpc. Only the gas component with temperature $\leqslant 10^4$ K is considered, and the line-of-sight turbulent velocity dispersion is calculated according to

$$\sigma^2_{{\rm los},g} = \frac{\langle |\mathbf{v}_i - \langle \mathbf{v}_i \rangle|^2 \rangle}{3}, \tag{37}$$

where $\{\mathbf{v}_i\}$ are the velocity vectors of the gas cells in each radial bin, and angled brackets denote mass-weighted averages over these cells. The gas sound speed $c_{\rm s} = \sqrt{k_{\rm B}T/\mu m_{\rm H}} \sim 6$ kms^{-1} for our galaxies (dashed lines in the upper panel) is consistent with the observed temperature of the neutral ISM phases in the Milky Way (e.g. Kalberla & Kerp 2009). Similarly, our combined turbulent/thermal velocity dispersion $\sqrt{c_{\rm s}^2 + \sigma_{\rm los,g}}$ (solid lines in the upper panel) also falls squarely within the observed range of $\sim 10 \pm 2$ kms^{-1} (Tamburro et al. 2009). Our total gas surface densities (solid lines in the central panel) are inside the observed range of 7 to 11 M$_\odot$ pc^{-2} for galactocentric radii between 3 and 16 kpc in the Milky Way (Yin et al. 2009). Our molecular hydrogen surface densities (dashed lines in the central panel) fall between values of 1 and 4 M$_\odot$ pc^{-2} for galactocentric radii from 2 to 10 kpc, in agreement with the Milky Way values from Figure 1 of Wolfire et al. (2003) and Figure 7 of Kennicutt & Evans (2012). Finally, the lower panel of Figure 11 demonstrates that our values for the Toomre Q parameter agree with the observed values in the discs of spiral galaxies, which are seen to vary across the range of $Q \sim [1, 10]$ (Leroy et al. 2008).

3.4 ISM phase structure

The top panel of Figure 12 displays the mass-weighted distribution of the gas temperature as a function of the gas volume density (phase diagram) for the FLAT simulation. The distribution is peaked along the 'thermal equilibrium curve': the state of thermal equilibrium in which the rate of cooling (dominated by line emission from C^+, O and Si^+) balances the heating rate due to photoelectric emission from dust grains and PAHs. The position

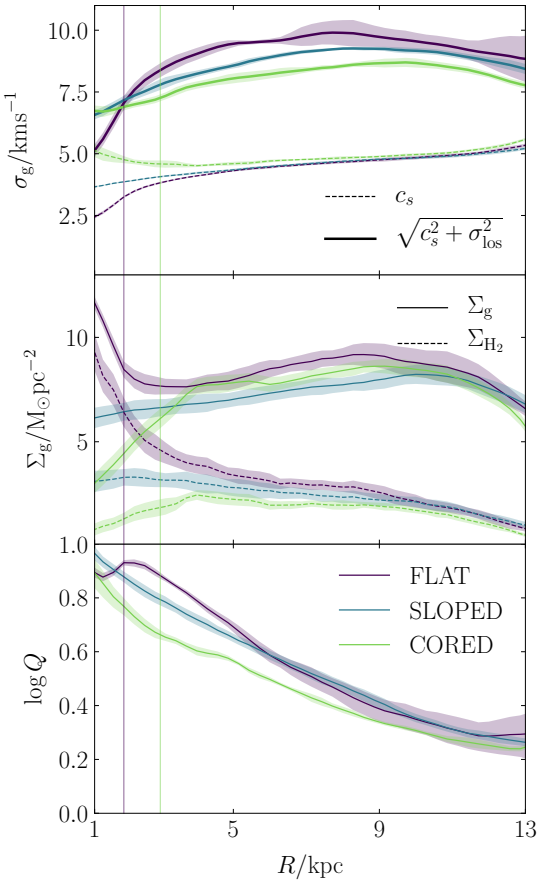

Figure 11. Azimuthally- and temporally-averaged cold-gas ($\leqslant 10^4$ K) velocity dispersion (upper panel), column density (centre panel) and Toomre Q parameter (lower panel) as a function of the galactocentric radius for each simulated galaxy, across the simulation time interval from 600 Myr to 1 Gyr. The thermal c_s and total (thermal plus turbulent) velocity dispersions are denoted by the dashed and solid lines, respectively. The vertical lines denote the minimum radii for cloud identification for the FLAT and CORED simulations (see Section 4.3).

of our thermal equilibrium curve matches the analysis of Wolfire et al. (2003), who studied the thermal structure of the ISM in the Milky Way. It also agrees with the thermal evolution expected from SGCHEM live chemistry, according to Glover & Mac Low (2007a,b). Along the curve, the gas can be divided into four major components: the warm neutral medium (WNM), the thermally-unstable phase (Unstable), the cold neutral medium (CNM) and the star-forming gas (SF). The non-equilibrium components of the gas, heated by stellar feedback from supernovae (SN) and HII regions (HII), fall above the thermal equilibrium curve. In particular, the horizontal line at $T \sim 7000$ K is formed from gas cells heated by HII region feedback, as described in Section 2.6.3. The phase structure of the gas in our simulations agrees closely with the isolated galaxy simulations of Goldbaum et al. (2016), as well as those of Hopkins et al. (2012); Agertz et al. (2013); Keller et al. (2014); Fujimoto et al. (2018), all of which use similar feedback models to ours. In the lower panel of Figure 12, we display the partitioning

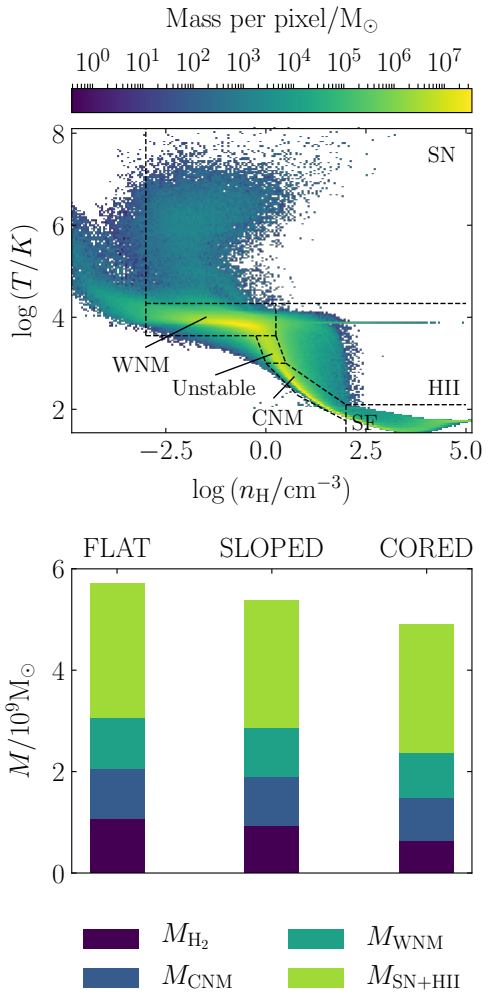

Figure 12. *Upper panel:* Density-temperature phase diagram for the FLAT simulation run at a simulation time of 600 Myr. Dashed lines delineate the regions of phase-space corresponding to the warm neutral medium (WNM), the thermally-unstable phase (Unstable), the cold neutral medium (CNM), gas heated by supernovae (SN), gas heated by HII regions (HII) and star-forming gas (SF). *Lower panel:* Partitioning of the gas mass in each galaxy simulation into four ISM phases from warmest to coolest: hot gas that has received thermal energy from stellar feedback ($M_{\rm SN+HII}$), the warm neutral medium ($M_{\rm WNM}$), the cold neutral medium ($M_{\rm CNM}$), and the star-forming gas in the molecular phase ($M_{\rm H_2}$).

of gas mass between the phase components in the upper panel. The mass of CO-traced molecular gas ($M_{\rm H_2}$) is calculated using the DESPOTIC model described in Section 2.8, and approximately equals the mass of star-forming gas (SF) in the upper panel. For all simulated discs, around half of the total gas mass is partitioned approximately-equally between the molecular, CNM and WNM components, such that $M_{\rm H_2}/(M_{\rm CNM}+M_{\rm WNM}) \in \{0.3, 0.4, 0.3\}$ for the FLAT, SLOPED and CORED simulations, in agreement with Saintonge et al. (2011).

Although the mass reservoirs for each of the phases described above are relatively static over the simulation times from 600 to 1000 Myr examined here, there exists an ISM baryon cycle that continually shifts gas between star-forming and non-star-forming phases, as explored in Semenov et al. (2017, 2018, 2019); Chevance et al. (2020a). The time spent in each of these reservoirs sets the global star-forming properties of the ISM (e.g. gas depletion times and SFEs). In this work, we examine the time-independent properties of GMCs and their relation to the large-scale galactic-dynamical environment. In a follow-up paper (Jeffreson et al. subm), we explore the influence of galactic dynamics on the time-evolving GMC lifecycle, and relate these findings to the environmental variation in the ISM baryon cycle.

4 THEORY

In Jeffreson & Kruijssen (2018), we introduced an analytic theory that quantifies the influence of galactic dynamics on molecular cloud evolution. Here we provide an overview of the theory, and explain how the environmental parameter space spanned by its variables is used to reveal the presence of galactic-dynamical trends in the physical properties of our simulated GMCs.

4.1 Dynamical time-scales for GMC evolution

In Jeffreson & Kruijssen (2018), the time-averaged influence of galactic dynamics on the evolution and destruction of GMCs is determined by the five dynamical time-scales for gravitational free-fall in the galactic mid-plane ($\tau_{\rm ff,g}$), galactic shear (τ_β), spiral-arm interactions ($\tau_{\Omega_{\rm P}}$), cloud-cloud collisions ($\tau_{\rm cc}$) and orbital epicyclic perturbations (τ_κ). With the exception of the time-scale for spiral arm perturbations, which is not relevant for the flocculent discs simulated in this work, each time-scale is defined in terms of its physical variables in Table 2. Here, Ω is the angular velocity of the mid-plane ISM around the galactic centre, and the galactic shear parameter is defined by

$$\beta = \frac{{\rm d}\ln v_c}{{\rm d}\ln R}, \tag{38}$$

for a circular velocity $v_{\rm c}(R)$ at galactocentric radius R. The Toomre (1964) Q parameter for the gravitational stability of the mid-plane gas is given by

$$Q = \frac{\kappa\sqrt{\sigma_{\rm g}^2 + c_{\rm s}^2}}{\pi G \Sigma_{\rm g}}, \tag{39}$$

with an epicyclic frequency κ, a mid-plane gas velocity dispersion $\sigma_{\rm g}$, a mid-plane sound speed $c_{\rm s}$, and a mid-plane gas surface density $\Sigma_{\rm g}$. The variable ϕ_P quantifies the relative gas and stellar contributions to the mid-plane hydrostatic pressure $P_{\rm mp} = \pi G \phi_{\rm P} \Sigma_{\rm g}^2/2$, defined in Elmegreen (1989) as

$$\begin{aligned} \phi_P &= 1 + \frac{\Sigma_{\rm s}}{\Sigma_{\rm g}}\frac{\sigma_{\rm g}}{\sigma_{\rm s}} \\ &\approx 1 + \frac{\sigma_{\rm g}}{\Sigma_{\rm g}}\sqrt{\frac{2\rho_{\rm s}}{\pi G}}. \end{aligned} \tag{40}$$

Here, $\sigma_{\rm s}$, $\Sigma_{\rm s}$ and $\rho_{\rm s}$ denote the stellar velocity dispersion, surface density, and volume density, respectively. The second approximate equality is obtained by assuming that the scale-height of the stellar disc is much larger than the gas disc scale-height, so that the stellar disc maintains its own state of collisionless equilibrium, $\Sigma_{\rm s} = \sigma_{\rm s}\sqrt{2\rho_{\rm s}/\pi G}$ (c.f. Blitz & Rosolowsky 2004). The

Table 2. The dynamical time-scales used in the cloud lifetime theory of Jeffreson & Kruijssen (2018) and their physical interpretations.

Time-scale	Physical meaning	Analytic form	Physical variables
τ_κ	Time-scale for a molecular cloud to make a 'maximal' orbital excursion along the galactic radial direction (defined as one quarter of the average orbital radius).	$\frac{4\pi}{\Omega\sqrt{2(1+\beta)}}\frac{1}{\sqrt{3+\beta}}$	Ω, β
$\tau_{\rm ff,g}$	Time-scale for the gravitational collapse of the ISM on sub-Toomre length scales, as in Krumholz et al. (2012).	$\sqrt{\frac{3\pi^2}{32\phi_P(1+\beta)}}\frac{Q}{\Omega}$	Q, Ω, β, ϕ_P
$\tau_{\rm cc}$	Average time-scale between cloud collisions (Tan 2000).	$\frac{2\pi Q}{9.4 f_G \Omega(1+0.3\beta)(1-\beta)}$	Q, Ω, β
τ_β	Time-scale for a spherical GMC to become ellipsoidal under the influence of galactic differential rotation (shear-induced azimuthal offset across the cloud becomes equal to its radial extent).	$\frac{2}{\Omega(1-\beta)}$	Ω, β

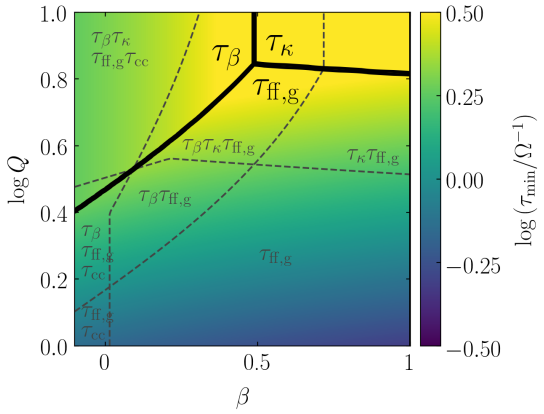

Figure 13. The minimum of the four galactic-dynamical time-scales for gravitational free-fall ($\tau_{\rm ff,g}$), galactic shear (τ_β), cloud-cloud collisions ($\tau_{\rm cc}$), and orbital epicyclic perturbations (τ_κ), normalised by the orbital period of the galaxy Ω^{-1}, as a function of the galactic-dynamical parameters β and Q. The solid black contours delineate the regions of parameter space in which each of the time-scales is shortest, and so has the greatest potential to influence molecular cloud evolution. The dashed grey contours delineate the regions for which each time-scale is shorter than twice the minimum dynamical time-scale ($\tau > 2\tau_{\rm min}$), or else shorter than twice the cloud lifetime ($\tau > 2\tau_{\rm life}$), if $\tau_{\rm life} > \tau_{\rm min}$. They provide a rough indication of the parameter space regions in which multiple dynamical mechanisms are likely to influence molecular cloud evolution. The positions of all contours are determined for the fiducial value of $\phi_{\rm P} = 3$.

cloud-cloud 'collision probability' parameter $f_{\rm G}$ is defined and constrained by comparison to observations in Tan (2000).

All of the time-scales in Table 2 depend inversely on the angular velocity Ω. As such, they can be compared within a parameter space spanned by the four physical variables β, Q, $\phi_{\rm P}$ and f_G. Of these, we fix $f_G = 0.5$ to its fiducial value. Jeffreson & Kruijssen (2018) therefore describes the influence of galactic dynamics on GMC evolution within a fundamental parameter space spanned by β, Q and $\phi_{\rm P}$. This parameter space is displayed in Figure 13 for Milky Way-like environments, with $\beta \in [0, 1]$, $\log Q \in [0, 10]$, and $\phi_{\rm P} = 3$. The minimum galactic-dynamical time-scale $\tau_{\rm min} = \min\left(\tau_{\rm ff,g}, \tau_\beta, \tau_\kappa, \tau_{\rm cc}\right)$ is shown in colour, and we indicate the regions of parameter space in which each time-scale is shorter than all others, such that its corresponding dynamical process has the dominant influence on cloud evolution (solid black lines). With the grey dashed contours, we also indicate the regions of parameter space over which the galactic-dynamical time-scales have comparable values, to within a factor of two. Formally, these contours appear for a time-scale τ where $\tau = 2\tau_{\rm min}$, or where $\tau = 2\tau_{\rm life}$, if the cloud lifetime $\tau_{\rm life}$ is shorter than the minimum dynamical time-scale $\tau_{\rm min}$, where the cloud lifetime is defined in Jeffreson & Kruijssen (2018) as the linear combination of dynamical Poisson rates, $\tau_{\rm life} = |\tau_{\rm ff,g}^{-1} - \tau_\beta^{-1} + \tau_{\rm cc}^{-1} + \tau_\kappa^{-1}|^{-1}$. In this expression, we assume a simple form for the support provided by galactic shear against gravitational collapse, so that τ_β^{-1} is subtracted from $\tau_{\rm ff,g}^{-1}$.

4.2 Choice of Toomre Q parameter

In this work, we use the Toomre Q stability parameter associated with the gaseous component of the interstellar medium, and do not include the influence of the stellar component as described in Elmegreen (1995). We do this for two reasons. Practically, we use an external background potential in our simulations to model the gravitational force due to the stellar disc and stellar bulge (see Section 2.2). The live stellar particles formed during the simulation make up only 6 per cent of the stellar mass, at maximum. We are therefore unable to obtain an accurate estimate of the stellar velocity dispersion from our simulations. Physically, the use of a background potential also means that the stellar component cannot respond dynamically to the growth of gravitational instabilities, such that the gas-only Toomre Q parameter is the best quantification of dynamical instability in our simulations. Both of the above considerations make the gas-only Toomre Q the natural choice to compare the analytic theory presented here to the numerical results presented in Section 5.

4.3 Simulated galaxies in galactic-dynamical parameter space

Our galaxies resemble the Milky Way in their total masses ($\sim 10^{12}$ M$_\odot$), gas masses ($\sim 6 \times 10^9$ M$_\odot$), and total gas disc scale-lengths (~ 7 kpc), but cover a range of different galactic-dynamical environments. Galactic-dynamical variation is induced via differences in the external gravitational potential (see Table 1), leading to variations in the circular velocities and scale-heights of the gas discs. Figure 14 presents the span of our simulations within the galactic-dynamical parameter space of Jeffreson & Kruijssen (2018). The two left-hand panels show the azimuthally- and temporally-averaged values of the circular velocity (top) and of the cold-gas scale-height (bottom) for each simulation, as a function of the galactocentric radius R. These profiles are computed in 50 overlapping environmental bins of width 1 kpc, between galactocentric radii of $R = 1$ kpc and $R = 13$ kpc. The temporal standard deviation is indicated by the translucent shaded regions. In the

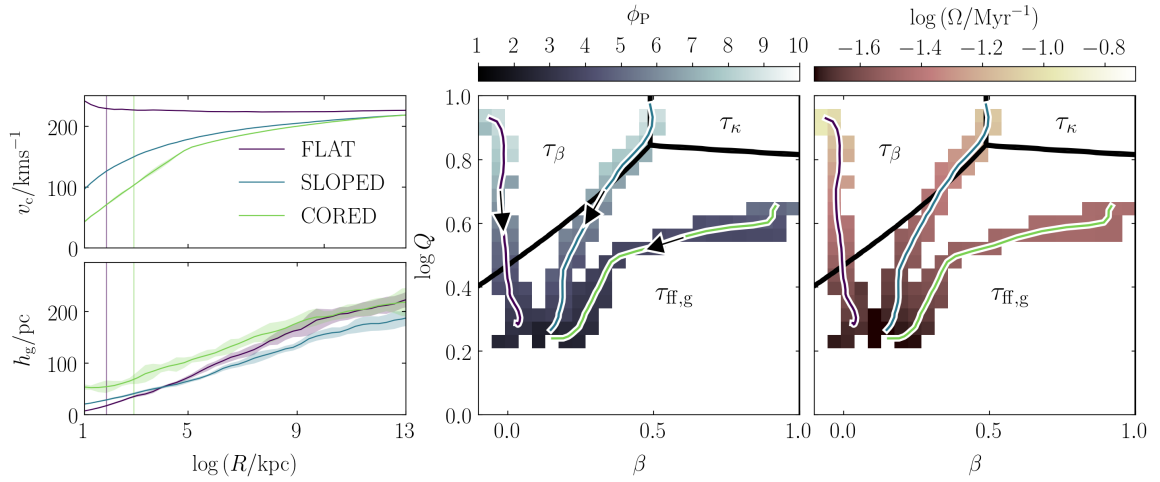

Figure 14. *Left:* Circular velocity v_c (upper panel) and cold-gas ($\leqslant 10^4$ K) scale-height $h_{\rm g}$ (lower panel) for each simulated galaxy as a function of the galactocentric radius, averaged over the time interval from 600 Myr to 1 Gyr (solid lines). The temporal standard deviation at each radius is given by the translucent shaded regions, and the vertical lines denote the radial cuts for cloud identification (see Section 4.3). *Centre:* Median value of the $\phi_{\rm P}$ parameter in each simulation as a function of the shear β and Toomre Q parameters. The black arrows mark the direction in which the galactocentric radius increases. *Right:* Median value of the galactic angular velocity Ω in each simulation as a function of β and Q. The temporally-averaged radial trajectories of each disc through the parameter space are denoted by the solid lines, and all values are compiled on the time interval from 600 Myr to 1 Gyr. The black solid lines enclose the regions of parameter space for which the minimum dynamical time-scale is τ_κ (orbital epicyclic perturbations), τ_β (galactic shear) and $\tau_{\rm ff,g}$ (gravitational free-fall).

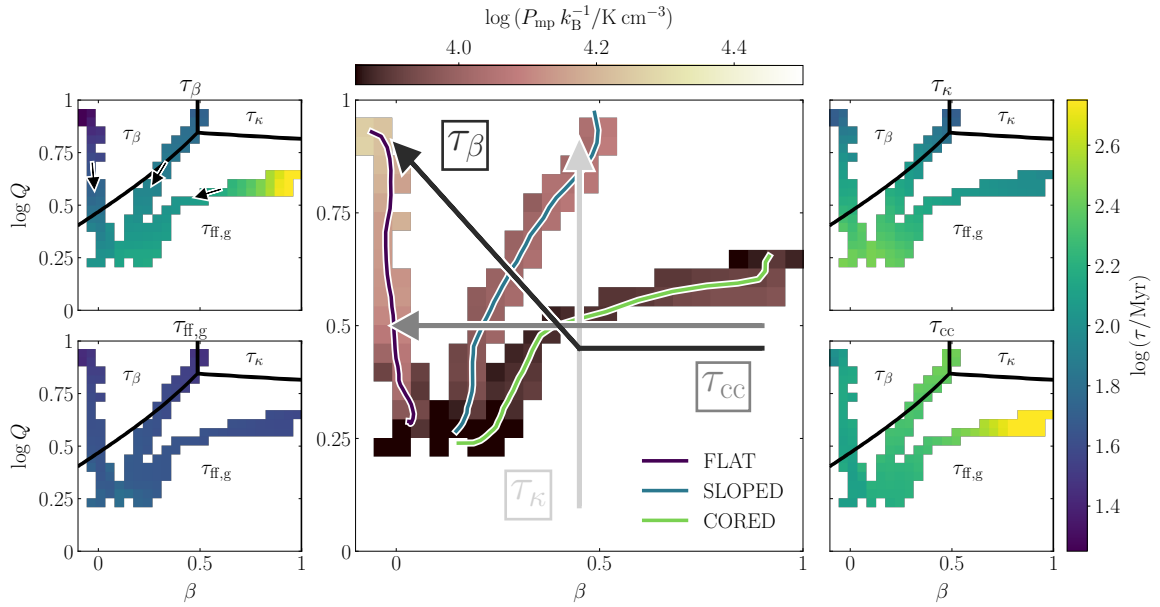

Figure 15. Mid-plane pressure ($P_{\rm mp}$, centre) and dynamical time-scales for galactic shear (τ_β, upper left), gravitational free-fall ($\tau_{\rm ff,g}$, lower left), orbital excursions (τ_κ, upper right) and cloud-cloud collisions ($\tau_{\rm cc}$, lower right), as a function of the shear parameter β and the Toomre Q stability parameter, i.e. across the galactic-dynamical parameter space of Jeffreson & Kruijssen (2018). The black arrows mark the direction in which the galactocentric radius increases. All quantities are compiled over the time interval from 600 Myr to 1 Gyr, and the time-scales are defined quantitatively in Table 2. The central panel additionally shows a schematic for the direction in which each dynamical rate *increases* (time-scale *decreases*), so becomes *more likely* to influence GMC evolution, along with solid lines denoting the positions of the FLAT, SLOPED and CORED galaxies.

two right-hand panels, we show the azimuthally- and temporally-averaged values of the parameters β and Q for each galaxy as solid lines of matching colour. We achieve the mapping $R \rightarrow (\beta, Q)$ by constructing the azimuthally-averaged profiles of β and Q for each galaxy, using the same 50 overlapping bins. We then plot Q as a function of β, where the black arrows in the central panel denote the direction in which R increases. Further details on the computation of each radial profile are given in Appendix A.

The locus of the simulated GMC population on the time interval from 600 Myr to 1 Gyr is indicated by the spread of (β, Q) bins behind each solid line. We sample both the cloud population and the radial profiles of β, Q, Ω and $\phi_{\rm P}$ at time intervals of 50 Myr, treating each snapshot as a distinct population of clouds.[5] We calculate the position of each cloud in the parameter space by interpolating the smooth radial profiles of the four environmental variables β, Q, Ω and $\phi_{\rm P}$ at the galactocentric radius of the cloud centre of mass. Via this method, we retrieve a cumulative total of $\sim 80,000$ molecular clouds and $\sim 55,000$ HI clouds across the three simulations. The spread of the environmental bins behind each temporally-averaged solid line arises due to the small but significant temporal variation in the Toomre Q profile (recall Figure 11). On the scale of 1 kpc used to compute the environmental variables, the azimuthal variation in the value of the Toomre Q parameter is negligible relative to its temporal variation, owing to the approximate axisymmetry of our simulated discs. In Figure 14 and in every following appearance of the parameter space, we show only those bins that contain $\geqslant 100$ GMCs, ensuring that a sufficiently-large distribution of clouds is present in each galactic-dynamical environment to reliably compute a mean and a standard deviation for each cloud property. We note that for the FLAT and CORED simulations, we take stricter minimum radii of $R = 2$ kpc and $R = 3$ kpc for cloud identification, respectively, indicated by the vertical lines that cut through the radial profiles in Figures 11 and 14. We do this to exclude the ring of zero star-formation at $R \sim 1$ kpc in the FLAT simulation, and to exclude the very low inner surface densities for the CORED simulation.

The colours of the pixels in the two right-hand panels of Figure 14 correspond to the mean values of the $\phi_{\rm P}$ parameter (blue pixels) and the orbital angular velocity Ω (pink pixels). Together, we see that the simulated galaxies span approximately an order of magnitude in the Toomre Q stability parameter ($\log Q \in [0.2, 1]$), the angular velocity ($\log (\Omega / {\rm Myr}) \in [-1.75, -0.75]$), and the parameter $\phi_{\rm P} \in [1, 9]$, and cover the full range of galactic shear parameters from $\beta \sim 0$ (flat rotation curve) to $\beta = 1$ (solid-body rotation). We note that the parameter $\phi_{\rm P}$ appears only in the time-scale for gravitational free-fall, to the power $1/2$. In determining the regions of parameter space for which each dynamical time-scale is minimum (enclosed by the solid black lines), we therefore set $\phi_{\rm P} \sim 3$, corresponding to its environment-averaged mean value.

Figure 14 shows that both Ω and $\phi_{\rm P}$ increase monotonically with the Toomre Q parameter. The relation between Q and Ω is almost linear, because the kpc-scale velocity dispersion and surface density of the gas disc are roughly constant with galactocentric radius (see Section 3.3), leaving the gravitational stability to vary with the degree of centrifugal support (Toomre 1964), which is proportional to Ω. This degeneracy between Ω and Q has the important consequence that the ratio Q/Ω is roughly constant across all simulated environments, such that the time-scale $\tau_{\rm ff,g}$ varies only by a factor of two from 25 up to 50 Myr across galactic-dynamical parameter space.

[5] In a companion paper Jeffreson et al. (subm), we study the time evolution of GMCs and find that their lifetimes have a maximum value of $\sim$ 40-50 Myr. As such, we can be confident that there are very few duplicate clouds in our sample.

4.4 Simulated galaxies and their galactic-dynamical time-scales

In Figure 15 we show the variation in the galactic-dynamical time-scales for galactic shear (τ_β, top left panel), gravitational free-fall ($\tau_{\rm ff,g}$, bottom left panel), epicyclic perturbations (τ_κ, top right panel) and cloud-cloud collisions ($\tau_{\rm cc}$, bottom right panel) across the environments spanned by our three simulations. The direction in which each time-scale decreases in value (and so the rate of the associated dynamical process increases) is indicated by the arrows in the central panel. We can make the following key observations.

(i) The galactic-dynamical environments spanned by our simulations are partitioned between two regimes: a 'gravity-dominated regime' for which the gravitational free-fall time-scale $\tau_{\rm ff,g}$ is the shortest dynamical time-scale, and a 'shear-dominated regime' for which the time-scale τ_β for galactic shearing is the shortest.

(ii) $\tau_{\rm ff,g}$ is always close in value to the shortest dynamical time-scale, even in environments for which τ_β is the shortest time-scale.

(iii) $\tau_{\rm ff,g}$ varies over a small dynamic range of just ~ 0.4 dex across our Milky Way-pressured environments.

(iv) τ_κ and $\tau_{\rm cc}$ are around an order of magnitude longer than the free-fall time-scale across all simulated environments, and so epicyclic perturbations and cloud-cloud collisions are not likely to be significant drivers of cloud properties, relative to gravitational free-fall and galactic shearing.

The time-scale for gravitational free-fall is short across our simulated environments, but has a small dynamic range. In the following, we also consider the mid-plane hydrostatic pressure $P_{\rm mp} = \pi G / 2 \phi_{\rm P} \Sigma_{\rm g}^2$ (see Elmegreen 1989) and Blitz & Rosolowsky (2004), which is closely related to the free-fall time, as

$$\tau_{\rm ff,g} = \sigma_{\rm g} \sqrt{\frac{3\pi}{32 G P_{\rm mp}}}, \tag{41}$$

but has a greater dynamic range across our sample of galactic environments. The variation in $P_{\rm mp}$ across the galactic-dynamical parameter space of Jeffreson & Kruijssen (2018) is shown in the central panel of Figure 15.

5 GALACTIC-DYNAMICAL TRENDS IN CLOUD PROPERTIES

In this section, we analyse the physical properties of the GMC and HI cloud populations across the FLAT, SLOPED and CORED galaxies at simulation times from 600 Myr to 1 Gyr. We consider the variation of the mean for each property as a function of its galactic-dynamical environment in the parameters β, Q, Ω and $\phi_{\rm P}$, demonstrating the interplay between stabilising dynamical influences (galactic rotation and pressure) and de-stabilising dynamical influences (gravity) in driving the evolution of clouds. We find that the variation of GMC and HI cloud properties across this parameter space indicates the presence of statistically-significant correlations between these properties and the key galactic-dynamical time-scales τ_β and $\tau_{\rm ff,g}$, as well as with the mid-plane pressure $P_{\rm mp}$.

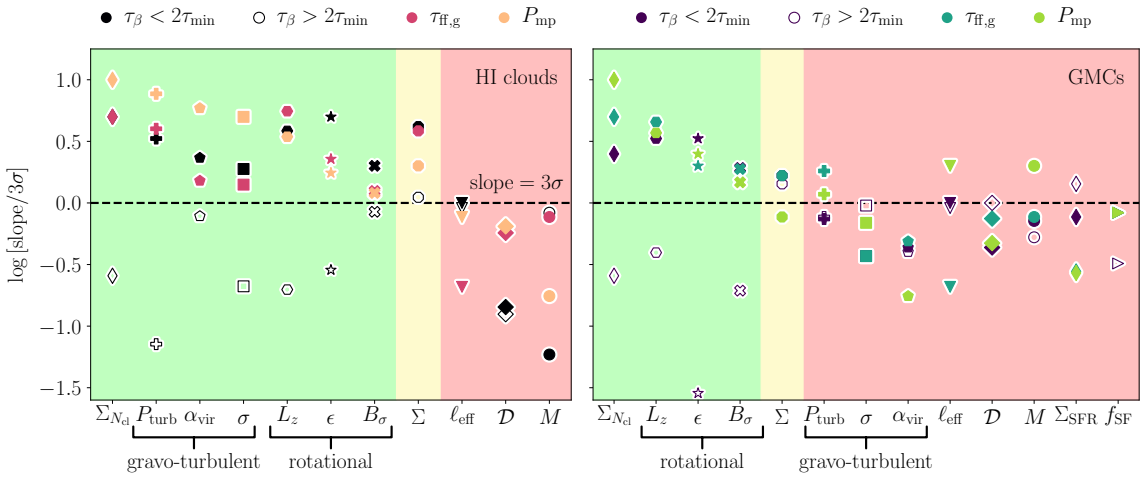

Figure 16. Summary of the correlations investigated in this work between galactic-dynamical quantities (top legend) and the properties (x-axis) of HI clouds (left) and GMCs (right). The y-axis gives the slope of each correlation, divided by its 3σ variation. The dashed line divides the trends that are significant on the 3σ level (above) from those that are not (below). The clouds are ordered so that the net significance of the dynamical correlations decreases towards the right. For both types of clouds, the green shaded region highlights the cloud properties that display galactic-dynamical correlations with τ_β, $\tau_{\rm ff,g}$ and $P_{\rm mp}$ at the 3σ significance level. The red shaded region highlights the cloud properties that display significant correlations with at most one of these time-scales. The yellow-shaded region highlights cloud properties that display significant correlations, but over a very small dynamic range (< 0.05 dex for the HI cloud and GMC surface densities). Correlations with the time-scale τ_β for galactic shearing are divided into two distinct regimes: one in which the shear time-scale is less than twice the minimum evolutionary time-scale (filled points), and one in which it is greater than twice the minimum evolutionary time-scale (unfilled points). We note that for cloud properties with significant galactic-dynamical trends in τ_β, $\tau_{\rm ff,g}$ and $P_{\rm mp}$, there exists a clear break between the two regimes.

Table 3. Summary of the environmental trends in GMC properties that are discussed in Section 5. For each cloud property, we give the global mean value, the span (lowest-highest) of mean values across the $(\beta, Q, \Omega, \phi_{\rm P})$ parameter space, and the environmental trends followed by each property, when the correlation is significant at the 3σ confidence level. In the two right-most columns we give the Section in which each GMC property is discussed, along with the Figure showing its galactic-dynamical trend.

Cloud property/unit	Symbol	Mean		Span of mean values		3σ correlation		Sec.	Fig.
		H_2	HI	H_2	HI	H_2	HI		
Mass/$10^5 M_\odot$	M	1.3	0.65	$1.0 \rightarrow 1.7$	$0.49 \rightarrow 1.3$	None	None	5.2	–
Size/pc	$\ell_{\rm eff}$	24	65	$22 \rightarrow 26$	$51 \rightarrow 80$	None	None	5.2	–
Surface density/$M_\odot pc^{-2}$	Σ	226	16	$202 \rightarrow 254$	$14 \rightarrow 18$	Marginal		5.3	18
Velocity dispersion/kms^{-1}	σ	3.3	6.7	$2.8 \rightarrow 3.8$	$5.0 \rightarrow 8.1$	None	τ_β, $\tau_{\rm ff,g}$, $P_{\rm mp}$	5.3	18
Virial parameter	$\alpha_{\rm vir}$	1.2	22	$0.9 \rightarrow 1.5$	$12 \rightarrow 32$	None	τ_β, $\tau_{\rm ff,g}$, $P_{\rm mp}$	5.3	18
Turbulent pressure/$10^5 k_{\rm B}$ Kcm^{-3}	$P_{\rm turb}$	2.3	0.21	$1.9 \rightarrow 3.6$	$0.14 \rightarrow 0.36$	None	τ_β, $\tau_{\rm ff,g}$, $P_{\rm mp}$	5.3	18
Velocity divergence/kms^{-1}	$\mathcal{D}$	−1.0	−0.2	$-1.3 \rightarrow -0.6$	$-1.6 \rightarrow 0.6$	None	$\sigma_{\rm mp}$	5.4	–
Aspect ratio	ϵ	2.3	2.3	$1.9 \rightarrow 3.2$	$1.7 \rightarrow 3.1$	τ_β, $\tau_{\rm ff,g}$, $P_{\rm mp}$		5.5	21
Angular momentum/pc kms^{-1}	L_z	4.2	34	$3 \rightarrow 9$	$17 \rightarrow 101$	τ_β, $\tau_{\rm ff,g}$, $P_{\rm mp}$		5.5	22
Velocity anisotropy	B_σ	−0.5	−0.2	$-0.9 \rightarrow -0.3$	$-0.4 \rightarrow 0.1$	τ_β, $\tau_{\rm ff,g}$, $P_{\rm mp}$		5.5	23
No. clouds per unit area/kpc^{-2}	$\Sigma_{N_{\rm cl}}$	7.4	5	$2.9 \rightarrow 19$	$2.4 \rightarrow 18$	τ_β, $\tau_{\rm ff,g}$, $P_{\rm mp}$		5.6	24
SFR surface density/$M_\odot kpc^{-2} yr^{-1}$	$\Sigma_{\rm SFR,cl}$	0.63	–	$0.36 \rightarrow 0.89$	–	None	–	5.6	25
Fraction star-forming clouds	$f_{\rm SF}$	32%	–	$24\% \rightarrow 43\%$	–	None	–	5.6	25

5.1 Overview of galactic-dynamical correlations

In Figure 16 and Table 3, we summarise the galactic-dynamical correlations between all physical cloud properties analysed in this work and the dynamical variables τ_β, $\tau_{\rm ff,g}$ and $P_{\rm mp}$. The correlations themselves are presented in Appendix B, where we also describe in detail the procedures used for constraining the slope of each relationship. We find that at the 3σ confidence level, statistically-significant correlations are present in all three variables for $7/11$ HI cloud properties, and for $4/13$ GMC properties, shaded green in Figure 16. The y-axis in both panels gives the slope of the best-fit relationship between variables, divided by the 3σ variation on this slope. The statistically-significant correlations are therefore given by the points that fall above the dashed line. The red-shaded regions highlight the cloud properties that display statistically-significant correlations with fewer than three of the dynamical variables (none, in most cases). The yellow-shaded region highlights the cloud surface density Σ, which displays a significant correlation in all three variables for HI clouds, but over a very small dynamic range (< 0.05 dex). Figure 16 demonstrates the following three general results for our simulated cloud population.

(i) HI clouds display galactic-dynamical correlations in their gravo-turbulent cloud properties (internal turbulent pressures $P_{\rm turb}$, virial parameters $\alpha_{\rm vir}$ and velocity dispersions σ), but GMCs do not.

(ii) Both HI clouds and GMCs display statistically-significant galactic-dynamical correlations in their rotational cloud properties (aspect ratios ϵ, specific angular momenta L_z and velocity anisotropies B_σ).

(iii) There exist two distinct regimes for the time-scale τ_β for galactic shearing. The unfilled points in both panels represent the statistical significance of correlations between each physical cloud property and the shear time-scale, in galactic environments for which the shear time-scale is long (more than twice the length of the minimum dynamical time-scale, $\tau_\beta > 2\tau_{\rm min}$). For the dynamically-correlated cloud properties (green shaded regions in Figure 16) the break in the slope of the correlation between the two regimes manifests itself as a division of filled points ($\tau_\beta < 2\tau_{\rm min}$) and unfilled points ($\tau_\beta > 2\tau_{\rm min}$) across the dashed line. By contrast, the time-scale for gravitational free-fall $\tau_{\rm ff,g}$ has a very small dynamic range and so always remains close in value to the minimum dynamical time-scale. No such break is seen for dynamical correlations with $\tau_{\rm ff,g}$.

In the following sections we examine each cloud property in detail, and so shed light on the galactic-dynamical trends in the gravo-turbulent and rotational properties of GMCs and HI clouds.

5.2 Mass and size

The masses and sizes of GMCs and HI clouds in our simulations are not significantly correlated with the galactic dynamical environment. Their mean values are approximately invariant under changes in the galactic-dynamical time-scales τ_β and $\tau_{\rm ff,g}$, and in the mid-plane pressure $P_{\rm mp}$. On average, the molecular clouds are around three times smaller but two times more massive than the HI clouds in each environment, with a global mean diameter of 24 pc (relative to 65 pc for HI clouds) and a global mean mass of 1.3×10^5 M$_\odot$ (relative to 0.65×10^5 M$_\odot$ for HI clouds). In fact, it is plausible that the mean GMC diameter would appear even smaller at a higher simulation resolution, given that its average value is close to the minimum value of 18 pc enforced by our GMC identification criterion (see Section 2.9). The small mean size and high mean volume density of the identified GMCs relative to the HI clouds is consistent with the idea that in Milky Way-pressure galaxies like ours, the GMCs are high-density 'iceberg tips' poking up above the CO emissivity threshold.

In the upper panel of Figure 17, we demonstrate that the mass distribution of GMCs in each galaxy reproduces the upper limit of $\sim$ 3 to 8×10^6 M$_\odot$ observed by Rosolowsky et al. (2003) in M33, by Freeman et al. (2017) in M83 and by Miville-Deschênes et al. (2017) and Colombo et al. (2019) in the Milky Way. This upper limit has been predicted to arise due to a combination of centrifugal forces and stellar feedback (Reina-Campos & Kruijssen 2017). We also find a turnover in the mass spectrum between $10^{4.8}$ and 10^5 M$_\odot$, consistent with the behaviour of the GMC mass distribution in the Milky Way (Miville-Deschênes et al. 2017), although we cannot rule out the possibility that the turnover we see in the simulations is influenced by their limited mass resolution. Above the turnover, the GMC mass function has a power-law form with $\beta \sim 1.9$, close to the observed range of $\beta \in [1.6, 1.8]$ for clouds in the Milky Way (Solomon et al. 1987; Williams & McKee 1997; Heyer et al. 2009; Roman-Duval et al. 2010; Miville-Deschênes et al. 2017; Colombo et al. 2019) over the same mass range ($\log M \in [4.8, 6.5]$). In the lower panel of Figure 17, we display the spectrum of GMC sizes for each simulated galactic disc, given by the effective cloud radius $\ell_{\rm eff}$, such that

$$\ell_{\rm eff} = 1.91\sqrt{\Delta\ell^2_{\rm maj} + \Delta\ell^2_{\rm min}}, \tag{42}$$

where $\Delta\ell_{\rm maj}$ and $\Delta\ell_{\rm min}$ are the second moments of an ellipse fitted to the footprint of each cloud in the galactic mid-plane, using ASTRODENDRO. We adopt this definition of the cloud size in order to make a direct comparison to works in the existing observational literature (e.g. Solomon et al. 1987; Bertoldi & McKee 1992; Rosolowsky & Leroy 2006; Colombo et al. 2019). The factor of 1.91 is the correction first defined by Solomon et al. (1987) for converting the RMS cloud extent to an estimate of the spherical cloud size. The smallest resolved cloud has a diameter of 18 pc, so we do not capture the observed turnover of the distribution at $\sim$ 30 pc (Miville-Deschênes et al. 2017). Likewise, our

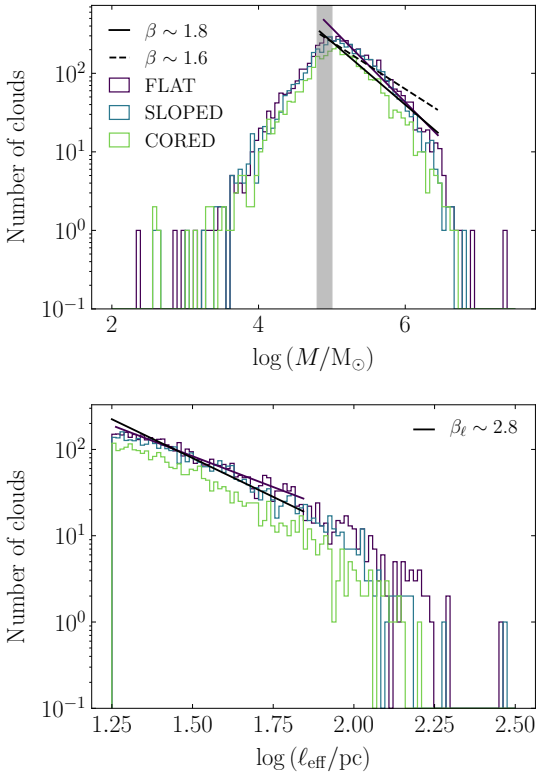

Figure 17. *Upper panel:* Mass distribution of the GMCs identified in each simulated galaxy at $t = 600$ Myr. The solid black and dashed black lines denote the range of power-law slopes for the observed cloud mass distribution in the Milky Way, given by $\mathrm{d}N/\mathrm{d}M \propto M^{-\beta}$ with $\beta \in [1.6, 1.8]$. The purple line gives the power-law fit to mass spectrum of the FLAT simulation, corresponding to $\beta = 1.94 \pm 0.05$. The grey shaded region indicates the range of observed values for the turnover of the mass spectrum at $M \sim 10^{4.8}$-10^5 M$_\odot$. *Lower panel:* Size distribution of GMCs at $t = 600$ Myr. The black line denotes the power-law slope of the observed cloud size distribution in the Milky Way, given by $\mathrm{d}N/\mathrm{d}M \propto M^{-\beta_\ell}$ with $\beta_\ell \sim 2.8$. The purple line gives the power-law fit to the size spectrum of the FLAT simulation, corresponding to $\beta_\ell = 2.43 \pm 0.06$.

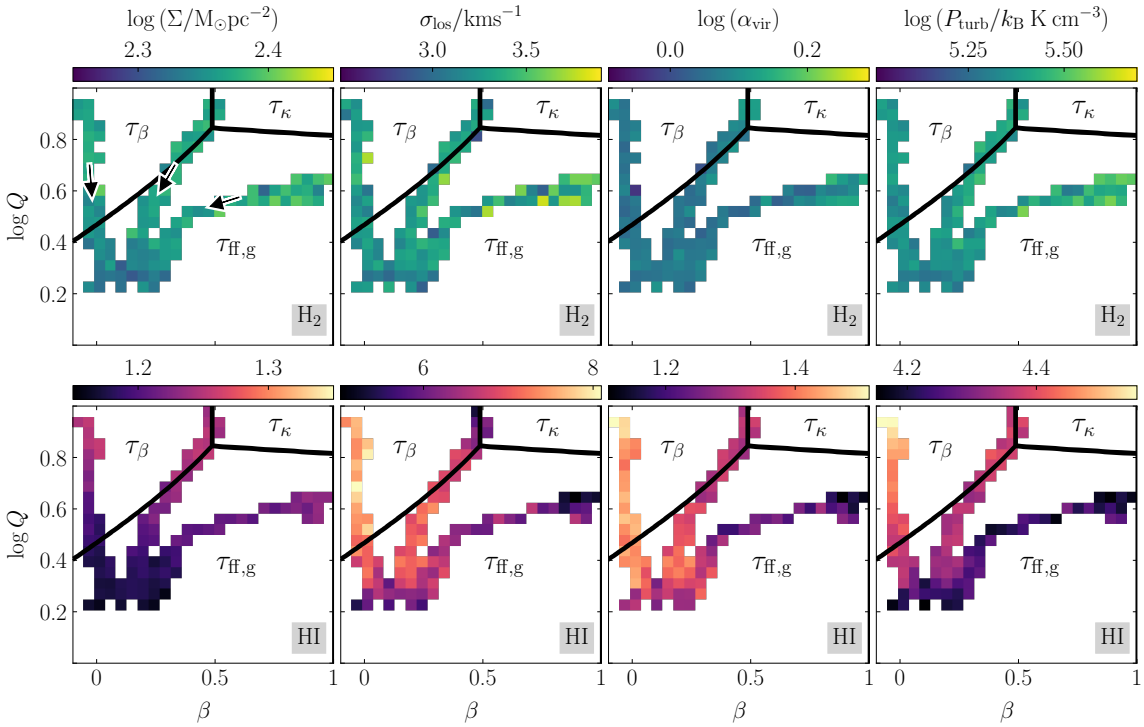

Figure 18. Mean surface density Σ (left), line-of-sight velocity dispersion $\sigma_{\rm los}$ (centre-left), virial parameter $\alpha_{\rm vir}$ (centre-right), and turbulent pressure $P_{\rm turb}$ (right) of the GMCs (upper panels) and HI clouds (lower panels) in our simulations, as a function of the shear parameter β and the Toomre Q stability parameter. Each distinct set of connected pixels corresponds to the total cloud population of one isolated disc galaxy, compiled across the simulation time interval from 600 Myr to 1 Gyr, at a sampling interval of 50 Myr. The color of each pixel represents the mean value of the relevant cloud property at the indicated value of (β, Q). The black arrows in the upper left panel mark the direction in which the galactocentric radius increases. The black solid lines enclose the regions of parameter space for which the minimum dynamical time-scale is τ_κ (orbital epicyclic perturbations), τ_β (galactic shear) and $\tau_{\rm ff,g}$ (gravitational free-fall).

largest clouds slightly exceed the truncation size of 70 pc observed by Colombo et al. (2019), with a maximum diameter of ~ 200 pc. Importantly, we do approximately reproduce the observed power-law slope of $\mathrm{d}N/\mathrm{d}R \sim R^{-\beta_\ell}$ with $\beta_\ell \sim 2.8$ (Colombo et al. 2019). This is given by the black line in Figure 17, while our best fit to the simulation data over the observed range of cloud sizes $\ell_{\rm eff} \in [18, 70]$ pc is given by the purple line, with a slightly shallower slope of $\beta_\ell = 2.43 \pm 0.06$.

5.3 Cloud self-gravity and turbulence

Observationally, giant molecular clouds living in similar galactic environments exhibit a tight correlation between their surface densities Σ and their line-of-sight turbulent velocity dispersions $\sigma_{\rm los}$ (e.g. Larson 1981; Heyer et al. 2009; Longmore et al. 2013; Leroy et al. 2017; Sun et al. 2018; Colombo et al. 2019). For each GMC or HI cloud in our simulations, we define these quantities as

$$\Sigma_x = \frac{\sum_i^N m_{i,x}}{A_x}, \tag{43}$$

and

$$\sigma_{{\rm los},x} = \frac{\sigma_x}{\sqrt{3}} = \sqrt{\frac{\langle |\mathbf{v}_i - \langle \mathbf{v}_i \rangle_x|^2 \rangle_{i,x}}{3}}, \tag{44}$$

where $x = \{\mathrm{H}_2, \mathrm{HI}\}$. That is, $\{m_{i,x}\}$ are the masses of H_2 or HI in the gas cells $i = 1...N$ of each cloud, $\{\mathbf{v}_i\}$ are the velocities of the gas cell centroids, A_x is the pixel-by-pixel area of the cloud's footprint on the galactic mid-plane, and $\langle ... \rangle_x$ denotes a mass-weighted average. The exact position of each cloud in the Σ-$\sigma_{\rm los}$ plane probes its virial parameter

$$\alpha_{\rm vir} = \frac{5\sigma_{\rm los}^2}{G\sqrt{\pi M \Sigma}}, \tag{45}$$

and turbulent pressure

$$P_{\rm turb} \approx \rho \sigma_{\rm los}^2 \approx \frac{\Sigma \sigma_{\rm los}^2}{L}, \tag{46}$$

which provide insight into the cloud's state of self-gravitational and external confinement, respectively (see also Sun et al. 2018). We have adopted the standard definition of the virial parameter from MacLaren et al. (1988b); Bertoldi & McKee (1992), and have assumed a spherical cloud[6] of radius L to arrive at the

[6] We use the standard definition of the virial parameter to allow for direct comparison to the existing literature, but our GMCs and HI clouds are ellipsoidal rather than spherical, with an average aspect ratio of $\epsilon \sim 2.3$ (see Table 3). According to Figure 2 and Equation (21) of Bertoldi & McKee

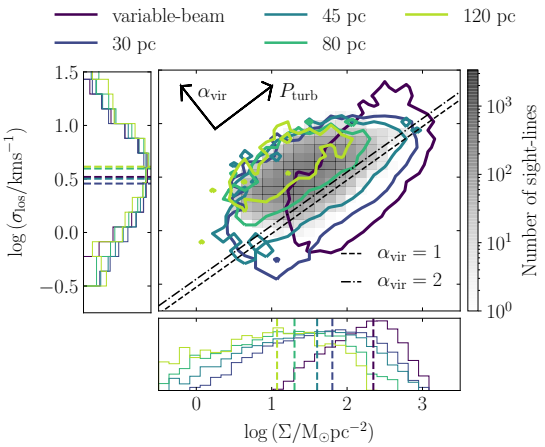

Figure 19. Relationship between the molecular gas surface density Σ and the line-of-sight velocity dispersion $\sigma_{\rm los}$ for the combined GMC populations of our three simulations between simulation times of 600 Myr and 1 Gyr, sampled at 50 Myr intervals. The dark purple contour encloses 90 per cent of data points for GMCs identified using ASTRODENDRO, as described in Section 2.9. The remaining contours enclose 90 per cent of the data points for molecular gas 'sight-lines' at fixed spatial scales of 30, 45, 80 and 120 pc, following the cloud-identification method described in Sun et al. (2018). The grey-shaded histogram in the central panel contains the observational data at 120 pc-scale from Sun et al. (2018), combining the results from the flocculent Milky Way-mass galaxies NGC 628, NGC 2835, NGC 5068, NGC 4254 and NGC 6744. In the lower- and side-panels, the distributions of Σ and $\sigma_{\rm los}$ are shown on a logarithmic y-axis scale, where the median values at each beam resolution are given by the dashed lines.

right-hand side of Equation (46). A collapsing molecular cloud that is over-pressured relative to its ambient environment must be gravitationally-bound, with $\alpha_{\rm vir} \lesssim 2$, though we emphasise that this threshold is approximate, as the virial parameter is an approximate measure of gravitational boundedness (e.g. Mao et al. 2019). Conversely, a super-virial cloud with $\alpha_{\rm vir} \gtrsim 2$ may still be confined if its internal turbulent pressure $P_{\rm turb}$ is exceeded by that of the surrounding medium. To discern whether or not a cloud is confined, measurements both of $\alpha_{\rm vir}$ and of $P_{\rm turb}$ are required.

5.3.1 *The dynamical decoupling of GMCs relative to HI clouds*

Figure 18 demonstrates that the molecular clouds (top row) in our simulations display a much lesser degree of environmental variation in their gravo-turbulent properties than do the HI clouds (bottom row). On average, they have surface densities that are ten times smaller than those of the GMCs ($\Sigma_{\rm HI} \sim 16\,{\rm M}_\odot\,{\rm pc}^{-2}$ vs. $\Sigma_{\rm H_2} \sim 226\,{\rm M}_\odot\,{\rm pc}^{-2}$), and velocity dispersions that are two times higher ($\sigma_{\rm los,HI} \sim 6.7\,{\rm km\,s}^{-1}$ vs. $\sigma_{\rm los,H_2} \sim 3.7\,{\rm km\,s}^{-1}$). This means that the turbulent pressures of the GMCs in our simulations are ten times larger than those of the HI clouds ($P_{\rm turb,H_2} \sim 2.3 \times 10^5\,k_{\rm B}\,{\rm K\,cm}^{-3}$ vs. $P_{\rm turb,HI} \sim 2.1 \times 10^4\,k_{\rm B}\,{\rm K\,cm}^{-3}$), and while the GMCs are gravitationally-bound across all galactic-dynamical environments ($\alpha_{\rm vir,H_2} \sim 1.2$), the HI clouds are far from gravitational equilibrium, with an average virial parameter of $\alpha_{\rm vir,HI} \sim 22$. The large difference in the mean pressures and densities of the GMCs relative to the HI clouds points to an explanation for the dichotomy in their degree of environmental variation: the molecular clouds in our Milky Way-pressured galaxies are too over-dense and over-pressured to be turbulently-coupled to the ambient medium.

The dynamical decoupling of our GMCs is best examined in the Σ-$\sigma_{\rm los}$ plane, and in the plane comparing the mid-plane hydrostatic pressure to the cloud turbulent pressure $P_{\rm mp}$-$P_{\rm turb}$, as studied in observations by Sun et al. (2020). In Figure 19, we compare the combined population of GMCs from all three simulations (coloured contours) to the observed molecular Σ-$\sigma_{\rm los}$ distribution of Sun et al. (2018) for five flocculent, bar-less Milky Way-mass galaxies, at 120 pc-resolution (grey-shaded histogram). The GMCs identified by these authors are independent of any clump-finding algorithm; instead they are assumed to fill a 'sight-line' of size equal to the observational resolution. Only those sight-lines with signal-to-noise ratios of ${\rm S/N} \geqslant 5$ in two consecutive channels of CO emission are considered. We therefore produce ray-tracing maps of $\Sigma_{\rm H_2}$ at resolutions of $\Delta x = 120$ pc, 80 pc, 45 pc and 30 pc, and identify all pixels with $\log(\Sigma_{\rm H_2}/{\rm M}_\odot){\rm pc}^{-2} > -3.5$ as 'GMC sight-lines'. This removes the low-level CO emission as depicted in Figure 4, and we calculate the properties of each sight-line using the gas cells masked by each pixel, in the same way as for the 'beam-filling' clouds of variable scale (i.e. the clouds that we identify as isodensity contours in ASTRODENDRO). Figure 19 demonstrates good agreement between simulations and observations for GMC sight-lines at a resolution of 120 pc (light-green contour), but shows a systematic decrease in the median virial parameter as the resolution is increased, combined with a systematic increase in the turbulent pressure. The black arrows denote the direction of increasing value for each of these quantities in the Σ-$\sigma_{\rm los}$ plane. The virial parameter is lowest, and the turbulent pressure highest, for the beam-filling clouds (purple contour). The reason for this is revealed in the lower- and left-hand side panels: the molecular gas velocity dispersion is approximately independent of the resolution Δx, but the molecular gas surface density depends on the beam filling-factor, which scales as $(\Delta x)^{-2}$. This leads to an increase in the virial parameter and a decrease in the turbulent pressure, in proportion to $(\Delta x)^2$. While the sight-lines at 120 pc have an average overdensity of just $\sim 10\times$ relative to the ambient medium, the beam-filling GMCs have an overdensity of $\sim 100\times$.

In Figure 20, we demonstrate the impact of this overdensity on the over-pressure of beam-filling GMCs. The horizontal axis gives the kpc-scale mid-plane hydrostatic pressure $P_{\rm mp} = \pi G/2\ \phi_{\rm P} \Sigma_{\rm g}^2$, combining the ISM and stellar-gravity contributions. We calculate this using 2D ray-tracing projections at 120 pc-resolution, as described in Appendix A, and perform the kpc-average by resampling the array into larger bins. The vertical axis of Figure 20 gives the cloud-scale turbulent pressure according to Equation (46). Again, the coloured contours enclose 90 per cent of the combined simulation data at resolutions of $\Delta x = 120$ pc (light-green contour), 80 pc, 45 pc and 30 pc, along with the beam-filling clouds (purple contour). The grey-shaded histogram shows the combined data from the sample of 28 nearby galaxies studied by Sun et al. (2020). As seen in the Σ-$\sigma_{\rm los}$ distribution, the overlap between observations and simulations is greatest for molecular gas sight-lines at 120 pc-resolution. We find an average over-pressure of $\sim 4\times$ for these sight-lines: very close to the observed value of $\sim 2.8\times$. The GMC turbulent pressure increases with resolution, reaching a peak over-pressure of $\sim 25\times$ for the beam-filling

(1992), the virial parameter is reduced by a factor of 0.8 for an aspect ratio of $\epsilon \sim 2.3$. Each cloud is slightly more tightly-bound than the presented values would indicate

GMCs. By contrast, 90 per cent of the data for the HI clouds is enclosed by the thin black line. We see that their internal turbulent pressures are much closer to the mid-plane hydrostatic pressure than are the internal turbulent pressures of the beam-filling GMCs.

Given the information contained in Figures 19 and 20, the dichotomy in the degree of dynamical variation for GMC and HI cloud gravo-turbulent properties is likely caused by the difference in their internal turbulent pressures. Comparing the purple and black contours in Figure 20, this offset spans around two orders of magnitude. The HI clouds are close to the pressure of the galactic mid-plane, and so are dynamically-coupled to it. The GMCs sit high above the pressure of the galactic mid-plane, and so are dynamically-decoupled. At mid-plane pressures higher than those in Milky Way-like galaxies (right-hand side of the grey-shaded histogram in Figure 20), we hypothesise that the dynamical-coupling of GMCs will increase substantially. A higher fraction of the mid-plane gas will be molecular, and so the beam filling-factor at 120 pc resolution will be much higher. That is, the purple contour (beam-filling clouds) and the green contour (clouds identified at a fixed resolution of 120 pc) will overlap at high $\langle P_{\rm mp}\rangle_{\rm 1kpc}$, leading to galactic-dynamical trends in $\sigma_{\rm los,H_2}$, $\alpha_{\rm vir,H_2}$ and $P_{\rm turb,H_2}$ for beam-filling GMCs. In galaxies with significantly-higher mid-plane pressures than the Milky Way, we expect to find substantial variation in these properties as a function of $(\beta, Q, \Omega, \phi_{\rm P})$. A first observational indication for a this trend has been identified by Chevance et al. (2020b), who find that GMC lifetimes in galaxies with kpc-scale molecular gas surface densities $\Sigma_{\rm H_2} > 8$ M$_\odot$ pc^{-2} correlate with galactic dynamical time-scales rather than internal dynamical ones, contrary to those at lower surface densities.

5.3.2 *Self-gravity and turbulence in HI clouds*

The velocity dispersions $\sigma_{\rm HI}$, virial parameters $\alpha_{\rm vir,HI}$ and turbulent pressures $P_{\rm turb,HI}$ of the HI clouds in our simulations display a clear environmental variation across the galactic-dynamical parameter space $(\beta, Q, \Omega, \phi_{\rm P})$. In the bottom right-hand panel of Figure 18, we show that the HI cloud turbulent pressure increases towards high-shear, high gravitational-stability environments with $\beta \rightarrow 0$ and $Q \rightarrow 10$. The trend comes predominantly from an increase in the cloud velocity dispersion, while the cloud surface density varies over a much smaller dynamic range (lower-left and centre-left panels of Figure 18). As such, the HI cloud virial parameter (centre-right panel of Figure 18) also increases with the degree of shearing and gravitational stability. This environmental variation in each HI cloud gravo-turbulent property corresponds to a statistically-significant correlation with the two shortest galactic-dynamical time-scales for shearing (τ_β) and gravitational free-fall ($\tau_{\rm ff,g}$), as well as with the mid-plane pressure $P_{\rm mp}$, as summarised in Figure 16. The HI cloud pressures therefore trace the ambient pressure, density and dynamical state of the galactic mid-plane, while the GMCs are dynamically-decoupled and gravitationally-collapsing (discussed further in Section 5.4).

5.4 Cloud collapse

The degree to which a cloud is collapsing globally towards its centre of mass can be quantified by the magnitude of its internal radial velocity streaming, as

$$\mathcal{D}_x = \langle v_{r,i}\rangle_x, \quad x \in \{\rm H_2, HI\} \tag{47}$$

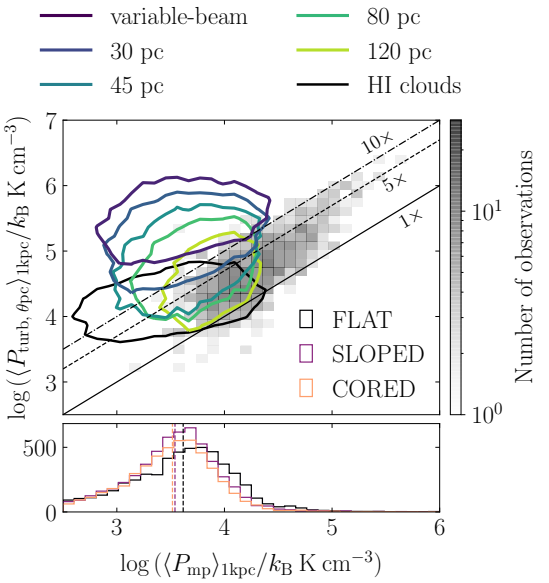

Figure 20. The kpc-scale averaged turbulent pressure $\langle P_{\rm turb,\,\theta pc}\rangle_{\rm 1kpc}$ at varied spatial resolution θ for the combined GMC population across our three simulations at times between 600 Myr and 1 Gyr, as a function of the kpc-averaged mid-plane hydrostatic pressure, $\langle P_{\rm mp}\rangle_{\rm 1kpc}$. The dark purple contour encloses 90 per cent of data points for molecular clouds identified using ASTRODENDRO, as described in Section 2.9. The remaining contours enclose 90 per cent of data points for molecular gas 'sight-lines' at fixed spatial scales of 30, 45, 80 and 120 pc, following the cloud-identification method described in Sun et al. (2018). The grey-shaded histogram in the upper panel contains the observational data at $\theta = 120$ pc from Sun et al. (2020), across their sample of 28 nearby star-forming galaxies. The solid, dashed and dot-dashed lines denote overpressures $\langle P_{\rm turb,\theta pc}\rangle_{\rm 1kpc}/\langle P_{\rm mp}\rangle_{\rm 1kpc}$ of 1, 5 and 10 times, respectively. In the lower panel, the cloud populations of the FLAT, SLOPED and CORED runs are separated to show the similarity in their mid-plane turbulent pressure distributions, on kpc scales.

where $\{v_{r,i}\}$ are the radial velocities of the gas cells in the cloud, with respect to the velocity of its centre of mass. We find that the GMC velocity divergence is negative and invariant across all galactic-dynamical environments, with a mean value of $\mathcal{D}_{\rm H_2} \sim (-0.99 \pm 0.08)$ km s^{-1}, where the error indicates the standard deviation of the measurements. That is, averaged across dynamical environments, the simulated molecular clouds are collapsing at a uniform rate towards their centres of mass, consistent with the high degree of gravitational boundedness indicated by their virial parameters, $\alpha_{\rm vir,H_2} \sim 1.2$. The parent HI clouds display a much weaker level of collapse (mean value $\mathcal{D}_{\rm HI} \sim (-0.2 \pm 0.4)$ kms^{-1}), which follows a statistically-significant correlation with the mid-plane velocity dispersion of the galaxy, shown in Appendix B. At the highest mid-plane velocity dispersions of $\sigma_{\rm mp} \sim 10$ kms^{-1}, HI clouds are not collapsing, reaching near-zero velocity divergences. At the lowest velocity dispersions ($\sigma_{\rm mp} \sim 6$ kms^{-1}), HI clouds are collapsing at their maximum average rate of $\mathcal{D}_{\rm HI} \sim -1$ kms^{-1}. This trend is consistent with HI clouds that are coupled to the galactic mid-plane, so are more-effectively supported against collapse at higher mid-plane velocity dispersions.

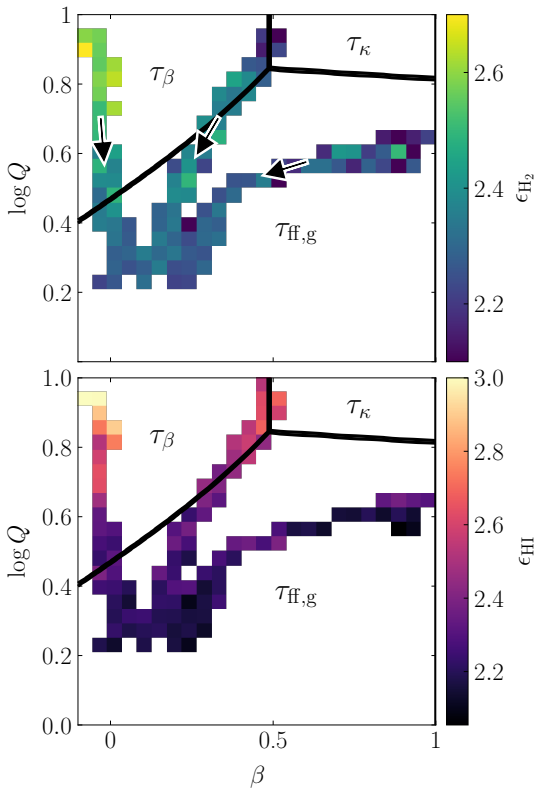

Figure 21. The mean aspect ratio ϵ of the GMCs (upper panel) and HI clouds (lower panel) in our simulations, as a function of the shear parameter β and the Toomre Q stability parameter. Each distinct set of connected pixels corresponds to the total cloud population of one isolated disc galaxy, compiled across the simulation time interval from 600 Myr to 1 Gyr, at a sampling interval of 50 Myr. The color of each pixel represents the mean value of ϵ at the indicated value of (β, Q). The black arrows in the top panel mark the direction in which the galactocentric radius increases. The black solid lines enclose the regions of parameter space for which the minimum dynamical time-scale is τ_κ (orbital epicyclic perturbations), τ_β (galactic shear) and $\tau_{\rm ff,g}$ (gravitational free-fall).

5.5 Cloud rotational properties

The GMC population in our simulations is highly over-dense and over-pressured relative to the ambient ISM, leading to its turbulent and gravitational decoupling from the properties of the galactic mid-plane. Nevertheless, we find statistically-significant galactic-dynamical trends in the rotational properties of our clouds (aspect ratios, angular momenta and velocity anisotropies). As shown in Figure 16, each of these properties correlates with the time-scales τ_β and $\tau_{\rm ff,g}$ for galactic shear and gravitational free-fall, as well as with the mid-plane pressure $P_{\rm mp}$. In the environmental parameter space $(\beta, Q, \Omega, \phi_{\rm P})$, this manifests itself as a monotonic gradient towards the top left-hand corner of the (β, Q) plane, as seen in the top left-hand panel of Figure 15. The rotational trends observed for GMCs are mirrored by the parent HI clouds, indicating either that (1) both GMCs and HI clouds are affected in the same way by the interplay between galactic rotation and gravitational free-fall, or (2) that GMCs retain the rotational properties of their parent HI clouds as they collapse.

5.5.1 *Aspect ratio*

The elongation of each GMC and HI cloud within the galactic mid-plane can be quantified by the aspect ratio, ϵ_x, as

$$\epsilon_x = \frac{\Delta \ell_{{\rm maj},x}}{\Delta \ell_{{\rm min},x}}, \quad x \in \{{\rm H_2}, {\rm HI}\} \tag{48}$$

where $\Delta \ell_{\rm maj}$ and $\Delta \ell_{\rm min}$ are the major and minor axes, respectively, of an ellipse fitted to the footprint of each cloud in the galactic mid-plane. Both the GMC and HI cloud populations in our galaxies have the same mean aspect ratio ($\epsilon_{\rm H_2}, \epsilon_{\rm HI} \sim 2.3$), and both increase monotonically with the degree of differential rotation in the galactic mid-plane ($\beta \rightarrow 0$) and with the degree of gravitational stability ($Q \rightarrow 10$). This qualitative trend is shown in Figure 21. The particular role of galactic shearing in stretching HI clouds and molecular clouds is indicated by the following two results.

(i) The direction of elongation points along the direction of galactic rotation in every dynamical environment, with mean position angles of $-1.7^\circ \pm 9^\circ$ and $-2.3^\circ \pm 9^\circ$ for GMCs and HI clouds, respectively.

(ii) In environments for which clouds are controlled primarily by gravity (region $\tau_{\rm ff,g}$ of the dynamical parameter space), the HI clouds and GMCs have approximately-constant and equal aspect ratios of $\epsilon_{\rm H_2}, \epsilon_{\rm HI} \sim 2.2$, but in environments for which galactic shear dominates (region τ_β), the GMC aspect ratio anticorrelates with the shear time-scale as

$$\epsilon_{\rm H_2} \propto (-0.39 \pm 0.03) \log \tau_\beta, \tag{49}$$

and the HI cloud aspect ratio anticorrelates as

$$\epsilon_{\rm HI} \propto (-0.81 \pm 0.04) \log \tau_\beta, \tag{50}$$

as demonstrated in Appendix B.

The HI clouds in our simulations are significantly more suceptible to elongation than are the GMCs, which is not surprising given their lower over-densities and over-pressures, and their correspondingly larger degree of dynamical coupling.

5.5.2 *Specific angular momentum*

The specific angular momentum of GMCs and HI clouds provides a measure of their internal rotation about the cloud centre of mass. The specific angular momentum vector for a given cloud is defined as

$$\begin{aligned} \mathbf{L}_x &= L_{z,x}\hat{\mathbf{z}} + L_{\theta,x}\hat{\theta} + L_{R,x}\hat{\mathbf{R}} \\ &= \langle \mathbf{r}_i \times \mathbf{v}_i \rangle_x, \quad x \in \{{\rm H_2}, {\rm HI}\} \end{aligned} \tag{51}$$

where $\{\mathbf{r}_i\}$ are the positions of the gas cell centroids relative to the cloud centre of mass, and $\{\hat{\mathbf{R}}, \hat{\theta}, \hat{\mathbf{z}}\}$ are the galactic unit vectors in cylindrical polar coordinates. The component L_z is therefore the magnitude of the angular momentum within the galactic mid-plane and about an axis perpendicular to it, while $L_\theta \hat{\theta}$ and $L_R \hat{\mathbf{R}}$ are the components of the vector within the galactic mid-plane.

In the parameter space of Figure 22, the cloud angular momentum displays a clear variation with the galactic-dynamical environment. This environmental variation leads to clear, statistically-significant correlations with the galactic-dynamical time-scales τ_β

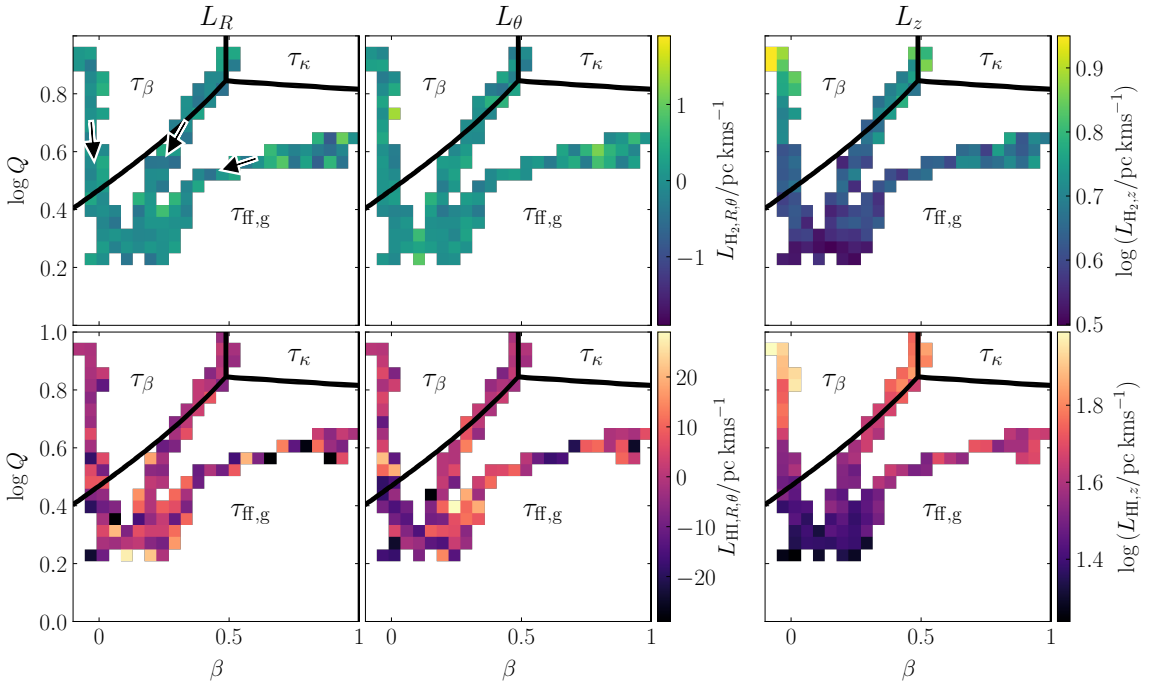

Figure 22. The mean angular velocity $\mathbf{L}$ of the GMCs (upper panel) and HI clouds (lower panel) in our simulations, as a function of the shear parameter β and the Toomre Q stability parameter. The three columns display the three orthogonal components of the angular momentum vector $\mathbf{L} = (L_R, L_\theta, L_z)$. Each distinct set of connected pixels corresponds to the total cloud population of one isolated disc galaxy, compiled across the simulation time interval from 600 Myr to 1 Gyr, at a sampling interval of 50 Myr. The color of each pixel represents the mean value of the L_R, L_θ or L_R at the indicated value of (β, Q). The black arrows in the upper left panel mark the direction in which the galactocentric radius increases. The black solid lines enclose the regions of parameter space for which the minimum dynamical time-scale is τ_κ (orbital epicyclic perturbations), τ_β (galactic shear) and $\tau_{\rm ff,g}$ (gravitational free-fall).

and $\tau_{\rm ff,g}$, presented in Figure 16 and in Table 3. However, given the preferentially prograde sense of rotation for our simulated cloud population, these trends are likely to be driven by the variation of L_z with the orbital angular velocity Ω, which dictates the strength of the fictitious Coriolis force in the galactic rest-frame, rather than the strength of shearing. For our simulated galaxies, all of which have shear parameters in the range $0 < \beta < 1$, we would expect shear-driven rotation to be exclusively retrograde. Only for a rising rotation curve with $\beta \geqslant 1$ would we expect clouds to be spun up in a prograde direction by galactic shear. Therefore, while the degree of internal rotation for our GMCs and HI clouds is determined by the galactic rotation curve, it is not due to differential rotation across a cloud. We also find that the GMCs in our sample display a factor of ten reduction in angular momentum relative to the HI clouds across all galactic-dynamical environments, which is a factor of three greater than can be accounted for by their smaller sizes. It is therefore unlikely that the GMCs themselves are torqued by galactic rotation, but rather inherit their angular momentum from their parent HI clouds. On average, some of the inherited angular momentum is then partially converted into turbulent motion of the surrounding gas during gravitational collapse.

5.5.3 *Velocity anisotropy*

In addition to the line-of-sight velocity dispersion presented in Section 5.3, we can compute the radial σ_r and tangential σ_t components of the cloud velocity dispersion with respect to the cloud centre of mass, such that

$$\sigma_r^2 = \langle |\mathbf{v}_i \cdot \hat{\mathbf{r}}_i - \langle \mathbf{v}_i \cdot \hat{\mathbf{r}}_i \rangle_{i,x}|^2 \rangle_{i,x} \tag{52}$$

and

$$\begin{aligned} \sigma_t^2 &= \sigma_\theta^2 + \sigma_\phi^2 \\ \sigma_\theta^2 &= \langle |\mathbf{v}_i \cdot \hat{\theta}_i - \langle \mathbf{v}_i \cdot \hat{\theta}_i \rangle_{i,x}|^2 \rangle_{i,x} \\ \sigma_\phi^2 &= \langle |\mathbf{v}_i \cdot \hat{\phi}_i - \langle \mathbf{v}_i \cdot \hat{\phi}_i \rangle_{i,x}|^2 \rangle_{i,x}. \end{aligned} \tag{53}$$

providing the velocity anisotropy as

$$B_{\sigma,x} = 1 - \frac{\sigma_{t,x}}{2\sigma_{r,x}}, \tag{54}$$

with $x \in \{{\rm H_2}, {\rm HI}\}$. In the above equations, $\{\hat{\theta}_i\}$ are the longitudinal unit vectors of the gas cells in each cloud with respect to the cloud centre of mass, and $\{\hat{\phi}_i\}$ are the corresponding azimuthal unit vectors. If all motions within a cloud are radial, then $\sigma_t = 0$ and $B_\sigma = 1$. Conversely, if all motions are circular, then $\sigma_r = 0$ and $B_\sigma \to -\infty$ (Binney & Tremaine 1987). The velocity anisotropy of the internal turbulent motion in a GMC or HI cloud therefore tells us about the origin of turbulence in this cloud

(e.g. Ossenkopf & Mac Low 2002; Lazarian et al. 2002; Esquivel & Lazarian 2011; Burkhart et al. 2014; Otto et al. 2017). Significant radial bias ($B_\sigma > 0$) indicates that turbulence is primarily driven by spherically-symmetric processes such as global gravitational collapse. Significant tangential bias ($B_\sigma < 0$) indicates that turbulence is driven either by non-spherically symmetric processes in the cloud's environment (e.g. galactic shearing or compression driven by external feedback) or by processes that occur inside the cloud but that may be far from its centre of mass (e.g. hierarchical collapse and internal feedback). We note that magnetic fields in particular (not included in our simulations) may significantly alter the velocity anisotropy by directing the bulk gas flow within the ambient ISM (e.g. Kim & Ostriker 2017; Seifried et al. 2017, 2020). We discuss this further in Section 6.2.

Figure 23 shows that in all galactic-dynamical environments, our simulated GMCs and HI clouds are tangentially-biased, with mean anisotropy parameters ranging from -0.9 to -0.3 for $B_{\sigma,\mathrm{H_2}}$ and from -0.4 to 0.1 for $B_{\sigma,\mathrm{HI}}$. For the GMCs, this means that the tangential velocity dispersions are 30 to 90 per cent higher than the radial velocity dispersions, displaying a monotonic increase in the degree of tangential bias with the rate of galactic shearing, as

$$B_{\sigma,\mathrm{H_2}} \propto (0.35 \pm 0.04) \log \tau_\beta . \quad (55)$$

This monotonic increase is consistent with the presence of shear-induced internal circular motions, although given the prograde orientation of the specific angular momentum, we cannot rule out the contribution of the fictitious Coriolis force in the rotating galactic frame. The slope is shallower for the HI clouds in our sample, with a value of

$$B_{\sigma,\mathrm{HI}} \propto (0.18 \pm 0.03) \log \tau_\beta . \quad (56)$$

That is, both the degree of anisotropy, and its dependence on the shear rate, is reduced. In fact, in the gravity-dominated regime $\tau_{\mathrm{ff,g}}$ of the galactic-dynamical parameter space, the tangential velocity dispersion of the HI clouds approaches equality with the radial component ($B_\sigma \to 0$). The disparity between the shear-correlated degree of anisotropy in GMCs and HI clouds is likely to arise from the conservation of angular momentum during the collapse of the GMCs, which enhances the shear-driven tangential velocity dispersion present in their parent HI clouds (see also Kruijssen et al. 2019a).

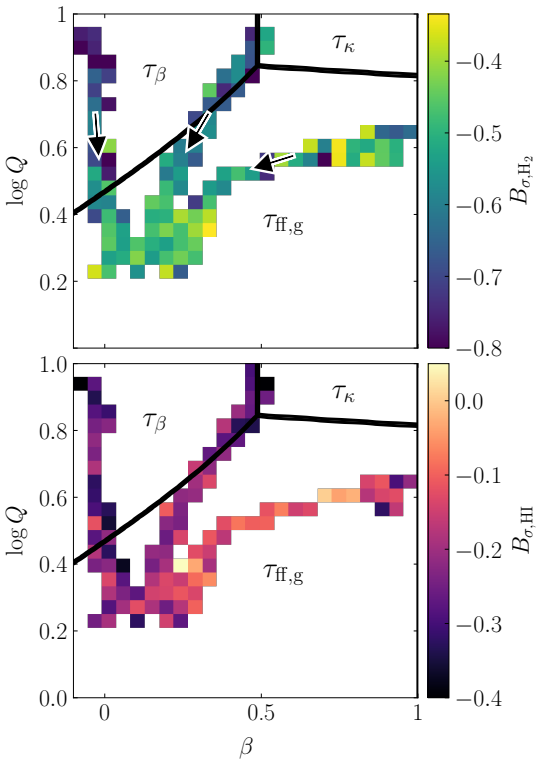

Figure 23. The mean velocity anisotropy B_σ of the GMCs (upper panel) and HI clouds (lower panel) in our simulations, as a function of the shear parameter β and the Toomre Q stability parameter. Each distinct set of connected pixels corresponds to the total cloud population of one isolated disc galaxy, compiled across the simulation time interval from 600 Myr to 1 Gyr, at a sampling interval of 50 Myr. The color of each pixel represents the mean value of the anisotropy at the indicated value of (β, Q). The black arrows mark the direction in which the galactocentric radius increases. The black solid lines enclose the regions of parameter space for which the minimum dynamical time-scale is τ_κ (orbital epicyclic perturbations), τ_β (galactic shear) and $\tau_{\mathrm{ff,g}}$ (gravitational free-fall).

5.6 Molecular cloud star formation rate

Across the galactic-dynamical environments $(\beta, Q, \Omega, \phi_{\mathrm{P}})$ spanned by our simulations, we find a quantitative correlation between the kpc-scale star formation rate $\langle \Sigma_{\mathrm{SFR}} \rangle_{1\mathrm{kpc}}$ and the kpc-scale mid-plane hydrostatic pressure $\langle P_{\mathrm{mp}} \rangle_{1\mathrm{kpc}}$. The relationship between the azimuthally-averaged values of $\langle P_{\mathrm{mp}} \rangle_{1\mathrm{kpc}}$ and $\langle \Sigma_{\mathrm{SFR}} \rangle_{1\mathrm{kpc}}$ for our simulations shows a large degree of overlap with the observed relationship presented by Sun et al. (2020) (also originally by Blitz & Rosolowsky (2004)) for 28 nearby galaxies, as shown in the left-hand panel of Figure 24. In turn, this is consistent with a state of approximate dynamical equilibrium between feedback and gravitational collapse (see Ostriker et al. 2010; Ostriker & Shetty 2011; Benincasa et al. 2016). As for the relationship between the cloud-scale turbulent pressure and the mid-plane hydrostatic pressure (Section 5.3) our simulated discs fall at the low-pressure end of the observed relationship, corresponding to the discs of Milky Way-pressure, flocculent galaxies.

Within our sample, we find that the rise in star formation rate surface density with mid-plane pressure is primarily due to a rise in the number of GMCs per unit area of the galactic mid-plane, and not due to environmental variations in the properties of the GMCs themselves. In the central and right-hand panels of Figure 24, we show the environmental trends in $\langle \Sigma_{\mathrm{SFR}} \rangle_{1\mathrm{kpc}}$ and $\langle P_{\mathrm{mp}} \rangle_{1\mathrm{kpc}}$, and compare these to the environmental trend in the number of GMCs per unit area of the galactic mid-plane on kpc-scales, $\langle \Sigma_{N_{\mathrm{cl}}} \rangle_{1\mathrm{kpc}}$. Qualitatively, the trends match across all galactic environments. In Figure 16 and in Appendix B, we show that the correlation between $\langle \Sigma_{N_{\mathrm{cl}}} \rangle_{1\mathrm{kpc}}$ and $\langle P_{\mathrm{mp}} \rangle_{1\mathrm{kpc}}$ is statistically-significant at the 3σ confidence level.

By comparison to the dynamic ranges of the environmental trends in $\langle \Sigma_{\mathrm{SFR}} \rangle_{1\mathrm{kpc}}$, $\langle P_{\mathrm{mp}} \rangle_{1\mathrm{kpc}}$ and $\langle \Sigma_{N_{\mathrm{cl}}} \rangle_{1\mathrm{kpc}}$, the qualitative variation in the internal star-forming properties of GMCs is much smaller. On the right-hand side of Figure 25, we show the mean turbulent pressure P_{turb} of GMCs in our simulations as a function of the galactic-dynamical parameters (β, Q), as well as their mean internal star formation rate surface densities $\Sigma_{\mathrm{SFR,cl}}$ and the fraction

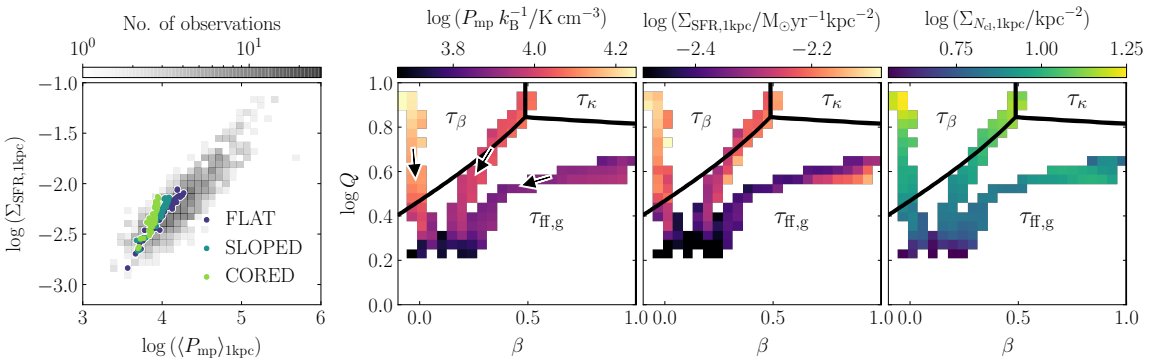

Figure 24. *Left:* The kpc-scale star formation rate surface density $\langle\Sigma_{\rm SFR}\rangle_{\rm 1kpc}$ as a function of the kpc-scale mid-plane pressure $\langle P_{\rm mp}\rangle_{\rm 1kpc}$. The grey-shaded histogram shows the observational data of Sun et al. (2020), aggregated across 28 nearby galaxies. The three sets of scattered points correspond to the azimuthally-averaged values for our FLAT, SLOPED and CORED simulations at intervals of 50 Myr between simulation times of 600 Myr and 1 Gyr. The simulation data fall at the lowest mid-plane pressures present in the observed sample. *Centre-left:* The azimuthally-averaged value of $\langle\Sigma_{\rm SFR}\rangle_{\rm 1kpc}$ as a function of the galactic-dynamical variables (β, Q). The black arrows mark the direction in which the galactocentric radius increases. *Centre-right:* The azimuthally-averaged value of $\langle P_{\rm mp}\rangle_{\rm 1kpc}$, as a function of the galactic-dynamical variables (β, Q). This obeys a very similar environmental trends to $\langle\Sigma_{\rm SFR}\rangle_{\rm 1kpc}$. *Right:* The number of GMCs per unit area of the galactic mid-plane, as a function of the galactic-dynamical variables (β, Q). This obeys a very similar trend to the kpc-scale star formation rate, indicating that the global star formation rate correlates with the number of star-forming regions. The black solid lines enclose the regions of parameter space for which the minimum dynamical time-scale is τ_κ (orbital epicyclic perturbations), τ_β (galactic shear) and $\tau_{\rm ff,g}$ (gravitational free-fall).

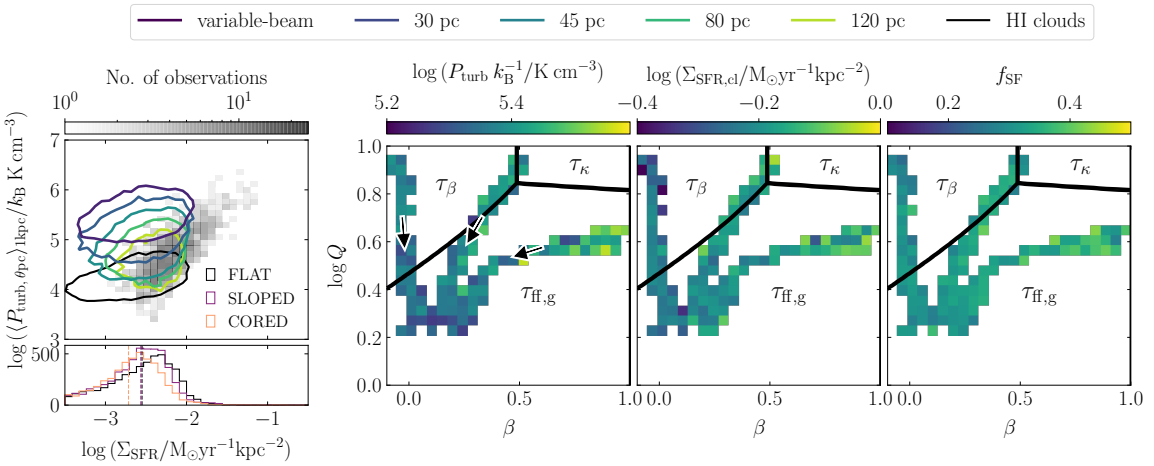

Figure 25. *Left:* The kpc-scale averaged turbulent pressure $\langle P_{\rm turb,\,\theta pc}\rangle_{\rm 1kpc}$ at varied spatial resolution θ for the combined GMC population across our three simulations at times between 600 Myr and 1 Gyr, as a function of the kpc-averaged star formation rate surface density $\langle\Sigma_{\rm SFR}\rangle_{\rm 1kpc}$. The dark purple contour encloses 90 per cent of beam-filling molecular clouds identified using ASTRODENDRO. The remaining contours represent molecular gas 'sight-lines' at fixed spatial scales of 30, 45, 80 and 120 pc, following the method of cloud identification described in Sun et al. (2018). The grey-shaded histogram in the upper panel contains the observational data at $\theta = 120$ pc from Sun et al. (2020), across a sample of 28 nearby star-forming galaxies. *Centre-left:* Turbulent pressure of the beam-filling GMCs in our simulations, as a function of the galactic-dynamical variables (β, Q). The black arrows mark the direction in which the galactocentric radius increases. *Centre-right/Right:* Star-forming properties of the simulated GMCs: the mean turbulent pressure $P_{\rm turb}$, star formation rate surface density per molecular cloud $\Sigma_{\rm SFR,cl}$, and the fraction of clouds in each environment that are star-forming $f_{\rm SF}$. The scale used for each colorbar is expanded to 0.4 dex, to match the span of global star formation rate surface densities across our simulations. The dynamic ranges of these cloud-scale properties are much smaller than that of the global galactic star forming properties, and of the number of GMCs per unit area of the galactic mid-plane. The black solid lines enclose the regions of parameter space for which the minimum dynamical time-scale is τ_κ (orbital epicyclic perturbations), τ_β (galactic shear) and $\tau_{\rm ff,g}$ (gravitational free-fall).

$f_{\rm SF}$ of identified GMCs that are currently star-forming. We have expanded the colorbars of each plot to match the dynamic range of the global kpc-scale star formation rate of the host galaxy, emphasising the small contribution to the overall trend in star formation that is made by each cloud-scale property. On the left-hand side of Figure 25, we demonstrate the reason for the environmental independence of the star-forming properties of our GMCs: as discussed in Section 5.3, they are decoupled from the galactic-midplane, with much higher pressures ($\sim 25\times$), densities ($\sim 100\times$) and star formation rates ($\sim 100\times$) than the surrounding medium. The dark purple contour encloses 90 per cent of the beam-filling GMCs analysed in this work, while the lighter-coloured contours represent molecular gas sight-lines corresponding to those analysed in Sun et al. (2020) across 28 nearby galaxies. These observational data are given by the grey-shaded histogram. At the observational 120 pc-resolution (light-green contour), a good level of overlap between simulations and observations is recovered. At higher resolutions, the measured cloud-scale turbulent pressures increase relative to the galactic mid-plane pressure, pushing their values above the SFR-pressure correlation that is observed on larger scales. This decoupling of GMCs from the mid-plane, which we also discussed in Section 5.3, is responsible for the lack of a correlation between the internal star-forming properties of GMCs and the properties of the mid-plane. In order to observe GMCs for which the star-forming properties are significantly influenced by the ambient environment and by its galactic dynamics, we would need to additionally simulate high-pressure, high-star formation rate environments towards the upper end of the observed pressure-SFR relation. These environments can be found in the spiral arms and bars of massive galaxies, and in galaxy discs with higher masses and gas fractions.

6 DISCUSSION

6.1 Comparison to previous work

This work addresses the statistical variation in GMC properties as a function of the galactic-dynamical environment. To this end, we have produced a large sample of $\sim 80,000$ molecular clouds that spans the dynamical parameter space of Jeffreson & Kruijssen (2018), encompassing the full range of shear parameters β, and spanning around an order of magnitude in the Toomre Q parameter, the angular velocity Ω and the stellar contribution $\phi_{\rm P}$ to the mid-plane pressure. Although the analysis and coverage of dynamical environments is unique, a number of other works have simulated and studied large samples of GMCs in isolated disc galaxies. The single-isothermal-phase simulations of Dobbs et al. (2006), and the two-isothermal-phase simulations of Dobbs & Bonnell (2007); Dobbs (2008) studied the role of spiral shocks, agglomeration and self-gravity in forming populations of GMCs in spiral galaxies. Dobbs et al. (2011a) additionally include magnetic fields and thermal SNe feedback, finding that the low degree of gravitational binding in GMCs can be attributed to a combination of feedback and cloud-cloud collisions, producing virial parameters in the range $0.1 \lesssim \alpha_{\rm vir} \lesssim 10$. In the current work, we find the same range of GMC virial parameters, despite the fact that our feedback prescription is physically-motivated and significantly more sophisticated (we include momentum and thermal energy injection due to SNe and HII-region feedback, and mass injection from stellar winds). At the typical hydrogen number densities of molecular clouds ($n_H \gtrsim 30$ cm^{-3}), this suggests that the self-regulation of turbulence does not depend on the mode of energy injection. The GMC virial parameter also appears to be independent of the method used for identifying clouds (we use contours in projected CO luminosity, rather than clump-finding in total 3D gas density). In this work, we find that the mean virial parameter of GMCs is independent of the galactic-dynamical environment, with a global mean value of $\alpha_{\rm vir} \sim 1.6$. Our GMCs are therefore marginally gravitationally-bound on average. Our virial parameters are independent of the time-scale for cloud-cloud collisions, which is up to ten times longer than the time-scale for gravitational free-fall.

More similar to our discs are the spiral galaxies of Dobbs et al. (2011b, 2012); Dobbs & Pringle (2013), and the simulated M33-analogues of Dobbs et al. (2018, 2019), which include thermal feedback from supernovae, ISM heating and cooling with H_2 and CO formation, and live stellar and gas particles at a mass resolution of 400 $M_\odot$. As in our simulations, the M33-like galaxies reproduce the observed cloud virial relation and the observed range of cloud velocity dispersions. They also reproduce the observed distribution of cloud angular momenta in M33, spanning a range of $-100{\rm pc\ kms^{-1}} \lesssim L_z \lesssim 100{\rm pc\ kms^{-1}}$. The authors find that the GMC angular momentum correlates with the GMC mass, which we confirm for our simulated GMCs and HI clouds in the central-left panel of Figure 26. This correlation persists when the clouds are binned by galactic-dynamical environment. The significance of the trend between these two observables is demonstrated in the central-right and right-hand panels of Figure 26, where we find a non-zero slope at the 3σ signficance level. Finally, in the left-hand panel of Figure 26, we show the spectrum of angular momenta for our sample of GMCs and HI clouds. We find that the span and skew in angular momentum space is comparable to that shown in Dobbs et al. (2019) (see also Braine et al. 2020).

The angular momenta of our simulated GMCs and HI clouds can also be compared to the recent study of cloud-scale circulating velocities in isolated disc simulations, conducted by Utreras et al. (2020). These authors quantify the degree of coupling between cloud-scale circulation and large-scale galactic rotation by modelling the galactic velocity field as a linear superposition of two components: the contribution from rotation plus a Gaussian random velocity field. Applying this analytic theory to three simulated discs with flat rotation curves, the authors find that cloud-scale spin is coupled to large-scale rotation only in the very centres of galaxies ($\lesssim$ 3-5 kpc). By contrast, we have found that, in galaxies with flat rotation curves, the radial gradient of the galactic rotation curve (i.e. the rate of galactic shearing) correlates significantly with the cloud angular momentum out to galactocentric radii of $\gtrsim 10$ kpc. A possible explanation for the additional rotational decoupling seen in Utreras et al. (2020) is evident in the surface density profiles of their galaxies. Their disc morphologies are highly-filamentary relative to ours, with surface densities reaching up to ten times higher in the densest clumps, despite their lower spatial resolution of ~ 30 pc, and their comparable gas, stellar and halo masses. This may be due to ineffective stellar feedback in their simulations, which is unable to disrupt the densest gas. The only source of momentum injection in their simulations is from photo-ionisation and stellar winds, both of which inject hundreds of times less energy than SNe explosions, which they treat thermally. The importance of momentum injection from unresolved SNe blast-waves has been confirmed by Kimm & Cen (2014); Slyz et al. (2005); Smith et al. (2018), among others. In the absence of effective disruption, the cloud-scale gas in the simulations of Utreras et al. (2020) may be dominated to a greater extent by self-gravity than the GMCs and HI clouds in our simulations, explaining the lower degree of coupling between cloud rotation and galactic rotation. This effect may

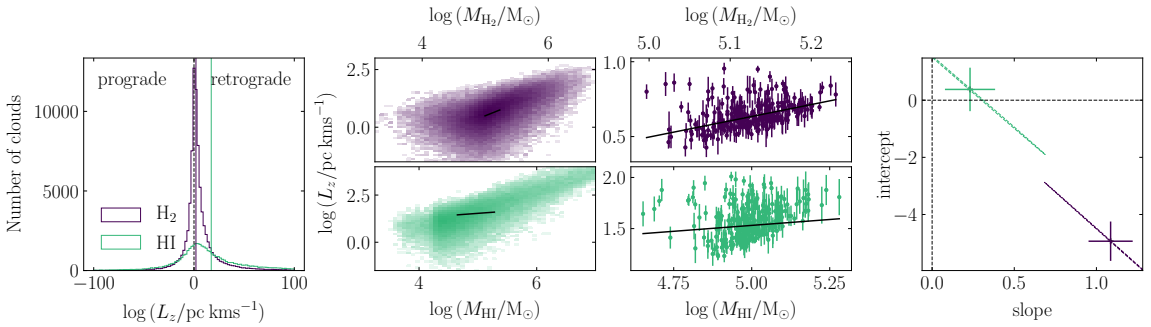

Figure 26. Analysis of GMC and HI cloud rotation, compiled across the FLAT, SLOPED and CORED discs at simulation times between 600 Myr and 1 Gyr. *Left:* Distribution of molecular cloud angular momenta (purple line) and HI cloud angular momenta (green line). The vertical lines give the means of the distributions. The black dashed vertical line denotes the state of zero angular momentum. We note that both distributions are skewed towards retrograde rotation (positive values of L_z. *Centre left:* Distribution of GMC (purple) and HI cloud (green) angular momenta, as functions of their respective masses. We note a clear correlation between the cloud mass and angular momentum in both cases. *Centre right:* Mean angular momentum of GMCs (purple) and of HI clouds (green) as a function of mean cloud mass, when the clouds are binned according to their galactic-dynamical environments, $(\beta, Q, \Omega, \phi_{\rm P})$. The error bars denote the error on the mean in each environmental bin. The black lines (in all panels) show the non-linear least-squares fit to the environmentally-binned data. *Right:* The 1σ (filled) and 3σ (dashed lines) confidence ellipses for each fit. The error-bars correspond to the projection of the 1σ confidence ellipse onto each of the parameter axes. Neither trend is significant at the 3σ level.

also be enhanced by the additional numerical viscosity in Eulerian codes such as ENZO, relative to the moving-mesh of AREPO (see Benincasa et al. 2013).

The Milky Way-mass galaxies with different rotation profiles studied by Nguyen et al. (2018) have similarly-high densities and filamentary morphologies to the simulations of (Utreras et al. 2020), due to the total absence of stellar feedback. They therefore contain no hot ISM phase, and the resulting GMCs are systematically larger and more massive than ours. The authors focus on the formation of GMCs via dynamics and cooling, but also conclude that the properties of GMCs (including the virial parameter, angular momentum, mass and size) are largely unaffected by the galactic rotation curve. The difference in stellar feedback prescription makes little difference to the distribution of virial parameters and turbulent velocity dispersions, which we find to be similar between this work, Nguyen et al. (2018) and Dobbs et al. (2011a), as mentioned earlier. It therefore appears that stellar feedback does not play a major role in the self-regulation of gravity and turbulence at molecular cloud scales and densities, in Milky Way-pressured galaxies: a finding that is consistent with the results of the smaller-scale simulations by Seifried et al. (2018) and Ibáñez-Mejía et al. (2016). We also concur that GMC masses and sizes are unaffected by galactic rotation, and in fact are largely unaffected by any dynamical process in Milky Way-pressured galaxies. However, we again note that for our simulations, a statistically-significant coupling between galactic shearing and cloud rotation is retrieved, in contrast to the conclusion of Nguyen et al. (2018) that cloud rotation is largely invariant of galactic rotation, in all but the largest clouds. This may be attributed to a smaller number of highly self-gravitating, high-density clumps in our simulations, owing to the efficacy of stellar feedback in disrupting such dense regions, consistent with observations (see below).

In terms of physics and resolution, the simulations most similar to ours are presented by Fujimoto et al. (2018, 2019), which include thermal energy and momentum from SNe, thermal energy from HII regions, mass injection from stellar winds, stochastic stellar population synthesis, and ISM heating and cooling. For a sample of GMCs in an isolated Milky Way-like disc galaxy, reaching $\sim$ 7 pc resolution in the densest gas, these authors are able to reproduce all of the galaxy-scale, kpc-scale and cloud-scale observables that we show in this work, with the exception of the observed decorrelation between stellar and gas peaks on small spatial scales (Kruijssen et al. 2018, 2019b; Chevance et al. 2020b). Given that the major difference between the two sets of simulations is the momentum-injection model for unresolved and marginally-resolved HII regions presented in Section 2, we tentatively attribute the adequate (rapid) disruption of gas peaks in our galaxies to this component of our models. This finding will be discussed further in an upcoming paper, Jeffreson et al. (prep).

Moving beyond isolated disc galaxies to galactic encounters and mergers, Tress et al. (2020) have compared the ISM on cloud scales in an isolated M51-analogue to the ISM in a simulation of the interaction between M51 and its companion. The authors find that although the interaction produces spiral structure and generates galaxy-scale gas flows, it does not have a significant influence on the global star formation rate or on the fraction of gas that is dense and molecular. Although the influence of galaxy interactions is beyond the scope of this work, the finding of Tress et al. (2020) is broadly consistent with star-forming dense gas that is over-pressured and over-dense, therefore decoupled from the ambient medium in its gravo-turbulent and star-forming properties, as seen for our GMCs. Such gas would be moved around by large-scale gas flows, but its internal properties would not be significantly altered.

Finally, on cosmological scales and at lower resolutions, Benincasa et al. (2019) have studied GMC populations in Milky Way-like zoom-in simulations selected from the FIRE-2 sample (Hopkins et al. 2018b). These authors find a variation of the molecular cloud lifetime with galactocentric radius, confirming observational (e.g. Kruijssen et al. 2019b; Chevance et al. 2020b), numerical (e.g. Dobbs & Pringle 2013), and theoretical (e.g. Jeffreson & Kruijssen 2018) findings that the cloud lifetime is environmentally-dependent. They use a complete suite of stellar feedback mechanisms, including radiation pressure, photo-ionisation, stellar winds

and supernovae. In a follow-up paper, Jeffreson et al. (subm), we study the explicit influence of the galactic-dynamical environment on the time-dependent properties of molecular clouds (i.e. their lifetimes, merger histories and evolution) and will connect these to the instantaneous properties studied in this work. We will then be able to make a more direct comparison to the cosmological-scale work of Benincasa et al. (2019).

6.2 Caveats of our simulations

In order to produce a realistic population of GMCs in our simulations, we require a realistic model of the interstellar medium. In Section 3, we have therefore compared the kpc-scale and galaxy-scale properties of our simulations to the corresponding sets of observables, and have found a high level of agreement. However, our simulations do not include every physical mechanism known to have a relevant influence on the baryon cycle and on the structure of the ISM. Local, higher-resolution studies such as the TIGRESS simulations (Kim & Ostriker 2017, 2018) and the SILCC simulations (Walch et al. 2015), demonstrate the relevance of magnetic fields, binary stars, cosmic rays, resolved SN bubbles and the self-consistent injection of momentum from stellar winds and outflows in setting the properties and structure of the three-phase ISM.

Firstly, we do not include the effect of magnetic fields in our simulations. Although GMCs themselves are generally observed to be magnetically super-critical (see the review by Crutcher 2012), the lower-density gas that forms the bulk of the ISM volume is threaded by field-lines and evolves according to the equations of magnetohydrodynamics. There is no clear observational consensus as to the role of these field lines in the formation of molecular clouds (see review by Hennebelle & Inutsuka 2019). The scales on which magnetic field lines are ordered and regular may be similar to the galactic dynamical scales considered in our work (Beck 2001), and may be coupled to galactic-dynamical processes such as differential rotation and the evolution of spiral arm structure (Beck 1996; Kim & Ostriker 2015b). As such, large-scale magnetic fields may affect the rates of GMC formation and destruction by galactic dynamics, as well as the environmental trends in the GMC properties presented here. The local velocity anisotropy of the ISM (Section 5.5.3) is expected to vary substantially with the magnetic field direction (e.g. Ossenkopf & Mac Low 2002; Otto et al. 2017), so the introduction of magnetic fields may substantially disrupt the shear-correlated trend in velocity anisotropy shown in Figure 23. Simulations by Girichidis et al. (2018) find that magnetic fields may also control the shapes and fragmentation of the sub-critical overdensities from which GMCs form, with the potential to influence their aspect ratios (Section 5.5.1).

Although we include mass injection from stellar winds, we do not include the momentum that they impart to the ISM. At solar metallicities, simulations of stellar winds within molecular clouds have demonstrated a profound influence on the masses of the stellar clusters they host (e.g. Gatto et al. 2017; Peters et al. 2017), and therefore on GMC morphologies and the duration of GMC lifetimes. The evolution of the HII regions within each cloud may also be altered by stellar winds, changing the time-scale over which pre-SN feedback is deposited into the ISM, along with the geometry of the subsequent SN explosions (e.g. Shull 1980). At our resolutions, we expect that the major effect of neglecting stellar wind energy is to shorten the duration of early-time stellar feedback and thus to reduce its overall efficacy in destroying GMCs.

Lastly, the resolution of our simulations is lower than in studies such as TIGRESS and SILCC, such that we do not explicitly resolve the Sedov-Taylor phase of SN blast-wave expansion. Instead, we use the mechanical feedback algorithm outlined in Section 2.6.1 to compute the final momentum of the blast-wave. Kim & Ostriker (2017) and Kim & Ostriker (2018) have shown that the hot gas generated during the resolved Sedov-Taylor phase of expansion is required to correctly reproduce the phase structure of the superbubbles driven by clustered supernovae, and so to correctly model the mass-loading and the phase structure of the galactic outflows associated with these bubbles. However, given that the assembly of our discs is not dependent on the high-redshift phase of galactic evolution, during which strong outflows may strongly affect the structure of the ISM, it is unlikely that the properties of our simulated GMCs and HI clouds are strongly affected by the exact multiphase structure of our winds. (Muratov et al. 2015) in particular have shown that the behaviour of such unresolved winds is roughly-correct in the low-redshift case, and consistent with these results, our model produces outflows out to several kpc above the galactic mid-plane (see Figure 6).

In addition to the missing physics outlined above, we note the possibility that our procedure for cloud identification has an influence on the GMC and HI cloud properties presented here, as explored by Grisdale et al. (2018). These authors model a time-evolving GMC population in a Milky Way-like disc at a spatial resolution of 4.5 pc, with thermal and kinetic stellar feedback from supernovae, stellar winds and HII regions. In agreement with our results, they find a close match between the properties of their simulated cloud population (specifically scaling relations, masses, sizes, densities and virial parameters) and observations of GMCs in the Milky Way. However, they also note that the cloud scaling relations are significantly steepened when GMCs are identified in 3D rather than 2D. In this work we have aimed to provide a direct comparison to observations by identifying clouds in 2D only, but in the future it will also be possible to examine the ways in which each GMC property is influenced by the number of spatial dimensions included during cloud identification, along with the algorithm used to define the boundaries of each GMC.

6.3 Future work

In the simulations presented here, we can distinguish clear galactic-dynamical correlations with the time-scales for gravitational free-fall and galactic shearing, as well as with the mid-plane hydrostatic pressure. However, we note that the dynamic range of the free-fall time-scale is small, and that the time-scales for epicyclic perturbations and for cloud-cloud collisions are ten times longer than the minimum dynamical time-scale, such that they play a negligible role in determining the physical properties of GMCs and HI clouds in Milky Way-pressured galaxies. In the future, we will extend the range of environments studied to include early-type galaxies (shorter epicyclic time-scales), spiral galaxies (shorter cloud-collision time-scales), and higher-pressure discs such as those observed at higher redshifts $z \sim 2$ (greater dynamic range in the free-fall time-scale). In the latter case, we expect GMCs to have lower over-pressures and over-densities relative to the galactic mid-plane, and so to be more strongly-coupled to the galactic-dynamical environment.

7 SUMMARY OF RESULTS

In this work, we have investigated the large-scale galactic-dynamical trends in the properties of GMCs and HI clouds within Milky Way-pressured galaxies. We have found that:

(i) The shortest galactic-dynamical time-scale across Milky Way-pressured environments is either the time-scale for galactic shearing τ_β or the time-scale for gravitational free-fall, $\tau_{\rm ff,g}$. Such environments span ~ 1 dex in the Toomre Q parameter, the orbital angular velocity Ω and the stellar contribution $\phi_{\rm P}$ to the mid-plane hydrostatic pressure, along with all values of the shear parameter from $\beta = 0$ (flat rotation curve) to $\beta = 1$ (solid-body rotation). Clouds that evolve under the influence of galactic dynamics in such galaxies are therefore most likely to have properties that correlate with τ_β and $\tau_{\rm ff,g}$.

(ii) The simulated GMCs in Milky Way-like environments are small, gravitationally-bound and gravitationally-collapsing, as well as highly over-dense and over-pressured relative to the ambient ISM. As such, they are decoupled from the gravitational and turbulent properties of the galactic mid-plane, and follow no galactic-dynamical trends in these properties. That is, the GMC velocity dispersions $\sigma_{\rm H_2}$, virial parameters $\alpha_{\rm vir,H_2}$ and turbulent pressures $P_{\rm turb,H_2}$ are decoupled from the galactic-dynamical environment.

(iii) The simulated HI clouds are gravitationally-unbound across all Milky Way-like environments, with much lower pressures and densities than the GMCs. Their velocity dispersions $\sigma_{\rm HI}$, virial parameters $\alpha_{\rm vir,HI}$ and turbulent pressures $P_{\rm turb,HI}$ all display statistically-significant (at the 3σ confidence level) trends with the mid-plane hydrostatic pressure $P_{\rm mp}$, with the time-scale $\tau_{\rm ff,g}$ for gravitational collapse, and with the time-scale τ_β for galactic shearing.

(iv) By contrast with the turbulent/gravitational properties of the GMCs and HI clouds, the rotational properties of both types of clouds display statistically-significant correlations with the galactic-dynamical variables $P_{\rm mp}$, $\tau_{\rm ff,g}$ and τ_β. The aspect ratio ϵ (along the galactic azimuthal direction) increases monotonically with the shear and free-fall rates. The plane-perpendicular angular momentum L_z also increases with the degree of shearing and gravitational stability, but its preferentially-prograde orientation implies that its magnitude is controlled primarily by the strength of the fictitious Coriolis force in the galaxy frame. Steeper trends and higher values of ϵ and L_z are observed for the HI clouds than for the GMCs. This is likely due to two effects: (1) GMCs have smaller sizes, higher densities and higher pressures than HI clouds, so are less susceptible to galactic-dynamical influences, and (2) GMCs inherit their rotational properties from their parent HI clouds, and the dynamical imprints in these properties are partially erased during their collapse.

(v) Like the cloud aspect ratios and angular momenta, the cloud velocity anisotropy B_σ is correlated with the rates of galactic shearing and gravitational free-fall, both for GMCs and for HI clouds. The clouds become more tangentially-biased at higher levels of galactic differential rotation and gravitational stability, indicating an increase in the prevalence of circulating gas about the cloud centre of mass, relative to radially-streaming gas. Both the absolute degree of anisotropy and its galactic-dynamical correlation is increased for GMCs, possibly due to the conservation of angular momentum during their collapse.

(vi) The number of GMCs per unit area of the galactic mid-plane sets the kpc-scale star formation rate across Milky Way-pressured galactic environments, which in turn is correlated with the mid-plane pressure, in agreement with observations.

(vii) The internal star-forming properties of GMCs are uncorrelated with the global SFR surface density, and are approximately-constant across all galactic-dynamic environments. That is, like the GMC turbulent pressures and velocity dispersions, the star-forming properties of GMCs are decorrelated from the galactic-dynamical environment.

(viii) The masses, sizes and surface densities of GMCs and HI clouds are uncorrelated with the galactic-dynamical environment.

(ix) All statistically significant, best-fitting relations between cloud properties and galactic-dynamical quantities are tabulated in Appendix B. We expect these predicted correlations to be testable using cloud-scale observations of the atomic and molecular ISM in nearby galaxies, such as those obtained by the PHANGS collaboration (e.g. Sun et al. 2018, Leroy et al. in prep.; Rosolowsky et al. in prep.).

We also make a comparison between the measured properties of beam-filling GMCs, identified via clump-finding, and molecular gas sight-lines at fixed spatial scale, independent of any clump-finding algorithm. We compare the latter to observations of molecular gas velocity dispersion, surface density, virial parameter and turbulent pressure by Sun et al. (2018, 2020), and find the following:

(i) The molecular gas sight-lines at 120-pc resolution have an average over-pressure of $\sim 4\times$, relative to the galactic mid-plane pressure on kpc-scales: approximately consistent with the average over-pressure of $2.8\times$ observed at the same resolution by Sun et al. (2020). As we increase the fixed resolution through 80, 45 and 30 pc, the over-pressure increases monotonically. We attribute the dependence of over-pressure on resolution to the dependence of the measured cloud surface density on the beam/sight-line filling factor.

(ii) Our beam-filling GMCs have an average over-pressure of $\sim 25\times$ and an over-density of $\sim 100\times$, relative to the galactic mid-plane. It is therefore unsurprising that the turbulent, gravitational and star-forming properties of GMCs are decoupled from the galactic-dynamical environment.

(iii) By contrast, our HI clouds have an average over-pressure of only $\sim 2\times$, relative to the galactic mid-plane. The HI clouds show clear galactic-dynamical trends in their turbulent and gravitational properties.

(iv) Given the above observations, we predict that galactic-dynamical trends *can* be obtained for the turbulent, gravitational and star-forming properties of GMCs. Such trends should be visible in higher-pressure galaxies (i.e. galaxies with $\log\left(P/k_{\rm B}\ {\rm K\ cm^{-3}}\right) > 4.5$), where a larger fraction of the total mid-plane gas is molecular, and so the cloud turbulent pressures are closer to the hydrostatic pressures of the galactic mid-plane. This is consistent with the observations of Chevance et al. (2020b), who find that the decoupling of GMC evolution from galactic dynamical processes occurs for kpc-scale molecular gas surface densities of $\Sigma_{\rm H_2} < 8\ {\rm M_\odot\ pc^{-2}}$.

In closing, we expect the galactic-dynamical trends in GMC and HI cloud properties identified here to produce corresponding trends in their lifecycles. In a follow-up paper, we will discuss the interplay between galactic dynamics and the cloud lifecycle in these simulations.

ACKNOWLEDGEMENTS

We thank the anonymous referee for an attentive and insightful report that improved the presentation of the results in our manuscript. We thank Volker Springel for allowing us access to AREPO. We thank Mark Krumholz for calculating and providing the DESPOTIC table of CO luminosities for interpolation. The authors acknowledge support by the High Performance and Cloud Computing Group at the Zentrum für Datenverarbeitung of the University of Tübingen, the state of Baden-Württemberg through bwHPC and the German Research Foundation (DFG) through grant no INST 37/935-1 FUGG. SMRJ, JMDK and MC gratefully acknowledge funding from the Deutsche Forschungsgemeinschaft (DFG, German Research Foundation) through an Emmy Noether Research Group (grant number KR4801/1-1) and the DFG Sachbeihilfe (grant number KR4801/2-1). SMRJ, JMDK and BWK gratefully acknowledge funding from the European Research Council (ERC) under the European Unions Horizon 2020 research and innovation programme via the ERC Starting Grant MUSTANG (grant agreement number 714907). BWK acknowledges funding in the form of a Postdoctoral Research Fellowship from the Alexander von Humboldt Stiftung. JMDK and SCOG acknowledge funding from the German Research Foundation (DFG) via the collaborative research center (SFB 881, Project-ID 138713538) 'The Milky Way System' (subproject B2 for JMDK and B1, B2 and B8 for SCOG). SCOG acknowledges financial support through Germanys Excellence Strategy project EXC-2181/1 - 390900948 (the Heidelberg STRUCTURES Cluster of Excellence). We are very grateful to Bruce Elmegreen, Mark Krumholz, Dominik Lentrodt, Adam Leroy, Eve Ostriker, Matthew Smith, Jiayi Sun, Robin Treß and Jacob Ward for helpful discussions.

REFERENCES

Agertz O., Kravtsov A. V., Leitner S. N., Gnedin N. Y., 2013, ApJ, 770, 25
Beck R., 1996, Nachr. Akad. Wiss. Göttingen II, 1996, 262
Beck R., 2001, Space Sci. Rev., 99, 243
Benincasa S. M., Tasker E. J., Pudritz R. E., Wadsley J., 2013, ApJ, 776, 23
Benincasa S. M., Wadsley J., Couchman H. M. P., Keller B. W., 2016, MNRAS, 462, 3053
Benincasa S. M., et al., 2019, arXiv e-prints, p. arXiv:1911.05251
Bertoldi F., McKee C. F., 1992, ApJ, 395, 140
Bigiel F., Leroy A., Walter F., Brinks E., de Blok W. J. G., Madore B., Thornley M. D., 2008, AJ, 136, 2846
Bigiel F., et al., 2016, ApJ, 822, L26
Binney J., Tremaine S., 1987, Galactic dynamics
Blanc G. A., Heiderman A., Gebhardt K., Evans II N. J., Adams J., 2009, ApJ, 704, 842
Bland-Hawthorn J., Gerhard O., 2016, ARA&A, 54, 529
Blitz L., Rosolowsky E., 2004, ApJ, 612, L29
Bolatto A. D., Wolfire M., Leroy A. K., 2013, ARA&A, 51, 207
Braine J., Hughes A., Rosolowsky E., Gratier P., Colombo D., Meidt S., Schinnerer E., 2020, A&A, 633, A17
Burkhart B., Lazarian A., Leão I. C., de Medeiros J. R., Esquivel A., 2014, ApJ, 790, 130
Calzetti D., Liu G., Koda J., 2012, ApJ, 752, 98
Chabrier G., 2003, PASP, 115, 763
Chevance M., et al., 2020a, Space Sci. Rev., 216, 50
Chevance M., et al., 2020b, MNRAS, 493, 2872
Chomiuk L., Povich M. S., 2011, AJ, 142, 197
Clark P. C., Glover S. C. O., Klessen R. S., 2012, MNRAS, 420, 745
Colombo D., et al., 2018, MNRAS, 475, 1791
Colombo D., et al., 2019, MNRAS, 483, 4291
Corbelli E., 2003, MNRAS, 342, 199
Crutcher R. M., 2012, ARA&A, 50, 29
Dobbs C. L., 2008, MNRAS, 391, 844
Dobbs C. L., Bonnell I. A., 2007, MNRAS, 376, 1747
Dobbs C. L., Pringle J. E., 2013, MNRAS, 432, 653
Dobbs C. L., Bonnell I. A., Pringle J. E., 2006, MNRAS, 371, 1663
Dobbs C. L., Burkert A., Pringle J. E., 2011a, MNRAS, 413, 2935
Dobbs C. L., Burkert A., Pringle J. E., 2011b, MNRAS, 417, 1318
Dobbs C. L., Pringle J. E., Burkert A., 2012, MNRAS, 425, 2157
Dobbs C. L., Pettitt A. R., Corbelli E., Pringle J. E., 2018, MNRAS, 478, 3793
Dobbs C. L., Rosolowsky E., Pettitt A. R., Braine J., Corbelli E., Sun J., 2019, MNRAS, 485, 4997
Elmegreen B. G., 1989, ApJ, 338, 178
Elmegreen B. G., 1995, MNRAS, 275, 944
Elmegreen D. M., Elmegreen B. G., Kaufman M., Brinks E., Struck C., Bournaud F., Sheth K., Juneau S., 2017, ApJ, 841, 43
Engargiola G., Plambeck R. L., Rosolowsky E., Blitz L., 2003, ApJS, 149, 343
Esquivel A., Lazarian A., 2011, ApJ, 740, 117
Faesi C. M., Lada C. J., Forbrich J., 2018, ApJ, 857, 19
Fagotto F., Bressan A., Bertelli G., Chiosi C., 1994a, A&AS, 104, 365
Fagotto F., Bressan A., Bertelli G., Chiosi C., 1994b, A&AS, 105, 29
Federrath C., Banerjee R., Clark P. C., Klessen R. S., 2010, ApJ, 713, 269
Feldmann R., Gnedin N. Y., Kravtsov A. V., 2011, ApJ, 732, 115
Freeman P., Rosolowsky E., Kruijssen J. M. D., Bastian N., Adamo A., 2017, MNRAS, 468, 1769
Fujimoto Y., Krumholz M. R., Tachibana S., 2018, MNRAS, 480, 4025
Fujimoto Y., Chevance M., Haydon D. T., Krumholz M. R., Kruijssen J. M. D., 2019, MNRAS, 487, 1717
Fukui Y., Mizuno N., Yamaguchi R., Mizuno A., Onishi T., 2001, PASJ, 53, L41
Gallagher M. J., et al., 2018, ApJ, 858, 90
Gatto A., et al., 2017, MNRAS, 466, 1903
Gensior J., Kruijssen J. M. D., Keller B. W., 2020, MNRAS, 495, 199
Gentry E. S., Krumholz M. R., Dekel A., Madau P., 2017, MNRAS, 465, 2471
Girichidis P., Seifried D., Naab T., Peters T., Walch S., Wünsch R., Glover S. C. O., Klessen R. S., 2018, MNRAS, 480, 3511
Glover S. C. O., Clark P. C., 2012, MNRAS, 421, 116
Glover S. C. O., Mac Low M.-M., 2007a, ApJS, 169, 239
Glover S. C. O., Mac Low M.-M., 2007b, ApJ, 659, 1317
Glover S. C. O., Federrath C., Mac Low M.-M., Klessen R. S., 2010, MNRAS, 404, 2
Gnat O., Ferland G. J., 2012, ApJS, 199, 20
Goldbaum N. J., Krumholz M. R., Forbes J. C., 2016, ApJ, 827, 28
Goldsmith P. F., Li D., Krčo M., 2007, ApJ, 654, 273
Gong M., Ostriker E. C., Wolfire M. G., 2017, ApJ, 843, 38
Grisdale K., Agertz O., Renaud F., Romeo A. B., 2018, MNRAS, 479, 3167
Gritschneder M., Naab T., Walch S., Burkert A., Heitsch F., 2009, ApJ, 694, L26
Habing H. J., 1968, Bull. Astron. Inst. Netherlands, 19, 421
Haid S., Walch S., Naab T., Seifried D., Mackey J., Gatto A., 2016, MNRAS, 460, 2962
Haid S., Walch S., Seifried D., Wünsch R., Dinnbier F., Naab T., 2018, MNRAS, 478, 4799
Hennebelle P., Inutsuka S.-i., 2019, Frontiers in Astronomy and Space Sciences, 6, 5
Hernquist L., 1990, ApJ, 356, 359
Heyer M. H., Carpenter J. M., Snell R. L., 2001, ApJ, 551, 852
Heyer M., Krawczyk C., Duval J., Jackson J. M., 2009, ApJ, 699, 1092
Ho I. T., et al., 2019, ApJ, 885, L31
Hopkins P. F., Quataert E., Murray N., 2012, MNRAS, 421, 3522
Hopkins P. F., et al., 2018a, MNRAS, 477, 1578
Hopkins P. F., et al., 2018b, MNRAS, 480, 800
Ibáñez-Mejía J. C., Mac Low M.-M., Klessen R. S., Baczynski C., 2016, ApJ, 824, 41

Iffrig O., Hennebelle P., 2015, A&A, 576, A95
Indriolo N., McCall B. J., 2012, ApJ, 745, 91
Jeffreson S. M. R., Kruijssen J. M. D., 2018, MNRAS, 476, 3688
Jeffreson S. M. R., et al., in prep., MNRAS
Jeffreson S. M. R., et al., to be subm., MNRAS
Joshi P. R., Walch S., Seifried D., Glover S. C. O., Clarke S. D., Weis M., 2019, MNRAS, 484, 1735
Joung M. R., Mac Low M.-M., Bryan G. L., 2009, ApJ, 704, 137
Kalberla P. M. W., Kerp J., 2009, ARA&A, 47, 27
Katz N., 1992, ApJ, 391, 502
Kauffmann J., Pillai T., Zhang Q., Menten K. M., Goldsmith P. F., Lu X., Guzmán A. E., 2017, A&A, 603, A89
Keller B. W., Kruijssen J. M. D., 2020, arXiv e-prints, p. arXiv:2004.03608
Keller B. W., Wadsley J., Benincasa S. M., Couchman H. M. P., 2014, MNRAS, 442, 3013
Keller B. W., Jeffreson S. M. R., Kruijssen J. M. D., inprep., MNRAS
Kennicutt Jr. R. C., 1998, ARA&A, 36, 189
Kennicutt R. C., Evans N. J., 2012, ARA&A, 50, 531
Kim C.-G., Ostriker E. C., 2015a, ApJ, 802, 99
Kim C.-G., Ostriker E. C., 2015b, ApJ, 815, 67
Kim C.-G., Ostriker E. C., 2017, ApJ, 846, 133
Kim C.-G., Ostriker E. C., 2018, ApJ, 853, 173
Kim J.-G., Kim W.-T., Ostriker E. C., 2018, ApJ, 859, 68
Kimm T., Cen R., 2014, ApJ, 788, 121
Klessen R. S., Hennebelle P., 2010, A&A, 520, A17
Koda J., et al., 2009, ApJ, 700, L132
Kreckel K., et al., 2018, ApJ, 863, L21
Kruijssen J. M. D., Longmore S. N., 2013, MNRAS, 435, 2598
Kruijssen J. M. D., Longmore S. N., 2014, MNRAS, 439, 3239
Kruijssen J. M. D., Schruba A., Hygate A. P. S., Hu C.-Y., Haydon D. T., Longmore S. N., 2018, MNRAS, 479, 1866
Kruijssen J. M. D., et al., 2019a, MNRAS, 484, 5734
Kruijssen J. M. D., et al., 2019b, Nature, 569, 519
Krumholz M. R., 2013, DESPOTIC: Derive the Energetics and SPectra of Optically Thick Interstellar Clouds, Astrophysics Source Code Library (ascl:1304.007)
Krumholz M. R., Matzner C. D., 2009, ApJ, 703, 1352
Krumholz M. R., Tan J. C., 2007, ApJ, 654, 304
Krumholz M. R., Dekel A., McKee C. F., 2012, ApJ, 745, 69
Krumholz M. R., Fumagalli M., da Silva R. L., Rendahl T., Parra J., 2015, MNRAS, 452, 1447
Krumholz M. R., McKee C. F., Bland -Hawthorn J., 2018, arXiv e-prints, p. arXiv:1812.01615
Larson R. B., 1981, MNRAS, 194, 809
Larson R. B., 1994, in Wilson T. L., Johnston K. J., eds, Lecture Notes in Physics, Berlin Springer Verlag Vol. 439, The Structure and Content of Molecular Clouds. p. 13, doi:10.1007/3540586210˙2
Lazarian A., Pogosyan D., Esquivel A., 2002, in Taylor A. R., Landecker T. L., Willis A. G., eds, Astronomical Society of the Pacific Conference Series Vol. 276, Seeing Through the Dust: The Detection of HI and the Exploration of the ISM in Galaxies. p. 182 (arXiv:astro-ph/0112368)
Leitherer C., et al., 1999, ApJS, 123, 3
Leroy A. K., Walter F., Brinks E., Bigiel F., de Blok W. J. G., Madore B., Thornley M. D., 2008, AJ, 136, 2782
Leroy A. K., et al., 2013, AJ, 146, 19
Leroy A. K., et al., 2017, ApJ, 846, 71
Licquia T. C., Newman J. A., 2015, ApJ, 806, 96
Liu G., Koda J., Calzetti D., Fukuhara M., Momose R., 2011, ApJ, 735, 63
Longmore S. N., et al., 2013, MNRAS, 429, 987
Luna A., Bronfman L., Carrasco L., May J., 2006, ApJ, 641, 938
MacLaren I., Richardson K. M., Wolfendale A. W., 1988a, ApJ, 333, 821
MacLaren I., Richardson K. M., Wolfendale A. W., 1988b, ApJ, 333, 821
Mao S. A., Ostriker E. C., Kim C.-G., 2019, arXiv e-prints, p. arXiv:1911.05078
Marchuk A. A., 2018, MNRAS, 476, 3591
Martizzi D., Faucher-Giguère C.-A., Quataert E., 2015, MNRAS, 450, 504
Mathis J. S., Mezger P. G., Panagia N., 1983, A&A, 500, 259
Matzner C. D., 2002, ApJ, 566, 302
Meidt S. E., et al., 2013, ApJ, 779, 45
Meidt S. E., et al., 2018, ApJ, 854, 100
Meidt S. E., et al., 2020, ApJ, 892, 73
Miville-Deschênes M.-A., Murray N., Lee E. J., 2017, ApJ, 834, 57
Miyamoto M., Nagai R., 1975, PASJ, 27, 533
Mouschovias T. C., Tassis K., Kunz M. W., 2006, ApJ, 646, 1043
Muratov A. L., Kereš D., Faucher-Giguère C.-A., Hopkins P. F., Quataert E., Murray N., 2015, MNRAS, 454, 2691
Murray N., Rahman M., 2010, ApJ, 709, 424
Nelson A. F., 2006, MNRAS, 373, 1039
Nelson R. P., Langer W. D., 1997, ApJ, 482, 796
Nguyen N. K., Pettitt A. R., Tasker E. J., Okamoto T., 2018, MNRAS, 475, 27
Nixon C. J., Pringle J. E., 2018, preprint, (arXiv:1809.04921)
Oka T., Hasegawa T., Sato F., Tsuboi M., Miyazaki A., Sugimoto M., 2001, ApJ, 562, 348
Ossenkopf V., Mac Low M. M., 2002, A&A, 390, 307
Ostriker E. C., Shetty R., 2011, ApJ, 731, 41
Ostriker E. C., McKee C. F., Leroy A. K., 2010, ApJ, 721, 975
Otto F., Ji W., Li H.-b., 2017, ApJ, 836, 95
Padoan P., Pan L., Haugbølle T., Nordlund Å., 2016, ApJ, 822, 11
Padoan P., Haugbølle T., Nordlund Å., Frimann S., 2017, ApJ, 840, 48
Peters T., et al., 2017, MNRAS, 466, 3293
Plummer H. C., 1911, MNRAS, 71, 460
Pontzen A., Roškar R., Stinson G. S., Woods R., Reed D. M., Coles J., Quinn T. R., 2013, pynbody: Astrophysics Simulation Analysis for Python
Rahman N., et al., 2011, ApJ, 730, 72
Rahman N., et al., 2012, ApJ, 745, 183
Rahner D., Pellegrini E. W., Glover S. C. O., Klessen R. S., 2017, MNRAS, 470, 4453
Reina-Campos M., Kruijssen J. M. D., 2017, MNRAS, 469, 1282
Rice T. S., Goodman A. A., Bergin E. A., Beaumont C., Dame T. M., 2016, ApJ, 822, 52
Rix H.-W., Bovy J., 2013, A&A Rev., 21, 61
Robitaille T. P., Whitney B. A., 2010, ApJ, 710, L11
Roman-Duval J., Jackson J. M., Heyer M., Rathborne J., Simon R., 2010, ApJ, 723, 492
Rosolowsky E., Blitz L., 2005, ApJ, 623, 826
Rosolowsky E., Leroy A., 2006, PASP, 118, 590
Rosolowsky E., Engargiola G., Plambeck R., Blitz L., 2003, ApJ, 599, 258
Safranek-Shrader C., Krumholz M. R., Kim C.-G., Ostriker E. C., Klein R. I., Li S., McKee C. F., Stone J. M., 2017, MNRAS, 465, 885
Saintonge A., et al., 2011, MNRAS, 415, 32
Savage B. D., Wakker B. P., 2009, ApJ, 702, 1472
Schinnerer E., et al., 2013, ApJ, 779, 42
Schinnerer E., et al., 2019, ApJ, 887, 49
Schruba A., Leroy A. K., Walter F., Sand strom K., Rosolowsky E., 2010, ApJ, 722, 1699
Schruba A., et al., 2011, AJ, 142, 37
Seifried D., et al., 2017, MNRAS, 472, 4797
Seifried D., Walch S., Haid S., Girichidis P., Naab T., 2018, ApJ, 855, 81
Seifried D., Haid S., Walch S., Borchert E. M. A., Bisbas T. G., 2020, MNRAS, 492, 1465
Sembach K. R., Howk J. C., Ryans R. S. I., Keenan F. P., 2000, ApJ, 528, 310
Semenov V. A., Kravtsov A. V., Gnedin N. Y., 2017, ApJ, 845, 133
Semenov V. A., Kravtsov A. V., Gnedin N. Y., 2018, ApJ, 861, 4
Semenov V. A., Kravtsov A. V., Gnedin N. Y., 2019, ApJ, 870, 79
Shetty R., Beaumont C. N., Burton M. G., Kelly B. C., Klessen R. S., 2012, MNRAS, 425, 720
Shull J. M., 1980, ApJ, 238, 860
Slyz A. D., Devriendt J. E. G., Bryan G., Silk J., 2005, MNRAS, 356, 737
Smith M. C., Sijacki D., Shen S., 2018, MNRAS, 478, 302
Solomon P. M., Vanden Bout P. A., 2005, ARA&A, 43, 677
Solomon P. M., Rivolo A. R., Barrett J., Yahil A., 1987, ApJ, 319, 730
Springel V., 2010, MNRAS, 401, 791

Springel V., Di Matteo T., Hernquist L., 2005, MNRAS, 361, 776
Su K.-Y., Hopkins P. F., Hayward C. C., Faucher-Giguère C.-A., Kereš D., Ma X., Robles V. H., 2017, MNRAS, 471, 144
Sun J., et al., 2018, ApJ, 860, 172
Sun J., et al., 2020, ApJ, 892, 148
Suwannajak C., Tan J. C., Leroy A. K., 2014, ApJ, 787, 68
Tamburro D., Rix H. W., Leroy A. K., Mac Low M. M., Walter F., Kennicutt R. C., Brinks E., de Blok W. J. G., 2009, AJ, 137, 4424
Tan J. C., 2000, ApJ, 536, 173
Tasker E. J., 2011, ApJ, 730, 11
Tasker E. J., Tan J. C., 2009, ApJ, 700, 358
Tassis K., Mouschovias T. C., 2004, ApJ, 616, 283
Teyssier R., 2015, ARA&A, 53, 325
Toomre A., 1964, ApJ, 139, 1217
Tress R. G., Smith R. J., Sormani M. C., Glover S. C. O., Klessen R. S., Mac Low M.-M., Clark P. C., 2020, MNRAS, 492, 2973
Truelove J. K., Klein R. I., McKee C. F., Holliman John H. I., Howell L. H., Greenough J. A., 1997, ApJ, 489, L179
Usero A., et al., 2015, AJ, 150, 115
Utomo D., et al., 2018, ApJ, 861, L18
Utreras J., et al., 2020, ApJ, 892, 94
Vázquez G. A., Leitherer C., 2005, ApJ, 621, 695
Virtanen P., et al., 2020, Nature Methods, 17, 261
Walch S., Naab T., 2015, MNRAS, 451, 2757
Walch S. K., Whitworth A. P., Bisbas T., Wünsch R., Hubber D., 2012, MNRAS, 427, 625
Walch S., et al., 2015, MNRAS, 454, 238
Walter F., Brinks E., de Blok W. J. G., Bigiel F., Kennicutt Robert C. J., Thornley M. D., Leroy A., 2008, AJ, 136, 2563
Ward J. L., Chevance M., Kruijssen J. M. D., Hygate A. P. S., Schruba A., Longmore S. N., 2020, MNRAS submitted
Williams J. P., McKee C. F., 1997, ApJ, 476, 166
Wolfire M. G., McKee C. F., Hollenbach D., Tielens A. G. G. M., 2003, ApJ, 587, 278
Yin J., Hou J. L., Prantzos N., Boissier S., Chang R. X., Shen S. Y., Zhang B., 2009, A&A, 505, 497
da Silva R. L., Fumagalli M., Krumholz M., 2012, ApJ, 745, 145
da Silva R. L., Fumagalli M., Krumholz M. R., 2014, MNRAS, 444, 3275
de Avillez M. A., Breitschwerdt D., 2005, A&A, 436, 585

This paper has been typeset from a TEX/LATEX file prepared by the author.

SUPPORTING INFORMATION

Supplementary data are available at MNRAS online.

Tables. Catalogues of the physical properties and galactic-dynamical parameters of all GMCs and HI clouds presented in this paper.

Please note: Oxford University Press is not responsible for the content or functionality of any supporting materials supplied bby the authors. Any queries (other than missing material) should be directed to the corresponding author for the article.

APPENDIX A: CALCULATION OF LARGE-SCALE GALAXY PROPERTIES

The results presented in Section 5 depend on the large-scale environmental properties of the ISM in each simulated galaxy. Here we describe the data analysis procedures used to calculate the variation of these properties on kpc-scales as 1D radial profiles and as 2D projection maps.

A1 1D radial profiles of $(\beta, Q, \Omega, \phi_{\rm P})$

In order to examine the cloud properties presented in Section 5 as a function of the galactic-dynamical environment, we must compute the radial profiles of β, Q, Ω and $\phi_{\rm P}$, as described in Section 4.3. Between galactocentric radii of $R = 1$ kpc and $R = 13$ kpc, we use 50 overlapping bins with widths of 1-kpc, collecting the gas cells $i = 1...N$ and star particles $* = 1...M$ in each bin by performing a tree-walk of radius $\Delta R = 0.5$ kpc about the bin centre, and discarding gas cells with temperatures $T > 10^4$ K. We then calculate the gas line-of-sight velocity dispersion $\sigma_{\rm los,g}$, as

$$\sigma_{\rm los,g}(R) = \frac{\sigma_{\rm g}}{\sqrt{3}} = \sqrt{\frac{\langle |\mathbf{v}_i - \langle \mathbf{v}_i \rangle|^2 \rangle}{3}}, \tag{A1}$$

where the angled brackets denote the mass-weighted average over the gas cells in each radial bin, with velocity vectors $\{\mathbf{v}_i\}$. By using the above isotropic approximation, we assume that the turbulent length-scale is much shorter than the length-scale over which galactic rotation is noticeable, and also much shorter than the pressure scale-height of the galactic disc. In addition, we calculate the gas sound speed as

$$c_s = \Big\langle \Big(\frac{k_B T_i}{\mu m_p} \Big)^{\frac{1}{2}} \Big\rangle, \tag{A2}$$

the gas and live stellar surface densities $\Sigma_{\rm g}$ and $\Sigma_{\rm s_{live}}$ as

$$\Sigma_{\rm g,s_{live}}(R) = \frac{1}{\pi[(R+\Delta R)^2 - (R-\Delta R)^2]} \sum_{i,*=1}^{N,M} m_{i,*}, \tag{A3}$$

and the circular velocity v_c at the mid-plane, as

$$v_{\rm c}(R) = \Big\langle -\frac{y_i}{R} v_{x,i} + \frac{x_i}{R} v_{y,i} \Big\rangle. \tag{A4}$$

Using the circular velocity v_c, we obtain the angular velocity $\Omega(R) = v_{\rm c}/R$ and the shear parameter $\beta(R) = \partial \ln v_{\rm c} / \partial \ln R$, simultaneously smoothing the profile and performing the first-order derivative using a Savitzky-Golay kernel of window-length 35 and polynomial order 4. The parameters β and Ω allow us to calculate the epicyclic frequency $\kappa = \Omega\sqrt{2(1+\beta)}$, and from this quantity we obtain the Toomre Q parameter as

$$Q = \frac{\kappa \sqrt{\sigma^2 + c_s^2}}{\pi G \Sigma_{\rm g}}. \tag{A5}$$

Finally, the parameter $\phi_{\rm P}$ is obtained via Equation (A10), using the 1D radial profiles of $\sigma_{\rm g}$, $\Sigma_{\rm g}$, $\rho_{\rm s}$ and $\Sigma_{\rm s,live}$.

A2 2D projection maps of $\Sigma_{\rm H_2}$, $\Sigma_{\rm HI}$ and $\Sigma_{\rm g}$

We produce projection maps of gas surface densities using AREPO's native ray-tracing algorithm. Within each map, the value of the 2D field $F(x, y)$ at every pixel is computed by sending a ray from 1 kpc below to 1 kpc above the galactic mid-plane, then taking the density-weighted average of the relevant 3D field $f(x, y, z)$ over the set of intersected gas cells. Only those cells with temperatures $T \lesssim 1 \times 10^4$ K are considered, to ensure that the 2D projection approximates the value of the field at the galactic mid-plane. Given that the scale height of the cold gas in each disc is at maximum $\sim$400 pc, this vertical range safely captures all gas cells of interest. The resulting density-weighted projection F at the position (x, y) may be written as

$$F(x,y) = \Sigma_{\rm g}(x,y)^{-1} \int_{z=-1\ {\rm kpc}}^{z=+1\ {\rm kpc}} dz\ \rho_{\rm g} f(x,y,z), \tag{A6}$$

where $\Sigma_{\rm g}(x, y) = \int_{-\infty}^{\infty} {\rm d}z \rho_{\rm g}(z)$ is the total gas column density at the same position. The corresponding field pairs $[f(x, y, z), F(x, y)]$ for each gas surface density map are given by

$$\begin{aligned} f_{\rm H_2} &= \frac{2.3 \times 10^{-29} {\rm M_\odot (ergs^{-1})^{-1}}}{m_{\rm H}[{\rm M_\odot}]} L_{\rm CO}[{\rm ergs^{-1}}] \\ f_{\rm HI} &= x_{\rm HI} \\ f_{\rm g} &= 1, \end{aligned} \tag{A7}$$

where $x_{\rm HI}$ is the abundance of atomic hydrogen per unit mass, and

$$\begin{aligned} F_{\rm H_2} &= \Sigma_{\rm H_2} \Sigma_{\rm g}^{-1} \\ F_{\rm HI} &= \Sigma_{\rm HI} \Sigma_{\rm g}^{-1} \\ F_{\rm g} &= 1. \end{aligned} \tag{A8}$$

We then obtain $\Sigma_{\rm H_2}$ or $\Sigma_{\rm HI}$ by taking the product with $\Sigma_{\rm g}$.

A3 2D projection maps of Σ_*

The star particles in AREPO are not contained in the Voronoi mesh but are treated as collisionless point particles. As such, we use the `pynbody.sph` analysis module (Pontzen et al. 2013) to produce the 2D projection maps of all stellar properties. Within each simulation snapshot, an M4 spline SPH kernel is assigned to all star particles, with a variable smoothing length that encloses its 32 nearest neighbours. The value of the 2D field at each pixel is then computed by taking the kernel-weighted average of the relevant 3D field $f(x, y, z)$ over the set of star particles whose smoothing lengths overlap with the coordinate (x, y).

A4 2D projection maps of $\Sigma_{\rm SFR}$

The central row of panels in Figure 9 displays 2D maps of the SFR surface density $\Sigma_{\rm SFR}$ for each simulated galaxy. These are produced by calculating the stellar surface density maps for young stars only, with ages 0-5 Myr, approximately-matching the ages of stars traced by H-α emission. We simply divide the values in this map by the time interval (5 Myr) to obtain an estimate of $\Sigma_{\rm SFR}$.

A5 2D projection maps of $\phi_{\rm P}$

To quantify the relative influence of the stellar and gaseous components of the ISM in producing gravitational instability and setting the mid-plane pressure of the galactic disc, we have used the parameter $\phi_{\rm P}$ introduced in Elmegreen (1989), defined as

$$\phi_{\rm P} = 1 + \frac{\Sigma_{\rm s}}{\Sigma_{\rm g}} \frac{\sigma_{\rm g}}{\sigma_{\rm s}}, \tag{A9}$$

where $\Sigma_{\rm g}$, $\Sigma_{\rm s}$ are the gas and stellar surface densities, and $\sigma_{\rm g}$, $\sigma_{\rm s}$ are the gas and stellar velocity dispersions. Given that we use an external potential to model the stellar disc and bulge components, we are not able to obtain an accurate estimate of $\sigma_{\rm s}$. We therefore additionally assume that the scale-height of the stellar disc is significantly higher than that of the gas disc, so that the stars maintain their own state of collisionless equilibrium, independent of the gas (c.f. Blitz & Rosolowsky 2004). This leads to

$$\phi_{\rm P} = 1 + \frac{\sigma_{\rm g}}{\Sigma_{\rm g}} \sqrt{\frac{2\rho_{\rm s}}{\pi G}}, \tag{A10}$$

where $\rho_{\rm s}$ is the mid-plane stellar volume density, and we compute this quantity by combining the contribution of the live stellar particles with that of the external potential, such that

$$\rho_{\rm s} = \frac{1}{4\pi G} \frac{1}{R} \frac{\partial}{\partial R} \left[R \frac{\partial(\Phi_{\rm d} + \Phi_{\rm b})}{\partial R} \right] \Big|_{z=0} + \frac{\Sigma_{\rm s_{live}}}{4H}, \tag{A11}$$

where $\Sigma_{\rm s_{live}}$ is the stellar surface density of the live stellar particles (calculated per Section A3), H is the stellar disc scale-height (calculated per Section A7), and $\Phi_{\rm d}$ and $\Phi_{\rm b}$ are the disc and bulge components of the applied potential, given by Equations (2) and (4), respectively. The final two quantities in the 2D projection of Equation (A10) are then the total gas surface density $\Sigma_{\rm g}$ (Section A2) and the total gas velocity dispersion $\sigma_{\rm g}$ (Section A6).

A6 Gas velocity dispersion, $\sigma_{\rm g}$

In order to compute the 2D projection of $\phi_{\rm P}$, we require a 2D projection of the gas velocity dispersion $\sigma_{\rm g}$. The three-dimensional turbulent velocity dispersion at the position of each gas cell is not tracked during our simulations. We calculate this quantity in post-processing using the particle positions, densities and velocity vectors in each simulation snapshot, according to Gensior et al. (2020). For a given Voronoi cell, $\sigma_{\rm g}$ is given by

$$\sigma_{\rm g} = \langle |\mathbf{v}_i - \langle \mathbf{v}_i \rangle|^2 \rangle, \tag{A12}$$

where the angled brackets denote a (cubic spline) kernel-weighted average over the set of nearest-neighbour gas cells with velocity vectors $\{\mathbf{v}_i\}$, chosen according to the variable tree-walk radius defined in Equation (7) of Gensior et al. (2020). Briefly, this radius is set to $|\langle \rho_{\rm g} \rangle / \langle \nabla \rho_{\rm g} \rangle|$, where $\langle \nabla \rho_{\rm g} \rangle$ is the kernel-weighted average of the volume density gradient with respect to the radial distance from the central cell. In every case, the smoothing length for the cubic spline kernel is chosen to enclose the 32 nearest neighbour cells. We refer the reader to the cited work for a more detailed explanation.

Following the computation of the $\sigma_{\rm g}$ for each gas cell, we compute its 2D density-weighted projection along the z-axis using Equation (A6). The corresponding 2D projection of the line-of-sight velocity dispersion is then given by

$$\sigma_{\rm los} = \sigma_{\rm g} / \sqrt{3}. \tag{A13}$$

A7 Disc scale height and scale-length

The gas and stellar disc scale-heights $z_{\rm d}$ or disc scale-lengths $R_{\rm d}$ for an exponential disc are uniquely determined by the ratio of the mass enclosed within $z_{\rm d}$ or $R_{\rm d}$, relative to the total mass of the galactic disc, such that

$$\int_0^{z_{\rm d}} \rho(R, z)\, {\rm d}z = (1 - e^{-1}) \int_0^{\infty} \rho(R, z)\, {\rm d}z \tag{A14}$$

$$\int_0^{R_{\rm d}} \rho(R, z)\, {\rm d}R = (1 - 2e^{-1}) \int_0^{\infty} \rho(R, z)\, {\rm d}R. \tag{A15}$$

Azimuthally-averaged values for each disc are given in Table 1 and in Figure 14.

APPENDIX B: STATISTICAL SIGNIFICANCE OF GALACTIC-DYNAMICAL TRENDS

In Table 3 and Figure 16, we present the relative statistical significance of the correlation between each physical cloud property and the two minimum galactic-dynamical time-scales (τ_β and $\tau_{\rm ff,g}$) across Milky Way-pressured environments, along with the pressure $P_{\rm mp}$ at the galactic mid-plane. We determine the statistical significance by performing a non-linear least squares optimisation to fit a straight line $y = ax + b$ to each data set, where x corresponds to a set of 50 non-overlapping bins in one of the independent variables τ_β, $\tau_{\rm ff,g}$ or $P_{\rm mp}$. The dependent variable y is mean value of a given cloud property in each bin, a is the slope of the fit and b is its y-axis intercept. We use the CURVEFIT function from SCIPY (Virtanen et al. 2020) to perform the optimisation and to calculate the covariance matrix of the dataset as

$$C(x, y) = \begin{bmatrix} {\rm Var}(x) & {\rm Cov}(x, y) \\ {\rm Cov}(x, y) & {\rm Var}(y) \end{bmatrix}. \tag{B1}$$

We then compute the eigenvalues (E_1, E_2) and eigenvectors $(\hat{\mathbf{e}}_1, \hat{\mathbf{e}}_2)$ of the covariance matrix to obtain the confidence ellipse of the parameters a and b. The confidence ellipse is centred on the optimum values $(a = a_0, b = b_0)$ for the fit parameters, has major and minor axes lengths of $N\sqrt{E_1} = 3\sqrt{E_1}$ and $N\sqrt{E_2} = 3\sqrt{E_2}$ at the 3σ level, and has a position angle of $\theta = \arctan(\hat{\mathbf{e}}_2 \cdot \hat{\mathbf{x}} / \hat{\mathbf{e}}_1 \cdot \hat{\mathbf{x}})$. Crucially, the confidence ellipse shows both the correlation and the spread of the fit parameters. For each of our cloud properties, we find that the variance of the slope is typically small, however it displays a significant degree of correlation with the y-intercept, which has a much larger variance. The correlation can be seen in the elongation of any of the confidence ellipses presented in Figures B2 to B18. Rather than using the variance E_1 on the fit parameter a to calculate its error, we therefore consider the slope to be consistent with zero at the 3σ level if the ellipse crosses the line $a = 0$ at any point. If the ellipse makes no such crossing, then we consider that the data are consistent with a non-zero correlation between independent and dependent variables at the 3σ level. Correspondingly, the error on the slope is quoted as the projection of the 1σ confidence ellipse onto the a-axis of the fit parameter space.

In the case of the two galactic dynamical time-scales τ_β and $\tau_{\rm ff,g}$, we consider two distinct dynamical regimes. In one, the time-scale τ_X is competitive with the minimum galactic-dynamical time-scale $\tau_{\rm min}$ to within a factor of two, such that $\tau_X \leqslant \tau_{\rm min}$. In the other, it is longer and therefore less competitive, such that $\tau_X > \tau_{\rm min}$. We expect that in the former

regime, the influence of a given dynamical mechanism on the properties of GMCs and HI clouds is greater. As discussed in Section 4, a key result of this work is that the time-scale for gravitational free-fall $\tau_{\rm ff,g}$ is competitive across all Milky Way-pressured environments, and as such we need only to consider the first regime for $\tau_{\rm ff,g}$, represented by the filled data points in Figures B2 to B18. Conversely, the time-scale τ_β for galactic shearing partitions the simulation data between the two regimes. Where a statistically-significant correlation with τ_β is present, we observe a clear break in the slope at $\tau_\beta = \tau_{\rm min}$, and so we fit the two regimes separately.

In Tables B1, B2 and B3, we list those cloud properties that display statistically-significant correlations with the dynamical variables $P_{\rm mp}$, $\tau_{\rm ff,g}$ and τ_β, respectively. We give the range of the correlation in each independent variable, its slope and its intercept, along with the associated errors.

Table B1. Statistically-significant correlations between each cloud property (dependent variable, y) and the logarithm of the hydrostatic mid-plane pressure, $P_{\rm mp}$ (independent variable, x).

y-property	$y \propto \log\left(P_{\rm mp}/k_{\rm B}{\rm K\ cm^{-3}}\right)$			Figure
	x-range	Slope	y-intercept	
$\sigma_{\rm HI}/{\rm kms^{-1}}$	$3.6 \rightarrow 4.3$	4.30 ± 0.19	-9.5 ± 0.8	B2
$\log \alpha_{\rm vir,HI}$	$3.6 \rightarrow 4.3$	0.42 ± 0.02	-0.29 ± 0.06	B4
$\log\left(P_{\rm turb,HI}/k_{\rm B}{\rm K\ cm^{-3}}\right)$	$3.6 \rightarrow 4.3$	0.62 ± 0.02	1.91 ± 0.07	B6
$\epsilon_{\rm H_2}$	$3.6 \rightarrow 4.3$	0.54 ± 0.05	0.18 ± 0.19	B9
$\epsilon_{\rm HI}$	$3.6 \rightarrow 4.3$	0.74 ± 0.09	-0.6 ± 0.4	B10
$\log\left(L_{z,{\rm H_2}}/{\rm pc\ kms^{-1}}\right)$	$3.6 \rightarrow 4.3$	0.51 ± 0.03	-1.40 ± 0.13	B11
$\log\left(L_{z,{\rm HI}}/{\rm pc\ kms^{-1}}\right)$	$3.6 \rightarrow 4.3$	0.83 ± 0.05	-1.75 ± 0.20	B12
$B_{\sigma,{\rm H_2}}$	$3.6 \rightarrow 4.3$	-0.49 ± 0.06	1.4 ± 0.3	B13
$\log\left(\Sigma_{N_{\rm cl},{\rm H_2}}/{\rm kpc^{-2}}\right)$	$3.6 \rightarrow 4.3$	0.391 ± 0.004	-0.69 ± 0.01	B15
$\log\left(\Sigma_{N_{\rm cl},{\rm HI}}/{\rm kpc^{-2}}\right)$	$3.6 \rightarrow 4.3$	0.376 ± 0.003	-0.643 ± 0.013	B16

Table B2. Statistically-significant correlations between each cloud property (dependent variable, y) and the logarithm of the mid-plane free-fall time-scale $\tau_{\rm ff,g}$ (independent variable, x).

y-property	$y \propto \log\left(\tau_{\rm ff,g}/{\rm Myr}\right)$			Figure
	x-range	Slope	y-intercept	
$\sigma_{\rm HI}/{\rm kms^{-1}}$	$1.4 \rightarrow 1.9$	-4.0 ± 0.6	14.1 ± 1.1	B2
$\log \alpha_{\rm vir,HI}$	$1.4 \rightarrow 1.9$	-0.28 ± 0.06	1.84 ± 0.1	B4
$\log\left(P_{\rm turb,HI}/k_{\rm B}{\rm K\ cm^{-3}}\right)$	$1.4 \rightarrow 1.9$	-0.84 ± 0.05	5.73 ± 0.08	B6
$\epsilon_{\rm H_2}$	$1.4 \rightarrow 1.9$	-0.83 ± 0.08	3.71 ± 0.14	B9
$\epsilon_{\rm HI}$	$1.4 \rightarrow 1.9$	-1.8 ± 0.2	5.2 ± 0.3	B10
$\log\left(L_{z,{\rm H_2}}/{\rm pc\ kms^{-1}}\right)$	$1.4 \rightarrow 1.9$	-1.26 ± 0.05	2.70 ± 0.09	B11
$\log\left(L_{z,{\rm HI}}/{\rm pc\ kms^{-1}}\right)$	$1.4 \rightarrow 1.9$	-2.04 ± 0.10	4.91 ± 0.17	B12
$B_{\sigma,{\rm H_2}}$	$1.4 \rightarrow 1.9$	1.05 ± 0.12	-2.3 ± 0.2	B13
$\log\left(\Sigma_{N_{\rm cl},{\rm H_2}}/{\rm kpc^{-2}}\right)$	$1.4 \rightarrow 1.9$	-1.44 ± 0.06	3.24 ± 0.10	B15
$\log\left(\Sigma_{N_{\rm cl},{\rm HI}}/{\rm kpc^{-2}}\right)$	$1.4 \rightarrow 1.9$	-0.75 ± 0.05	1.98 ± 0.10	B16

Table B3. Statistically-significant correlations between each cloud property (dependent variable, y) and the logarithm of the time-scale τ_β for galactic shearing (independent variable, x).

y-property	$y \propto \log\left(\tau_\beta/{\rm Myr}\right)$			Figure
	x-range	Slope	y-intercept	
$\sigma_{\rm HI}/{\rm kms^{-1}}$	$1.2 \rightarrow 2.1$	-2.8 ± 0.3	13.0 ± 0.6	B2
$\log \alpha_{\rm vir,HI}$	$1.2 \rightarrow 2.1$	-0.22 ± 0.02	1.80 ± 0.03	B4
$\log\left(P_{\rm turb,HI}/k_{\rm B}{\rm K\ cm^{-3}}\right)$	$1.2 \rightarrow 2.1$	-0.36 ± 0.02	5.05 ± 0.04	B6
$\epsilon_{\rm H_2}$	$1.2 \rightarrow 2.1$	-0.39 ± 0.03	3.10 ± 0.05	B9
$\epsilon_{\rm HI}$	$1.2 \rightarrow 2.1$	-0.81 ± 0.04	3.89 ± 0.07	B10
$\log\left(L_{z,{\rm H_2}}/{\rm pc\ kms^{-1}}\right)$	$1.2 \rightarrow 2.1$	-0.41 ± 0.02	1.41 ± 0.04	B11
$\log\left(L_{z,{\rm HI}}/{\rm pc\ kms^{-1}}\right)$	$1.2 \rightarrow 2.1$	-0.79 ± 0.05	3.04 ± 0.10	B12
$B_{\sigma,{\rm H_2}}$	$1.2 \rightarrow 2.1$	0.35 ± 0.05	-1.23 ± 0.07	B13
$\log\left(\Sigma_{N_{\rm cl},{\rm H_2}}/{\rm kpc^{-2}}\right)$	$1.2 \rightarrow 2.1$	-0.77 ± 0.04	2.29 ± 0.06	B15
$\log\left(\Sigma_{N_{\rm cl},{\rm HI}}/{\rm kpc^{-2}}\right)$	$1.2 \rightarrow 2.1$	-0.72 ± 0.06	1.97 ± 0.09	B16

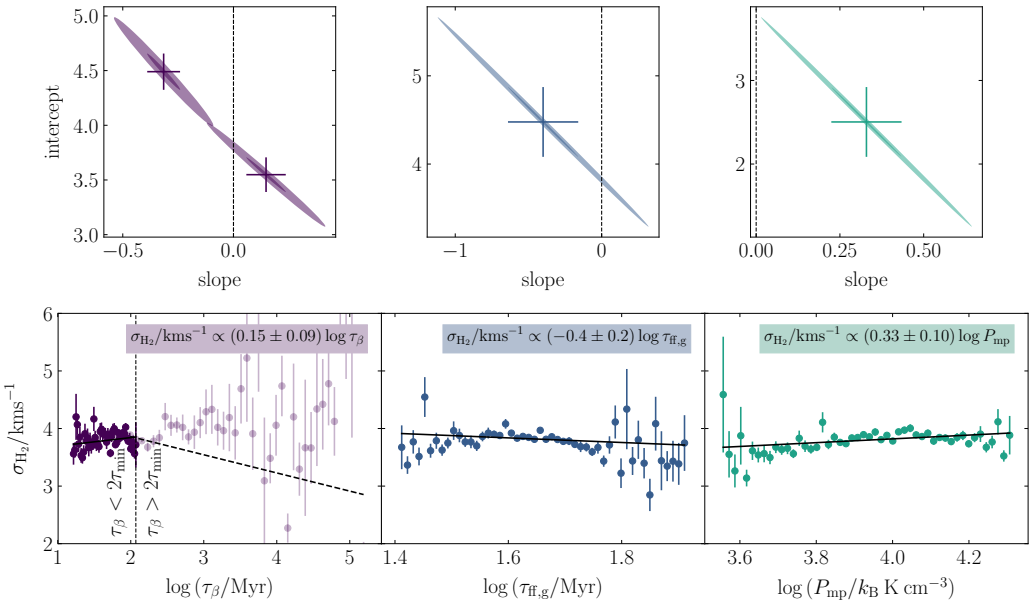

Figure B1. *Lower panels:* Mean line-of-sight GMC velocity dispersion σ_{H_2} as a function of the time-scale for galactic shearing (τ_β, left), the time-scale for gravitational free-fall ($\tau_{ff,g}$, centre) and the mid-plane pressure (P_{mp}, right). The error-bars correspond to the standard deviation on the mean for the distribution of values in each bin. The equations in each panel give the non-linear least-squares fit to the data in each panel. In the case of the shear time-scale (left), the data are fitted in two distinct regimes: one in which the shear time-scale is shorter than twice the minimum galactic-dynamical time-scale τ_{min} (dark purple points, left of the vertical dashed line) and one in which it is longer (transparent points, right of the vertical dashed line). *Upper panels:* The 1σ (dark-coloured) and 3σ (light-coloured) confidence ellipses for each fit. The error-bars correspond to the projection of the 1σ confidence ellipse onto each of the parameter axes.

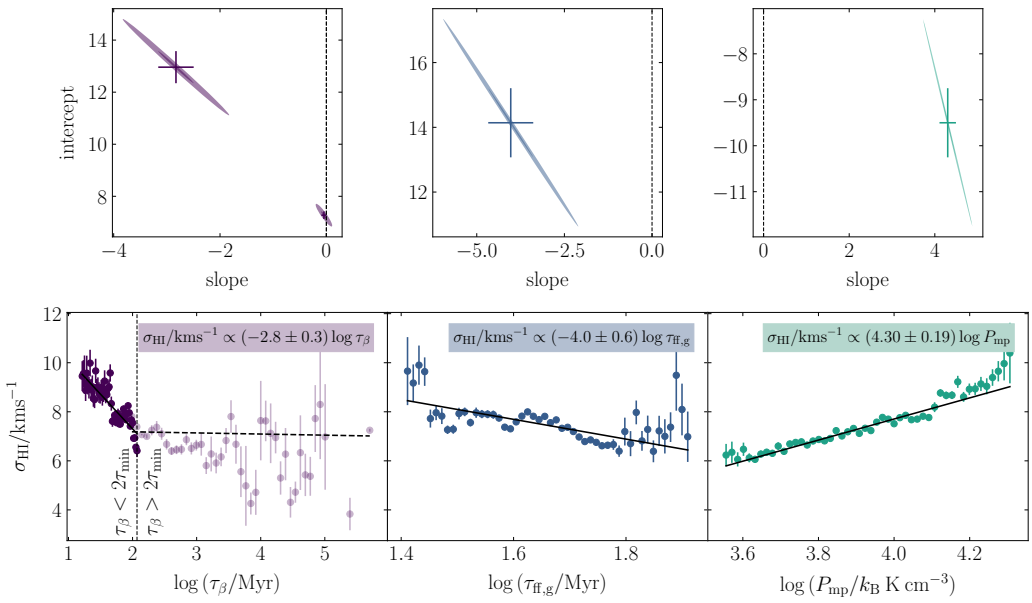

Figure B2. Same as Figure B1, but for the HI cloud velocity dispersion, σ_{HI}.

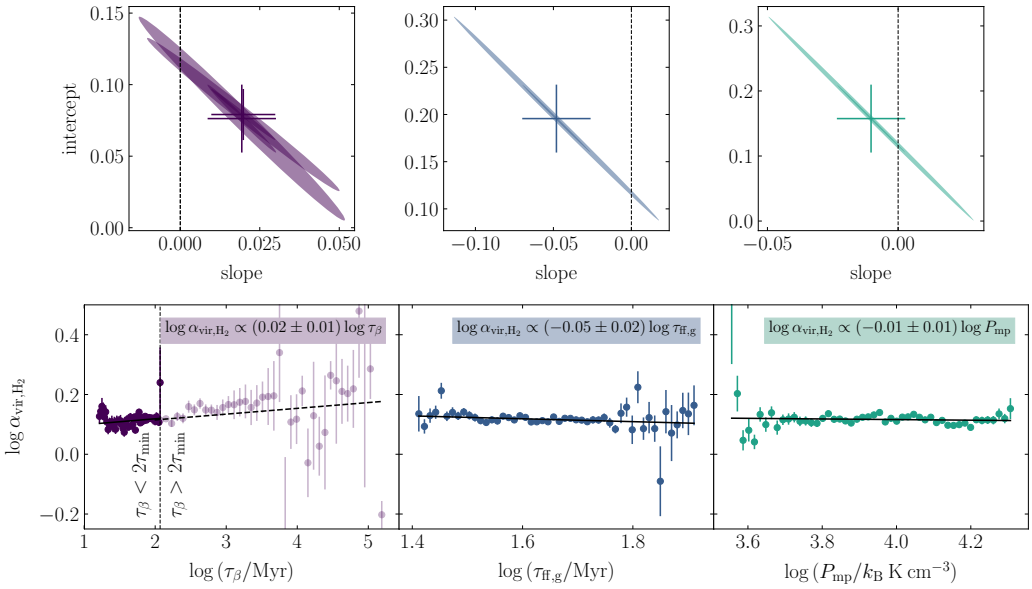

Figure B3. Same as Figure B1, but for the GMC virial parameter, $\alpha_{\rm vir,H_2}$.

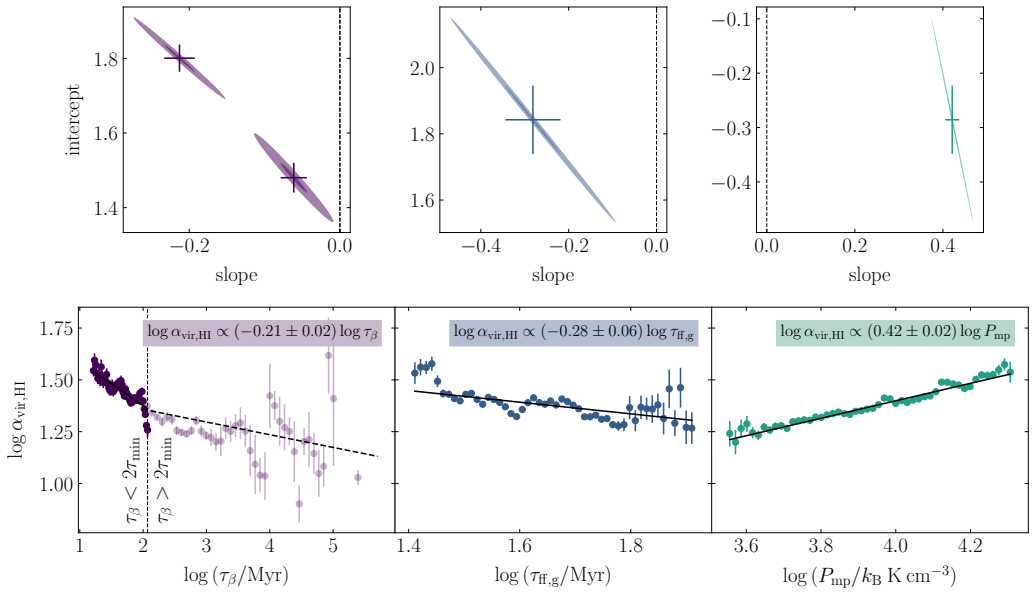

Figure B4. Same as Figure B1, but for the HI cloud virial parameter, $\alpha_{\rm vir,HI}$.

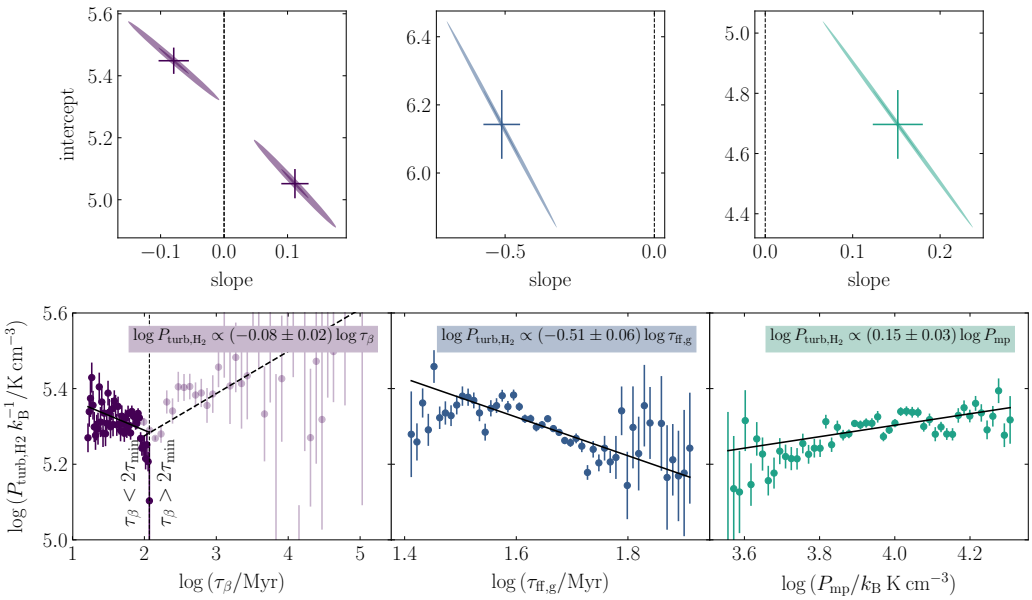

Figure B5. Same as Figure B1, but for the GMC internal turbulent pressure, $P_{\rm turb,H_2}$.

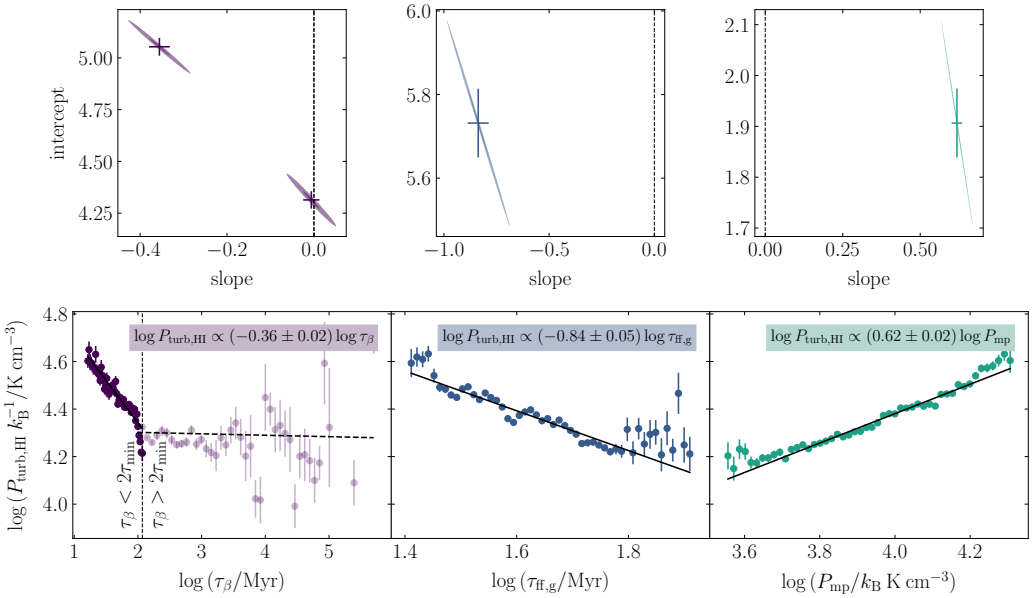

Figure B6. Same as Figure B1, but for the HI cloud internal turbulent pressure, $P_{\rm turb,HI}$.

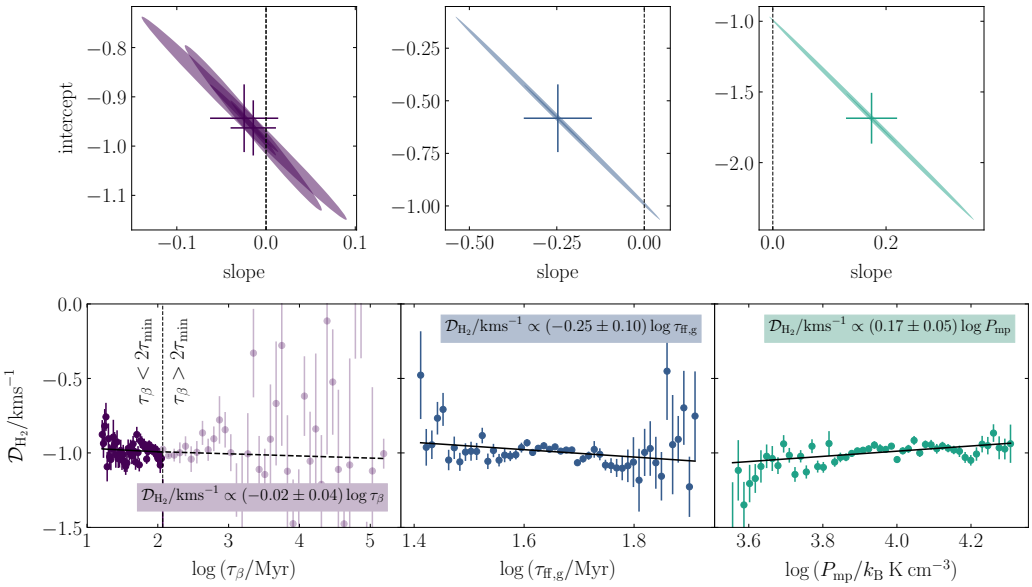

Figure B7. Same as Figure B1, but for the GMC velocity divergence, $\mathcal{D}_{\rm H_2}$.

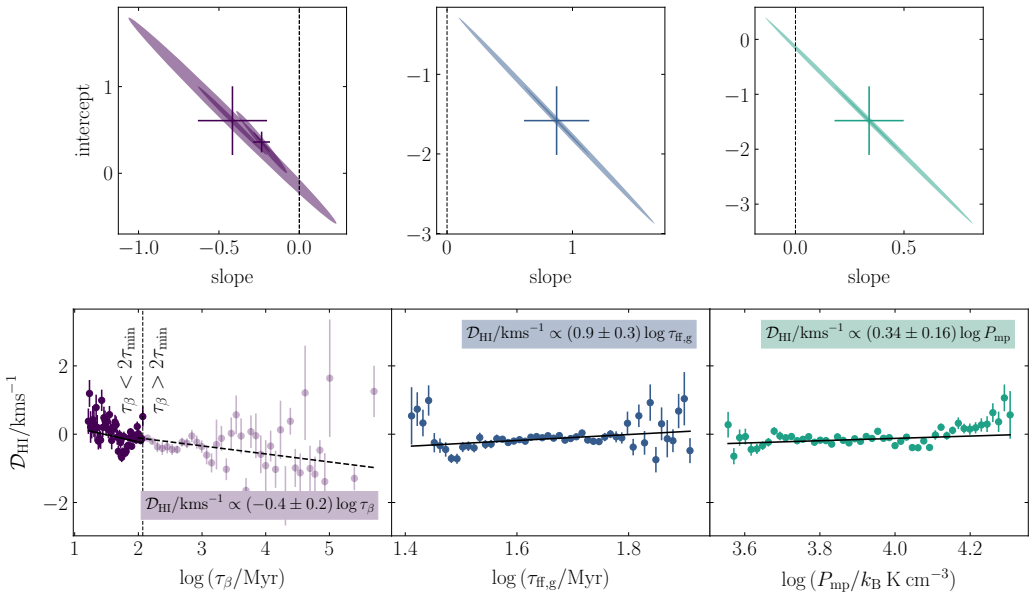

Figure B8. Same as Figure B1, but for the HI cloud velocity divergence, $\mathcal{D}_{\rm HI}$.

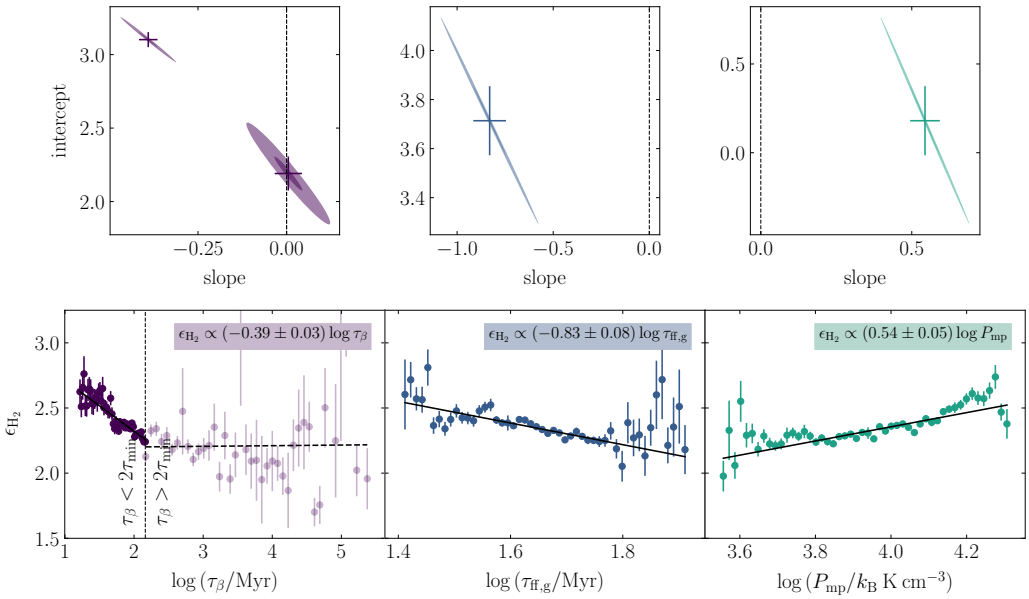

Figure B9. Same as Figure B1, but for the GMC aspect ratio, ϵ_{H_2}.

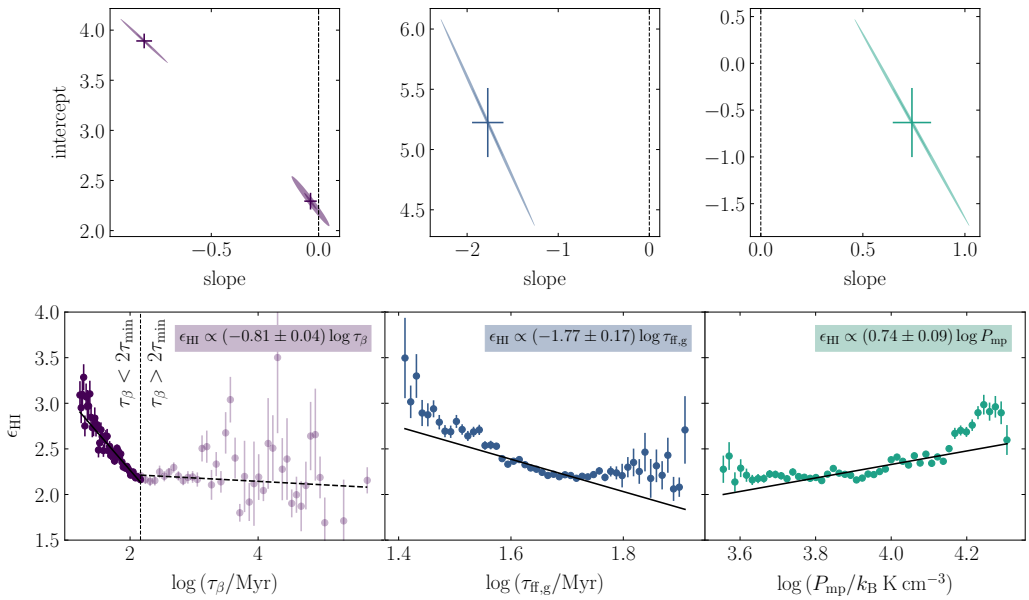

Figure B10. Same as Figure B1, but for the HI cloud aspect ratio, ϵ_{HI}.

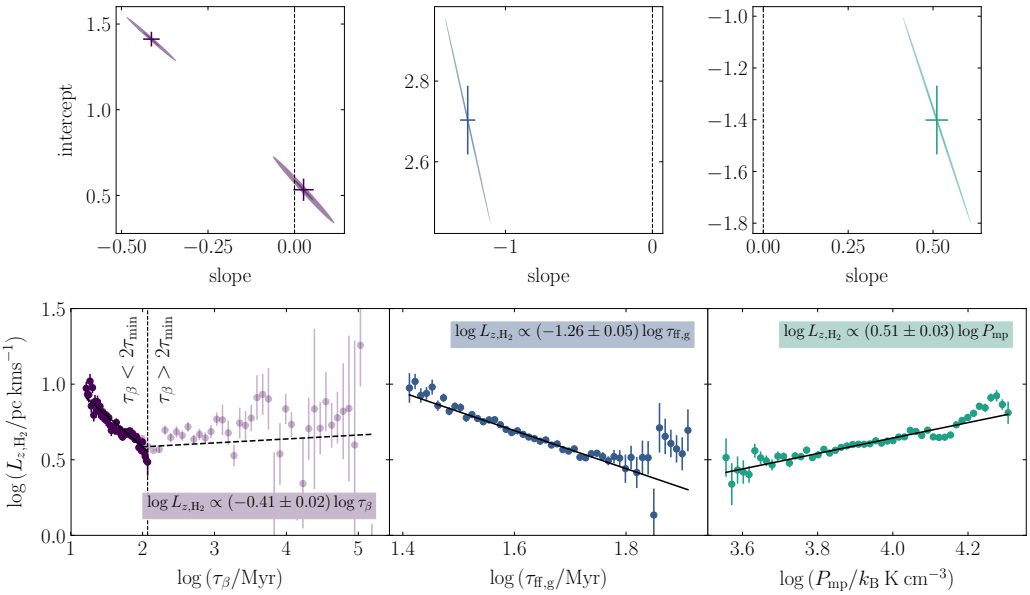

Figure B11. Same as Figure B1, but for the GMC specific angular momentum, $L_{z,\mathrm{H_2}}$.

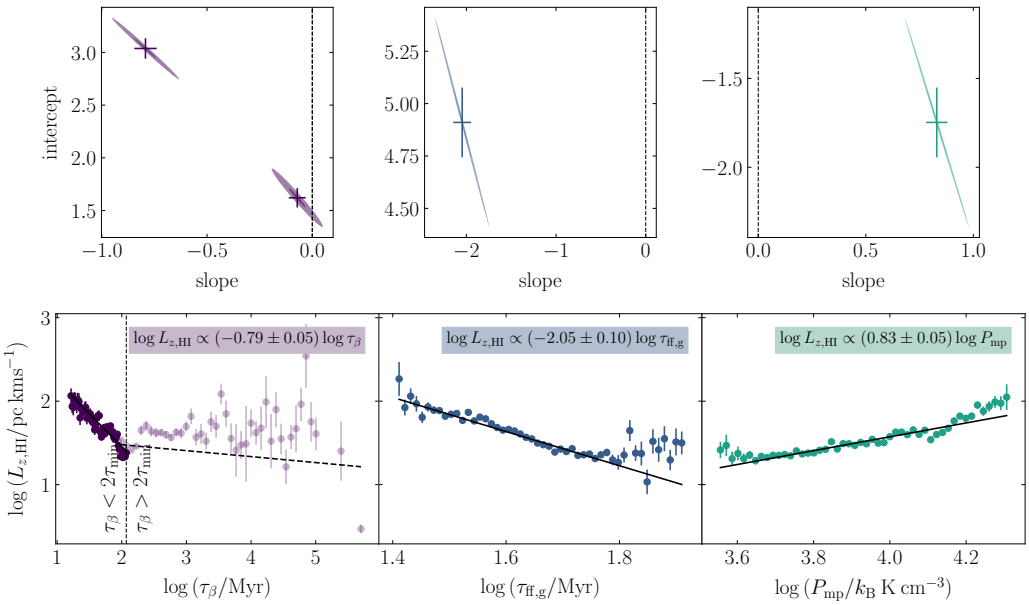

Figure B12. Same as Figure B1, but for the HI cloud specific angular momentum, $L_{z,\mathrm{HI}}$.

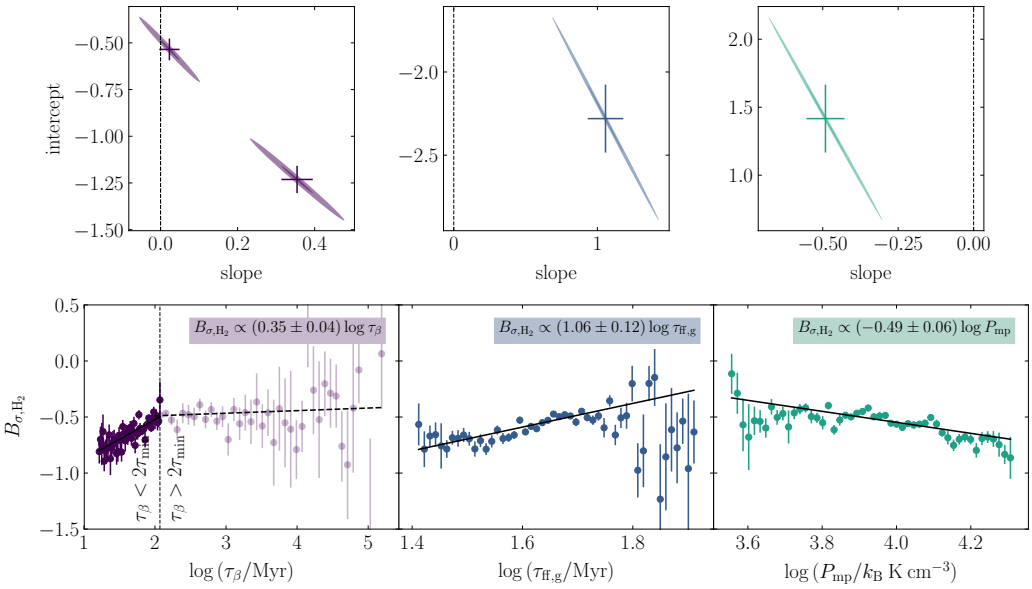

Figure B13. Same as Figure B1, but for the GMC velocity anisotropy, $B_{\sigma,\mathrm{H_2}}$.

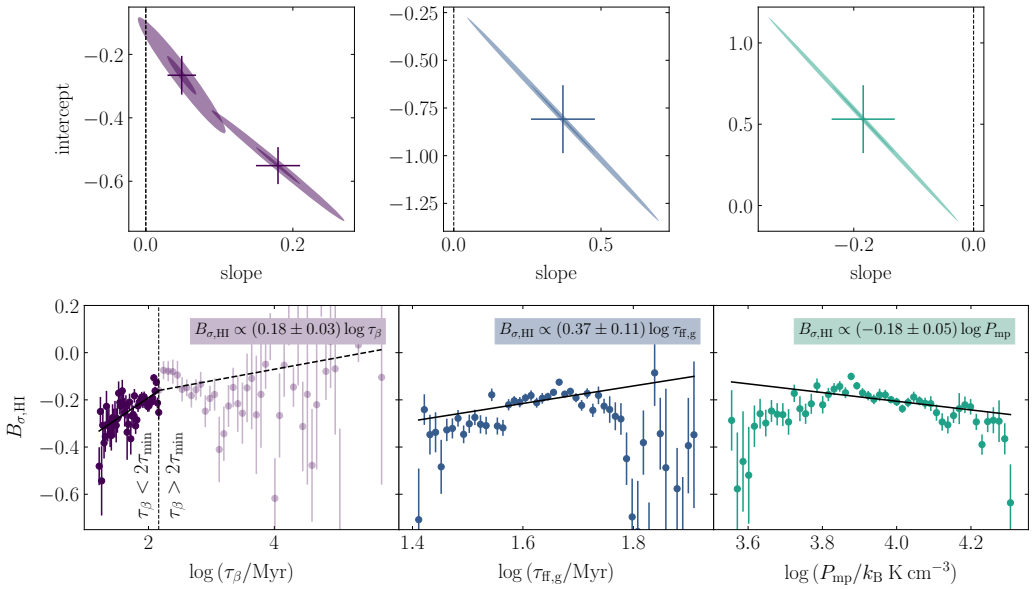

Figure B14. Same as Figure B1, but for the HI cloud velocity anisotropy, $B_{\sigma,\mathrm{HI}}$.

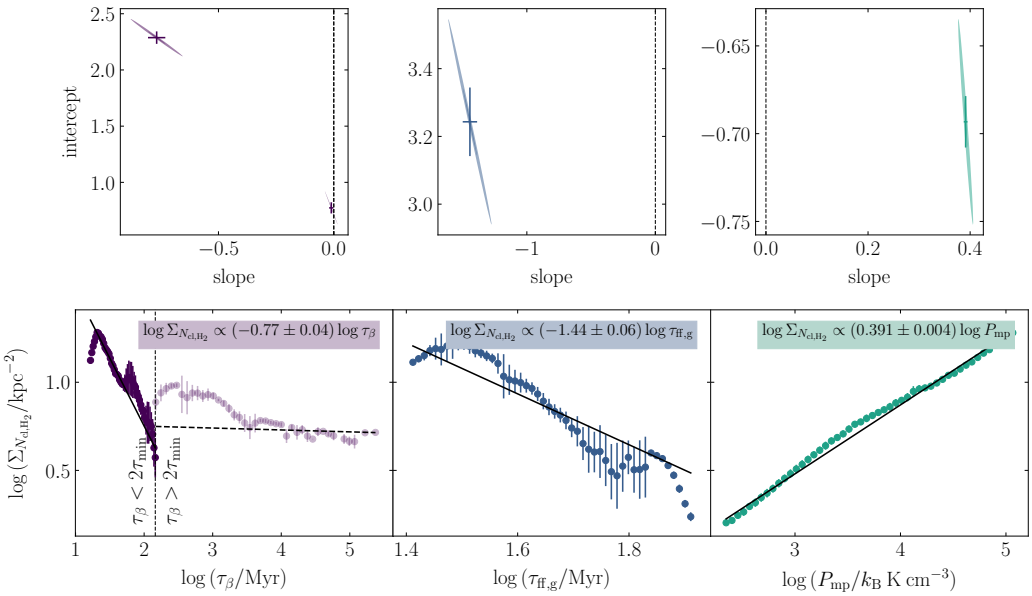

Figure B15. Same as Figure B1, but for the number of GMCs per unit area of the galactic mid-plane, $\Sigma_{N_{\rm cl,H_2}}$.

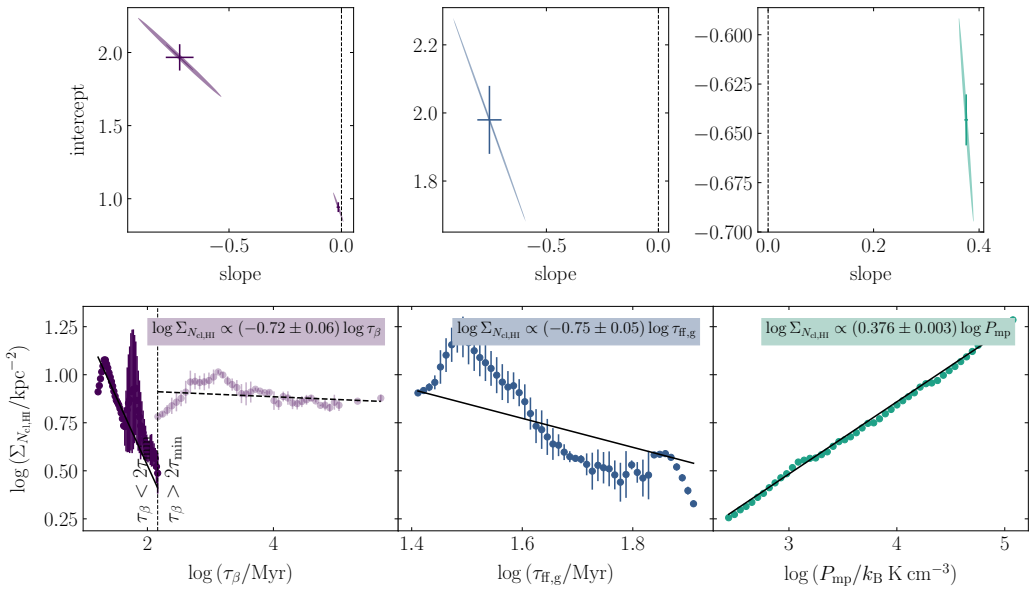

Figure B16. Same as Figure B1, but for the number of HI clouds per unit area of the galactic mid-plane, $\Sigma_{N_{\rm cl,HI}}$.

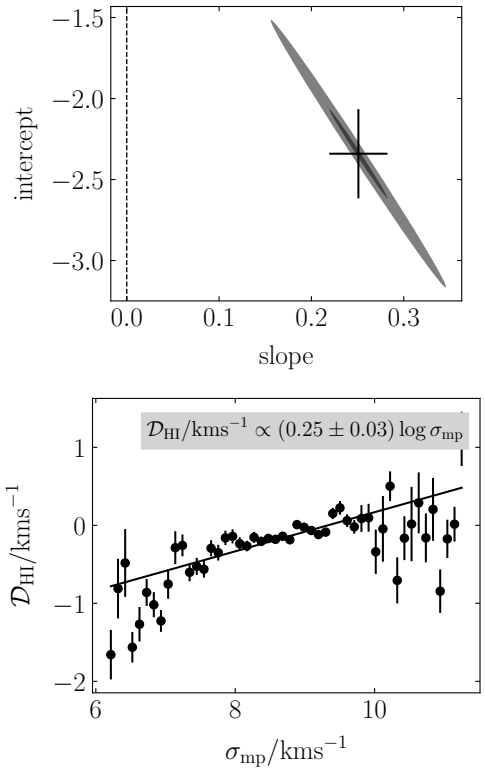

Figure B17. *Lower panel:* Mean HI cloud velocity divergence $\mathcal{D}_{\rm HI}$ as a function of the mid-plane velocity dispersion $\sigma_{\rm mp}$. The error-bars correspond to the standard deviation on the mean for the distribution of values in each bin. The equation gives the non-linear least-squares fit to the data. *Upper panel:* The 1σ (dark-coloured) and 3σ (light-coloured) confidence ellipses for the least-squares fit. The error-bars correspond to the projection of the 1σ confidence ellipse onto each of the parameter axes.

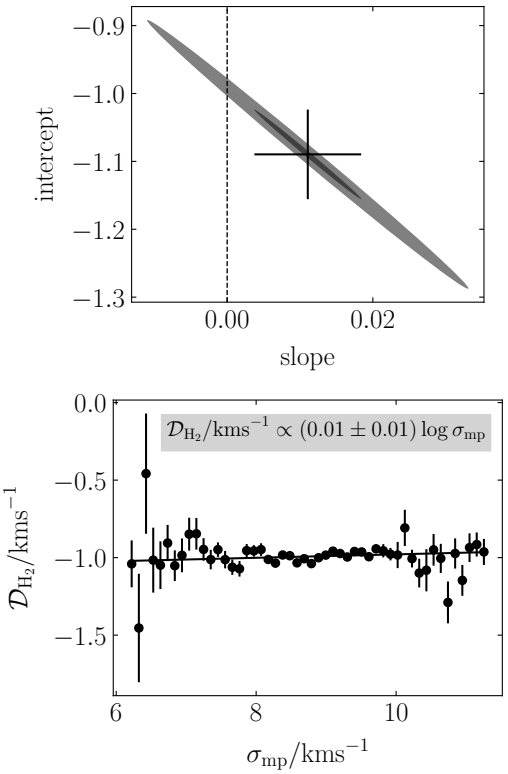

Figure B18. Same as Figure B17, but for the GMC velocity divergence, $\mathcal{D}_{\rm H_2}$.

Chapter 5

A scaling relation for the molecular cloud lifetime in Milky Way-like galaxies

The content of this chapter is a draft of a paper to be submitted.

MNRAS **000**, 1–19 (2020) Preprint 17 August 2020 Compiled using MNRAS LATEX style file v3.0

A scaling relation for the molecular cloud lifetime in Milky Way-like galaxies

Sarah M. R. Jeffreson⋆ et. al.
Astronomisches Rechen-Institut, Zentrum für Astronomie der Universität Heidelberg, Mönchhofstraße 12-14, 69120 Heidelberg, Germany

17 August 2020

ABSTRACT

We derive the detailed cloud evolution networks for three Milky Way-like isolated galaxy simulations at a temporal resolution of 1 Myr, spanning two orders of magnitude in spatial scale from ~ 10 pc up to ~ 1 kpc. The highest-resolution networks contain a cumulative total of $\sim 80,000$ separate molecular clouds in different galactic-dynamical environments. We calculate the characteristic cloud lifetime $\tau_{\rm life}$ for each galaxy as a function of the cloud spatial scale ℓ, finding that it obeys a broken scaling relation, with $\tau_{\rm life} \propto \ell^{-0.3}$ below the scale-height of the thin galactic gas disc, $\ell \lesssim 100$ pc, and $\tau_{\rm life} \sim {\rm constant}$ above the disc scale-height. The scaling relation of cloud lifetimes is consistent with the higher efficiency of star formation per free-fall time that is required to disperse small, dense regions of molecular gas against the pull of their own self-gravity, relative to larger, more diffuse regions. Consistent with the importance of self-gravity in driving the evolution of the simulated cloud population, the characteristic cloud lifetime is decoupled from the influence of galactic dynamics across all galactic environments. Clouds undergo mergers at a rate proportional to the crossing time between their centroids, but are inert to the interactions between their edges. At the gas disc scale-height, the molecular cloud lifetime converges to the crossing time of the gas disc, as clouds become vertically-confined and are no longer self-gravitating. At these scales, we find $\tau_{\rm life} \sim 13$ Myr, consistent with observations.

Key words: stars: formation — ISM: clouds — ISM: evolution — ISM: kinematics and dynamics — galaxies: evolution — galaxies: ISM

1 INTRODUCTION

Giant molecular clouds (GMCs) provide the reservoirs of cold molecular gas from which the majority of stars are formed (Kennicutt & Evans 2012). Their lifetimes place an upper bound on the time-scale for star formation at a given spatial scale, which in combination with observations of the gas and star formation rate surface densities (e.g. Kennicutt 1998; Bigiel et al. 2008; Leroy et al. 2008; Blanc et al. 2009; Schruba et al. 2010; Liu et al. 2011), constrains the value of the local star formation efficiency (SFE). As such, a prediction for the molecular cloud lifetime provides two key insights about the conversion of gas to stars in galaxies: (1) an understanding of the physics that limit the duration of star-formation episodes, and (2) a prediction for the fraction of gas that is converted to stars during these episodes.

Over the past two decades, observational evidence has mounted to support the view of molecular clouds as rapidly-evolving entities with lifetimes of order the dynamical time-scale, varying between 10 and 55 Myr (Engargiola et al. 2003; Blitz et al. 2007; Kawamura et al. 2009; Murray 2011; Miura et al. 2012; Meidt et al. 2015; Corbelli et al. 2017; Kruijssen et al. 2019; Chevance et al. 2020). These measurements contrast with past studies that tie molecular cloud lifetimes to the survival times of their constituent H_2 molecules (e.g. Scoville & Hersh 1979; Scoville & Solomon 1975; Koda et al. 2009). To complement these studies of giant molecular cloud time-scales, a growing body of observational evidence now points towards a correlation of cloud properties with their large-scale galactic environments, across a range of spatial scales. In particular, significant environmental variations have been found in the integrated star formation efficiency (Leroy et al. 2008), the SFE per free-fall time (Utomo et al. 2018), the molecular cloud surface density, turbulent velocity dispersion and turbulent pressure (e.g. Sun et al. 2018; Colombo et al. 2019; Sun et al. 2020), the molecular cloud size (Heyer et al. 2009; Roman-Duval et al. 2010; Rice et al. 2016; Miville-Deschênes et al. 2017; Colombo et al. 2019), and the galactic dense gas fraction (Usero et al. 2015; Bigiel et al. 2016). In accordance with both numerical simulations (Dobbs & Pringle 2013; Fujimoto et al. 2014; Dobbs et al. 2015; Benincasa et al. 2019) and analytic predictions (Meidt et al. 2018; Jeffreson & Kruijssen 2018), observed GMCs do not form and evolve in isolation, but are part of a network of galactic processes spanning from the kpc-scales of galactic dynamics down to the sub-cloud physics of star formation and stellar feedback.

Within this hierarchical baryon cycle, it has long been known

⋆ s.jeffreson@uni-heidelberg.de

that the time-scales associated with star formation vary as a function of spatial scale (e.g. Elmegreen & Efremov 1996; Efremov & Elmegreen 1998; Elmegreen 2000) according to the hierarchical (e.g. Scalo 1985; Bally et al. 1987; Scalo 1990; Lee et al. 1990; Falgarone et al. 1991; Bally et al. 1991; Elmegreen & Falgarone 1996; Falgarone et al. 2009) and supersonically-turbulent (e.g. Vazquez-Semadeni 1994; Passot et al. 1995; Passot & Vázquez-Semadeni 1998; Stone et al. 1998; Ostriker et al. 2001; Kim et al. 2003a; Federrath et al. 2009, 2010) structure of the interstellar medium. In recent years, theories of star formation have begun to explore the spatial dependence of empirical star formation relations (Krumholz et al. 2012; Semenov et al. 2017, 2018, 2019; Caplar & Tacchella 2019; Tacchella et al. 2020), and observations have begun to move towards the characterisation of molecular gas properties as an explicit function of spatial resolution (Leroy et al. 2013; Sun et al. 2018, 2020). Such analyses describe the duration and efficiency of galactic-scale star formation with respect to the hierarchy of time-scales for molecular gas evolution on sub-galactic spatial scales, and the physics that drive them.

In this work, we explore the time evolution of molecular cloud populations in Milky Way-mass galaxies as a function of spatial scale, using a set of three isolated galaxy simulations spanning a wide range of galactic-dynamical environments Jeffreson et al. (2020). We construct detailed cloud evolution networks spanning over two orders of magnitude in spatial resolution, allowing us to probe the time-evolution and star-forming behaviour of molecular gas across a range of hierarchical levels in the interstellar medium. We compute a characteristic molecular cloud lifetime and cloud merger rate as a function of spatial scale, and examine how these relate to the time-scales for star formation and gravitational collapse. Finally, we connect the derived scaling relations, where possible, to the galactic-dynamical environment and its influence (or lack thereof) on the clouds in our sample.

The remainder of this paper is structured as follows. In Section 2, we re-iterate the key details of the three isolated galaxy simulations analysed in this work, which were first presented in Jeffreson et al. (2020). Section 3 describes how these simulations are used to construct detailed cloud evolution networks spanning two orders of magnitude in spatial scale. In Sections 4 and 5 we report the key results of our analysis, relating to the spatial scaling of the cloud merger rate, and of the characteristic molecular cloud lifetime, respectively. Section 6 presents a discussion of our results in the context of existing simulations and observations of giant molecular cloud lifetimes and mergers. Finally, a summary of our conclusions is given in Section 7.

2 SIMULATIONS

We analyse the lifetimes of molecular clouds across the three Milky Way-like isolated galaxy simulations of Jeffreson et al. (2020), shown in Figure 1. Here we briefly describe the most important characteristics of our numerical method, and refer the reader to the cited work for a fuller and more detailed explanation.

2.1 Isolated galaxy models

The initial conditions for each isolated disc galaxy are generated using MAKENEWDISK (Springel et al. 2005), using a three-component external potential consisting of a spherical Hernquist (1990) dark matter halo, a Miyamoto & Nagai (1975) stellar disc, and a Plummer (1911) stellar bulge. The gas disc follows an exponential density profile of the form

$$\rho_{\rm gas}(R,z)\frac{M_{\rm gas}}{4\pi R_{\rm gas} z_{\rm gas}}\exp-\frac{R}{R_{\rm gas}}\exp-\frac{|z|}{z_{\rm gas}}, \qquad (1)$$

where $M_{\rm gas}$ is the total gas mass, $z_{\rm gas}$ is the disc scale-height set by the condition of hydrostatic equilibrium, and $R_{\rm gas}$ is the gas disc scale length, which is fully-determined by the external potential. We vary the external potential to set three different combinations of the disc scale-height and rotation curve, ensuring that each simulation spans a different set of galactic-dynamical environments.

Each simulation refines adaptively to a target gas cell mass of $900\ {\rm M}_{\odot}$. We avoid artificial fragmentation at scales larger than the Jeans length $\lambda_J = c_s/\sqrt{G\rho}$ by ensuring that the disc scale-height and Toomre mass are resolved at all scales (Nelson 2006), and by employing the adaptive gravitational softening scheme in AREPO, with a typical value of 1.5 times the Voronoi cell size and a minimum value of $\sim$ 3 pc, corresponding to the spatial resolution in the densest gas at our star formation threshold of $n_{\rm thresh} = 2000$ H/cc. As such, stars are formed only from gas cells that are gravitationally-collapsing (i.e. whose masses safely exceed the Jeans mass), assuming that all star-forming gas is in approximate thermal equilibrium and follows a cooling curve with a maximum temperature of 100 K. Our star formation prescription is chosen to locally reproduce the observed relation of Kennicutt (1998) between the SFR surface density and the gas surface density, following the equation

$$\frac{{\rm d}\rho_{*,i}}{{\rm d}t} = \begin{cases} \frac{\epsilon\rho_i}{t_{{\rm ff},i}}, & n_i \geqslant n_{\rm thresh} \\ 0, & n_i < n_{\rm thresh} \end{cases}, \qquad (2)$$

where the local free-fall time is given by $t_{{\rm ff},i} = \sqrt{3\pi/(32G\rho_i)}$. We use a star formation efficiency per free-fall time of $\epsilon = 1$ per cent, following measurements of the gas depletion time across nearby galaxies (Leroy et al. 2017; Krumholz & Tan 2007; Krumholz et al. 2018; Utomo et al. 2018).

The star particles generated via this prescription each spawn a stellar population drawn stochastically from a Chabrier (2003) initial stellar mass function (IMF) using the Stochastically Lighting Up Galaxies (SLUG) population synthesis model (da Silva et al. 2012, 2014; Krumholz et al. 2015). At each time-step, SLUG provides the ionising luminosity for each star particle, along with the number of supernovae (SN) it has generated and the mass it has ejected, by evolving the stellar populations along Padova solar metallicity tracks (Fagotto et al. 1994a,b; Vázquez & Leitherer 2005) using starburst99-like spectral synthesis (Leitherer et al. 1999). Star formation feedback from stellar winds consists of mass ejected from star particles without any accompanying SN events.

In addition to the mass from stellar winds, we include pre-SN photo-ionisation feedback from HII regions, according to the prescription of (Jeffreson et al. prep). We inject momentum into the gas cells surrounding the central 'host' cell for each star particle, corresponding to the momentum due to gas and radiation pressure from 'blister-type' HII regions, following the analytic description of Matzner (2002); Krumholz & Matzner (2009). The cells inside each HII region are self-consistently heated and held at or above a temperature floor of 7000 K. We inject mechanical SN feedback according to the prescription of Keller et al. (prep), which computes the terminal momentum of the (unresolved) SN remnant according to Gentry et al. (2017). The energy and momentum injected into each gas cell from all types of stellar feedback is weighted according to the face area shared between the central and receiving gas

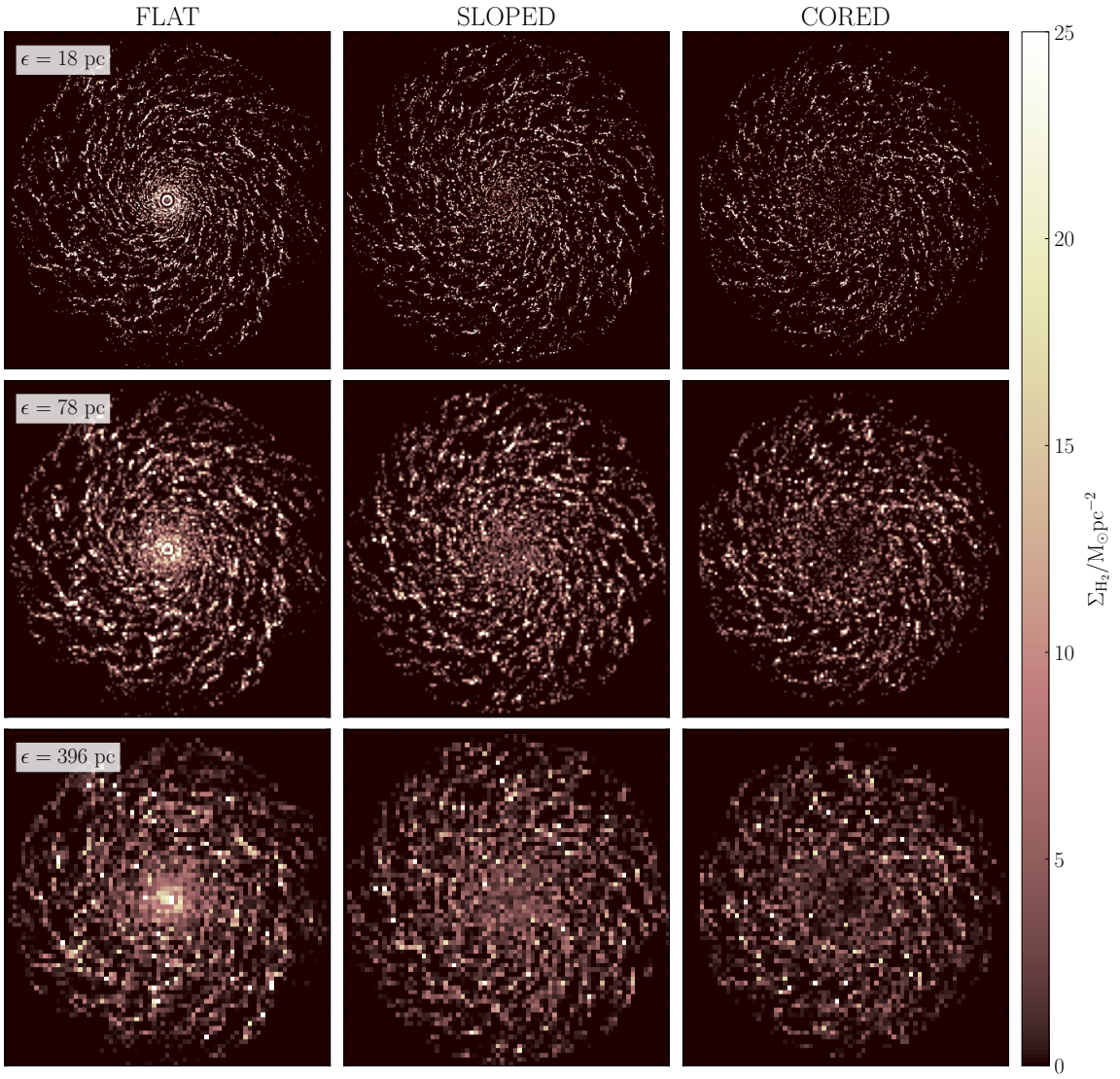

Figure 1. Column density maps of the molecular gas in each simulation, down-sampled from the native map resolution of $\epsilon = 6$ pc to spatial resolutions of $\epsilon = 18$ pc (top row), 78 pc (central row) and 396 pc (bottom row).

cells as in Hopkins et al. (2018), however for the HII region feedback we re-weight the momentum along a directed beam of the form

$$\begin{aligned} \Delta p_{k,\mathrm{HII}} &= w_k(\theta_k, A_k)\hat{\mathbf{r}}_{j\to k}\Delta p_{j,\mathrm{HII}} \\ w(\theta_k, A_k) &= \frac{A_{j\to k} f(\theta_k)}{\sum_k A_{j\to k} f(\theta_k)} \\ f(\theta_k) &= \left[\log\left(\frac{2}{\Theta}\right)(1 + \Theta^2 - \cos^2\theta_k)\right]^{-1}, \end{aligned} \tag{3}$$

where $\Delta p_{j,\mathrm{HII}}$ is the total momentum delivered to the central cell j that hosts the HII region, $\Delta p_{k,\mathrm{HII}}$ is the fraction of the momentum injected into the kth momentum-receiving cell, $\hat{\mathbf{r}}_{j\to k}$ defines the axis joining the centroids of the cells j and k, and $w_k(\theta_k, A_k)$ is the final weight-factor, dependent on the facing area A_k between the two cells and the angle θ_k between the axis $\hat{\mathbf{r}}_{j\to k}$ and the axis of the beam along which the momentum is directed. The beam has an opening angle of $\Theta = \pi/12$ radians.

Throughout each simulation, the thermal and chemical state of the simulated gas is determined via the chemical network of Nelson & Langer (1997); Glover & Mac Low (2007a,b), according to a simplified set of reactions that follow the fractional abundances of H, H_2, H^+, C^+, CO, O and e^-, with the abundances of Helium, silicon, carbon and oxygen set to their solar values of $x_{\mathrm{He}} = 0.1$, $x_{\mathrm{Si}} = 1.5 \times 10^{-5}$, $x_{\mathrm{C}} = 1.4 \times 10^{-4}$ and $x_{\mathrm{O}} = 3.2 \times 10^{-4}$, re-

spectively. The strength of the interstellar radiation field (ISRF) is set to a value of 1.7 Habing (1968) units according to Mathis et al. (1983), and a value of 2×10^{-16} s^{-1} is used for the cosmic ray ionisation rate (e.g. Indriolo & McCall 2012). A full list of the heating and cooling processes considered in our simulations is given in Jeffreson et al. (2020), and a detailed account of the chemical network and its coupling to the thermal and dynamical evolution of the gas is given in Glover & Mac Low (2007a,b); Glover et al. (2010).

2.2 Chemical post-processing

As described in Jeffreson et al. (2020), we compute the molecular hydrogen abundances of the Voronoi gas cells in our simulations in post-processing, using the DESPOTIC model for astrochemistry and radiative-transfer (Krumholz 2013). Each gas cell is treated as a one-zone spherical 'cloud' with a hydrogen atom number density $n_{\rm H}$, a column density $N_{\rm H}$ and a virial parameter $\alpha_{\rm vir}$. The escape probability formalism is applied to compute the line emission from each cell, coupled self-consistently to the chemical and thermal evolution of the gas. The carbon and oxygen chemistry is followed via the chemical network of Gong et al. (2017), with the addition of cosmic rays and the grain photo-electric effect, subject to dust- and self-shielding for each component, line cooling due to C^+, C, O and CO, and thermal exchange between dust and gas. The ISRF strength and cosmic ionisation rate are matched to those used to compute the live chemistry during run-time. The entire system of coupled rate equations is converged to a state of chemical and thermal equilibrium for each one-zone model.

Due to considerations of computational cost, we do not perform the above convergence calculation for all gas cells in the simulation, but instead interpolate over a table of pre-calculated models at logarithmically-spaced values of $n_{\rm H}$, $N_{\rm H}$ and $\alpha_{\rm vir}$. For a gas cell with mass density ρ, the hydrogen number density is given by

$$n_{\rm H} = \frac{\rho}{\mu m_{\rm H}}, \tag{4}$$

where $m_{\rm H}$ is the proton mass and $\mu = 1.4$ is the atomic mass per hydrogen nucleus at the standard cosmic composition. The hydrogen column density is then obtained following Fujimoto et al. (2019), via the local approximation of Safranek-Shrader et al. (2017), as

$$N_{\rm H} = \lambda_{\rm J} n_{\rm H}, \tag{5}$$

where $\lambda_{\rm J} = (\pi c_s^2 / G\rho)^{1/2}$ is the Jeans length, and is calculated with an upper limit of $T = 40$ K on the gas cell temperature. Finally, the virial parameter is defined according to MacLaren et al. (1988); Bertoldi & McKee (1992), as

$$\alpha_{\rm vir} = \frac{5\sigma_{\rm g}^2}{\pi G \rho L^2}, \tag{6}$$

where $\sigma_{\rm g}$ is the turbulent velocity dispersion of the gas cell following Gensior et al. (2020), and L is the smoothing length over which $\sigma_{\rm g}$ is calculated. Using the above three values, we constrain the ^{12}CO line luminosity $L_{\rm CO}$ for the $1 \rightarrow 0$ transition, from which we obtain the CO-bright molecular hydrogen surface density, according to

$$\begin{aligned}\Sigma_{\rm H_2}[{\rm M_\odot pc^{-2}}] = & \frac{2.3 \times 10^{-29} [{\rm M_\odot (erg\ s^{-1})^{-1}}]}{m_{\rm H}[{\rm M_\odot}]} \\ & \times \Sigma_{\rm g}[{\rm M_\odot pc^{-2}}] \\ & \times \frac{\int_{-\infty}^{\infty} dz' \rho_{\rm g}(z') L_{\rm CO}[{\rm erg\ s^{-1}}]}{\int_{-\infty}^{\infty} dz' \rho_{\rm g}(z')}.\end{aligned} \tag{7}$$

In the above, $\rho_{\rm g}(z)$ is the total gas volume density as a function of distance z from the galactic mid-plane and $\Sigma_{\rm g}$ is the total gas surface density. The mass-to-luminosity conversion factor $\alpha_{\rm CO} = 4.3 {\rm M_\odot (K\ kms^{-1} pc^{-2})^{-1}}$ of Bolatto et al. (2013) and the line-luminosity conversion factor $5.31 \times 10^{-30} {\rm (K\ kms^{-1} P pc^2)/(erg\ s^{-1})}$ of Solomon & Vanden Bout (2005) for the CO $J = 1 \rightarrow 0$ transition at redshift $z = 0$ are combined to produce the factor of $2.3 \times 10^{-29}\ {\rm (erg\ s^{-1})^{-1}}$. The ratio of integrals represents the two-dimensional density-weighted ray-tracing map of the CO line-luminosity.

3 CONSTRUCTION OF THE CLOUD EVOLUTION NETWORK

In this section, we describe the construction of a detailed *cloud evolution network* from the simulations outlined in Section 2. We produce the network at the (two-dimensional) native resolution of $\epsilon = 6$ pc for each simulation, as well as at degraded spatial resolutions of 12, 18, 36, 78, 198 and 396 pc, to examine the time-dependent properties of molecular clouds as a function of their spatial scale. We use a range of simulation times between 600 and 1000 Myr, for which the simulated galaxies are shown to be a state of dynamical equilibrium (Jeffreson et al. 2020).

3.1 Cloud identification

We identify giant molecular clouds at each simulation snapshot using a procedure similar to that described in Jeffreson et al. (2020). We compute a map of the molecular hydrogen surface density $\Sigma_{\rm H_2}$ at a spatial resolution of 6 pc, using AREPO's ray-tracing algorithm. For the typical gas cell mass of $\sim 900\ M_\odot$, this is equal to the radius of a Voronoi gas cell at the minimum volume density of $n_{\rm H} \gtrsim 30\ {\rm cm^{-3}}$ inside molecular clouds, ensuring that each pixel in every cloud contains at least one cell centroid. To obtain the maps at degraded spatial resolution, we downsample the original at factors of 2, 3, 6, 13, 33 and 66 times, by averaging the value of $\Sigma_{\rm H_2}$ across groups of adjacent pixels. In this way, we obtain equivalent maps of the molecular hydrogen surface density at spatial resolutions of 6, 12, 18, 36, 78, 198 and 396*b* pc.

As described in Section 2.9.1 and by Figure 4 of Jeffreson et al. (2020), we use the ASTRODENDRO package for Python to identify molecular clouds as a set of closed contours at $\log_{10}(\Sigma_{\rm H_2}/{\rm M_\odot pc^{-2}}) = -3.5$. This captures all of the dense CO-bright gas identified via the DESPOTIC model. The Voronoi gas cells associated with each cloud are then obtained by applying the ASTRODENDRO pixel mask for each cloud to the positions of the gas cell centroids with temperatures $T < 10^4$ K. In contrast to Jeffreson et al. (2020), at this stage of the analysis we do not impose any requirement on the number of pixels or the number of Voronoi cells spanned by each cloud. That is, we allow clouds with a diameter of just one pixel, containing one Voronoi cell. This ensures consistency of cloud-bidentification across maps of varying spatial resolution, while allowing a minimum cloud size of 396 pc at the lowest resolution. It also produces a population of unphysical artefacts of low mass and low velocity dispersion, which do not adhere to the observational properties of real molecular clouds, as shown on the left-hand side of the vertical dashed lines in Figure 2. Following the construction of the cloud evolution network, we 'prune' these artefacts away, according to the physical requirement that our identified clouds reproduce the observed distributions of the cloud mass and cloud velocity dispersion, as described in Section 3.3.

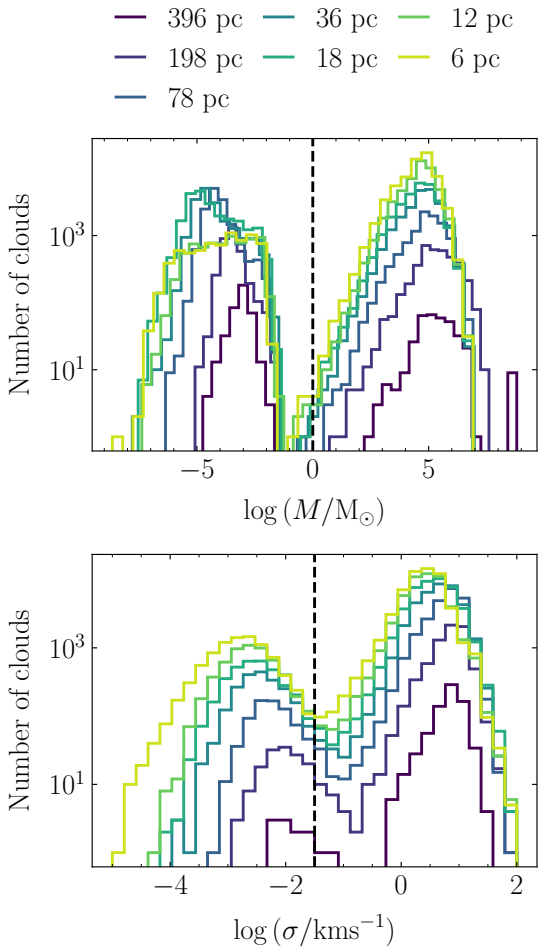

Figure 2. Distributions of cloud masses M and velocity dispersions σ in the cloud evolutionary network at each of the different spatial resolutions for cloud identification, before pruning is applied (see Section 3.3). There exists a large population of low-mass, low-velocity dispersion artefacts (left side of the vertical black dashed lines) that do not conform to observations of the cloud mass spectrum or velocity dispersion distribution. These artefacts are removed from the network before any analysis is performed.

3.2 Tracking clouds over time

Once we have identified the molecular clouds at every simulation time-step, we track their evolution as a function of time. To identify similar clouds in consecutive snapshots at times $t = t_1$ and $t = t_2 = t_1 + \Delta t$, where $\Delta t = 1$ Myr for our maps, we take the sets of gas cells comprising the clouds identified at $t = t_1$ and calculate their projected positions at t_2, according to

$$\begin{aligned} x_2 &= x_1 + v_x \Delta t \\ y_2 &= y_1 + v_y \Delta t. \end{aligned} \tag{8}$$

We then use ASTRODENDRO to compute the two-dimensional pixel masks for the closed contours around the time-projected gas cell positions, following the original cloud identification procedure. If any pixel in a time-projected mask overlaps with a pixel in one of the cloud masks at time $t = t_2$, then the clouds are considered indistinguishable at the spatial resolution of ϵ and time resolution of 1 Myr used for cloud identification. The clouds at $t = t_1$ are assigned as the parents of the clouds at $t = t_2$. Via this procedure, each cloud can spawn multiple children (*cloud splits*) or have multiple parents (*cloud mergers*). We connect and store the parents and children of every cloud using the NETWORKX package for python, producing the cloud evolution network. A 100-Myr section of this network for the FLAT simulation at the native resolution of $\epsilon = 6$ pc is shown in Figure 4 for galactocentric radii between 7.75 and 8.25 kpc (approximately at the solar radius for a Milky Way-like galaxy). The arrow of time points from the top to the bottom of the network, so that cloud mergers have the shape of downward-pointing triangles and cloud splits have the shape of upward-pointing triangles. Each node in the network represents a molecular cloud identified at a single simulation time, as described in Section 3.1. Directed edges (represented by time-directed arrows) join parent and child nodes in consecutive snapshots, and so all have a temporal length equal to the time $\Delta t = 1$ Myr between snapshots. The cloud evolution network can therefore be read from the top to the bottom of the graph, where distinct, non-interacting clouds correspond to distinct components of the graph that share no edges between them.

3.3 Pruning the cloud history graph

To obtain the final version of each cloud evolution network, we prune away any nodes that do not correspond to physical molecular clouds. These artefacts are produced by regions of faint background CO emission modelled in DESPOTIC, which appear as overdensities in the molecular hydrogen surface density and so are picked up by the cloud identification procedure described in Section 3.1, but which contain very little CO-luminous mass.

Figure 2 demonstrates the bi-modality of the resulting cloud mass M and velocity dispersion σ distributions, which provides a natural choice for the pruning requirement. The observable range of masses $M \gtrsim 10^4$ M$_\odot$ and velocity dispersions $0.5 \lesssim \sigma \lesssim 100$ kms^{-1} extends smoothly down to $M = 1$ M$_\odot$ and $\sigma = 0.03$ kms^{-1}. Pruning at these cut-offs removes the unphysical artefacts, leaving the spectra presented in Figure 3 for the cloud mass (left-hand panel), cloud size (central panel), and Voronoi cell number N_{cell} (right-hand panel). In the pruned sample, 99.3 per cent of clouds are resolved by 10 or more Voronoi cells across all spatial resolutions (95.4 per cent at the native resolution). The mass spectrum (left-hand panel) is consistent with empirical data over the observationally-constrained mass range, with $\beta = 1.90 \pm 0.08$ for a power-law distribution of cloud number with mass, $\mathrm{d}N/\mathrm{d}M \propto M^{-\beta}$. Values of $\beta \in [1.6, 1.8]$ are measured consistently in the Milky Way and across other nearby galaxies (Solomon et al. 1987; Williams & McKee 1997; Kramer et al. 1998; Heyer et al. 2001; Rosolowsky et al. 2003; Roman-Duval et al. 2010; Freeman et al. 2017; Miville-Deschênes et al. 2017; Colombo et al. 2019). Similarly, the upper truncation mass falls at around $M = 10^7$M$_\odot$ at all resolutions, consistent with the observed range of ~ 3 to 8×10^6M$_\odot$ in The Milky Way (Colombo et al. 2019), M33 (Rosolowsky et al. 2003) and M83 (Freeman et al. 2017). For spatial resolutions of $\epsilon < 396$ pc, our pruning requirements allow a significantly smaller value of the lower truncation mass than can be resolved by observations, but given that the slope of the mass spectrum preserves its form all the way down to $M = 1$ M$_\odot$, we consider these lower-mass clouds to be physical.

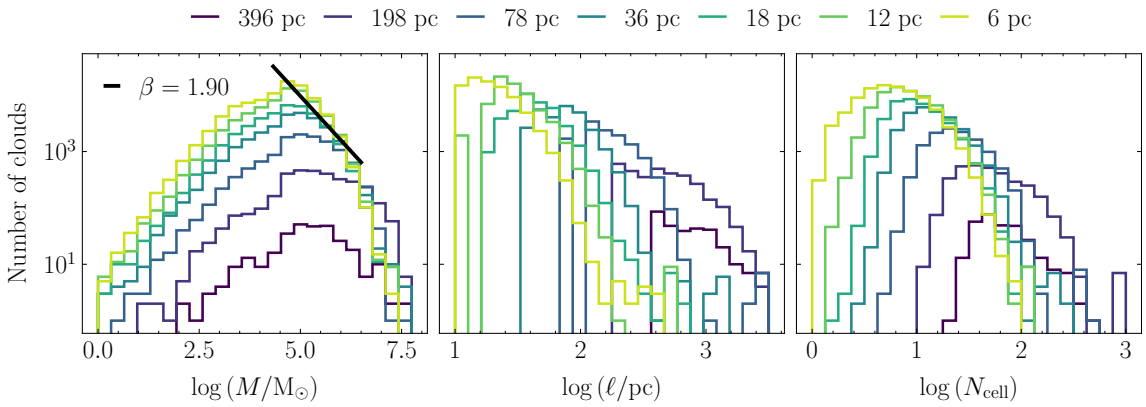

Figure 3. Distributions of masses M (left-hand panel), scales ℓ (central panel) and the number of Voronoi cells within each simulated cloud N_{cell} (right-hand panel) in the FLAT cloud evolution network, after the removal of low-mass, low-velocity dispersion artefacts (see Section 3.3). The solid black line gives the power-law fit to the mass spectrum, with $\beta = 1.90 \pm 0.08$, where $\mathrm{d}N/\mathrm{d}M \propto M^{-\beta}$. We see that after pruning, 99.3 per cent of clouds across all spatial resolutions are resolved by 10 or more Voronoi cells, and have masses that are consistent with the observed distribution, to within the limitations of observational resolution. We also note that the typical cloud size varies systematically with the spatial resolution.

The final point to note is that the characteristic scale ℓ of the identified clouds varies with spatial resolution. As such, clouds at different spatial resolutions correspond to coherent regions of molecular gas at different levels of hierarchy within the interstellar medium. Analysis of cloud properties as a function of spatial scale will be a key feature of the following analysis, allowing for the characterisation of hierarchical structure via 'scaling relations', and removing the requirement of an arbitrary spatial scale for cloud identification.

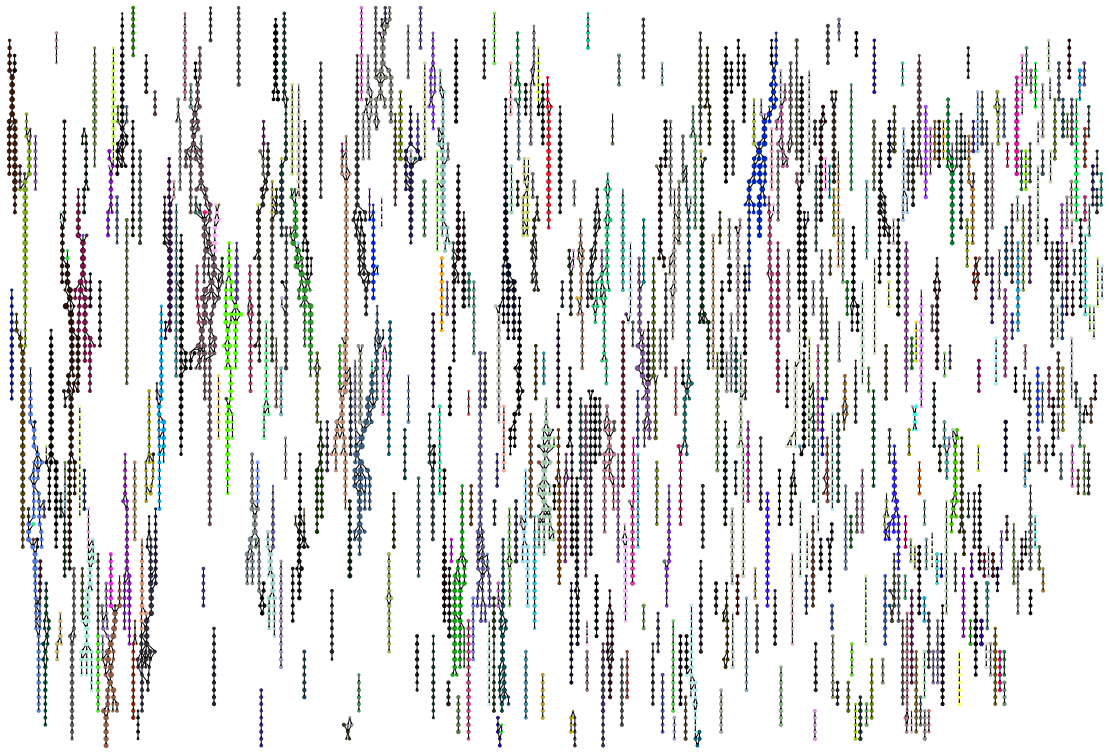

Figure 4. Section of the giant molecular cloud evolution network for the FLAT simulation, spanning the range of simulation times $t \in [600, 700]$ Myr and the range of galactocentric radii $R \in [7.75, 8.25]$ kpc (approximately at the solar radius for a Milky Way-like galaxy). The arrow of time points from the top to the bottom of the page (higher nodes are the parents of lower nodes). The network has been constructed according to the procedures described in Section 3. The sizes of the nodes scale as the logarithm of cloud mass, and the colours of the nodes follow the evolution of the most massive cloud involved in each split and merger.

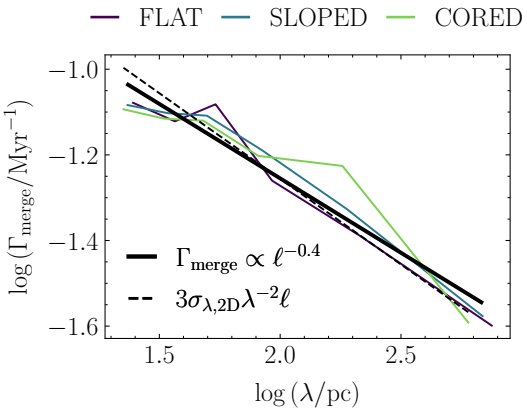

Figure 5. Rate of cloud mergers $\Gamma_{\rm merge}$ (solid lines) as a function of the median cloud separation length λ for each simulation. The solid black line gives the power-law fit to the combined data and the dashed black line gives the best-fit prediction of the collision rate in terms of the crossing time between cloud centroids (see Section 4.1 and Equation 10).

4 THE CLOUD MERGER RATE

The fractal, self-similar structure of the interstellar medium has been observed in maps probing a large dynamical range in spatial scale and gas density, and spanning a wide variety of different galactic environments (Scalo 1985; Bally et al. 1987; Scalo 1990; Lee et al. 1990; Falgarone et al. 1991; Bally et al. 1991; Elmegreen & Falgarone 1996; Falgarone et al. 2009). This spatial distribution of gas is shown to be reproducible via compressible supersonic turbulence in numerical simulations (e.g. Vazquez-Semadeni 1994; Passot & Vázquez-Semadeni 1998; Stone et al. 1998; Ostriker et al. 2001; Federrath et al. 2009, 2010). In this section, we show that the turbulent self-similarity of the interstellar medium also has important consequences for the time-evolution of the giant molecular clouds in our simulations, setting the rate of cloud mergers over scales from 10 pc to 1 kpc.

4.1 Scaling relation of the cloud merger rate

In Figure 5 we show the number of cloud mergers per unit time in each of our simulations as a function of the median cloud spatial separation λ, calculated as

$$\Gamma_{\rm merge} = \frac{\sum_{\theta=2}^{\infty} \theta N_{{\rm merge},\theta}}{N_{\rm nodes}}, \tag{9}$$

where $N_{{\rm merge},\theta}$ is the total number of merge-nodes in the network involving θ clouds. We find that $\theta = 2$ in 80 per cent of cases at the native resolution, with a maximum value of $\theta = 8$. The best-fit power-law to the scaling relation is given by the bold black line, with a form of $\Gamma_{\rm merge} \propto \lambda^{-0.4}$. At small λ, clouds enter mergers around oncee in every 10 Myr; at large λ, the rate drops to once in every 30 Myr. We can understand the scaling relation of the cloud merger rate by considering the size ℓ of a cloud as its 'collision cross-section', onto which other clouds impinge. This gives a two-dimensional version of the familiar kinetic collision rate

$$\Gamma_{\rm merge} = F \sigma_{\lambda,2{\rm D}} \lambda^{-2} \ell, \tag{10}$$

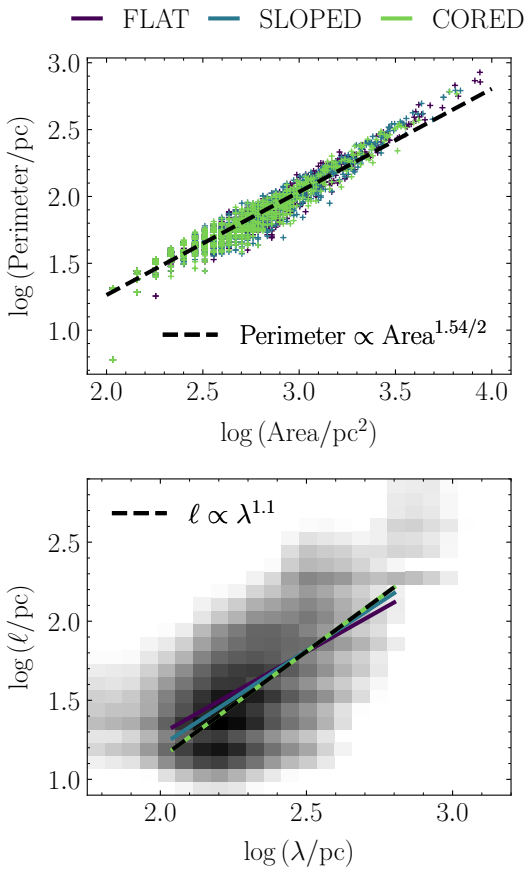

Figure 6. *Top:* Cloud perimeter as a function of cloud area for the combined molecular cloud population across all three simulated disc galaxies, at the native map resolution of $\epsilon = 6$ pc. The black dashed line gives the best-fit power-law to the sample, which yields a fractal dimension of $D = 1.54$. *Bottom:* Cloud size ℓ as a function of the cloud separation length λ. The grey-shaded histogram corresponds to the combined molecular cloud population across all three simulated disc galaxies and across all map resolutions ϵ, sampled at 50-Myr intervals across the time-span of each cloud evolution network, between simulation times of 600 and 1000 Myr. It is displayed on a logarithmic scale with a lower bound of 500 clouds per pixel. The black dashed lines show the best-fit power-law to the combined data.

where $\sigma_{\lambda,2{\rm D}}$ is the two-dimensional velocity dispersion of the cloud centroids within the galactic mid-plane, and F is a geometric factor accounting for the elongation and orientation of the clouds. In a self-similar interstellar medium the cloud size scales with separation as $\ell \propto \lambda$, so that the merger time-scale is, as expected, proportional to the crossing time between clouds,

$$\Gamma_{\rm merge} \propto \frac{\sigma_{\lambda,2{\rm D}}}{\lambda}. \tag{11}$$

The dashed black line in Figure 5 gives the merger rate predicted by Equation (10) when we substitute the following power-law fits

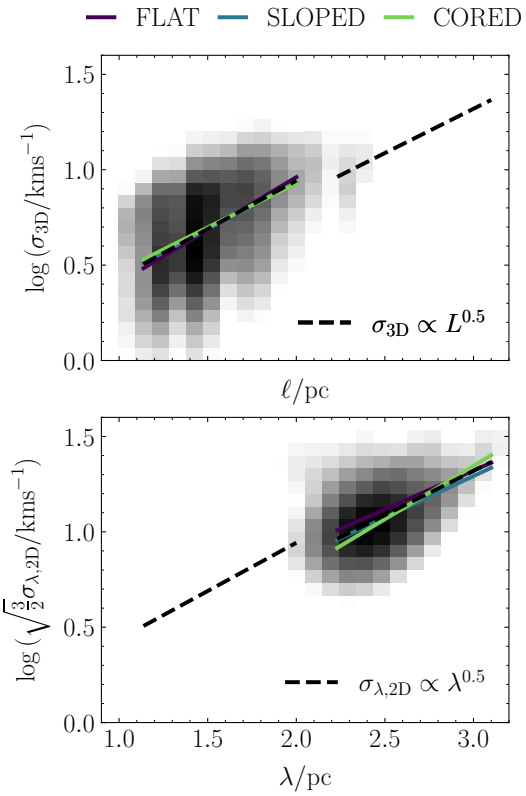

Figure 7. *Top:* Internal three-dimensional velocity dispersion σ_{3D} as a function of the typical cloud scale ℓ (size-linewidth relation). *Bottom:* Two-dimensional velocity dispersion of the cloud centroids $\sigma_{\lambda,2D}$ as a function of their typical separation length λ, scaled by a factor $\sqrt{3/2}$ to enable direct comparison with σ_{3D}. The grey-shaded histogram corresponds to the combined molecular cloud population across all three simulated disc galaxies and across all map resolutions ϵ, sampled at 50-Myr intervals across the time-span of each cloud evolution network, between simulation times of 600 and 1000 Myr. It is displayed on a logarithmic scale with a lower bound of 500 clouds per pixel. The black dashed lines show the best-fit power-law to the combined data. Both fits are shown on both panels, for reference.

to our simulated cloud population:

$$\begin{aligned} \ell/\mathrm{pc} &= 0.1(\lambda/\mathrm{pc})^{1.1} \\ \sigma_{\lambda,2D}/\mathrm{km\ s}^{-1} &= 0.7(\lambda/\mathrm{pc})^{0.5}, \end{aligned} \tag{12}$$

along with the best-fit geometric factor $F \sim 3$. That is, the cloud merger rate is well-described by the frequency of interactions between molecular clouds in a spatially self-similar interstellar medium ($\ell \propto \lambda$), with random centroid velocities induced by supersonic, compressible turbulence ($\sigma_{\lambda,2D} \propto \lambda^{0.5}$). In the following sub-sections, we describe in more detail each of the scaling relations in Equation (12), examine the dependence of Γ_{merge} on the galactic-dynamical environment, and evaluate the influence of cloud mergers on the physical properties of the interacting clouds.

4.1.1 *Cloud size vs. cloud separation*

In the lower panel of Figure 6, we show that the relationship of cloud size to cloud scale for our simulations is $\ell \propto \lambda^{1.1}$, not quite the exact one-to-one correspondence expected in the case of perfect self-similarity. This is most likely due to our method of calculating the cloud size ℓ, for which we have used the pixel-by-pixel area of the cloud's footprint on the galactic mid-plane as $\ell = \sqrt{A}$. We show in the top panel of Figure 6 that this assumption of approximately-circular clouds with smooth perimeters is not correct: the fractal dimension of the clouds, computed at our native resolution of 6 pc, is $D = 1.54$, such that the cloud perimeters P scale with their areas as

$$P \propto A^{D/2};\ D = 1.54. \tag{13}$$

This is significantly more complex than the circular case of $D = 1$, so the difference relative to the self-similar scaling relation may be due to an over-estimate of the cloud area that worsens at lower spatial resolutions, as the number of pixels characterising each cloud becomes smaller. The cloud separation length is calculated across a group of 100 nearest neighbours at the position of each cloud, as

$$\lambda = \sqrt{\frac{[\max(\lambda_{100})]^2}{100}}, \tag{14}$$

where λ_{100} is the distance to the furthest nearest neighbour. The value of λ is independent of cloud shape, and therefore should not be affected by the assumption of a circular fractal dimension.

4.1.2 *Cloud centroid velocity dispersion vs. cloud separation*

In the lower panel Figure 7, we show the second scaling relation required to compute Γ_{merge} via the cloud collision cross-section of Equation (10): the relation of the two-dimensional cloud centroid velocity dispersion $\sigma_{\lambda,2D}$ to the cloud separation length. The value of $\sigma_{\lambda,2D}$ for each cloud is measured across its nearest neighbours in the same way as the separation length, such that

$$\sigma_{\lambda,2D} = \sqrt{\langle |v_x - \langle v_x \rangle_{100}|^2 + |v_y - \langle v_y \rangle_{100}|^2 \rangle_{100}}, \tag{15}$$

where $\langle ... \rangle_{100}$ denotes an average over all neighbours, and $\{v_x, v_y\}$ are the x- and y-components of their centroid velocities. We retrieve the same scaling relation as is observed for the three-dimensional internal cloud velocity dispersion σ_{3D} with the cloud size, which is shown for our simulations in the upper panel. That is,

$$\begin{aligned} \sigma_{\lambda,2D} &\propto \lambda^{0.5} \\ \sigma_{3D} &\propto \ell^{0.5}. \end{aligned} \tag{16}$$

In the above, the three-dimensional internal velocity dispersion of each cloud is defined as

$$\sigma_{3D} = \sqrt{\langle |\mathbf{v}_i - \langle \mathbf{v}_i \rangle_{i,\mathrm{H_2}}|^2 \rangle_{i,\mathrm{H_2}}}, \tag{17}$$

where $\{\mathbf{v}_i\}$ are the velocities of the gas cells within each cloud, and $\langle ... \rangle_{i,\mathrm{H_2}}$ denotes the molecular gas mass-weighted average over these cells. Both scalings are consistent with the self-similar distribution of velocity dispersions induced by compressible, supersonic turbulence (e.g. Padoan 1995; Kritsuk et al. 2007; McKee & Ostriker 2007; Federrath & Klessen 2013), as observed in nearby Galactic molecular clouds (e.g. Ossenkopf & Mac Low 2002; Heyer & Brunt 2004; Roman-Duval et al. 2011).

Given the self-similar structure of the turbulent interstellar medium, at first glance it is not too surprising that the motions of the molecular cloud centroids obey the same scaling relation as

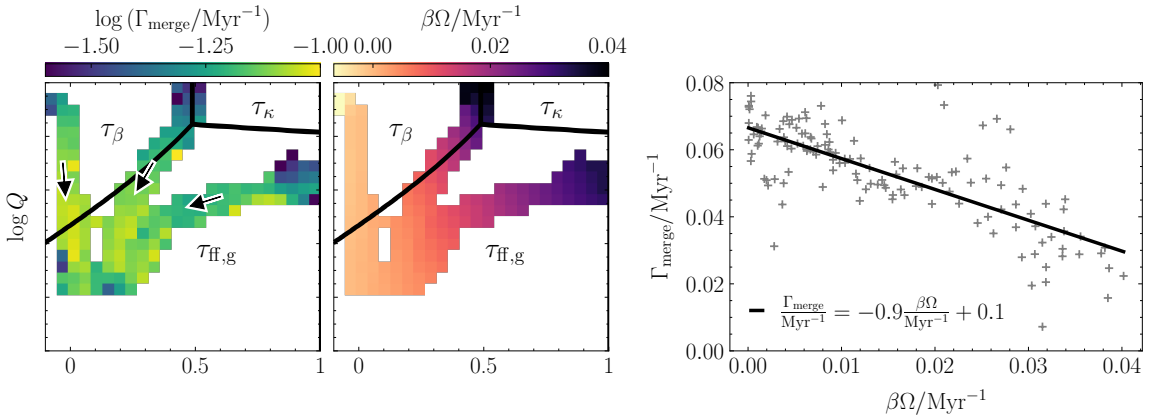

Figure 8. *Left:* Cloud merger rate $\Gamma_{\rm merge}$ for clouds as a function of the shear parameter β and the Toomre Q stability parameter. The data is compiled across all simulations and across all map resolutions ϵ. Each converging set of connected pixels corresponds to the locus of the cloud population for one isolated disc galaxy, where the black arrows mark the direction in which the galactocentric radius increases. The color of each pixel represents the value of $\Gamma_{\rm merge}$ at the indicated value of (β, Q). The black solid lines enclose the regions of parameter space for which the minimum galactic-dynamical time-scale is τ_κ (orbital epicyclic perturbations), τ_β (galactic shear) and $\tau_{\rm ff,g}$ (gravitational free-fall), when a value $\phi_{\rm P} = 3$ is adopted for the stellar contribution to the mid-plane pressure (Elmegreen 1989). *Centre:* The variation in the absolute differential velocity $\beta\Omega$ with (β, Q) at the positions of the cloud data. *Right:* The merger rate as a function of the absolute differential velocity, binned in (β, Q) as displayed in the left-hand panels.

their internal velocity dispersions. After all, the centroids of distinct clouds at high resolution are simply the turbulent sub-structure of a larger cloud at low resolution. What is surprising, however, is that the form of the power-law continues above the thin-disc scale-height, which is ~ 100 pc in our simulations (Jeffreson et al. 2020), and which places an upper limit on the sizes of the clouds. This implies that turbulent fragmentation on scales $\geqslant 1$ kpc in the galactic mid-plane proceeds independently of fragmentation perpendicular to the galactic mid-plane, consistent with the idea that the fractal spatial structure of the interstellar medium extends up to the scales of galactic spiral arms (Elmegreen 2000; Elmegreen et al. 2003a,b).

4.1.3 *The role of galactic shear*

Given that turbulence appears to play a central role in setting the rate of cloud mergers up to separation lengths of $\lambda = 1$ kpc in our simulations, we examine in addition the influence of galactic-dynamical processes, which operate on comparable scales. In particular, there are two primary mechanisms by which galactic shear may drive an increase in the interaction rate: (1) by stirring turbulence on galactic scales, so that its effect enters the merger rate $\Gamma_{\rm merge}$ via the turbulent velocity dispersion $\sigma_{\lambda,\rm 2D}$ (e.g. Kim & Ostriker 2001; Kim et al. 2003b; Kim & Ostriker 2007; Agertz et al. 2009), and (2) as a direct cause of cloud mergers due to the differential velocities $(1-\beta)\Omega\lambda$ of radially-separated cloud centroids along azimuthal trajectories in the rotating frame of the galaxy (e.g. Tan 2000; Tasker & Tan 2009; Whitworth et al. 2018). In the latter case, we would expect $\Gamma_{\rm merge}$ to scale as $\Gamma_{\rm merge} \propto (1-\beta)\Omega$ in a self-similar interstellar medium with $\ell \propto \lambda$. In Figure 8 we show that it depends instead on the velocity differential $\beta\Omega\lambda$ in the inertial frame (right-hand panel), such that

$$\frac{\Gamma_{\rm merge}}{\rm Myr^{-1}} = -1.4 \frac{\Omega\beta}{\rm Myr^{-1}} + 0.1, \tag{18}$$

where the shear parameter is defined as $\beta = {\rm d}\ln v_{\rm c}/{\rm d}\ln R$ for a rotation curve $v_{\rm c}(R)$, and Ω is the galactic orbital angular velocity. In the two left-hand panels, we bin each of the quantities $\Gamma_{\rm merge}$ and $\beta\Omega$ as a function of the galactic-dynamical environment spanned by our simulations, parametrised by β and the Toomre Q gravitational stability parameter (Toomre 1964). This parameter space can the be partitioned according to Jeffreson & Kruijssen (2018) into regions for which each one of three galactic-dynamical time-scales is shorter than all others: the time-scale τ_β for galactic shear, the time-scale $\tau_{\rm ff,g}$ for gravitational free-fall of overdensities at the disc scale-height, and the time-scale τ_κ on which radial epicycles introduce significant excursions to cloud orbits. These are respectively defined by

$$\begin{aligned} \tau_\beta &= \frac{2}{\Omega(1-\beta)} \\ \tau_{\rm ff,g} &= \sqrt{\frac{3\pi^2}{32\phi_{\rm P}(1+\beta)}}\frac{Q}{\Omega} \\ \tau_\kappa &= \frac{4\pi}{\Omega\sqrt{2(1+\beta)}}\frac{1}{\sqrt{3+\beta}}, \end{aligned} \tag{19}$$

where $\phi_{\rm P}$ represents the stellar contribution to the mid-plane hydrostatic pressure (Elmegreen 1989). In scenario (2), $\Gamma_{\rm merge}$ would therefore be expected to scale inversely with τ_β, and so to display a trend (represented by the pixel colour) towards the top left-hand corner of the (β, Q) parameter space. We see that there is no trend in the merger rate with the relative values of any of these time-scales: that is, there is no gradient orthogonal to the black partitioning lines.

Given that $\Gamma_{\rm merge}$ scales with $\Omega\beta$ and not with $\Omega(1-\beta)$, the influence of galactic shearing on the cloud merger rate is more complex than a model in which clouds 'catch up' to each other in the rotating frame of the galaxy. It may be that differential rotation is one of the drivers of turbulent eddies on galactic scales, which

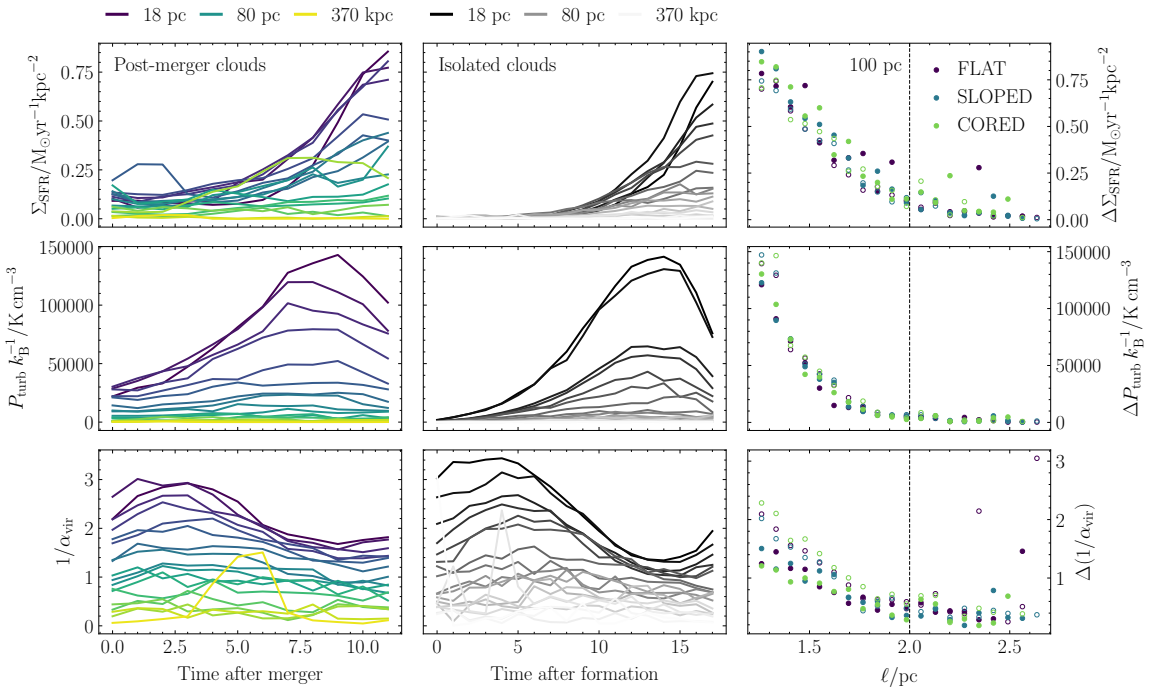

Figure 9. Comparison of the time-variation in the internal turbulent and star-forming properties of merging and isolated GMCs in our simulations. *Left:* Median star formation rate surface density $\Sigma_{\rm SFR}$, averaged over a 5-Myr interval (upper panel), turbulent pressure $P_{\rm turb}$ (central panel) and inverse virial parameter $1/\alpha_{\rm vir}$ (lower panel) as a function of time after a cloud merger, for time-directed trajectories in the cloud evolution network that begin at a merge-node and survive for 12 Myr before experiencing another interaction. *Centre:* The same three properties as a function of time after cloud formation, for time-directed trajectories in the cloud evolution network that display no interaction. *Right:* Maximum change in the median values of $\Sigma_{\rm SFR}$ (upper panel), $P_{\rm turb}$ (central panel) and $1/\alpha_{\rm vir}$ (lower panel) over the duration of post-merger/post-formation evolution, as a function of the cloud scale ℓ. The filled circles correspond to the interacting clouds and the open circles to the isolated clouds. We see that on scales above $\ell \sim 100$ pc, the internal properties of the GMCs are approximately scale- and time-independent.

then cascades down to drive the cloud centroid velocity dispersion across a range of smaller scales.

4.2 The physical impact of cloud mergers

The impact of cloud mergers on the turbulent and star-forming properties of the interacting clouds is a direct indicator of their role in setting the cloud lifecycle and the galactic star formation rate. We would like to determine whether mergers signal the presence of converging flows on smaller spatial scales, or whether the clouds are simply 'nudging' each other (see Dobbs et al. 2015).

In Figure 9, we demonstrate that collapse and star formation within our simulated giant molecular clouds sets in on approximately the local time-scale for self-gravity, regardless of whether or not the clouds are involved in a merger. In the left-hand column, we display the time evolution of the star formation rate surface density $\Sigma_{\rm SFR}$ (upper panel), the turbulent pressure $P_{\rm turb}$ (central panel) and the inverse virial parameter $1/\alpha_{\rm vir}$ (lower panel) with the time after a merger has occurred, for clouds that survive for 12 Myr after the merger without further interaction. The differently-coloured lines correspond to different bins in the cloud spatial scale ℓ[1]. In the central column we show the same three quantities, as a function of time after cloud formation, for clouds that survive for 18 Myr without any interaction at all. We have extended the considered time interval in the isolated case to account for the average time-scale of 6 Myr before which a cloud merger occurs on the smallest spatial scales. The only difference between the two columns is that the isolated clouds start with lower values of the turbulent pressure and star formation rate, as they have not yet begun to collapse. By contrast, the merging clouds have typically evolved for 6 Myr before the interaction occurs, and so have already contracted slightly to a state of higher $P_{\rm turb}$ and $\Sigma_{\rm SFR}$. In summary, it does not appear as though the mergers have any discernible effect on molecular cloud evolution. This finding is subject to the caveat that our numerical resolution does not allow us to resolve the detailed process of star formation, a point which is discussed in Section 6.

In the right-hand column of Figure 9, we show the gravitationally-driven increase in each cloud property for both

[1] The offset of ~ 5 Myr in the time-evolution of $\Sigma_{\rm SFR}$ relative to the other two quantities is due to the fact that we calculate the star formation rate as an average over young stars within each cloud, with ages between 0 and 5 Myr.

merging clouds (filled circles) and isolated clouds (unfilled circles), as a function of the median cloud scale ℓ. We see that at a spatial scale of $\ell \sim 100$ pc, i.e. around the thin-disc scale-height in our simulations, contraction and star formation never set in. That is, the clouds are self-gravitating and star-forming below the thin-disc scale-height, but not above it. We will return to this point in the following section, in the context of the giant molecular cloud lifetime.

5 THE MOLECULAR CLOUD LIFETIME

In the previous section, we showed that the fractal spatial structure of the molecular interstellar medium in our simulations sets a merger rate $\Gamma_{\rm merge} \propto \lambda^{-0.4}$ for giant molecular clouds of separation length λ. Although at our numerical resolution, mergers do not appear to play a significant role in setting the internal turbulent and star-forming properties of the molecular gas, their occurrence is frequent, and they introduce sub-structure to the cloud evolution network. Almost 80 per cent of clouds at scales $\ell \sim 10$ pc and separations $\lambda \sim 100$ pc experience a merger during their lifetime. Computing the molecular cloud lifetime from the cloud evolution network is therefore not as trivial as measuring the end-to-end temporal extent of all possible trajectories. In the following sub-sections, we describe how the distribution of cloud lifetimes is computed at each spatial resolution, and how this distribution is used to define the characteristic cloud lifetime $\tau_{\rm life}$ at each spatial scale.

5.1 Walking through the cloud evolution network

We require an approach that describes the distribution of temporal lengths for time-directed trajectories in the cloud merger network, while accounting for cloud interactions via the following two requirements:

(i) *Cloud uniqueness:* Each edge connecting two nodes (arrows in Figure 4) in the network represents a time-step in the evolution of a single cloud, and so can contribute to just one cloud lifetime. Edges must not be double-counted when calculating cloud lifetimes.

(ii) *Cloud number conservation:* Each cloud (unique trajectory in Figure 4) can be formed and destroyed only once, so the number of cloud lifetimes retrieved from the entire network must be equal to the number of cloud formation events and cloud destruction events.

In addition, we avoid making arbitrary choices between cloud-evolutionary paths as they pass through mergers and splits.[2] At a merger involving two clouds A and B, there are two mutually-exclusive outcomes: (1) that A continues to evolve while B is considered to have been destroyed, and (2) that A is destroyed and B continues to evolve. The method for satisfying (i) and (ii) while also sampling from the set of all unique time-directed trajectories through the network is the Monte Carlo (MC) walk described in Appendix A. For each MC iteraction, a number of walkers $\theta_{\rm split} - \theta_{\rm merge}$ are initialised at every *formation node* in the network, at which the net change in the number of clouds is positive, $\theta_{\rm split} > \theta_{\rm merge}$. Each walker steps along the edges between nodes, counting the number of time-steps it takes, until it reaches an *interaction node*[3] with $\theta_{\rm merge} > 1$ or $\theta_{\rm split} > 1$. A random number from the uniform distribution $U(0, 1)$ is assigned to all such interaction nodes for a given MC iteration, and this random number is used to choose between possible subsequent trajectories for the walker, including the possibility of cloud destruction. Upon destruction of a cloud, the walker is terminated, and returns a lifetime $t_{\rm life}$ for the trajectory. Via this algorithm, each edge joining pairs of nodes in the cloud evolution network is visited exactly once by a walker, during each MC iteration. We perform 70 such iterations to reach convergence of the characteristic molecular cloud lifetime $\tau_{\rm life}$ for the cloud population of an entire galaxy.

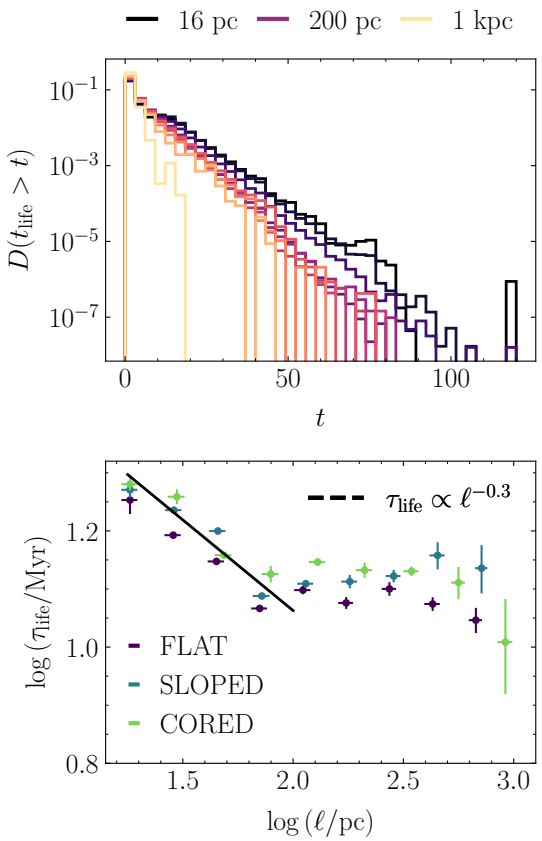

Figure 10. *Top:* Cumulative distribution of trajectory lifetimes $t_{\rm life}$ in ten different bins of cloud size, where smaller sizes correspond to darker colours. The median values of cloud size in three of the bins are given by the legend. The exponential form of each distribution is expected for a population of clouds obeying the rate equation (20). *Bottom:* Characteristic cloud lifetime $\tau_{\rm life}$ as a function of the median cloud size ℓ for each simulated galaxy. This is obtained directly from the exponential distributions in the top panel by fitting a function $\exp(-t/\tau_{\rm life})$, according to Equations (23) and (24). We see that the cloud lifetime is independent of scale for $\ell \gtrsim 100$ pc and obeys a power-law scaling relation $\tau_{\rm life} \propto \ell^{-0.3}$ for $\ell \lesssim 100$ pc, given by the solid black line.

[2] We present here the most basic form of the algorithm, with no assumptions about what constitutes the destruction of a cloud, other than that a node is removed from the cloud evolution network from one time-step to the next. In Section 6, we discuss how the algorithm could be altered to distinguish between cloud mergers and cloud accretion.

[3] Note that this may also be the formation node itself.

5.2 The characteristic molecular cloud lifetime, $\tau_{\rm life}$

Our walk through the cloud evolution network yields a distribution of lifetimes $t_{\rm life}$ for every cloud identified in our simulations, corresponding to the lengths of unique trajectories in Figure 4. We find that the range of possible lifetimes across all scales spans from 1 Myr (the temporal resolution of the network) up to 120 Myr. The clouds that survive the longest undergo many mergers and splits throughout their lifetimes. The distribution $D(t_{\rm life} > t)$ of the number of clouds surviving after a time t is shown in the top panel of Figure 10, for different cloud scales ℓ. Its exponential form is expected for a system in which the characteristic rate of cloud formation $\xi_{\rm form}$, and the characteristic lifetime $\tau_{\rm life}$ before cloud destruction, are approximately time-invariant.[4] In this case, the number of clouds $N_{\rm cl}$ in the population obeys the rate equation

$$\frac{{\rm d}N_{\rm cl}}{{\rm d}t} = -\tau_{\rm life}^{-1} N_{\rm cl} + \xi_{\rm form}. \quad (20)$$

Integrating yields the time-dependence of the population size as

$$N_{\rm cl} = \tau_{\rm life}\xi_{\rm form} + (N_{\rm cl,0} - \xi_{\rm form}\tau_{\rm life}) \exp\Big[-\frac{t}{\tau_{\rm life}}\Big], \quad (21)$$

where $N_{\rm cl,0}$ is the number density of clouds at time $t = 0$. We see that at times $t \gg \tau_{\rm life}$ we reach a steady state given by

$$N_{\rm cl}(t \to \infty) \to \tau_{\rm life}\xi_{\rm form}. \quad (22)$$

If we were suddenly to 'turn off' the process of cloud formation by setting $\xi_{\rm form} = 0$, then the number of clouds would decay exponentially as

$$N_{\rm cl}(t) = N_{\rm cl,0} \exp\Big[-\frac{t}{\tau_{\rm life}}\Big], \quad (23)$$

so that the characteristic cloud lifetime can be obtained directly from the fraction of all clouds $N_{\rm cl}(t)/N_{\rm cl,0}$ that survive at least for a time t, which is given by the distribution of trajectory lengths as

$$N_{\rm cl}(t) = \sum_{t_{\rm life}>t}^{\infty} D(t_{\rm life}) \equiv D(t_{\rm life} > t). \quad (24)$$

This argument explains the exponential form of the distributions $D(t_{\rm life} > t)$ in the upper panel of Figure 10. The characteristic time-scale $\tau_{\rm life}$ for cloud destruction is extracted by fitting a linear function to $\ln D(t_{\rm life} > t) \propto -t/\tau_{\rm life}$ and calculating the negative inverse of its slope.

5.3 Scaling relation of the characteristic molecular cloud lifetime

In the lower panel of Figure 10, we show the scaling relation of the characteristic molecular cloud lifetime $\tau_{\rm life}$, which varies across the range $\tau_{\rm life}/{\rm Myr} \in [13, 20]$. It is well-described by the piece-wise function

$$\tau_{\rm life}/{\rm Myr} = \begin{cases} 48(\ell/{\rm pc})^{-0.3} & \text{if } \ell < 100 \text{ pc} \\ 13 & \text{if } \ell \gtrsim 100 \text{ pc}. \end{cases}$$

The break in the scaling relation at the gas-disc scale-heightb $\ell \sim 100$ pc is the same as is observed for the increase in the cloud internal pressure, virial parameter and star formation rate during the process of gravitational collapse and star formation (right-hand column of Figure 9). This indicates that the cloud lifetime depends on the degree and efficiency with which the cloud is contracting and forming stars. In Figure 11 we show explicitly that this is the case. In the upper panels we show the typical time evolution of the median turbulent pressure $P_{\rm turb}$ and of the surface density Σ for a single set of unique trajectories through each cloud evolution network (corresponding to a single MC iteration). The colour of the line corresponds to the median cloud scale ℓ in each lifetime bin. We see that the time for which the cloud survives increases monotonically as its size decreases. The reason for this is shown in the lower panel, which gives the mean collapse-times $\Delta t_{\rm coll}$ taken for clouds at each spatial scale to reach their maximum turbulent pressures and surface densities, as well as the mean dispersal-times $\Delta t_{\rm disp}$

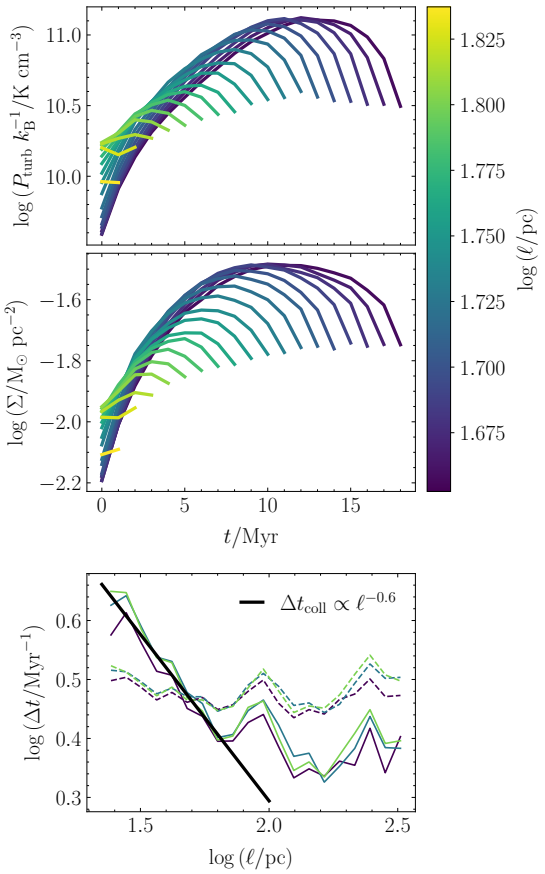

Figure 11. *Upper panels:* Time-evolution of the median cloud turbulent pressure $P_{\rm turb}$ (upper-most panel) and the median cloud surface density $\Sigma_{\rm turb}$ (lower panel) for isolated (non-interacting) clouds in the FLAT cloud evolution network, binned by their survival times $t_{\rm life}$. The colour of the lines indicates the logarithm of the median cloud size scale ℓ in each bin. *Lower panel:* The mean time-scale $\Delta t_{\rm coll}$ for clouds to collapse to their maximum densities and pressures, and the mean time-scale $\Delta t_{\rm disp}$ for dispersal by star formation feedback after this state is reached, as a function of the cloud scale ℓ/pc. The coloured lines correspond to the FLAT (purple), SLOPED (blue) and CORED (green) simulations, and the black solid line denotes the power-law fit to the combined data for the collapse time-scale across all three simulations.

[4] For our simulations, this assumption is a valid: over a period of 400 Myr, the global galactic SFR changes by just 0.5 M$_\odot$ yr^{-1} and the size of the cloud population varies by just 1 per cent.

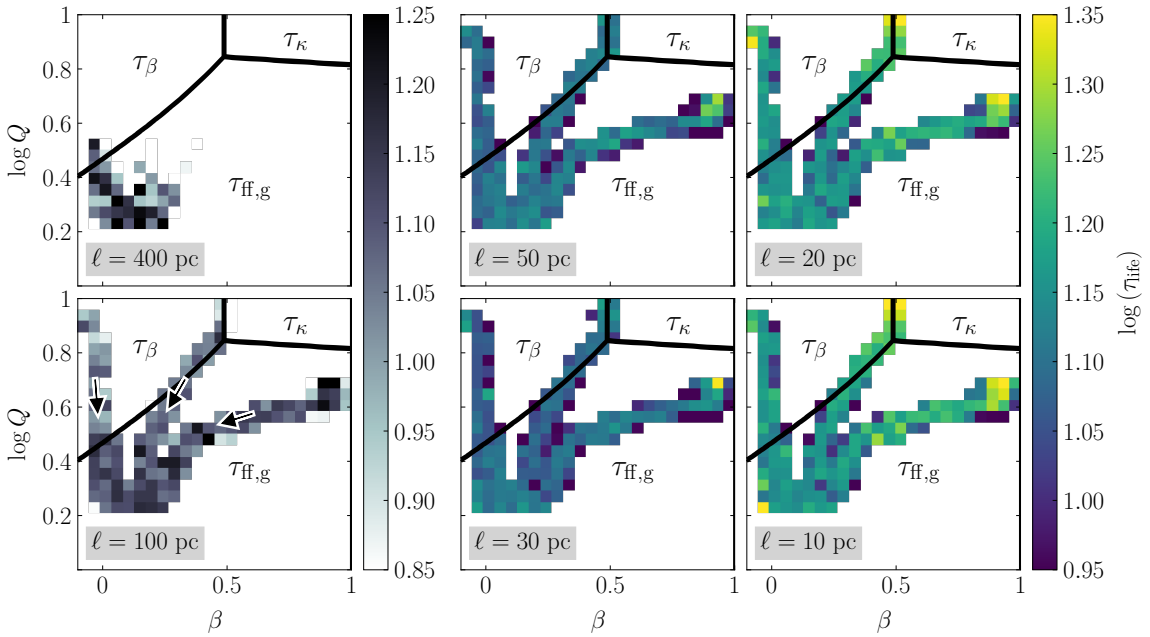

Figure 12. Characteristic cloud lifetime $\tau_{\rm life}$ for populations of clouds across different galactic-dynamical environments. The value of $\tau_{\rm life}$ (coloured pixel in each panel) is obtained via the exponential distribution of trajectory lengths in each bin of the shear parameter β (horizontal axis) and the Toomre Q stability parameter (vertical axis), via the method of Section 5.2. The data from the cloud evolution networks of all three simulated discs is compiled for each spatial resolution $\epsilon = 198$ pc through to the native resolution of 6 pc (top left panel to lower right panel). The median cloud scale ℓ for each cloud evolution network is annotated in the grey-shaded boxes, and each distinct set of connected pixels corresponds to the locus of the cloud population for one isolated disc galaxy. The black arrows mark the direction in which the galactocentric radius increases, and the black solid lines enclose the regions of parameter space for which the minimum galactic-dynamical time-scale is τ_κ (orbital epicyclic perturbations), τ_β (galactic shear) and $\tau_{\rm ff,g}$ (gravitational free-fall), when a value $\phi_{\rm P} = 3$ is adopted for the stellar contribution to the mid-plane pressure.

required for the clouds to be destroyed by star formation feedback, after this maximally-contracted state is reached. We find that the dispersal time-scale holds approximately constant at a mean value of ~ 3 Myr across all spatial scales, but the contraction time-scale obeys a scaling relation of $\Delta t_{\rm coll} \propto \ell^{-0.6}$ below the gas-disc scale-height, before levelling out to a mean value of ~ 2.5 Myr for scales $\ell \gtrsim 100$ pc.

Below the gas disc scale-height $\ell \lesssim 100$ pc, the sum of these two time-scales reproduces the scaling of the characteristic cloud lifetime, which can therefore be approximately described by

$$\begin{aligned} \tau_{\rm life} &\sim \Delta t_{\rm coll} + \Delta t_{\rm disp} \\ &\sim \ell^{-0.3} + {\rm const.} \end{aligned} \tag{25}$$

That is, the clouds are universally self-gravitating. As their scale decreases and their densities increase, they take an increasingly long time to reach the star formation efficiencies required to halt their collapse, but once the required star formation rate is reached, they disperse more vigorously than their larger, more diffuse counterparts, and therefore do so on a similar time-scale.

Above the gas disc scale-height $\ell \gtrsim 100$ pc, the molecular cloud lifetime becomes independent of spatial scale, settling to a value of 13 Myr. We attribute this to two related effects. The first is that regions of molecular gas of size equal to or larger than the disc scale-height are no longer self-gravitating. This can be seen in the two left-hand columns of Figure 9, in which the lines corresponding to scales $\ell \gtrsim 100$ pc are associated with cloud virial parameters $\alpha_{\rm vir} > 1$. This means that self-gravity and star formation are no longer expected to play an appreciable role in setting the molecular cloud lifetime, which is then approximately equal to the cloud crossing time-scale. The second effect is that molecular clouds on scales of $\ell \gtrsim 100$ pc within the galactic mid-plane are vertically-confined. That is, the crossing time on which bubbles of hot gas driven by supernova feedback (Kim & Ostriker 2017, 2018) reach the edges of clouds is approximately equal to to the crossing time of the disc. The scaling relation $\tau_{\rm life} \propto \ell^{-0.3}$ of the cloud lifetime in our simulations over the scale range 10 pc $\lesssim \ell \lesssim 100$ pc therefore converges to the gas-disc crossing time at scales of $\ell \gtrsim 100$ pc.

5.4 Variation of the cloud lifetime with the galactic environment

Given the universally self-gravitating behaviour of our simulated molecular clouds below the scale-height of the galactic disc, we do not expect that the characteristic molecular cloud lifetime $\tau_{\rm life}$ will depend on the galactic-dynamical environment at any scale $\ell \lesssim 100$ pc. That is, the cloud lifetime varies with the time-scale $\Delta t_{\rm coll}$ for gravitational contraction and with the time-scale $\Delta t_{\rm disp}$ for dispersal by means of star formation, which are local quantities that depend on the cloud density and on the physics of stellar feedback, and not on the larger-scale properties of the galaxy. In Fig-

ure 12 we verify our suspicion by examining value of the characteristic cloud lifetime for populations of clouds in different galactic-dynamical environments, across all three simulated galaxies. Each of the six panels corresponds to the population of molecular clouds in the FLAT, SLOPED and CORED simulations, identified using the two-dimensional map at spatial resolutions from $\epsilon = 198$ pc (top left panel) to the native resolution of $\epsilon = 6$ pc (bottom right panel). The grey boxes display the median cloud scale ℓ within each map. Across all resolutions and scales, no clear colour gradient is visible, indicating that there is no appreciable trend with the galactic-dynamical environment. This result is in agreement with the finding of Jeffreson et al. (2020) that the molecular clouds in these Milky Way-pressured simulations are highly over-dense and over-pressured relative to the galactic mid-plane, such that their turbulent and star-forming properties are decoupled from galactic dynamics, and driven instead by local gravitational effects. We note that we would expect some small degree of variation of $\tau_{\rm life}$ with the galactocentric radius (indicated by the black arrows in the lower left-hand panel) at a scale of 198 pc, due to the variation of the gas-disc scale-height and thus the gas-disc crossing time. Unfortunately there is insufficient data across environments to distinguish such a trend at this low resolution.

6 DISCUSSION

Our discussion of the time evolution of giant molecular clouds is closely-related to work by Dobbs et al. (2015), who have also constructed cloud evolutionary networks in order to characterise cloud interactions as a function of time. In their flocculent disc galaxy simulation, they find a cloud merger rate of one in 28 Myr, which is comparable to the values we obtain at our lowest spatial resolutions, for clouds of size $\ell \sim 100$ pc. At higher resolutions, we obtain cloud merger rates almost three times faster, up to one in every 10-12 Myr. This is probably due to our threshold for cloud identification, which is much more lenient than that adopted by Dobbs et al. (2015). While these authors consider only those clouds with masses $M > 1.5 \times 10^4$ M$_\odot$ and require a numerical resolution of 50 cells, we have allowed clouds all the way down to a few solar masses, containing only ten Voronoi cells at the highest spatial resolutions. Our lenient cloud identification threshold is chosen to ensure the consistency of our cloud-tracking procedure across maps at different spatial resolutions, and it is validated to an extent by the lack of a spurious small-scale turnover in the scaling relations we derive, however a result of our leniency may be an elevated frequency of 'mergers' occurring between clouds of very different masses (i.e. very low-mass clouds with very high-mass clouds). These events might better be considered as accretion events and excluded from the merger sample. In this work we have remained as agnostic as possible towards definitions of mergers and splits via their mass ratios, but in future work this could easily be incorporated into the MC random walk described in Section 5.1 by means of a non-uniform MC sampling criterion.

A particular point of agreement between our work and that of Dobbs et al. (2015) is that cloud interactions, though frequent, do not have an appreciable effect on the internal turbulent or star-forming properties of the interacting clouds. We have shown this via a comparison between interacting and isolated time-directed trajectories through our cloud evolution network. Dobbs et al. (2015) additionally show two-dimensional projections of specific cloud mergers at subsequent time-steps, where it can be seen that the two clouds join without the obvious presence of converging flows on smaller scales. Although it is tempting to conclude that cloud interactions have no effect on the galactic star formation rate, we must be careful to state the caveat that neither our simulations (at mass resolution ~ 900 M$_\odot$), nor those of Dobbs et al. 2015 (at mass resolution ~ 300 M$_\odot$), is able to resolve star formation, instead relying on a parametrisation of the empirical form of Kennicutt 1998 (see our Equation 2). This means that star formation resulting from slow gravitational collapse will be well-characterised in our simulations, but gas that is bumped into the high-density regime at shorter time-scales, as in shocks, may not be properly modelled. Simulations of discrete colliding clouds at high spatial resolution do indeed find an elevation of the star formation efficiency owing to the formation of filamentary structures and sheets on sub-cloud scales (Takahira et al. 2014; Balfour et al. 2015, 2017; Wu et al. 2017; Tanvir & Dale 2020). Similarly, previous simulations have investigated colliding flows driven by magnetohydrodynamic turbulence (e.g. Passot et al. 1995; Padoan 1995; Ballesteros-Paredes et al. 1999a,b; Hennebelle & Pérault 2000; Li & Nakamura 2002; Clark et al. 2005; Heitsch et al. 2005, 2006; Zamora-Avilés & Vázquez-Semadeni 2014) or due to expanding bubbles driven by stellar feedback (e.g. Rosen & Bregman 1995; Korpi et al. 1999; Slyz et al. 2005; Mac Low et al. 2005; Kim & Ostriker 2015a,b), which in theory should operate and trigger star formation on all levels of the interstellar medium hierarchy examined in this work (Sasao 1973; Elmegreen 1991, 1993; Elmegreen & Falgarone 1996; Elmegreen 2007). Such simulations find continuous velocity fields that cut across the boundaries of discrete, identified clouds, indicating the presence of converging flows at their edges. At our resolutions, no such triggered star formation is observed, but we cannot rule out its presence at higher resolutions. Ultimately, both a large statistical sample of clouds like the one presented here, plus sufficient numerical resolution to resolve shocks at the interfaces of converging flows and cloud interactions, is required to rule out such effects. This could possibly be achieved using zoom-in simulations of a small sample of clouds from a larger isolated-galaxy simulation.

The large size of our molecular cloud sample ($\sim 80,000$ clouds) allows us to determine a characteristic cloud lifetime $\tau_{\rm life}$ in each simulated galaxy and in each galactic environment, which is proportional to the half-life of the population (see Section 5.2). At a given spatial scale, this time-scale is directly-comparable to the distributions of cloud lifetimes derived in similar numerical simulations from the literature (Dobbs & Pringle 2013; Fujimoto et al. 2019; Dobbs et al. 2019; Benincasa et al. 2019). Relative to these works, one significant difference is clear in our method of cloud-tracking: we identify clouds in two dimensions, rather than by directly tracking the three-dimensional flow of molecular gas from one time to the next, as in the cited works. We do this in order to make a direct comparison to observations across a set of well-defined cloud scales ℓ, without assuming that the boundaries of observed clouds move along with a given proportion of the total gas or molecular gas mass. Numerical simulations of the turbulent gas flow into, and out of, gas overdensities (Ballesteros-Paredes et al. 1999b; Semenov et al. 2017, 2018, 2019) suggest that tracking in this way may not be representative of the hierarchical and fluctuating density structure of the interstellar medium. Nevertheless, we find that our range of characteristic lifetimes $12 \, {\rm Myr} \lesssim \tau_{\rm life} \lesssim 20 \, {\rm Myr}$ across the scale range $10 \, {\rm pc} \lesssim \ell \lesssim 400 \, {\rm pc}$ is comparable to the typical span of 4-25 Myr found by Dobbs & Pringle (2013) at a similar numerical resolution. At our largest spatial scales $\ell \gtrsim 100$ pc, our values are still around twice the mean cloud lifetimes measured by Benincasa et al. (2019), however their

mass resolution is around ten times lower than ours, and so this effect may be attributed to missing the lower-mass 'tails' of cloud formation and destruction that we resolve. Our range of lifetimes is significantly shorter than the mean values of 30-50 Myr computed by Fujimoto et al. (2019), however as studied in detail by these authors, their elongated cloud lifetimes are likely due to spuriously-inefficient stellar feedback in their simulated discs.

We may also make a comparison here between our numerically-derived cloud lifetimes and observed values from nearby galaxies. Historically, the lack of temporal information in observations means that these values have been determined either by (1) measuring the velocities and separations of clouds that are assumed to form part of an evolutionary sequence (Scoville & Hersh 1979; Solomon et al. 1979; Engargiola et al. 2003; Meidt et al. 2015), or (2) using the numbers of clouds in different evolutionary phases as a proxy for the time intervals they spend in these phases (Blitz et al. 2007; Kawamura et al. 2009; Murray 2011; Corbelli et al. 2017). In Milky Way-mass galaxies, these studies generally yield cloud lifetimes in the range 10-30 Myr, in agreement with our simulated values. In addition to these techniques, recent work by Kruijssen & Longmore (2014); Kruijssen et al. (2018, 2019) has allowed for the relaxation of an inconvenient assumption implicit in previous methods: that the numbers of clouds in each cloud-evolutionary phase are directly-proportional to the time spent in each. Instead, these authors fit the variation of the observed flux ratio bias for gas and stellar tracers over a range of different scales. This allows for the derivation of the characteristic cloud lifetime for regions of molecular gas that are spatially-distinct on the scale-height of the galactic gas-disc (Kruijssen et al. 2019; Chevance et al. 2020). As such, they are directly-comparable to our results at cloud scales of $\ell \gtrsim 100$ pc. Values of 11-12 Myr have been obtained for the Milky Way-mass galaxies NGC 628 and NGC 4254 by Chevance et al. (2020) and values of ~ 10 Myr have been measured in NGC 300 by Kruijssen et al. (2019); very close to our derived values of ~ 13 Myr at the gas disc scale-height.

Finally, we note here that the scaling relation for molecular cloud lifetimes shown in Figure 10 is not in contradiction with the age-spreads of Cepheid variables and stellar clusters observed by Elmegreen & Efremov (1996); Efremov & Elmegreen (1998); Elmegreen (2000). These observations demonstrate that star formation occurs on 1-2 crossing times across three orders of magnitude in spatial scale, from 10 pc up to ~ 1 kpc. Although our cloud lifetimes decrease with spatial scale below the gas disc scale-height, while the crossing time increases, we show in Figure 9 that the majority of a cloud's lifetime is spent in the quiescent phase, after which the star formation ramps up and destroys the cloud in a small fraction of its lifetime (~ 3 Myr). By virtue of the fractal structure of the interstellar medium, these short bursts of star formation at the smallest scales will still have temporal offsets of up to a crossing time at lower-density levels of the hierarchical interstellar medium.

7 CONCLUSIONS

In this work, we have examined the time-evolution of giant molecular clouds across Milky Way-like environments, using a set of three isolated galaxy simulations in the moving-mesh code AREPO. The galaxies are designed to probe a wide range of galactic-dynamical environments, spanning an order of magnitude in the Toomre Q gravitational stability parameter, the galactic orbital angular velocity Ω, and the mid-plane hydrostatic pressure (Jeffreson et al. 2020), as well as the full range of galactic shear parameters β from the case of solid-body rotation ($\beta = 1$) up to the case of a flat rotation curve ($\beta = 0$). We have found that:

(i) The cloud evolutionary network of each galaxy is highly-substructured in space and in time. Around 80 per cent of clouds at spatial scales of $\ell = 10$-20 pc interact with other clouds during their lifetimes, with a merger rate of $\Gamma_{\rm merge} \sim 0.1$ Myr^{-1}. This rate drops to one in thirty at cloud scales of $\ell \sim 400$ pc.

(ii) The merger rate is well-described by the crossing time in a supersonically-turbulent, fractally-structured interstellar medium, with a fractal index of $D \sim 1.54$. This relationship depends on the two-dimensional velocity dispersion $\sigma_{\lambda,\rm 2D}$ of molecular cloud centroids within the galactic mid-plane, which is found to obey the same scaling relation with cloud separation λ as is obeyed by the three-dimensional internal cloud velocity dispersion $\sigma_{\rm 3D}$ with cloud scale ℓ (Larson 1981; Heyer et al. 2009). This correspondence extends up to scales ten times larger than the gas disc scale-height. That is, supersonic turbulence sets the two-dimensional structure in the molecular gas of our galaxies over a scale range of 10 pc $\lesssim \lambda \lesssim 1$ kpc, in agreement with Elmegreen (2000); Elmegreen et al. (2003a,b).

(iii) Across galactic-dynamical environments, the cloud merger rate is proportional to $\beta\Omega$ and uncorrelated with $(1-\beta)\Omega$, indicating that it is driven by the absolute velocity offset in the inertial frame, rather than by the differential velocity between clouds in the rotational frame of the galaxy. This suggests that the role of shear in driving mergers is not simply set by the time-scale on which clouds catch up to each other along azimuthal trajectories about the galactic centre. It may instead have to do with turbulence driving on galactic scales.

(iv) Despite the frequency of cloud mergers, they do not appear to have any influence on the internal turbulent and star-forming properties of the molecular clouds in our simulations. Clouds that evolve in isolation collapse and form stars on the same time-scale as clouds that are involved in mergers.

(v) The distribution of molecular cloud lifetimes in each galaxy takes an exponential form with values between 1 and 120 Myr, indicating that the cloud population $N_{\rm cl}$ is well-described by a rate equation of the form

$$\frac{{\rm d}N_{\rm cl}}{{\rm d}t} = \tau_{\rm life}^{-1} N_{\rm cl} + \xi_{\rm form}, \tag{26}$$

where $\xi_{\rm form}$ is the rate of cloud formation and $\tau_{\rm life}$ is the characteristic cloud lifetime for the population (the characteristic time-scale of cloud destruction).

(vi) We find that $\tau_{\rm life}$ obeys a scaling relation of the form $\tau_{\rm life} \propto \ell^{-0.3}$ across all three galaxies below the gas disc scale-height, driven by the competition between gravitational contraction and stellar feedback. Above the scale-height, the characteristic lifetime is constant and set by the crossing time of the galactic disc, in agreement with observations (Kruijssen et al. 2019; Chevance et al. 2020). The range of characteristic lifetimes across spatial scales is 10 Myr $\lesssim \tau_{\rm life} \lesssim 20$ Myr.

(vii) The simulated populations of galaxies are self-gravitating and their lifetimes are consequently independent of the galactic-dynamical environment.

REFERENCES

Agertz O., Lake G., Teyssier R., Moore B., Mayer L., Romeo A. B., 2009, MNRAS, 392, 294

Balfour S. K., Whitworth A. P., Hubber D. A., Jaffa S. E., 2015, MNRAS, 453, 2471

Balfour S. K., Whitworth A. P., Hubber D. A., 2017, MNRAS, 465, 3483
Ballesteros-Paredes J., Vázquez-Semadeni E., Scalo J., 1999a, ApJ, 515, 286
Ballesteros-Paredes J., Hartmann L., Vázquez-Semadeni E., 1999b, ApJ, 527, 285
Bally J., Stark A. A., Wilson R. W., Henkel C., 1987, ApJS, 65, 13
Bally J., Langer W. D., Wilson R. W., Stark A. A., Pound M. W., 1991, in Falgarone E., Boulanger F., Duvert G., eds, IAU Symposium Vol. 147, Fragmentation of Molecular Clouds and Star Formation. p. 11
Benincasa S. M., et al., 2019, arXiv e-prints, p. arXiv:1911.05251
Bertoldi F., McKee C. F., 1992, ApJ, 395, 140
Bigiel F., Leroy A., Walter F., Brinks E., de Blok W. J. G., Madore B., Thornley M. D., 2008, AJ, 136, 2846
Bigiel F., et al., 2016, ApJ, 822, L26
Blanc G. A., Heiderman A., Gebhardt K., Evans II N. J., Adams J., 2009, ApJ, 704, 842
Blitz L., Fukui Y., Kawamura A., Leroy A., Mizuno N., Rosolowsky E., 2007, in Reipurth B., Jewitt D., Keil K., eds, Protostars and Planets V. p. 81 (arXiv:astro-ph/0602600)
Bolatto A. D., Wolfire M., Leroy A. K., 2013, ARA&A, 51, 207
Caplar N., Tacchella S., 2019, MNRAS, 487, 3845
Chabrier G., 2003, PASP, 115, 763
Chevance M., et al., 2020, MNRAS, 493, 2872
Clark P. C., Bonnell I. A., Zinnecker H., Bate M. R., 2005, MNRAS, 359, 809
Colombo D., et al., 2019, MNRAS, 483, 4291
Corbelli E., et al., 2017, A&A, 601, A146
Dobbs C. L., Pringle J. E., 2013, MNRAS, 432, 653
Dobbs C. L., Pringle J. E., Duarte-Cabral A., 2015, MNRAS, 446, 3608
Dobbs C. L., Rosolowsky E., Pettitt A. R., Braine J., Corbelli E., Sun J., 2019, MNRAS, 485, 4997
Efremov Y. N., Elmegreen B. G., 1998, MNRAS, 299, 588
Elmegreen B. G., 1989, ApJ, 338, 178
Elmegreen B. G., 1991, ApJ, 378, 139
Elmegreen B. G., 1993, ApJ, 419, L29
Elmegreen B. G., 2000, ApJ, 530, 277
Elmegreen B. G., 2007, ApJ, 668, 1064
Elmegreen B. G., Efremov Y. N., 1996, ApJ, 466, 802
Elmegreen B. G., Falgarone E., 1996, ApJ, 471, 816
Elmegreen B. G., Elmegreen D. M., Leitner S. N., 2003a, ApJ, 590, 271
Elmegreen B. G., Leitner S. N., Elmegreen D. M., Cuillandre J.-C., 2003b, ApJ, 593, 333
Engargiola G., Plambeck R. L., Rosolowsky E., Blitz L., 2003, ApJS, 149, 343
Fagotto F., Bressan A., Bertelli G., Chiosi C., 1994a, A&AS, 104, 365
Fagotto F., Bressan A., Bertelli G., Chiosi C., 1994b, A&AS, 105, 29
Falgarone E., Phillips T. G., Walker C. K., 1991, ApJ, 378, 186
Falgarone E., Pety J., Hily-Blant P., 2009, A&A, 507, 355
Federrath C., Klessen R. S., 2013, ApJ, 763, 51
Federrath C., Klessen R. S., Schmidt W., 2009, ApJ, 692, 364
Federrath C., Roman-Duval J., Klessen R. S., Schmidt W., Mac Low M. M., 2010, A&A, 512, A81
Freeman P., Rosolowsky E., Kruijssen J. M. D., Bastian N., Adamo A., 2017, preprint, (arXiv:1702.07728)
Fujimoto Y., Tasker E. J., Habe A., 2014, MNRAS, 445, L65
Fujimoto Y., Chevance M., Haydon D. T., Krumholz M. R., Kruijssen J. M. D., 2019, MNRAS, 487, 1717
Gensior J., Kruijssen J. M. D., Keller B. W., 2020, arXiv e-prints, p. arXiv:2002.01484
Gentry E. S., Krumholz M. R., Dekel A., Madau P., 2017, MNRAS, 465, 2471
Glover S. C. O., Mac Low M.-M., 2007a, ApJS, 169, 239
Glover S. C. O., Mac Low M.-M., 2007b, ApJ, 659, 1317
Glover S. C. O., Federrath C., Mac Low M.-M., Klessen R. S., 2010, MNRAS, 404, 2
Gong M., Ostriker E. C., Wolfire M. G., 2017, ApJ, 843, 38
Habing H. J., 1968, Bull. Astron. Inst. Netherlands, 19, 421
Heitsch F., Burkert A., Hartmann L. W., Slyz A. D., Devriendt J. E. G., 2005, ApJ, 633, L113
Heitsch F., Slyz A. D., Devriendt J. E. G., Hartmann L. W., Burkert A., 2006, ApJ, 648, 1052
Hennebelle P., Pérault M., 2000, A&A, 359, 1124
Hernquist L., 1990, ApJ, 356, 359
Heyer M. H., Brunt C. M., 2004, ApJ, 615, L45
Heyer M. H., Carpenter J. M., Snell R. L., 2001, ApJ, 551, 852
Heyer M., Krawczyk C., Duval J., Jackson J. M., 2009, ApJ, 699, 1092
Hopkins P. F., et al., 2018, MNRAS, 477, 1578
Indriolo N., McCall B. J., 2012, ApJ, 745, 91
Jeffreson S. M. R., Kruijssen J. M. D., 2018, MNRAS, 476, 3688
Jeffreson S. M. R., Kruijssen J. M. D., Keller B. W., Chevance M., Glover S. C. O., 2020, MNRAS,
Jeffreson S. M. R., et al., in prep., MNRAS
Kawamura A., et al., 2009, ApJS, 184, 1
Keller B. W., Jeffreson S. M. R., Kruijssen J. M. D., inprep., MNRAS
Kennicutt Jr. R. C., 1998, ARA&A, 36, 189
Kennicutt R. C., Evans N. J., 2012, ARA&A, 50, 531
Kim W.-T., Ostriker E. C., 2001, ApJ, 559, 70
Kim W.-T., Ostriker E. C., 2007, ApJ, 660, 1232
Kim C.-G., Ostriker E. C., 2015a, ApJ, 802, 99
Kim C.-G., Ostriker E. C., 2015b, ApJ, 815, 67
Kim C.-G., Ostriker E. C., 2017, ApJ, 846, 133
Kim C.-G., Ostriker E. C., 2018, ApJ, 853, 173
Kim W.-T., Ostriker E. C., Stone J. M., 2003a, ApJ, 599, 1157
Kim W.-T., Ostriker E. C., Stone J. M., 2003b, ApJ, 599, 1157
Koda J., et al., 2009, ApJ, 700, L132
Korpi M. J., Brandenburg A., Shukurov A., Tuominen I., Nordlund Å., 1999, ApJ, 514, L99
Kramer C., Stutzki J., Rohrig R., Corneliussen U., 1998, A&A, 329, 249
Kritsuk A. G., Norman M. L., Padoan P., Wagner R., 2007, ApJ, 665, 416
Kruijssen J. M. D., Longmore S. N., 2014, MNRAS, 439, 3239
Kruijssen J. M. D., Schruba A., Hygate A. P. S., Hu C.-Y., Haydon D. T., Longmore S. N., 2018, MNRAS, 479, 1866
Kruijssen J. M. D., et al., 2019, Nature, 569, 519
Krumholz M. R., 2013, DESPOTIC: Derive the Energetics and SPectra of Optically Thick Interstellar Clouds, Astrophysics Source Code Library (ascl:1304.007)
Krumholz M. R., Matzner C. D., 2009, ApJ, 703, 1352
Krumholz M. R., Tan J. C., 2007, ApJ, 654, 304
Krumholz M. R., Dekel A., McKee C. F., 2012, ApJ, 745, 69
Krumholz M. R., Fumagalli M., da Silva R. L., Rendahl T., Parra J., 2015, MNRAS, 452, 1447
Krumholz M. R., McKee C. F., Bland -Hawthorn J., 2018, arXiv e-prints, p. arXiv:1812.01615
Larson R. B., 1981, MNRAS, 194, 809
Lee Y., Snell R. L., Dickman R. L., 1990, ApJ, 355, 536
Leitherer C., et al., 1999, ApJS, 123, 3
Leroy A. K., Walter F., Brinks E., Bigiel F., de Blok W. J. G., Madore B., Thornley M. D., 2008, AJ, 136, 2782
Leroy A. K., et al., 2013, ApJ, 769, L12
Leroy A. K., et al., 2017, ApJ, 835, 217
Li Z.-Y., Nakamura F., 2002, ApJ, 578, 256
Liu G., Koda J., Calzetti D., Fukuhara M., Momose R., 2011, ApJ, 735, 63
Mac Low M.-M., Balsara D. S., Kim J., de Avillez M. A., 2005, ApJ, 626, 864
MacLaren I., Richardson K. M., Wolfendale A. W., 1988, ApJ, 333, 821
Mathis J. S., Mezger P. G., Panagia N., 1983, A&A, 500, 259
Matzner C. D., 2002, ApJ, 566, 302
McKee C. F., Ostriker E. C., 2007, ARA&A, 45, 565
Meidt S. E., et al., 2015, ApJ, 806, 72
Meidt S. E., et al., 2018, ApJ, 854, 100
Miura R. E., et al., 2012, ApJ, 761, 37
Miville-Deschênes M.-A., Murray N., Lee E. J., 2017, ApJ, 834, 57
Miyamoto M., Nagai R., 1975, PASJ, 27, 533
Murray N., 2011, ApJ, 729, 133
Nelson A. F., 2006, MNRAS, 373, 1039

Nelson R. P., Langer W. D., 1997, ApJ, 482, 796
Ossenkopf V., Mac Low M. M., 2002, A&A, 390, 307
Ostriker E. C., Stone J. M., Gammie C. F., 2001, ApJ, 546, 980
Padoan P., 1995, MNRAS, 277, 377
Passot T., Vázquez-Semadeni E., 1998, Phys. Rev. E, 58, 4501
Passot T., Vazquez-Semadeni E., Pouquet A., 1995, ApJ, 455, 536
Plummer H. C., 1911, MNRAS, 71, 460
Rice T. S., Goodman A. A., Bergin E. A., Beaumont C., Dame T. M., 2016, ApJ, 822, 52
Roman-Duval J., Jackson J. M., Heyer M., Rathborne J., Simon R., 2010, ApJ, 723, 492
Roman-Duval J., Federrath C., Brunt C., Heyer M., Jackson J., Klessen R. S., 2011, ApJ, 740, 120
Rosen A., Bregman J. N., 1995, ApJ, 440, 634
Rosolowsky E., Engargiola G., Plambeck R., Blitz L., 2003, ApJ, 599, 258
Safranek-Shrader C., Krumholz M. R., Kim C.-G., Ostriker E. C., Klein R. I., Li S., McKee C. F., Stone J. M., 2017, MNRAS, 465, 885
Sasao T., 1973, PASJ, 25, 1
Scalo J. M., 1985, in Black D. C., Matthews M. S., eds, Protostars and Planets II. pp 201–296
Scalo J., 1990, Perception of interstellar structure - Facing complexity. pp 151–176, doi:10.1007/978-94-009-0605-1˙12
Schruba A., Leroy A. K., Walter F., Sand strom K., Rosolowsky E., 2010, ApJ, 722, 1699
Scoville N. Z., Hersh K., 1979, ApJ, 229, 578
Scoville N. Z., Solomon P. M., 1975, ApJ, 199, L105
Semenov V. A., Kravtsov A. V., Gnedin N. Y., 2017, ApJ, 845, 133
Semenov V. A., Kravtsov A. V., Gnedin N. Y., 2018, ApJ, 861, 4
Semenov V. A., Kravtsov A. V., Gnedin N. Y., 2019, ApJ, 870, 79
Slyz A. D., Devriendt J. E. G., Bryan G., Silk J., 2005, MNRAS, 356, 737
Solomon P. M., Vanden Bout P. A., 2005, ARA&A, 43, 677
Solomon P. M., Sanders D. B., Scoville N. Z., 1979, in Burton W. B., ed., IAU Symposium Vol. 84, The Large-Scale Characteristics of the Galaxy. p. 35
Solomon P. M., Rivolo A. R., Barrett J., Yahil A., 1987, ApJ, 319, 730
Springel V., Di Matteo T., Hernquist L., 2005, MNRAS, 361, 776
Stone J. M., Ostriker E. C., Gammie C. F., 1998, ApJ, 508, L99
Sun J., et al., 2018, ApJ, 860, 172
Sun J., et al., 2020, arXiv e-prints, p. arXiv:2002.08964
Tacchella S., Forbes J. C., Caplar N., 2020, MNRAS, 497, 698
Takahira K., Tasker E. J., Habe A., 2014, ApJ, 792, 63
Tan J. C., 2000, ApJ, 536, 173
Tanvir T. S., Dale J. E., 2020, MNRAS, 494, 246
Tasker E. J., Tan J. C., 2009, ApJ, 700, 358
Toomre A., 1964, ApJ, 139, 1217
Usero A., et al., 2015, AJ, 150, 115
Utomo D., et al., 2018, ApJ, 861, L18
Vázquez G. A., Leitherer C., 2005, ApJ, 621, 695
Vazquez-Semadeni E., 1994, ApJ, 423, 681
Whitworth A., Lomax O., Balfour S., Mège P., Zavagno A., Deharveng L., 2018, PASJ, 70, S55
Williams J. P., McKee C. F., 1997, ApJ, 476, 166
Wu B., Tan J. C., Christie D., Nakamura F., Van Loo S., Collins D., 2017, ApJ, 841, 88
Zamora-Avilés M., Vázquez-Semadeni E., 2014, ApJ, 793, 84
da Silva R. L., Fumagalli M., Krumholz M., 2012, ApJ, 745, 145
da Silva R. L., Fumagalli M., Krumholz M. R., 2014, MNRAS, 444, 3275

This paper has been typeset from a TEX/LATEX file prepared by the author.

APPENDIX A: CALCULATION OF CLOUD LIFETIMES

As described in Section 5, we extract the cloud lifetime $\tau_{\rm life}$ from the cloud evolution network according to a Monte Carlo (MC) algorithm that samples from the set of all unique time-directed trajectories through the network. The pseudocode for a single MC iteration is presented in Algorithm 1. During an iteration, a trajectory is sourced at the site of every cloud formation node in the network (see Figure A1), and subsequently iterates the cloud lifetime by increments of $\Delta t = 1$ Myr as it steps along edges from parent nodes to their children. At nodes with multiple parents or children ($\theta_{\rm merge} > 1$ or $\theta_{\rm split} > 1$, respectively), we apply an unbiased MC assignment for the path taken by choosing a random number from the uniform distribution $U(0, 1)$. Figure A3 illustrates the MC assignment for different types of nodes, where formation nodes are coloured blue and destruction nodes are coloured orange. The arrow labels indicate the probability of each outcome. At cloud formation nodes (e)-(h), all possible MC outcomes correspond to paths for continued cloud evolution, while at cloud destruction nodes (a)-(d), a fraction of the possible MC outcomes $(\theta_{\rm merge} - \theta_{\rm split})/\theta_{\rm merge}$ corresponds to termination of the trajectory. It is also possible to have multiple MC outcomes at nodes such as (j), for which there is no net change in the number of clouds, $\theta_{\rm split} = \theta_{\rm merge}$[5]. By performing 70 MC iterations, we obtain a converged distribution of cloud lifetimes that accounts for all interactions in the cloud evolution network. The procedure satisfies the requirements for cloud number conservation and cloud uniqueness, which are defined for the network as follows:

(i) *Cloud uniqueness:* Each edge connecting two nodes in the network

Algorithm 1 A single Monte Carlo iteration of the algorithm used to extract the cloud lifetime $\tau_{\rm life}$ from the cloud evolution network. A worded description of the algorithm is given in the text.

$\mathcal{F} = \{f_i\} \leftarrow$ set of unique formation nodes.
$\Delta t \leftarrow$ time interval between consecutive nodes.

$\mathcal{R} = \{r_i\} \in U(0,1) \leftarrow$ set of random numbers for all nodes.
$\mathcal{I} = \{I_i = 0\} \leftarrow$ no. of times that each node has been accessed.

for f in $\mathcal{F}$ **do**
    $N_f = \theta_{\rm split}(f) - \theta_{\rm merge}(f)$
    for $j = 0 \rightarrow N_f$ **do**
        $\tau_{\rm life} =$ NEXTSTEP$(f, 0)$

function NEXTSTEP$(n, \tau_{\rm life})$
    $\mathcal{C}_n \leftarrow$ children of node n; $\theta_{\rm split}(n) \equiv |\mathcal{C}_n|$.
    $\mathcal{P}_n \leftarrow$ parents of node n; $\theta_{\rm merge}(n) \equiv |\mathcal{P}_n|$.

    $N_{\rm outcomes} \leftarrow$ total no. of MC outcomes at n.
    $N_{\rm outcomes} = \max\left[\theta_{\rm merge}(n), \theta_{\rm split}(n)\right]$.

    $N_{\rm term} \leftarrow$ no. outcomes that result in path termation at n.
    $N_{\rm term} = \max\left[0, \theta_{\rm merge}(n) - \theta_{\rm split}(n)\right]$.

    $k = 0$.
    while $r_n > k/N_{\rm outcomes}$ **do**
        $k = k + 1$.
    $k = (k + I_n) \mod N_{\rm outcomes}$.
    $I_n = I_n + 1$.
    if $k < N_{\rm term}$ **then**
        return $\tau_{\rm life}$
    else
        $\tau_{\rm life} = \tau_{\rm life} + \Delta t$.
        return NEXTSTEP$(\mathcal{C}_n[k - N_{\rm term}], \tau_{\rm life})$

[5] At nodes with $\theta_{\rm split} = \theta_{\rm merge}$, we could consider a different physical interpretation: that one or all of the incoming clouds are destroyed and re-formed. We choose the interpretation that all clouds survive because the interaction is shorter-lived than the temporal resolution of our simulations, with a duration of < 3 Myr. At the resolution of our simulations, we therefore have no evidence that a merger has occurred; only that the clouds have interacted and may have exchanged mass.

represents a time-step in the evolution of a single cloud, and so can contribute to just one cloud lifetime. Edges must not be double-counted when calculating cloud lifetimes.

(ii) *Cloud number conservation:* Each cloud can be formed and destroyed only once, so the number of cloud lifetimes retrieved from the entire network must be equal to the number of cloud formation events and cloud destruction events.

In the following, we give a detailed worded description of Algorithm 1.

- Lines 1-2: Define variables for the entire cloud evolution network, for all MC iterations. A cloud formation node $f_i \in \mathcal{F} = \{f_i\}$ is any node that generates a net increase in the number of clouds, $\theta_{\rm split} > \theta_{\rm merge}$. The time interval $\Delta t = 1$ Myr is the time between simulation snapshots, and so between consecutive nodes joined by edges in the network.
- Lines 3-4: Define the variables for a single MC iteration. At the beginning of each iteration, we generate a set random number $r_n \in \mathcal{R} = \{r_i\}$ for every node n in the network. At nodes with multiple MC outcomes ($\theta_{\rm split} > 1$ or $\theta_{\rm merge} > 1$), this number is used to choose between outcomes. We also keep track of the number of times $I_n \in \mathcal{I} = \{I_i\}$ that node n has been accessed, so that each outcome is accessed exactly once. In this sense, the random number r_n sets the first outcome to be accessed.
- Lines 5-8: Loop over the unique cloud formation nodes $f_i \in \mathcal{F}$. Each formation node f sources N_f separate paths, where N_f is the net increase in cloud number generated at f. For each separate path initiation, the cloud lifetime is calculated via the recursive function NEXTSTEP (lines 7-8). In the first call to the function NEXTSTEP$(f, 0)$, the cloud lifetime is initialised to zero.
- Line 9: Define the function NEXTSTEP, taking a node n and a cloud lifetime $\tau_{\rm life}$ as inputs.
- Lines 10-11: Define the local variables for node n. The set of children of n is given by $\mathcal{C}_n$ and the set of parents is given by $\mathcal{P}_n$. As such, the numbers of children/parents at node n are given by the sizes of the sets.
- Line 13: Calculate the number of MC outcomes at node n. This is equal to the number of child nodes (outgoing paths) if n is a formation node ($\theta_{\rm split}(n) > \theta_{\rm merge}(n)$), equal to the number of parent nodes (incoming paths) if n is a destruction node ($\theta_{\rm split}(n) < \theta_{\rm merge}(n)$), and equal to either quantity if n is an intersection node ($\theta_{\rm split}(n) = \theta_{\rm merge}(n)$). In general, it is therefore given by the maximum value of $\theta_{\rm split}$ and $\theta_{\rm merge}$.
- Line 15: Calculate the number of MC outcomes that result in path termination at n. This is equal to zero if n is a formation node or an intersection node, and equal to the reduction in the node number, $\theta_{\rm merge}(n) - \theta_{\rm split}(n)$, if n is a destruction node. In general, it is therefore given by the reduction in node number at any node, with a lower limit of zero.
- Lines 16-18: Use the random number r_n for node n to choose the first path taken at node n by the first trajectory in the loop over $f \in \mathcal{F}$ to access n. The index of the outcome is k.
- Line 19: Cycle the path taken according to how many times node n has already been accessed. For example, if node n has $N_{\rm outcomes} = 3$ possible MC outcomes and has already been accessed $I_n = 1$ time and taken the outcome $k = 2$, then the outcome is updated as $k = (2+1) \mod 3 = 0$.
- Line 20: Update the number of times that node n has been accessed, for the next iteration.
- Lines 21-22: For a destruction node, the first $N_{\rm term}$ outcomes are designated as cloud destructions. The path/recursion is terminated and we return the cloud lifetime $\tau_{\rm life}$. For any other node type, $N_{\rm term} = 0$ and so this option is not accessed.
- Lines 23-25: If the path has not been terminated in the preceding if-clause, proceed to the $(k - N_{\rm term})$th child node of n by continuing the recursion on this node. Iterate the cloud lifetime by the time interval Δt and pass both arguments back to the start of the function.

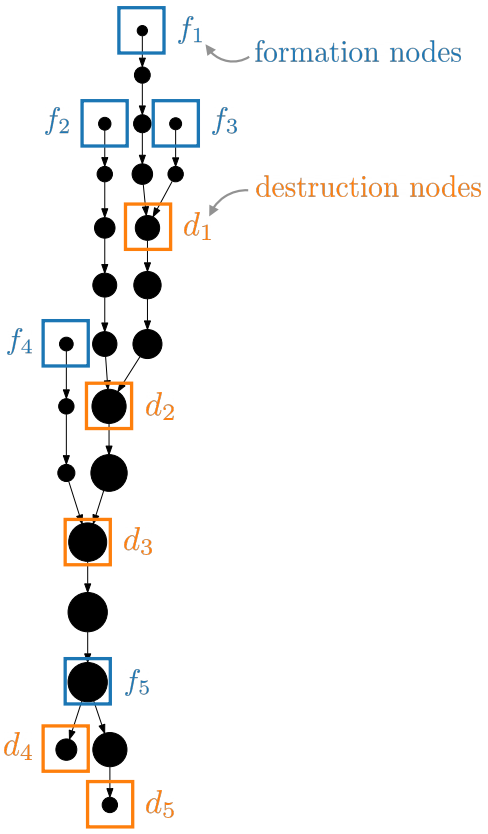

Figure A1. Schematic illustrating the positions of the cloud-formation nodes f_i; $i = 1...5$ and cloud-destruction nodes d_j; $j = 1...5$ in a single component of the FLAT cloud evolution network. Formation nodes generate a net increase in cloud number, while destruction nodes correspond to a net decrease.

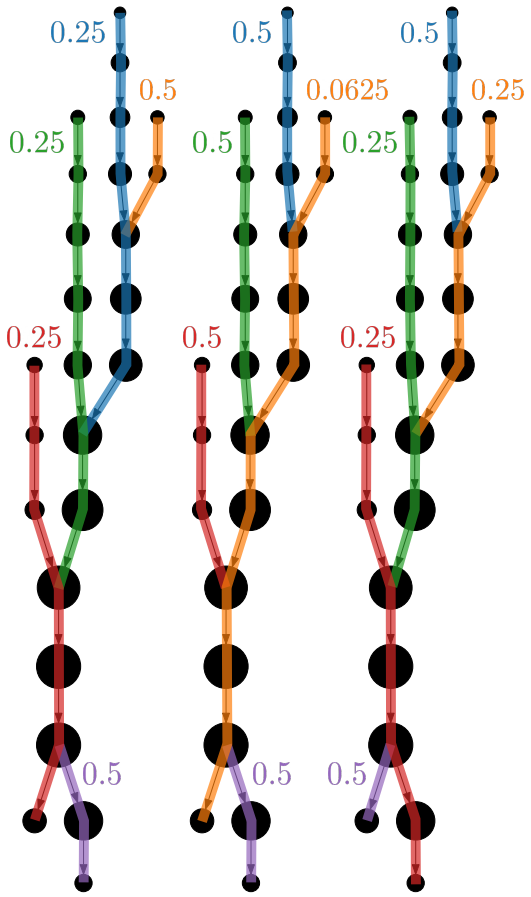

Figure A2. Schematic illustrating $3/16$ unique Monte Carlo realisations of trajectories through one connected component of the FLAT cloud history graph, obtained via the application of Algorithm 1. The probability of obtaining each trajectory, relative to the case of a perfectly-straight path (no mergers or splits) is given by the number at each formation node. The illustration emphasises that a trajectory becomes exponentially less-likely as it passes through more mergers and splits. There are fewer Monte Carlo realisations containing such paths, although all of the Monte Carlo realisations (including the three depicted here) are equally-likely.

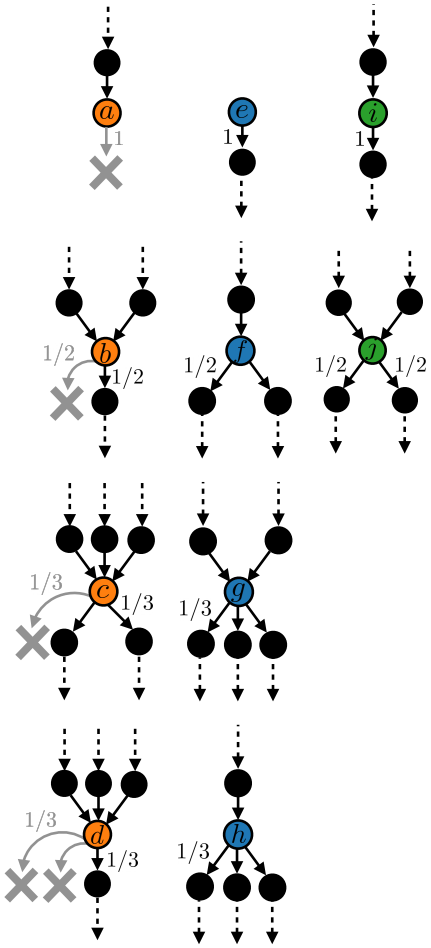

Figure A3. Schematic illustrating the MC outcomes at different types of node in the cloud evolution network. Destruction nodes are coloured orange (nodes a-d), formation nodes are coloured blue (e-h), and nodes that generate no net change in cloud number are coloured green (nodes i-j). The probabilities of the different MC outcomes in each case are given by the arrow labels. In the case of destruction nodes, a fraction $(\theta_{\rm merge}-\theta_{\rm split})/\theta_{\rm merge}$ of the total MC outcomes result in termination of the cloud evolutionary path, illustrated by grey crosses.

Chapter 6

Conclusions

In this thesis, we have investigated the physics of giant molecular clouds with the aim to understand the connection of their properties and lifecycles to the galactic environment on large scales, and on smaller scales to the star formation occurring within them. In so doing, we have provided some stepping stones along one possible path connecting observations of galactic-scale star formation to the sub-galactic processes that drive it. Specifically, we have found that giant molecular clouds in Milky Way-like environments are decoupled from galactic dynamics, and instead have internal star-forming properties that evolve in accordance with their own self-gravity. Their lifetimes and star formation efficiencies are driven by the process of collapse and subsequent dispersal by stellar feedback, leading to an evolutionary sequence that is hierarchically-structured in both space and time.

In the first section of this chapter, we present a brief overview the main results from each of the preceding chapters. In the second section, we bring these results back into the wider context of the existing literature, to determine what we have learned from this work. Finally, we present the possible future directions to be taken, to extend our findings and to contribute to the development of a global, coherent view of galactic star formation.

6.1 Summary

In this section, we provide a summary of each of the chapters following the introduction of Chapter 1, highlighting the salient points and conclusions without the burden of methodological detail.

Chapter 2

In Chapter 2 we put forward a hypothesis to be tested: that giant molecular cloud properties and lifetimes are set exclusively by large-scale galactic-dynamical processes. This hypothesis creates a framework on which to hang the remainder of the work presented in this thesis, as it leads to two testable conclusions:

1. Dynamically-dependent molecular cloud properties vary systematically across a parameter space spanned by the degree of galactic shear β, the degree of gravitational stability Q, the orbital angular velocity Ω of the host galaxy, and the stellar contribution $\phi_{\rm P}$ to the mid-plane pressure (Elmegreen, 1989).

2. The characteristic average molecular cloud lifetime in a particular galactic-dynamic environment is the sum of the Poisson rates of the different dynamical processes, if these are assumed to be independent of one another, and to destroy just one cloud at a time. This also varies throughout the same parameter space $(\beta, Q, \Omega, \phi_{\rm P})$.

The above theoretical framework avoids making assumptions about the exact nature of a giant molecular clouds: a common problem in theories of cloud evolution, as related in Chapter 1. Instead, it relies on the assumption that on average, molecular clouds survive for time-scales comparable to those of the galactic-dynamical processes considered, so that they may be affected by these processes. This assumption is corroborated by observations (Blitz et al., 2007; Corbelli et al., 2017; Engargiola et al., 2003; Kawamura et al., 2009; Kruijssen et al., 2019; Meidt et al., 2015; Miura et al., 2012; Murray, 2011). We also find that we must assume that clouds are large-enough and of a low-enough density that they are not simply dominated by their own local self-gravity, as we find this time-scale to be universally-shorter than all other galactic-dynamical time-scales considered. This is a point to which we return in Chapters 3 and 4.

One of the nice things about this theory is that it depends on just three observable properties of the host galaxy: the galactic rotation curve, and the velocity dispersions and surface densities of the gas and stellar components. As a first test of the approach, we calculate the expected galactic-dynamical cloud lifetime in four different galaxies for which these observables are available: M31, M51, M83 and the Milky Way. We find a median cloud lifetime of $\sim$ 64 Myr in M31, of $\sim$ 21 Myr in M51, between 15 and 100 Myr in M83 and between 30 and 40 Myr in the Milky Way. These numbers are promising given that they are in the right ballpark for observed giant molecular cloud lifetimes: in particular the profile of cloud lifetimes with galactocentric radius in M51 is consistent with observations (Meidt et al., 2015).

The work presented in this Chapter provides a testing bed to be addressed by the simulations presented in Chapters 3 and 4. It is extremely simple in its ignorance of any physical processes other than dynamical ones, and in its ignorance of the non-linear interactions between such processes. We leave the full complexity of a realistic interstellar medium to be addressed via the numerical simulations, with which we can test conclusions (1) and (2) in Milky Way-like environments.

Chapter 3

Chapter 3 is a simple application of the theoretical framework presented in Chapter 2 to the particular case of the Milky Way's Galactic centre, otherwise known as the Central Molecular Zone. This region of the Galaxy is of particular interest to studies of molecular gas physics, due to its elevated pressure, temperature, molecular gas abundance and density, relative to most other observable environments. In fact, it has been considered that the Central Molecular Zone could be a useful nearby litmus test for the physics of molecular gas in high-redshift galaxies, which display similarly-high pressures.

To apply the analytic theory, we use the observed rotation curve of Launhardt et al. (2002), and obtain the degree of gravitational stability from the numerical simulation of the Galactic centre by Krumholz et al. (2017). In doing so, we divide the Central Molecular Zone into two galactic-dynamical regimes:

1. A shear-dominated regime, extending over the majority of the Galactic centre's volume, from $\sim$ 0-45 pc and from 120-500 pc. In this regime, the time-scale for

galactic shear is much shorter than the time-scale for gravitational free-fall at the Toomre scale/disc scale-height. In this region we predict that the internal rotation and azimuthal stretching induced by galactic differential rotation can provide support against gravitational collapse, in line with the low observed star formation efficiencies at these radii.

2. A gravity-dominated regime known as the '100 pc-stream', accounting for the majority of the Galactic Centre's molecular gas density, from $\sim$ 45-120 pc. Here the gravitational free-fall time-scale is much shorter than any other dynamical time-scale, leading to cloud collapse and star formation.

At the interface between these two regimes, as gas flows inwards towards radii of $\sim$ 100 pc, we find that all of the galactic-dynamical time-scales attain comparable values. In particular, the time-scale for orbital epicyclic perturbations is only a factor of a few longer than the shear time-scale in the shear-dominated regime, and it overtakes shear in dominance at the same time as the gravitational free-fall time-scale drops. We can make an estimate of the number of clouds that will suffer tidal compressions on this interface, as is proposed in the observational and numerical literature (Henshaw et al., 2016; Kruijssen et al., 2015; Longmore et al., 2013a), and find this number to be around 20 per cent. The other 80 per cent of clouds should, on average, undergo gravitational collapse and destruction by stellar feedback before such a pericentre passage can occur.

The work presented in this paper is an example of a simple analytic calculation of the probabilities associated with different modes of dynamical giant molecular cloud evolution, via the linear theory presented in Chapter 2. It is this stochastic argument that will be tested, using the full complexity of numerical simulations, in Chapters 4 and 5.

Chapter 4

The measured internal properties of giant molecular clouds are observed to vary significantly as a function of their large-scale galactic environment (Bigiel et al., 2016; Chevance et al., 2020; Colombo et al., 2019; Heyer et al., 2009; Leroy et al., 2017, 2013b; Roman-Duval et al., 2010; Sun et al., 2020, 2018; Usero et al., 2015; Utomo et al., 2018). In this third chapter of the thesis, we present numerical simulations of both giant molecular clouds and their parent HI clouds across a range of galactic-dynamical environments that span the parameter space presented in Chapters 2 and 3. We examine the time-independent properties of the molecular cloud sample, and leave the analysis of the time-dependent cloud lifecycle to be explored in Chapter 5. At this stage, we study clouds in Milky Way-like galaxies exclusively, and leave as future work the extension of our framework to other galaxy types and redshifts.

The over-arching result of this chapter is that the giant molecular clouds across Milky Way-like environments are highly over-dense, over-pressured and as such decoupled from galactic dynamics in their turbulent and star-forming properties. This relates back to the finding in Chapter 1: given a sufficient local density, the local gravitational free-fall time-scale is much shorter than the time-scales of all large-scale galactic-dynamical processes, and clouds are destroyed via collapse before they can become dynamically-coupled. However, we do find that the rotational properties of the same giant molecular clouds vary systematically with the influence of galactic rotation and shear, relative to the influence of gravity on the Toomre scale. That is, as the time-scale for galactic shear

decreases relative to the hydrostatic pressure of the galactic disc, clouds are on average spun up in the prograde rotational direction by the influence of the Coriolis force. They are also slightly elongated along the azimuthal direction by galactic differential rotation, and their velocity dispersions become ever more tangentially-biased. Nevertheless, these effects are not of sufficient magnitude to provide support against the collapse of the clouds, which we find to have universally inward-pointing streaming motions.

By contrast, the HI clouds examined in this Chapter display significant large-scale dynamical correlations, both in their rotational and in their turbulent properties. This is due to their much lower densities and turbulent pressures, which are comparable to the hydrostatic pressure of the galactic mid-plane. We hypothesise that the dynamical imprints in the rotational properties of the molecular clouds in our sample are in fact inherited from their progenitor HI clouds by virtue of the conservation of angular momentum. These galactic-dynamical trends in the HI cloud population also highlight a productive avenue for future investigation: in galaxies with higher mid-plane hydrostatic pressures, the molecular gas will have a larger filling-factor, alower over-pressure and a lower over-density, predisposing it to a greater degree of galactic-dynamical interaction. We propose that in order to see galactic-dynamical coupling of the turbulent and star-forming properties of giant molecular clouds, we should look to higher-mass galaxies than the Milky Way, and to higher-pressure regions within smaller galaxies, such as galactic bars and spiral arms.

Chapter 5

A key advantage of performing numerical simulations is that they allow for the analysis of the time-dependent evolution of complex astrophysical systems, which are not directly accessible from observations performed over a human life-span. In Chapter 5 we extend the analysis of static cloud properties presented in Chapter 4, by characterising the full life-cycles of the giant molecular clouds identified in our simulated Milky Way-like galaxies. For each identified population of clouds, we obtain the evolutionary history in the form of a 'cloud evolution network' involving every molecular cloud identified at time-steps of 1 Myr. Analysis of the structure of each cloud evolution network reveals that it is highly-substructured in both space and time. Across two orders of magnitude in spatial scale, we find scaling relations for the molecular cloud lifetime, the collapse time-scale before which self-gravity is balanced by stellar feedback, and the rate of cloud mergers.

The characteristic molecular cloud lifetime in our simulations varies from values of 10 Myr, at cloud scales equal to and larger than the gas disc scale-height, up to 20 Myr at cloud scales of around 10 pc. It obeys a scaling relation of the form

$$\tau_{\rm life}/{\rm Myr} = \begin{cases} 48(\ell/{\rm pc})^{-0.3} & \text{if } \ell < 100 \text{ pc} \\ 13 & \text{if } \ell > 100 \text{ pc}, \end{cases}$$

where ℓ is the median cloud scale and $\tau_{\rm life}$ is the characteristic cloud lifetime. We show that the sloped part of the scaling relation results directly from self-gravitation: clouds collapse to a state of maximum pressure, density and star formation rate, before the pressure exerted by stellar feedback overcomes their self-gravity, and they are dispersed. The process of collapse occurs on a time-scale that is proportional to $\ell^{-0.6}$, by virtue of the fact that smaller, denser clouds require a higher level of stellar feedback in order to be dispersed. The process of dispersal occurs on a time-scale of 3 Myr that is approximately

independent of the spatial scale. We interpret this as a coincidental cancelling of two effects: (1) the higher density of smaller star-forming regions, which tends to lengthen the time-scale, and (2) the higher level of star formation reached in these regions, which tends to shorten the time-scale. Finally, the flat part of the scaling relation ($\tau_{\rm life} \sim 13$ Myr) is consistent with the crossing time of the gas disc scale-height, indicating that clouds at scales larger than $\ell \sim 100$ pc are not self-gravitating in our simulations. This result can also be seen in the scaling relation of the cloud virial parameter.

The rate of cloud mergers in our simulations is relatively frequent, with a maximum value of 0.1 $\rm Myr^{-1}$ at the smallest spatial scales. The merger rate scales with the crossing time between cloud centroids, and we find its scaling relation to be well-described by supersonic turbulence within a fractally-structured interstellar medium. We determine the fractal index using clouds identified at the native resolution of our simulations, yielding a value of $D \sim 1.54$. Despite the frequency of cloud mergers, we find that at the numerical mass resolution of our simulations (900 $\rm M_{\odot}$), they have no effect on the turbulent or star-forming properties of the interacting clouds, relative to the case of clouds evolving in isolation. In our simulations, we therefore conclude that cloud interactions do not appreciably enhance the galactic star formation rate.

Finally, we examine the dependence of time-dependent molecular cloud properties on the galactic-dynamical environment, and find in accordance with the results of Chapter 4 that the molecular cloud lifetime is decoupled from dynamical influences. The cloud merger rate, on the other hand, is well-correlated with the absolute velocity differential between giant molecular clouds in the inertial frame, possibly indicating that galactic differential rotation plays a role in stirring turbulence on galactic scales.

6.2 Context and future work

The aim of this thesis has been to study giant molecular clouds as the communication channels between galactic scales and the sub-cloud physics of star formation. In Chapters 2-5, we have built up a narrative that begins with a simple analytic theory to quantify the large-scale influence of galactic dynamics on molecular clouds (Chapters 2 and 3). In Chapter 4 we have constructed a systematic, numerical experiment to test the concrete predictions of this theoretical framework, and have used it to interpret the environmental variation of a large population of simulated clouds. Finally, in Chapter 5 we have connected back to galactic scales, showing that the molecular cloud lifetime is scale-dependent for self-gravitating gas, and bound from below by the crossing time of the thin-disc scale-height. In the following sub-sections, we highlight the two general conclusions that we have reached in this work, drawing together the results summarised in Section 6.1. By relating these to current work in the field of star formation, we suggest possible avenues of research to pursue in the future.

6.2.1 Coupling to galactic dynamics is pressure- and density-dependent

In its aim to pin down the physical relationship between giant molecular clouds and their large-scale galactic environments, a central topic addressed in this thesis has been the role of galactic dynamics in shaping the molecular cloud lifecycle. In the simple analytic theory put forward in Chapter 2, we derived five time-scales associated with

key dynamical processes in the interstellar medium: galactic shearing (τ_β), gravitational free-fall ($\tau_{\rm ff,g}$), radial orbital excursions due to epicyclic perturbations (τ_κ), spiral-arm and galactic-bar interactions ($\tau_{\Omega_{\rm P}}$), and interactions between clouds, otherwise known as 'cloud-cloud collisions' ($\tau_{\rm cc}$). Each of these time-scales is around an orbital time in length, so if molecular clouds survive for a few orbital times (on the order of 5-50 Myr on average, as observed), then galactic dynamics has time to play a role in their evolution. However, it is immediately clear from the analytic theory (see Figure 3 of Chapter 2) that if molecular clouds are locally self-gravitating, with free-fall time-scales $\tau_{\rm ff,cl}$ that are much shorter than the mid-plane free-fall time-scale $\tau_{\rm ff,g}$, then they will be *dynamically-decoupled*. In order for this to occur, the densities (and therefore turbulent pressures) of these clouds must significantly exceed the density and hydrostatic pressure of the galactic mid-plane.

In Chapter 4, we presented a set of Milky Way-like numerical simulations to span the galactic-dynamical parameter space over which the time-scales (τ_β, $\tau_{\rm ff,g}$, τ_κ, $\tau_{\Omega_{\rm P}}$, $\tau_{\rm cc}$) vary. The physical properties for the statistical set of $\sim 80,000$ giant molecular clouds retrieved from these simulations show that they are highly over-dense and over-pressured relative to the galactic mid-plane, by one hundred times and twenty-five times, respectively. According to the theory of Chapter 2 they should therefore be dynamically-decoupled, and indeed we find upon analysis of their properties (Figures 18 and 21-25 of Chapter 4) that their turbulent and star-forming properties are independent of all galactic-dynamical time-scales. The only properties that display dynamical correlations are those that are associated with molecular cloud rotation within the galactic mid-plane (namely cloud elongation, angular momentum and velocity dispersion anisotropy): dynamical imprints which may be inherited from the lower-density parent HI clouds, via the conservation of angular momentum. The conclusion that the giant molecular clouds in Milky Way-like galaxies are dynamically-decoupled is hammered home in Chapter 5, in which we examine the time-evolution of the same set of numerically-simulated clouds and demonstrate that below the gas-disc scale-height at ~ 100 pc, all are gravitationally bound and collapsing. They are inert to the constant mergers and interactions that result from the hierarchical, fractal structure of the interstellar medium (Figure 9 of Chapter 5), proceeding to star formation on approximately a local free-fall time-scale. They are dispersed by the resulting stellar feedback on a time-scale of around ~ 3 Myr. The molecular gas survival time below the scale-height increases as the cloud scale decreases, due to the higher level of star formation required to unbind the gas from its self-gravitating state.

Although the numerical simulations presented in this thesis are limited to Milky Way-pressured galaxies and so to dynamically-decoupled molecular clouds, a clue to the behaviour and galactic-dynamical coupling of clouds in higher-mass galaxies is provided by the analysis of HI clouds in Chapter 4. These have an over-density of just seven times and an over-pressure of just three times relative to the galactic mid-plane, and correspondingly display clear dynamical trends in their turbulent properties (velocity dispersions, turbulent pressures and virial parameters). That is, they are *dynamically-coupled*. The observational work of Sun et al. (2020), showing a dependence of the average molecular gas turbulent pressure on the hydrostatic pressure of the galactic mid-plane, therefore points the way towards environments for future study, in which our simulated molecular clouds would display lower levels of over-pressuring, by virtue of their larger filling factors within the galactic disc. Indeed, the result that dynamical-coupling depends on the mid-plane properties of the host galactic environment is one that has recently

been demonstrated explicitly in observations by Chevance et al. (2020) across a sample of nine nearby disc galaxies. These authors find a threshold for dynamical coupling in the molecular gas surface density Σ_{H_2} which scales with the galaxy mass and mid-plane hydrostatic pressure. Dynamical coupling sets in at $\Sigma_{H_2} \geq 8$ $M_\odot$ pc^{-2} and influences the lifetimes of molecular clouds at spatial scales of ~ 100 pc. Ultimately, a thorough study of the influence of galactic dynamics on molecular clouds will require observations and numerical simulations that span several orders of magnitude in galaxy mass, spatial scale, mid-plane pressure and structure. Specifically, galaxies with molecular gas surface densities of $\Sigma_{H_2} \geq 8$ $M_\odot$ pc^{-2}, or mid-plane hydrostatic pressures of $P > 10^{4.5}$ k_B K cm^{-3}, are the obvious next galactic targets for the kind of analysis presented in Chapters 4 and 5. In addition to high-mass nearby galaxies, such environments can be found at high-redshifts (Madau and Dickinson, 2014), or in the higher-density environments of spiral arms or galactic bars.

6.2.2 Molecular cloud time-scales are scale-dependent below the gas disc scale-height

In Chapter 5, we have derived detailed cloud evolution networks from our numerically-simulated galaxies, exploring the cycle of molecular cloud evolution in Milky Way-like galaxies as a function of time, and crucially, of spatial scale. The spatial dependence of the star formation time-scale is certainly not a new concept, and has been observed for decades across a variety of different galactic environments (de la Fuente Marcos and de la Fuente Marcos, 2009; Efremov and Elmegreen, 1998; Elmegreen, 2000; Elmegreen and Efremov, 1996). It leads to the increased decoherence, on small spatial scales, of overdensities in molecular gas and star formation tracers (Bigiel et al., 2008; Leroy et al., 2013b; Schruba et al., 2011) that can be used to constrain molecular cloud lifetimes in observations (Kruijssen and Longmore, 2014; Kruijssen et al., 2019, 2018). However, the scaling relations we have presented for the cloud lifetime and cloud merger rate have also highlighted the usefulness of examining explicitly the variations in *simulated* molecular cloud lifetimes and properties with spatial scale, especially given that numerical simulations can probe spatial scales over a wide range of galactic environments that observations can only reach in single, nearby targets. By virtue of producing a scaling relation for the characteristic molecular cloud lifetime, we have been pointed towards the physical origin of this time-scale for clouds smaller than the disc scale-height (the competition between self-gravity and stellar feedback) relative to clouds larger than the disc scale-height (which are destroyed on the turbulent crossing time of the disc). The scaling relation can also be used to characterise the star formation efficiencies of the self-gravitating clumps, by proxy of their longer collapse time-scales. In the case of the cloud merger rate, the form of the scaling relation has revealed that cloud interactions can be explained by supersonic turbulence within a fractally-structured interstellar medium, and we have also interpreted the role of galactic differential rotation in this context.

In this vein, the last few years have seen a number of theoretical studies characterising galactic star formation as a function of spatial scale and temporal evolutionary cycling (Caplar and Tacchella, 2019; Krumholz et al., 2012; Semenov et al., 2017, 2018, 2019; Tacchella et al., 2020), matched by the shunning of cloud-identification thresholds in favour of fixed-resolution measurements in observations of molecular gas properties (Leroy et al., 2013b; Sun et al., 2020, 2018). The spatial variation of the correlation between molecular gas and stellar over-densities over a wide range of spatial scales has now also

been used by Chevance et al. (2020); Kruijssen et al. (2019) to derive cloud lifetimes at the disc scale-height from observed maps of CO and H-α emission. Measurements such as these can be used to calibrate simulated scaling relations of molecular gas properties and time-scales, and in turn, the simulations can be used to extend these data to higher resolutions, to investigate the physics at smaller scales.

Connecting spatial scales in this way is one of the general aims toward which the work in this thesis has been directed, as outlined in Chapter 1. That is, we started out with the idea that the time-scales associated with localised regions of star formation on sub-galactic scales may provide clues to the physics that drive star formation on galactic scales. The opportunity to extend the spatial range of observations to the smallest scales that can numerically be resolved is an exciting and potentially-fruitful avenue for future research.

Acknowledgements

My time in Heidelberg has been an incredibly happy period in my life, and I owe this experience to the people I have shared it with.

Firstly, I thank my advisor (not supervisor) Diederik for allowing me the time, space and intellectual freedom to develop my own research, while always being around to point me in the right direction when I needed it. I am very grateful to have been a part of a wonderful group, to have had so many lively coffee breaks and lunchtimes and after-work drinks full of great discussions, loud arguments and louder laughter. Every single member has truly been a friend to me, and has made Heidelberg feel like home. In order of appearance: Dan and Alex, Marta, Mélanie and Jake, Jindra, Ben and Sebastian, Maya, Jaeyeon, Verena and Andrew.

The work I have presented would not have been possible without the great ideas and mentorship I have received from my collaborators. I am particularly grateful to Mark Krumholz, Steven Longmore and Ben Keller and for their academic support throughout my PhD.

I thank Mum, Dad and Rachel for their constant love, support, patience and encouragement in everything I do.

I acknowledge the generous funding I have received from the German Research Foundation in the form of an Emmy Noether Research grant KR4801/1-1, via my supervisor Diederik, and similarly from the European Research Council under the European Union's Horizon 2020 research and innovation programme, grant 714907.

Bibliography

Adams, W. S. (1949). Observations of Interstellar H and k, Molecular Lines, and Radial Velocities in the Spectra of 300 O and B Stars. , 109:354.

Ao, Y., Henkel, C., Menten, K. M., Requena-Torres, M. A., Stanke, T., Mauersberger, R., Aalto, S., Mühle, S., and Mangum, J. (2013). The thermal state of molecular clouds in the Galactic center: evidence for non-photon-driven heating. , 550:A135.

Ballesteros-Paredes, J., Hartmann, L., and Vázquez-Semadeni, E. (1999a). Turbulent Flow-driven Molecular Cloud Formation: A Solution to the Post-T Tauri Problem? , 527(1):285–297.

Ballesteros-Paredes, J., Vázquez-Semadeni, E., and Scalo, J. (1999b). Clouds as Turbulent Density Fluctuations: Implications for Pressure Confinement and Spectral Line Data Interpretation. , 515(1):286–303.

Bally, J., Langer, W. D., Wilson, R. W., Stark, A. A., and Pound, M. W. (1991). On the Structure and Kinematics of Molecular Clouds from Large Scale Mapping of Mm-Lines. In Falgarone, E., Boulanger, F., and Duvert, G., editors, *Fragmentation of Molecular Clouds and Star Formation*, volume 147 of *IAU Symposium*, page 11.

Bally, J., Stark, A. A., Wilson, R. W., and Henkel, C. (1987). Galactic Center Molecular Clouds. I. Spatial and Spatial Velocity Maps. , 65:13.

Barnes, A. T., Longmore, S. N., Battersby, C., Bally, J., Kruijssen, J. M. D., Henshaw, J. D., and Walker, D. L. (2017). Star formation rates and efficiencies in the Galactic Centre. , 469(2):2263–2285.

Beaumont, C. N., Goodman, A. A., Alves, J. F., Lombardi, M., Román-Zúñiga, C. G., Kauffmann, J., and Lada, C. J. (2012). A simple perspective on the mass-area relationship in molecular clouds. , 423(3):2579–2586.

Benincasa, S. M., Loebman, S. R., Wetzel, A., Hopkins, P. F., Murray, N., Bellardini, M. A., Faucher-Giguère, C.-A., Guszejnov, D., and Orr, M. (2019). Live Fast, Die Young: GMC lifetimes in the FIRE cosmological simulations of Milky Way-mass galaxies. *arXiv e-prints*, page arXiv:1911.05251.

Bertoldi, F. and McKee, C. F. (1992). Pressure-confined clumps in magnetized molecular clouds. , 395:140–157.

Bigiel, F., Leroy, A., Walter, F., Brinks, E., de Blok, W. J. G., Madore, B., and Thornley, M. D. (2008). The Star Formation Law in Nearby Galaxies on Sub-Kpc Scales. , 136:2846–2871.

Bigiel, F., Leroy, A. K., Jiménez-Donaire, M. J., Pety, J., Usero, A., Cormier, D., Bolatto, A., Garcia-Burillo, S., Colombo, D., and González-García, M. (2016). The EMPIRE Survey: Systematic Variations in the Dense Gas Fraction and Star Formation Efficiency from Full-disk Mapping of M51. , 822(2):L26.

Blaauw, A. (1952). The age and evolution of the ζ Persei group of O- and B-type stars. , 11:405.

Blitz, L., Fukui, Y., Kawamura, A., Leroy, A., Mizuno, N., and Rosolowsky, E. (2007). Giant Molecular Clouds in Local Group Galaxies. In Reipurth, B., Jewitt, D., and Keil, K., editors, *Protostars and Planets V*, page 81.

Blitz, L. and Thaddeus, P. (1980). Giant molecular complexes and OB associations. I. The Rosette molecular complex. , 241:676–696.

Bolatto, A. D., Leroy, A. K., Rosolowsky, E., Walter, F., and Blitz, L. (2008). The Resolved Properties of Extragalactic Giant Molecular Clouds. , 686(2):948–965.

Bolatto, A. D., Wolfire, M., and Leroy, A. K. (2013). The CO-to-H_2 Conversion Factor. , 51:207–268.

Burkhart, B. (2018). The Star Formation Rate in the Gravoturbulent Interstellar Medium. , 863(2):118.

Burton, W. B. and Gordon, M. A. (1978). Carbon monoxide in the Galaxy. III. The overall nature of its distribution in the equatorial plane. , 63(1-2):7–27.

Caplar, N. and Tacchella, S. (2019). Stochastic modelling of star-formation histories I: the scatter of the star-forming main sequence. , 487(3):3845–3869.

Carruthers, G. R. (1970). Rocket Observation of Interstellar Molecular Hydrogen. , 161:L81.

Caselli, P. and Myers, P. C. (1995). The Line Width–Size Relation in Massive Cloud Cores. , 446:665.

Chevance, M., Kruijssen, J. M. D., Hygate, A. P. S., Schruba, A., Longmore, S. N., Groves, B., Henshaw, J. D., Herrera, C. N., Hughes, A., Jeffreson, S. M. R., Lang, P., Leroy, A. K., Meidt, S. E., Pety, J., Razza, A., Rosolowsky, E., Schinnerer, E., Bigiel, F., Blanc, G. A., Emsellem, E., Faesi, C. M., Glover, S. C. O., Haydon, D. T., Ho, I. T., Kreckel, K., Lee, J. C., Liu, D., Querejeta, M., Saito, T., Sun, J., Usero, A., and Utomo, D. (2020). The lifecycle of molecular clouds in nearby star-forming disc galaxies. , 493(2):2872–2909.

Cho, J., Vishniac, E. T., Beresnyak, A., Lazarian, A., and Ryu, D. (2009). Growth of Magnetic Fields Induced by Turbulent Motions. , 693(2):1449–1461.

Clark, B. G. (1965). An Interferometer Investigation of the 21-CENTIMETER Hydrogen-Line Absorption. , 142:1398.

Colombo, D., Hughes, A., Schinnerer, E., Meidt, S. E., Leroy, A. K., Pety, J., Dobbs, C. L., García-Burillo, S., Dumas, G., Thompson, T. A., Schuster, K. F., and Kramer, C. (2014). The PdBI Arcsecond Whirlpool Survey (PAWS): Environmental Dependence of Giant Molecular Cloud Properties in M51. , 784(1):3.

Colombo, D., Rosolowsky, E., Duarte-Cabral, A., Ginsburg, A., Glenn, J., Zetterlund, E., Hernand ez, A. K., Dempsey, J., and Currie, M. J. (2019). The integrated properties of the molecular clouds from the JCMT CO(3-2) High-Resolution Survey. , 483(4):4291–4340.

Corbelli, E., Braine, J., Bandiera, R., Brouillet, N., Combes, F., Druard, C., Gratier, P., Mata, J., Schuster, K., Xilouris, M., and Palla, F. (2017). From molecules to young stellar clusters: the star formation cycle across the disk of M 33. , 601:A146.

Daddi, E., Elbaz, D., Walter, F., Bournaud, F., Salmi, F., Carilli, C., Dannerbauer, H., Dickinson, M., Monaco, P., and Riechers, D. (2010). Different Star Formation Laws for Disks Versus Starbursts at Low and High Redshifts. , 714(1):L118–L122.

Dame, T. M., Ungerechts, H., Cohen, R. S., de Geus, E. J., Grenier, I. A., May, J., Murphy, D. C., Nyman, L. A., and Thaddeus, P. (1987). A Composite CO Survey of the Entire Milky Way. , 322:706.

de la Fuente Marcos, R. and de la Fuente Marcos, C. (2009). Hierarchical Star Formation in the Milky Way Disk. , 700(1):436–446.

Dobbs, C. L. (2008). GMC formation by agglomeration and self gravity. , 391(2):844–858.

Dobbs, C. L. and Bonnell, I. A. (2007). Spiral shocks and the formation of molecular clouds in a two-phase medium. , 376(4):1747–1756.

Dobbs, C. L., Bonnell, I. A., and Pringle, J. E. (2006). The formation of molecular clouds in spiral galaxies. , 371(4):1663–1674.

Dobbs, C. L., Burkert, A., and Pringle, J. E. (2011). Why are most molecular clouds not gravitationally bound? , 413(4):2935–2942.

Dobbs, C. L., Glover, S. C. O., Clark, P. C., and Klessen, R. S. (2008). The ISM in spiral galaxies: can cooling in spiral shocks produce molecular clouds? , 389(3):1097–1110.

Dobbs, C. L., Krumholz, M. R., Ballesteros-Paredes, J., Bolatto, A. D., Fukui, Y., Heyer, M., Low, M. M. M., Ostriker, E. C., and Vázquez-Semadeni, E. (2014). Formation of Molecular Clouds and Global Conditions for Star Formation. In Beuther, H., Klessen, R. S., Dullemond, C. P., and Henning, T., editors, *Protostars and Planets VI*, page 3.

Dobbs, C. L., Pettitt, A. R., Corbelli, E., and Pringle, J. E. (2018). Simulations of the flocculent spiral M33: what drives the spiral structure? , 478(3):3793–3808.

Dobbs, C. L., Pringle, J. E., and Duarte-Cabral, A. (2015). The frequency and nature of 'cloud-cloud collisions' in galaxies. , 446(4):3608–3620.

Dobbs, C. L., Rosolowsky, E., Pettitt, A. R., Braine, J., Corbelli, E., and Sun, J. (2019). Comparing the properties of GMCs in M33 from simulations and observations. , 485(4):4997–5009.

Efremov, Y. N. and Elmegreen, B. G. (1998). Hierarchical star formation from the time-space distribution of star clusters in the Large Magellanic Cloud. , 299(2):588–594.

Elmegreen, B. G. (1989). A pressure and metallicity dependence for molecular cloud correlations and the calibration of mass. , 338:178–196.

Elmegreen, B. G. (1990). A Wavelike Origin for Clumpy Structure and Broad Line Wings in Molecular Clouds. , 361:L77.

Elmegreen, B. G. (1991). Cloud Formation by Combined Instabilities in Galactic Gas Layers: Evidence for a Q Threshold in the Fragmentation of Shearing Wavelets. , 378:139.

Elmegreen, B. G. (1993). Star Formation at Compressed Interfaces in Turbulent Self-gravitating Clouds. , 419:L29.

Elmegreen, B. G. (2000). Star Formation in a Crossing Time. , 530(1):277–281.

Elmegreen, B. G. (2002). Star Formation from Galaxies to Globules. , 577(1):206–220.

Elmegreen, B. G. (2003). Gas phase processes affecting galactic evolution. , 284(2):819–832.

Elmegreen, B. G. (2007). On the Rapid Collapse and Evolution of Molecular Clouds. , 668(2):1064–1082.

Elmegreen, B. G. and Efremov, Y. N. (1996). An Extension of Hierarchical Star Formation to Galactic Scales. , 466:802.

Elmegreen, B. G. and Falgarone, E. (1996). A Fractal Origin for the Mass Spectrum of Interstellar Clouds. , 471:816.

Elmegreen, D. M., Elmegreen, B. G., Kaufman, M., Brinks, E., Struck, C., Bournaud, F., Sheth, K., and Juneau, S. (2017). ALMA CO Clouds and Young Star Complexes in the Interacting Galaxies IC 2163 and NGC 2207. , 841(1):43.

Engargiola, G., Plambeck, R. L., Rosolowsky, E., and Blitz, L. (2003). Giant Molecular Clouds in M33. I. BIMA All-Disk Survey. , 149:343–363.

Faesi, C. M., Lada, C. J., and Forbrich, J. (2018). The ALMA View of GMCs in NGC 300: Physical Properties and Scaling Relations at 10 pc Resolution. , 857(1):19.

Falgarone, E., Pety, J., and Hily-Blant, P. (2009). Intermittency of interstellar turbulence: extreme velocity-shears and CO emission on milliparsec scale. , 507(1):355–368.

Falgarone, E., Phillips, T. G., and Walker, C. K. (1991). The Edges of Molecular Clouds: Fractal Boundaries and Density Structure. , 378:186.

Falgarone, E., Puget, J. L., and Perault, M. (1992). The small-scale density and velocity structure of quiescent molecular clouds. , 257:715–730.

Federrath, C. and Klessen, R. S. (2012). The Star Formation Rate of Turbulent Magnetized Clouds: Comparing Theory, Simulations, and Observations. , 761(2):156.

Federrath, C. and Klessen, R. S. (2013). On the Star Formation Efficiency of Turbulent Magnetized Clouds. , 763(1):51.

Ferrière, K., Gillard, W., and Jean, P. (2007). Spatial distribution of interstellar gas in the innermost 3 kpc of our galaxy. , 467(2):611–627.

Field, G. B., Goldsmith, D. W., and Habing, H. J. (1969). Cosmic-Ray Heating of the Interstellar Gas. , 155:L149.

Freeman, P., Rosolowsky, E., Kruijssen, J. M. D., Bastian, N., and Adamo, A. (2017). The Varying Mass Distribution of Molecular Clouds Across M83. *ArXiv e-prints*.

Fujimoto, Y., Chevance, M., Haydon, D. T., Krumholz, M. R., and Kruijssen, J. M. D. (2019). A fundamental test for stellar feedback recipes in galaxy simulations. , 487(2):1717–1728.

Fujimoto, Y., Krumholz, M. R., and Tachibana, S. (2018). Short-lived radioisotopes in meteorites from Galactic-scale correlated star formation. , 480(3):4025–4039.

Genzel, R., Tacconi, L. J., Gracia-Carpio, J., Sternberg, A., Cooper, M. C., Shapiro, K., Bolatto, A., Bouché, N., Bournaud, F., Burkert, A., Combes, F., Comerford, J., Cox, P., Davis, M., Schreiber, N. M. F., Garcia-Burillo, S., Lutz, D., Naab, T., Neri, R., Omont, A., Shapley, A., and Weiner, B. (2010). A study of the gas-star formation relation over cosmic time. , 407(4):2091–2108.

Glover, S. C. O. and Mac Low, M.-M. (2007). Simulating the Formation of Molecular Clouds. I. Slow Formation by Gravitational Collapse from Static Initial Conditions. , 169:239–268.

Gnedin, N. Y., Tassis, K., and Kravtsov, A. V. (2009). Modeling Molecular Hydrogen and Star Formation in Cosmological Simulations. , 697(1):55–67.

Goldreich, P. and Kwan, J. (1974). Molecular Clouds. , 189:441–454.

Gordon, M. A. and Burton, W. B. (1976). Carbon monoxide in the Galaxy. I. The radial distribution of CO, H_2, and nucleons. , 208:346–353.

Gould, R. J. and Salpeter, E. E. (1963). The Interstellar Abundance of the Hydrogen Molecule. I. Basic Processes. , 138:393.

Hartmann, L., Ballesteros-Paredes, J., and Bergin, E. A. (2001). Rapid Formation of Molecular Clouds and Stars in the Solar Neighborhood. , 562(2):852–868.

Heiderman, A., Evans, Neal J., I., Allen, L. E., Huard, T., and Heyer, M. (2010). The Star Formation Rate and Gas Surface Density Relation in the Milky Way: Implications for Extragalactic Studies. , 723(2):1019–1037.

Heitsch, F., Ballesteros-Paredes, J., and Hartmann, L. (2009). Gravitational Collapse and Filament Formation: Comparison with the Pipe Nebula. , 704(2):1735–1742.

Heitsch, F., Burkert, A., Hartmann, L. W., Slyz, A. D., and Devriendt, J. E. G. (2005). Formation of Structure in Molecular Clouds: A Case Study. , 633(2):L113–L116.

Heitsch, F., Slyz, A. D., Devriendt, J. E. G., Hartmann, L. W., and Burkert, A. (2006). The Birth of Molecular Clouds: Formation of Atomic Precursors in Colliding Flows. , 648(2):1052–1065.

Hennebelle, P. and Chabrier, G. (2011). Analytical Star Formation Rate from Gravoturbulent Fragmentation. , 743(2):L29.

Hennebelle, P. and Pérault, M. (2000). Dynamical condensation in a magnetized and thermally bistable flow. Application to interstellar cirrus. , 359:1124–1138.

Henshaw, J. D., Longmore, S. N., and Kruijssen, J. M. D. (2016). Seeding the Galactic Centre gas stream: gravitational instabilities set the initial conditions for the formation of protocluster clouds. , 463(1):L122–L126.

Heyer, M., Krawczyk, C., Duval, J., and Jackson, J. M. (2009). Re-Examining Larson's Scaling Relationships in Galactic Molecular Clouds. , 699(2):1092–1103.

Heyer, M. H., Carpenter, J. M., and Snell, R. L. (2001). The Equilibrium State of Molecular Regions in the Outer Galaxy. , 551(2):852–866.

Ho, L. C., Filippenko, A. V., and Sargent, W. L. W. (1997). The Influence of Bars on Nuclear Activity. , 487(2):591–602.

Hollenbach, D. and Salpeter, E. E. (1971). Surface Recombination of Hydrogen Molecules. , 163:155.

Hopkins, P. F. (2012). An excursion-set model for the structure of giant molecular clouds and the interstellar medium. , 423(3):2016–2036.

Jeans, J. H. (1928). *Astronomy and cosmogony*.

Kauffmann, J., Pillai, T., Shetty, R., Myers, P. C., and Goodman, A. A. (2010a). The Mass-Size Relation from Clouds to Cores. I. A New Probe of Structure in Molecular Clouds. , 712(2):1137–1146.

Kauffmann, J., Pillai, T., Shetty, R., Myers, P. C., and Goodman, A. A. (2010b). The Mass-size Relation from Clouds to Cores. II. Solar Neighborhood Clouds. , 716(1):433–445.

Kauffmann, J., Pillai, T., Zhang, Q., Menten, K. M., Goldsmith, P. F., Lu, X., and Guzmán, A. E. (2017). The Galactic Center Molecular Cloud Survey. I. A steep linewidth-size relation and suppression of star formation. , 603:A89.

Kawamura, A., Mizuno, Y., Minamidani, T., Filipović, M. D., Staveley-Smith, L., Kim, S., Mizuno, N., Onishi, T., Mizuno, A., and Fukui, Y. (2009). The Second Survey of the Molecular Clouds in the Large Magellanic Cloud by NANTEN. II. Star Formation. , 184(1):1–17.

Kennicutt, R. C. and Evans, N. J. (2012). Star Formation in the Milky Way and Nearby Galaxies. , 50:531–608.

Kennicutt, Jr., R. C. (1998). Star Formation in Galaxies Along the Hubble Sequence. , 36:189–232.

Kim, C.-G. and Ostriker, E. C. (2015a). Momentum Injection by Supernovae in the Interstellar Medium. , 802:99.

Kim, C.-G. and Ostriker, E. C. (2015b). Vertical Equilibrium, Energetics, and Star Formation Rates in Magnetized Galactic Disks Regulated by Momentum Feedback from Supernovae. , 815(1):67.

Klessen, R. S. (2000). One-Point Probability Distribution Functions of Supersonic Turbulent Flows in Self-gravitating Media. , 535(2):869–886.

Klessen, R. S. and Hennebelle, P. (2010). Accretion-driven turbulence as universal process: galaxies, molecular clouds, and protostellar disks. , 520:A17.

Koyama, H. and Inutsuka, S.-i. (2002). An Origin of Supersonic Motions in Interstellar Clouds. , 564(2):L97–L100.

Kramer, C., Stutzki, J., Rohrig, R., and Corneliussen, U. (1998). Clump mass spectra of molecular clouds. , 329:249–264.

Kritsuk, A. G., Norman, M. L., Padoan, P., and Wagner, R. (2007). The Statistics of Supersonic Isothermal Turbulence. , 665(1):416–431.

Kruijssen, J. M. D., Dale, J. E., and Longmore, S. N. (2015). The dynamical evolution of molecular clouds near the Galactic Centre - I. Orbital structure and evolutionary timeline. , 447(2):1059–1079.

Kruijssen, J. M. D. and Longmore, S. N. (2014). An uncertainty principle for star formation - I. Why galactic star formation relations break down below a certain spatial scale. , 439:3239–3252.

Kruijssen, J. M. D., Longmore, S. N., Elmegreen, B. G., Murray, N., Bally, J., Testi, L., and Kennicutt, R. C. (2014). What controls star formation in the central 500 pc of the Galaxy? , 440:3370.

Kruijssen, J. M. D., Schruba, A., Chevance, M., Longmore, S. N., Hygate, A. e. P. S., Haydon, D. T., McLeod, A. F., Dalcanton, J. J., Tacconi, L. J., and van Dishoeck, E. F. (2019). Fast and inefficient star formation due to short-lived molecular clouds and rapid feedback. , 569(7757):519–522.

Kruijssen, J. M. D., Schruba, A., Hygate, A. P. S., Hu, C.-Y., Haydon, D. T., and Longmore, S. N. (2018). An uncertainty principle for star formation - II. A new method for characterizing the cloud-scale physics of star formation and feedback across cosmic history. , 479:1866–1952.

Krumholz, M. R. (2014). The big problems in star formation: The star formation rate, stellar clustering, and the initial mass function. , 539:49–134.

Krumholz, M. R. (2015). Notes on Star Formation. *arXiv e-prints*, page arXiv:1511.03457.

Krumholz, M. R., Burkhart, B., Forbes, J. C., and Crocker, R. M. (2018). A unified model for galactic discs: star formation, turbulence driving, and mass transport. , 477(2):2716–2740.

Krumholz, M. R., Dekel, A., and McKee, C. F. (2012). A Universal, Local Star Formation Law in Galactic Clouds, nearby Galaxies, High-redshift Disks, and Starbursts. , 745(1):69.

Krumholz, M. R., Kruijssen, J. M. D., and Crocker, R. M. (2017). A dynamical model for gas flows, star formation and nuclear winds in galactic centres. , 466(1):1213–1233.

Krumholz, M. R. and McKee, C. F. (2005). A General Theory of Turbulence-regulated Star Formation, from Spirals to Ultraluminous Infrared Galaxies. , 630:250.

Krumholz, M. R., McKee, C. F., and Bland -Hawthorn, J. (2019). Star Clusters Across Cosmic Time. , 57:227–303.

Krumholz, M. R., McKee, C. F., and Tumlinson, J. (2008). The Atomic-to-Molecular Transition in Galaxies. I. An Analytic Approximation for Photodissociation Fronts in Finite Clouds. , 689(2):865–882.

Krumholz, M. R., McKee, C. F., and Tumlinson, J. (2009). The Atomic-to-Molecular Transition in Galaxies. II: H I and H_2 Column Densities. , 693(1):216–235.

Kutner, M. L., Tucker, K. D., Chin, G., and Thaddeus, P. (1977). The molecular complexes in Orion. , 215:521–528.

Lada, C. J. (1976). Detailed observations of the M17 molecular cloud complex. , 32:603–629.

Larson, R. B. (1981). Turbulence and star formation in molecular clouds. , 194:809–826.

Launhardt, R., Zylka, R., and Mezger, P. G. (2002). The nuclear bulge of the Galaxy. III. Large-scale physical characteristics of stars and interstellar matter. , 384:112–139.

Lazarian, A. (1995). Study of turbulence in HI using radiointerferometers. , 293:507–520.

Lee, Y., Snell, R. L., and Dickman, R. L. (1990). Analysis of 12CO and 13CO Emission in a 3 Square Degree Region of the Galactic Plane between L = 23 degrees and 25 degrees. , 355:536.

Leisawitz, D. (1990). A CO Survey of Regions around 34 Open Clusters. II. Physical Properties of Cataloged Molecular Clouds. , 359:319.

Leroy, A. K., Lee, C., Schruba, A., Bolatto, A., Hughes, A., Pety, J., Sandstrom, K., Schinnerer, E., and Walter, F. (2013a). Clumping and the Interpretation of kpc-scale Maps of the Interstellar Medium: Smooth H I and Clumpy, Variable H_2 Surface Density. , 769(1):L12.

Leroy, A. K., Schinnerer, E., Hughes, A., Kruijssen, J. M. D., Meidt, S., Schruba, A., Sun, J., Bigiel, F., Aniano, G., Blanc, G. A., Bolatto, A., Chevance, M., Colombo, D., Gallagher, M., Garcia-Burillo, S., Kramer, C., Querejeta, M., Pety, J., Thompson, T. A., and Usero, A. (2017). Cloud-scale ISM Structure and Star Formation in M51. , 846:71.

Leroy, A. K., Walter, F., Bigiel, F., Usero, A., Weiss, A., Brinks, E., de Blok, W. J. G., Kennicutt, R. C., Schuster, K.-F., Kramer, C., Wiesemeyer, H. W., and Roussel, H. (2009). Heracles: The HERA CO Line Extragalactic Survey. , 137(6):4670–4696.

Leroy, A. K., Walter, F., Brinks, E., Bigiel, F., de Blok, W. J. G., Madore, B., and Thornley, M. D. (2008). The Star Formation Efficiency in Nearby Galaxies: Measuring Where Gas Forms Stars Effectively. , 136:2782–2845.

Leroy, A. K., Walter, F., Sandstrom, K., Schruba, A., Munoz-Mateos, J.-C., Bigiel, F., Bolatto, A., Brinks, E., de Blok, W. J. G., Meidt, S., Rix, H.-W., Rosolowsky, E., Schinnerer, E., Schuster, K.-F., and Usero, A. (2013b). Molecular Gas and Star Formation in nearby Disk Galaxies. , 146(2):19.

Liszt, H. S., Wilson, R. W., Penzias, A. A., Jefferts, K. B., Wannier, P. G., and Solomon, P. M. (1974). CO and CS in the Orion Nebula. , 190:557–564.

Lombardi, M., Alves, J., and Lada, C. J. (2010). Larson's third law and the universality of molecular cloud structure. , 519:L7.

Longmore, S. N., Bally, J., Testi, L., Purcell, C. R., Walsh, A. J., Bressert, E., Pestalozzi, M., Molinari, S., Ott, J., Cortese, L., Battersby, C., Murray, N., Lee, E., Kruijssen, J. M. D., Schisano, E., and Elia, D. (2013a). Variations in the Galactic star formation rate and density thresholds for star formation. , 429:987–1000.

Longmore, S. N., Kruijssen, J. M. D., Bally, J., Ott, J., Testi, L., Rathborne, J., Bastian, N., Bressert, E., Molinari, S., Battersby, C., and Walsh, A. J. (2013b). Candidate super star cluster progenitor gas clouds possibly triggered by close passage to Sgr a*. , 433:L15–L19.

Mac Low, M. M. and Ossenkopf, V. (2000). Characterizing the structure of interstellar turbulence. , 353:339–348.

Madau, P. and Dickinson, M. (2014). Cosmic Star-Formation History. , 52:415–486.

Matzner, C. D. and McKee, C. F. (2000). Efficiencies of Low-Mass Star and Star Cluster Formation. , 545(1):364–378.

McCrea, W. H. and McNally, D. (1960). The formation of Population I stars, II. The formation of molecular hydrogen in interstellar matter. , 121:238.

McKee, C. F. and Ostriker, E. C. (2007). Theory of Star Formation. , 45(1):565–687.

Meidt, S. E., Hughes, A., Dobbs, C. L., Pety, J., Thompson, T. A., García-Burillo, S., Leroy, A. K., Schinnerer, E., Colombo, D., Querejeta, M., Kramer, C., Schuster, K. F., and Dumas, G. (2015). Short GMC Lifetimes: An Observational Estimate with the PdBI Arcsecond Whirlpool Survey (PAWS). , 806(1):72.

Meidt, S. E., Schinnerer, E., García-Burillo, S., Hughes, A., Colombo, D., Pety, J., Dobbs, C. L., Schuster, K. F., Kramer, C., Leroy, A. K., Dumas, G., and Thompson, T. A. (2013). Gas Kinematics on Giant Molecular Cloud Scales in M51 with PAWS: Cloud Stabilization through Dynamical Pressure. , 779:45.

Miura, R. E., Kohno, K., Tosaki, T., Espada, D., Hwang, N., Kuno, N., Okumura, S. K., Hirota, A., Muraoka, K., Onodera, S., Minamidani, T., Komugi, S., Nakanishi, K., Sawada, T., Kaneko, H., and Kawabe, R. (2012). Giant Molecular Cloud Evolutions in the Nearby Spiral Galaxy M33. , 761(1):37.

Miville-Deschênes, M.-A., Murray, N., and Lee, E. J. (2017). Physical Properties of Molecular Clouds for the Entire Milky Way Disk. , 834(1):57.

Morris, M. and Rickard, L. J. (1982). Molecular clouds in galaxies. , 20:517–545.

Morris, M. and Serabyn, E. (1996). The Galactic Center Environment. , 34:645–702.

Mouschovias, T. C. (1987). Star formation in magnetic interstellar clouds: I. Interplay between theory and observations. In Morfill, G. E. and Scholer, M., editors, *NATO ASIC Proc. 210: Physical Processes in Interstellar Clouds*, pages 453–489.

Murray, N. (2011). Star Formation Efficiencies and Lifetimes of Giant Molecular Clouds in the Milky Way. , 729(2):133.

Myers, P. C. and Benson, P. J. (1983). Dense cores in dark clouds. II. NH3 observations and star formation. , 266:309–320.

Nordlund, Å. K. and Padoan, P. (1999). The Density PDFs of Supersonic Random Flows. In Franco, J. and Carraminana, A., editors, *Interstellar Turbulence*, page 218.

Oka, T., Hasegawa, T., Sato, F., Tsuboi, M., Miyazaki, A., and Sugimoto, M. (2001). Statistical Properties of Molecular Clouds in the Galactic Center. , 562(1):348–362.

Oort, J. H. (1954). Outline of a theory on the origin and acceleration of interstellar clouds and O associations. , 12:177.

Oort, J. H. and Spitzer, Lyman, J. (1955). Acceleration of Interstellar Clouds by O-Type Stars. , 121:6.

Ostriker, E. C., Gammie, C. F., and Stone, J. M. (1999). Kinetic and Structural Evolution of Self-gravitating, Magnetized Clouds: 2.5-dimensional Simulations of Decaying Turbulence. , 513(1):259–274.

Ostriker, E. C. and Shetty, R. (2011). Maximally Star-forming Galactic Disks. I. Starburst Regulation Via Feedback-driven Turbulence. , 731(1):41.

Ostriker, E. C., Stone, J. M., and Gammie, C. F. (2001). Density, Velocity, and Magnetic Field Structure in Turbulent Molecular Cloud Models. , 546(2):980–1005.

Padoan, P. (1995). Supersonic turbulent flows and the fragmentation of a cold medium. , 277(2):377–388.

Padoan, P., Federrath, C., Chabrier, G., Evans, N. J., I., Johnstone, D., Jørgensen, J. K., McKee, C. F., and Nordlund, Å. (2014). The Star Formation Rate of Molecular Clouds. In Beuther, H., Klessen, R. S., Dullemond, C. P., and Henning, T., editors, *Protostars and Planets VI*, page 77.

Padoan, P. and Nordlund, Å. (2011). The Star Formation Rate of Supersonic Magnetohydrodynamic Turbulence. , 730(1):40.

Pelupessy, F. I., Papadopoulos, P. P., and van der Werf, P. (2006). Incorporating the Molecular Gas Phase in Galaxy-sized Numerical Simulations: First Applications in Dwarf Galaxies. , 645(2):1024–1042.

Pfenniger, D. and Combes, F. (1994). Is dark matter in spiral galaxies cold gas? II. Fractal models and star non-formation. , 285:94–118.

Rathborne, J. M., Longmore, S. N., Jackson, J. M., Kruijssen, J. M. D., Alves, J. F., Bally, J., Bastian, N., Contreras, Y., Foster, J. B., Garay, G., Testi, L., and Walsh, A. J. (2014). Turbulence Sets the Initial Conditions for Star Formation in High-pressure Environments. , 795(2):L25.

Rice, T. S., Goodman, A. A., Bergin, E. A., Beaumont, C., and Dame, T. M. (2016). A Uniform Catalog of Molecular Clouds in the Milky Way. , 822(1):52.

Roberts, W. W. (1969). Large-Scale Shock Formation in Spiral Galaxies and its Implications on Star Formation. , 158:123.

Roman-Duval, J., Jackson, J. M., Heyer, M., Rathborne, J., and Simon, R. (2010). Physical Properties and Galactic Distribution of Molecular Clouds Identified in the Galactic Ring Survey. , 723(1):492–507.

Rosolowsky, E., Engargiola, G., Plambeck, R., and Blitz, L. (2003). Giant Molecular Clouds in M33. II. High-Resolution Observations. , 599(1):258–274.

Rosolowsky, E. and Leroy, A. (2006). Bias-free Measurement of Giant Molecular Cloud Properties. , 118(842):590–610.

Rosolowsky, E. W., Goodman, A. A., Wilner, D. J., and Williams, J. P. (1999). The Spectral Correlation Function: A New Tool for Analyzing Spectral Line Maps. , 524(2):887–894.

Routly, P. M. and Spitzer, Lyman, J. (1952). A Comparison of the Components in Interstellar Sodium and Calcium. , 115:227.

Rownd, B. K. and Young, J. S. (1999). The Star Formation Efficiency within Galaxies. , 118(2):670–704.

Saintonge, A., Kauffmann, G., Kramer, C., Tacconi, L. J., Buchbender, C., Catinella, B., Fabello, S., Graciá-Carpio, J., Wang, J., Cortese, L., Fu, J., Genzel, R., Giovanelli, R., Guo, Q., Haynes, M. P., Heckman, T. M., Krumholz, M. R., Lemonias, J., Li, C., Moran, S., Rodriguez-Fernandez, N., Schiminovich, D., Schuster, K., and Sievers, A. (2011a). COLD GASS, an IRAM legacy survey of molecular gas in massive galaxies - I. Relations between H_2, H I, stellar content and structural properties. , 415(1):32–60.

Saintonge, A., Kauffmann, G., Wang, J., Kramer, C., Tacconi, L. J., Buchbender, C., Catinella, B., Graciá-Carpio, J., Cortese, L., Fabello, S., Fu, J., Genzel, R., Giovanelli, R., Guo, Q., Haynes, M. P., Heckman, T. M., Krumholz, M. R., Lemonias, J., Li, C., Moran, S., Rodriguez-Fernand ez, N., Schiminovich, D., Schuster, K., and Sievers, A. (2011b). COLD GASS, an IRAM legacy survey of molecular gas in massive galaxies - II. The non-universality of the molecular gas depletion time-scale. , 415(1):61–76.

Sanders, D. B., Solomon, P. M., and Scoville, N. Z. (1984). Giant molecular clouds in the Galaxy. I - The axisymmetric distribution of H2. , 276:182–203.

Scalo, J. (1990). *Perception of interstellar structure - Facing complexity*, volume 162 of *Astrophysics and Space Science Library*, pages 151–176.

Scalo, J. M. (1985). Fragmentation and hierarchical structure in the interstellar medium. In Black, D. C. and Matthews, M. S., editors, *Protostars and Planets II*, pages 201–296.

Schinnerer, E., Meidt, S. E., Pety, J., Hughes, A., Colombo, D., García-Burillo, S., Schuster, K. F., Dumas, G., Dobbs, C. L., Leroy, A. K., Kramer, C., Thompson, T. A., and Regan, M. W. (2013). The PdBI Arcsecond Whirlpool Survey (PAWS). I. A Cloud-scale/Multi-wavelength View of the Interstellar Medium in a Grand-design Spiral Galaxy. , 779(1):42.

Schmidt, M. (1959). The Rate of Star Formation. , 129:243.

Schruba, A., Leroy, A. K., Walter, F., Bigiel, F., Brinks, E., de Blok, W. J. G., Dumas, G., Kramer, C., Rosolowsky, E., Sandstrom, K., Schuster, K., Usero, A., Weiss, A., and Wiesemeyer, H. (2011). A Molecular Star Formation Law in the Atomic-gas-dominated Regime in Nearby Galaxies. , 142:37.

Scoville, N. Z. and Hersh, K. (1979). Collisional growth of giant molecular clouds. , 229:578–582.

Scoville, N. Z. and Solomon, P. M. (1975). Molecular clouds in the Galaxy. , 199:L105–L109.

Scoville, N. Z., Yun, M. S., Clemens, D. P., Sand ers, D. B., and Waller, W. H. (1987). Molecular Clouds and Cloud Cores in the Inner Galaxy. , 63:821.

Semenov, V. A., Kravtsov, A. V., and Gnedin, N. Y. (2017). The Physical Origin of Long Gas Depletion Times in Galaxies. , 845(2):133.

Semenov, V. A., Kravtsov, A. V., and Gnedin, N. Y. (2018). How Galaxies Form Stars: The Connection between Local and Global Star Formation in Galaxy Simulations. , 861(1):4.

Semenov, V. A., Kravtsov, A. V., and Gnedin, N. Y. (2019). What Sets the Slope of the Molecular Kennicutt-Schmidt Relation? , 870(2):79.

Shetty, R., Beaumont, C. N., Burton, M. G., Kelly, B. C., and Klessen, R. S. (2012). The linewidth-size relationship in the dense interstellar medium of the Central Molecular Zone. , 425(1):720–729.

Solomon, P. M., Rivolo, A. R., Barrett, J., and Yahil, A. (1987). Mass, Luminosity, and Line Width Relations of Galactic Molecular Clouds. , 319:730.

Solomon, P. M., Sanders, D. B., and Scoville, N. Z. (1979). Giant Molecular Clouds in the Galaxy; Distribution, Mass, Size and Age. In Burton, W. B., editor, *The Large-Scale Characteristics of the Galaxy*, volume 84 of *IAU Symposium*, page 35.

Solomon, P. M. and Vanden Bout, P. A. (2005). Molecular Gas at High Redshift. , 43(1):677–725.

Spitzer, Lyman, J. (1956). On a Possible Interstellar Galactic Corona. , 124:20.

Sun, J., Leroy, A. K., Ostriker, E. C., Hughes, A., Rosolowsky, E., Schruba, A., Schinnerer, E., Blanc, G. A., Faesi, C., Kruijssen, J. M. D., Meidt, S., Utomo, D., Bigiel, F., Bolatto, A. D., Chevance, M., Chiang, I.-D., Dale, D., Emsellem, E., Glover, S. C. O., Grasha, K., Henshaw, J., Herrera, C. N., Jimenez-Donaire, M. J., Lee, J. C., Pety, J., Querejeta, M., Saito, T., Sandstrom, K., and Usero, A. (2020). Dynamical

Equilibrium in the Molecular ISM in 28 Nearby Star-Forming Galaxies. *arXiv e-prints*, page arXiv:2002.08964.

Sun, J., Leroy, A. K., Schruba, A., Rosolowsky, E., Hughes, A., Kruijssen, J. M. D., Meidt, S., Schinnerer, E., Blanc, G. A., Bigiel, F., Bolatto, A. D., Chevance, M., Groves, B., Herrera, C. N., Hygate, A. P. S., Pety, J., Querejeta, M., Usero, A., and Utomo, D. (2018). Cloud-scale Molecular Gas Properties in 15 Nearby Galaxies. , 860:172.

Tacchella, S., Forbes, J. C., and Caplar, N. (2020). Stochastic modelling of star-formation histories II: star-formation variability from molecular clouds and gas inflow. , 497(1):698–725.

Tan, J. C. (2000). Star Formation Rates in Disk Galaxies and Circumnuclear Starbursts from Cloud Collisions. , 536:173.

Tasker, E. J. (2011). Star Formation in Disk Galaxies. II. The Effect Of Star Formation and Photoelectric Heating on the Formation and Evolution of Giant Molecular Clouds. , 730:11.

Tasker, E. J. and Tan, J. C. (2009). Star Formation in Disk Galaxies. I. Formation and Evolution of Giant Molecular Clouds via Gravitational Instability and Cloud Collisions. , 700:358–375.

Tress, R. G., Smith, R. J., Sormani, M. C., Glover, S. C. O., Klessen, R. S., Mac Low, M.-M., and Clark, P. C. (2020). Simulations of the star-forming molecular gas in an interacting M51-like galaxy. , 492(2):2973–2995.

Usero, A., Leroy, A. K., Walter, F., Schruba, A., García-Burillo, S., Sand strom, K., Bigiel, F., Brinks, E., Kramer, C., and Rosolowsky, E. (2015). Variations in the Star Formation Efficiency of the Dense Molecular Gas across the Disks of Star-forming Galaxies. , 150(4):115.

Utomo, D., Sun, J., Leroy, A. K., Kruijssen, J. M. D., Schinnerer, E., Schruba, A., Bigiel, F., Blanc, G. A., Chevance, M., and Emsellem, E. (2018). Star Formation Efficiency per Free-fall Time in nearby Galaxies. , 861(2):L18.

van de Hulst, H. C. (1948). *Evolution and Physics of Solid Particles*, volume 7, page 73.

van Dishoeck, E. F. and Black, J. H. (1986). Comprehensive Models of Diffuse Interstellar Clouds: Physical Conditions and Molecular Abundances. , 62:109.

Vazquez-Semadeni, E. (1994). Hierarchical Structure in Nearly Pressureless Flows as a Consequence of Self-similar Statistics. , 423:681.

Vázquez-Semadeni, E. (2004). Fragmentation and Structure Formation. , 292(1):187–192.

Vázquez-Semadeni, E., Gómez, G. C., Jappsen, A. K., Ballesteros-Paredes, J., González, R. F., and Klessen, R. S. (2007). Molecular Cloud Evolution. II. From Cloud Formation to the Early Stages of Star Formation in Decaying Conditions. , 657(2):870–883.

Vázquez-Semadeni, E., Ryu, D., Passot, T., González, R. F., and Gazol, A. (2006). Molecular Cloud Evolution. I. Molecular Cloud and Thin Cold Neutral Medium Sheet Formation. , 643(1):245–259.

Vestuto, J. G., Ostriker, E. C., and Stone, J. M. (2003). Spectral Properties of Compressible Magnetohydrodynamic Turbulence from Numerical Simulations. , 590(2):858–873.

Wada, K. and Norman, C. A. (2001). Numerical Models of the Multiphase Interstellar Matter with Stellar Energy Feedback on a Galactic Scale. , 547(1):172–186.

Whitworth, A., Lomax, O., Balfour, S., Mège, P., Zavagno, A., and Deharveng, L. (2018). Bipolar H II regions produced by cloud-cloud collisions. , 70:S55.

Williams, J. P. and McKee, C. F. (1997). The Galactic Distribution of OB Associations in Molecular Clouds. , 476(1):166–183.

Wilson, R. W., Jefferts, K. B., and Penzias, A. A. (1970). Carbon Monoxide in the Orion Nebula. , 161:L43.

Wong, T. and Blitz, L. (2002). The Relationship between Gas Content and Star Formation in Molecule-rich Spiral Galaxies. , 569(1):157–183.

Wyder, T. K., Martin, D. C., Barlow, T. A., Foster, K., Friedman, P. G., Morrissey, P., Neff, S. G., Neill, J. D., Schiminovich, D., Seibert, M., Bianchi, L., Donas, J., Heckman, T. M., Lee, Y.-W., Madore, B. F., Milliard, B., Rich, R. M., Szalay, A. S., and Yi, S. K. (2009). The Star Formation Law at Low Surface Density. , 696(2):1834–1853.

Wyse, R. F. G. (1986). A Schmidt Law for the Molecular Gas Profiles of Disk Galaxies. , 311:L41.

Wyse, R. F. G. and Silk, J. (1989). Star Formation Rates and Abundance Gradients in Disk Galaxies. , 339:700.

Zamora-Avilés, M. and Vázquez-Semadeni, E. (2014). An Evolutionary Model for Collapsing Molecular Clouds and their Star Formation Activity. II. Mass Dependence of the Star Formation Rate. , 793(2):84.

Zuckerman, B. and Palmer, P. (1974). Radio radiation from interstellar molecules. , 12:279–313.